

UC Berkeley

UC Berkeley Electronic Theses and Dissertations

Title

Development of Novel Small Scale Mechanical Tests to Assess the Mechanical Properties of Ex-Service Inconel X-750 CANDU Reactor Components

Permalink

<https://escholarship.org/uc/item/99k9w508>

Author

Howard, Cameron

Publication Date

2018

Peer reviewed|Thesis/dissertation

Development of Novel Small Scale Mechanical Tests to Assess the Mechanical
Properties of Ex-Service Inconel X-750 CANDU Reactor Components

by

Cameron Boyd Howard

A dissertation in partial satisfaction of the requirements for the degree of

Doctor of Philosophy

in

Engineering – Nuclear Engineering

in the

Graduate Division

of the

University of California, Berkeley

Dissertation Committee:

Professor Peter Hosemann, Chair

Professor Per Peterson

Professor Andrew M. Minor

Spring 2018

Abstract

Development of Novel Small Scale Mechanical Tests to Assess the Mechanical Properties of Ex-Service Inconel X-750 CANDU Reactor Components

by

Cameron Boyd Howard

Doctor of Philosophy in Nuclear Engineering

University of California, Berkeley

Professor Peter Hosemann, Chair

Inconel X-750 is a precipitation hardened nickel superalloy designed to have high strength and creep resistance at elevated temperatures. In Canada Deuterium Uranium (CANDU) reactors, this material serves as tight fitting fuel channel annulus spacers in the form of springs separating the cold calandria tube from the hot pressure tube. Unlike light water reactors (LWRs), CANDU reactors have an elevated thermal neutron flux spectrum which amplifies nickel transmutation reactions, producing more radiation damage and increased amounts of internal hydrogen and helium compared to all other current generation reactors. Bulk component testing performed over the last few years indicates that these spacers are losing ductility and strength after time in service, and that the quantity of this loss is dependent on the irradiation temperature and dose. In addition, observations of fracture surfaces reveal intergranular failure and transmission electron microscopy (TEM) shows that helium bubbles preferentially align along grain boundaries. However, a dearth of knowledge on the mechanical properties of these components at high dose exists because only one to three component tests are performed at each irradiation condition inside hot cells, and these component tests produce complicated stress states, making the extraction of yield stresses and failure stresses challenging. Thus, two first of their kind, in-situ, small scale mechanical tests (SSMTs) employing scanning electron microscopy (SEM) and focused ion beam (FIB) techniques were developed to test components irradiated to doses of 53, 67, and 81 dpa in CANDU reactors at average irradiation temperatures of 180 °C and 300 °C. The first, a lift-out, three-point bend test quantified the yield stresses of the components as a function of irradiation temperature and dose. Material irradiated at the higher temperature undergoes significant yield strength increases up to 1 GPa, whereas this is negligible for material irradiated at the lower temperature (≤ 310 MPa). Grain boundary cracking after yielding was observed in specimens irradiated to 67 dpa at 180 °C. The second new SSMT is a push-to-pull, micro-tensile test

quantifying the yield strengths, failure strengths, and total elongations of the components as a function of irradiation temperature and dose. For specimens irradiated to 81 dpa, intergranular failure was directly observed, so failure stresses quantify grain boundary strengths. Both novel SSMTs also revealed significant regional differences in mechanical properties between the inner diameter, center, and outer diameter due to variations in the cold working and grinding of the component that went undetected in bulk component testing. The conclusion of this work is a detailed analysis of the degradation of an Inconel X-750 CANDU component in terms of its quantitative mechanical properties through the invention of two novel SSMTs. These new testing methods and analyses are applicable for assessing the mechanical ageing of other reactor core components.

Contents

Dedication

List of tables

List of figures

Acknowledgements

Publications

1 Motivation

1.1 The Need for Current and Future Clean Nuclear Energy

1.2 CANDU Life Management Surveillance Programs

1.3 Relevance to Reactor Lifetime Extension Programs

1.4 The Need for SSMTs

1.5 Research Goals

2 Background: A Review of Small Scale Mechanical Testing (SSMT) Applied to Nuclear Materials

2.1 Introduction

2.2 Small Shear Punch Test (SPT)/Miniaturized Disk Bend Test (MDBT)

2.3 Miniaturized Charpy Subsize Fracture Tests

2.4 Microhardness Tests

2.5 Nanoindentation Tests

2.6 Micro-pillar Compression Tests

2.7 Micro-tensile Tests

2.8 Micro-Bend Tests

2.8.1 Micro-Cantilever Tests

2.8.2 Micro-Fatigue Tests

2.9 In-Situ Transmission Electron Microscope (TEM) Tests

3 Materials and Radiation Effects Theory

3.1 Nickel-Based Superalloys

3.2 Nickel-Based Superalloys in Nuclear Reactors

- 3.2.1 Inconel X-750 in CANDU Reactors
- 3.3 Radiation Damage Basics
 - 3.3.1 Radiation Damage in the CANDU Core
 - 3.3.1.1 Fast Neutron Damage
 - 3.3.1.2 Thermal Neutron Damage: (n,p) and (n, α) Transmutations
 - 3.3.1.3 Point Defects
 - 3.3.1.4 Helium and Hydrogen Gas Production
 - 3.3.1.5 Helium Bubble Nucleation and Growth
 - 3.3.1.6 Helium Bubble Pressure
 - 3.3.2 Mechanical Properties Evolution of Irradiated Nickel Superalloys
 - 3.3.2.1 Radiation Hardening Mechanisms
 - 3.3.2.2 γ' Disordering and Dissolution
 - 3.3.2.3 Dose Evolution of Mechanical Properties
 - 3.3.2.4 Mechanisms for Grain Boundary Embrittlement
- 4 Experimental Procedures
 - 4.1 Inconel X-750 Coils
 - 4.1.1 Ex-Service Neutron Irradiated Inconel X-750
 - 4.2 Sample Preparation
 - 4.2.1 Sample Preparation of Non-Irradiated Inconel X-750
 - 4.2.2 Sample Preparation of Neutron Irradiated Inconel X-750
 - 4.3 Bulk Component Crush Testing
 - 4.4 Microhardness Testing
 - 4.5 In-Situ Micro-Three-Point Bend Testing
 - 4.5.1 Micro-Three-Point Bend FIB Specimen Preparation
 - 4.5.2 Electron Backscattered Diffraction Pre-Test Analysis
 - 4.5.3 Testing Procedures
 - 4.6 In-Situ Micro-Push-to-Pull Tensile Testing

- 4.6.1 Push-to Pull Device
- 4.6.2 Tensile Specimen Sample Preparation
- 4.6.3 Electron Backscattered Diffraction Pre-Test Analysis
- 4.6.4 Testing Procedures
- 4.7 Nanoindentation: Non-Irradiated Inconel X-750
- 4.8 Room Temperature Ion Irradiation Studies
 - 4.8.1 Nanoindentation: Ion Irradiated Inconel X-750
 - 4.8.2 In-Situ Gripper Micro-Tensile Testing
- 5 Results
 - 5.1 Bulk Component Crush Testing
 - 5.2 Microhardness Testing
 - 5.3 In-Situ Micro-Three-Point Bend Testing
 - 5.3.1 Non-Irradiated Outer Edge Specimens
 - 5.3.2 Non-Irradiated Center Specimens
 - 5.3.3 54 dpa Low Irradiation Temperature Specimens
 - 5.3.4 54 dpa High Irradiation Temperature Specimens
 - 5.3.5 67 dpa Low Irradiation Temperature Specimens
 - 5.3.6 67 dpa High Irradiation Temperature Specimens
 - 5.3.7 Summary
 - 5.4 In-Situ Micro-Push-to-Pull Tensile Testing
 - 5.4.1 Non-Irradiated Outer Edge Specimens
 - 5.4.2 Non-Irradiated Center Specimens
 - 5.4.3 Non-Irradiated Inner Edge Specimens
 - 5.4.4 67 dpa Low Irradiation Temperature Specimens
 - 5.4.5 67 dpa High Irradiation Temperature Specimens
 - 5.4.6 81 dpa Low Irradiation Temperature Specimen
 - 5.4.7 81 dpa High Irradiation Temperature Specimens

5.4.8	Summary
5.5	Nanoindentation: Non-Irradiated Inconel X-750
5.6	Room Temperature Ion Irradiation Studies
5.6.1	Nanoindentation: Ion Irradiated Inconel X-750
5.6.2	In-Situ Gripper Micro-Tensile Testing
5.6.3	Summary
6	Discussion
6.1	In-Situ Micro-Three-Point Bend Testing
6.1.1	Testing Limitations
6.2	In-Situ Micro-Push-to-Pull Tensile Testing
6.2.1	Quantifying Cold Working Effects from Material Processing
6.2.2	Critical Resolved Shear Stress
6.2.3	Yield Strengths
6.2.4	Failure Strengths and Total Elongations
6.2.5	Grain Boundary Strengths
6.2.6	Resolved Normal Stresses on High Angle Grain Boundaries
6.2.7	Deformation Mechanisms
6.2.8	Testing Challenges
6.3	Room Temperature Ion Irradiation Studies
6.3.1	Nanoindentation: Ion Irradiated Inconel X-750
6.3.2	In-Situ Gripper Micro-Tensile Testing
6.4	Future Work with SSMT Tensile Testing
7	Conclusions
8	References

Dedication

This work is dedicated to my parents, Michelle Howard and Dewey Howard Jr. Without their love and incredible work ethic and sacrifice throughout my entire life, this journey would not have been possible.

List of Tables

Table 1. Ratio of Yield Strength to Shear Strength for Alloys with Indicated Base Element

Table 2. Room Temperature Properties of Commercially Pure (99.6%) Ni

Table 3. ^{58}Ni and ^{59}Ni transmutation reactions and their associated σ_{a-th} and displacement damage

Table 4. Chemical composition in wt. % and heat treatments for Inconel X-750 coils [191]

Table 5. Room Temperature Properties of Inconel X-750 [191]

Table 6. Ex-Service Neutron Irradiated Inconel X-750

Table 7. Struers Polishing Formula for Preparing Ni-Based Superalloys

Table 8. Root-Mean-Squared Absolute and Normalized Grain Interior Misorientations of Inconel X-750

Table 9. He^{2+} Ion Energies Exiting the Degraded Wheel and Their Associated Stopping Peak Depths in the Inconel X-750 Spacers

Table 10: Micro Three-Point Bend Yield Strength and Critical Resolved Shear Stress (CRSS) of Inconel X-750 Spring Material

Table 11. Mechanical Data Summary Table for Push-to-Pull Inconel X-750 Micro-tensile Specimens

Table 12. Mechanical Properties of Outer Edge Bulk Micro-Tensile Specimens

List of Figures

Figure 1. The temperature and dose range requirements for in-core structural materials that will operate in each of the 8 next generation reactor design concepts [8].

Figure 2. CANDU fuel channel with Inconel X-750 spacer coil highlighted [9]

Figure 3. Inconel X-750 spacer (a) before service and (b) ex-service view while handling for post-irradiation examinations inside the hot cell

Figure 4. Dose rate estimate for a bulk crush test specimen

Figure 5. Schematic of miniaturized disk bend test (MDBT) taken from [10]. The irradiated specimen is housed in a cylindrical die and pressed into a cavity as seen in (a). This set up is under an enclosed environment with temperature control as seen in (b). Performing tests at elevated temperature is also an option using an induction heating coil as seen in (c).

Figure 6. Representative shear punch test load-displacement curves for austenitic 12Cr-1Mo steel taken from [11]

Figure 7. Plotted linear correlations between uniaxial yield stress and total elongation and shear punch test effective yield stress and total elongation [17]

Figure 8. Representative subsize CVN specimen (center) with dimensions 3.33 mm x 3.33 mm x 16.7 mm in comparison to a standard CVN specimen (bottom) with dimensions 10 mm x 10 mm x 55 mm [17]

Figure 9. The absorbed energy as a function of test temperature for full sized ASTM (10 mm x 10 mm x 50 mm) CVN specimens compared against half-sized and one-third sized CVN specimens for a 9Cr-2W-0.1C ferritic steel [36]

Figure 10. CVN test specimen dimensions

Figure 11. Master empirical correlation curves plotting change in uniaxial tensile yield stress versus change in Vickers microhardness for austenitic stainless steels (a) and ferritic steels (b). [54]

Figure 12. Nanoindentation load versus displacement curves, indicating the peak load, P_{max} , displacement at peak load, h_{max} , and final contact depth after unloading, h_f in (a). The initial unloading stiffness, S , shown in both (a) and (b), determines the contact depth, h_c , along with a geometric constant, ϵ , as shown in (b) [63].

Figure 13. Schematic depiction of nanoindentation performed on ion irradiated materials (a) parallel to the incident ion beam and (b) perpendicular to the incident ion beam. Shallow ion irradiated samples are exemplified by the dashed line and deep ion implanted samples by the dotted line [75]

Figure 14. 200 nm deep cross-section nanoindentation of 10 dpa proton irradiated 304 SS with overlaid SRIM dose profile [78]

Figure 15. Measured tensile properties plotted against stress values calculated from two nanoindentation hardness-stress correlations: an absolute correlation (left) and change in stress correlation (right). The absolute correlation provides more accurate predictions of a non-irradiated material's flow stress and an irradiated material's yield stress. [81]

Figure 16. Continuous stiffness measurement (CSM) nanoindentation technique applied to three advanced engineering alloys depicting their hardness vs. depth profiles [82]

Figure 17. Indentation stress-strain curves calculated from spherical nanoindentation experiments performed on ion irradiated tungsten [89, 90]. Non-irradiated tungsten, red in (a) and orange in (b), shows behavior much like its predicted Hertzian elastic response up until yield. The irradiated yield and flow stresses, blue and green in (a) and black in (b) have increased noticeably.

Figure 18. Nanoindentation in SiC coating shell of TRISO advanced nuclear fuel form inducing cracking. (a) optical image (b) scanning probe microscopy (SPM) image of an indent with surrounding cracks, (c) high resolution image revealing the transgranular nature of the crack [97]

Figure 19. High temperature cross-section nanoindentation hardness profiles of proton irradiated 304 SS indicating clear sharp transitions between irradiated and non-irradiated material [106]

Figure 20. Nanoindentation creep curves depicting the strain rate as a function of holding time for a proton irradiated and a non-irradiated PM 2000 ODS steel [108]

Figure 21. Size effect strengthening in single-grained fcc micropillars. Normalized shear flow stress is plotted against specimen characteristic length (diameter normalized by Burgers vector) [113]

Figure 22. Schematic of size effects in polycrystalline micro-specimens, with a standard material shown in black and a high defect density/irradiated material shown in red. Adapted from [117].

Figure 23. Three-step process developed at UC Berkeley to efficiently fabricate batches of 4 square micropillars along the sample edge in preparation for in-situ SEM testing, where d is the final desired pillar length and width. The process is described as follows:

- 1) A rough trench is milled out at high current (1-15 nA) behind the edge region where the pillars will be made looking down onto the top surface of the sample.
- 2) The sample is viewed looking down onto the side surface, and rough pillar shapes are milled into the “wall” of material at high current (1-7 nA). Note that in this step, the maximum height of the micropillar is determined. For accurate mechanical properties measurements, the final pillar height should be 2-3 times the pillar width [118].
- 3) The sample is viewed from the top again and final polishing/ cleaning of the front and back pillar surfaces is performed at low currents (1.5-100 pA). Counter tilting of 1° is performed to reduce taper.
- 4) Similar cleaning is performed on the pillar side and top surfaces at low currents with the sample oriented as seen in step 2.

Figure 24. Experimental set up for fabricating micropillars in three distinct irradiation regions from the same grain of a proton irradiated 304 SS specimen and the resultant microcompression engineering stress-strain curves indicating the relative differences in mechanical properties [124]

Figure 25. Micropillar compression of SiC/SiC matrix-fiber composites: (a) pillar fabrication schematic, (b) resolved stresses under compression, (c) representative pillar pre-testing, (d) representative pillar with fractured interface post-test, (e) determination of debonding stress and internal friction coefficient according to the Mohr-Coulomb criterion [126]

Figure 26. Microcompression testing of irradiated and non-irradiated 304 SS at elevated temperature. (a) micropillar compression true stress-true strain curves, post-test SEM images of a representative (b) non-irradiated micropillar (many small dislocation slip steps) and (c) irradiated micropillar (few large dislocation slip step channels), and yield strength, (d), and critical resolved shear stress, (e), versus temperature [134]

Figure 27. Lift-out pillar compression technique: (a) large lift-out foil positioned over top of a flat Si stub, (b) a rough lift-out pillar mounted on top of the Si stub with a Pt GIS, (c) top and side images of a finished, cleaned lift-out pillar, (d) engineering stress-strain curves for irradiated and non-irradiated MA 957 lift-out pillars. Enhanced from [136]

Figure 28. Helium Ion Microscope (HIM) image of an array of micropillars manufactured on a lift-out foil sitting on top of a Mo TEM grid post. The pillars boxed in red have been implanted with a flux of 10^{18} He ions/cm². [137]

Figure 29. Bulk micro-tensile testing of proton irradiated 304 SS. (a) SEM image of pre-test experimental set up depicting tungsten gripper aligned to pull a test specimen. (b) Engineering stress-strain curves of irradiated and non-irradiated micro-tensile specimens. (c) Post-irradiation annealed micro-tensile specimens indicate some recovery of ductility and reduction in yield strength increase. [141]

Figure 30. Hook-based micro-tensile testing design which allows for larger sized specimens up to maximum approximate size $15\ \mu\text{m} \times 15\ \mu\text{m} \times 30\ \mu\text{m}$ to be tested in-situ in the SEM. An example single-crystal nickel specimen from [142] is depicted.

Figure 31. A lift-out, micro-tensile, cantilever-based, in-situ SSMT: (a) View of the complete experimental set up, (b) grain boundary oxidized Alloy 600 specimen notched and tested in a mixed-mode state producing grain boundary failure [143], (c) helium implanted 316 SS notched grain boundary tested in a pure debonding stress state inducing brittle grain boundary fracture [144]

Figure 32. Notched house-shaped micro-cantilever [145]

Figure 33. Array of micro-cantilevers milled into a well prepared surface of irradiated Fe-12% Cr. Accurate testing with good alignment can be performed easily ex-situ using scanning probe microscopy (SPM) to identify the loading point in the center of each cantilever [89].

Figure 34. Evidence of no correlation between grain boundary misorientation angle (boundary type) and fracture toughness of the associated fractured grain boundary in an oxidized Alloy 600 material exposed to pressurized water reactor primary water for 4500 hours [150]

Figure 35. Micro-cantilever testing of SiC coating layer encasing TRISO fuel material: (a) Batch of cantilevers milled into outer SiC coating in a polished cross-section of TRISO fuel material, (b) Fractured SiC micro-cantilever with blunt notch [97], (c) Fractured silicon oxide cantilever with sharp notch. The initial crack length, a , generated by the sharp notch can be easily measured [151].

Figure 36. Schematic of edge micro-cantilevers FIB milled into two passive oxide layers formed on a F/M steel exposed to a high temperature liquid metal environment. Testing of the micro-cantilever cut in cross-section revealed the existence of a high porosity region within the inner oxide serving as a fracture initiation point [152].

Figure 37. SEM image of a lift-out 304 SS neutron irradiated micro-cantilever about to be tested [117]

Figure 38. (a) sample holder machined for holding mini rod specimens to be electropolished, (b) electro-chemically sharpened needle tip, (c) FIB machined micro-bending beam, (d) SEM image of a tungsten wire with a FIB fabricated dove-tailed slit for gripping, (e) schematic depicting a micro-fatigue specimen with its labelled dimensions width, w , length, l , bending length l_b , and thickness t/h . Relative intensities of the elastic, $\epsilon_{el}(y)$, and plastic, $\epsilon_{pl}(y)$, strains and stress, $\sigma(y)$, along the y -axis, and the normalized bending moment $M_b(x)$ along the x -axis are drawn. [154-156]

Figure 39. Measured raw load vs. displacement data with insets showing SEM images recorded in-situ during a loading cycle to depict the contact between beam and gripper using to correct for compliance. The aligned beam before testing is shown with its measured length, L , and bending length, L_b . The sinusoidal loading cycle, displacement vs. time, is shown on the lower right. [156]

Figure 40. EBSD maps depicting the microstructural evolution of HPT Cu during cyclic loading after a specified number of cycles and strain amplitude. In location 1, the small orange grain is eaten by the larger green grain which grows to take its place. In location 2, the yellow-green grain is created and grows, and in location 3, the subgrains within the magenta grain are erased. [155]

Figure 41. (a) Selected stress-strain curves at cycles number 1, 10, 50, 100 for the plastic strain amplitude $\epsilon_a = 8.3 \times 10^{-3}$, (b) yield strength and maximum stress as a function of cycle number, (c) cyclic stress-strain curve, (d) energy dissipated per cycle as a function of cycle number at selected strain amplitudes [156]

Figure 42. Comparison of micro-fatigue (sample dimensions $4.7 \mu\text{m} \times 2.1 \mu\text{m} \times 23.9 \mu\text{m}$) and macroscopic fatigue cyclic stress-strain curves and maximum stress values as a function of cycle number for similar ODS steels: PM 2000 in the case of micro-fatigue and Eurofer 97 in the case of macroscopic fatigue. The data strongly agrees. [156]

Figure 43. Controlled frequency sweeping mechanism, left, used to measure the specific deflections of the vibrating cantilevers as a function of their positions and a frequency sweep plot on the right indicating the resonant frequencies producing maximum strain amplitudes of two tested cantilevers [160]

Figure 44. Commercially available in-situ TEM SSMT holders: (a) adapted version of the initial design in [164, 165] and (b) JEOL holder [168]

Figure 45. Schematic of deformation evolution in a material with high and low bubble densities. (a) general dislocation-bubble interaction inducing bubble cutting, (b) high bubble density specimen failing via bubble coalescence, (c) low bubble density specimen failing via bubble fragmentation leading to a bubble free channel where shear localization occurs. (d) in-situ TEM evidence of bubble elongation and fragmentation [181]

Figure 46. TEM image depicting a three-point bend specimen tested in-situ with its measurable dimensions labelled: P being applied load, $L/2$ half of the bending span, b the ligament thickness, a_0 the initial crack length, and δ_c the crack tip opening displacement [184]

Figure 47. Ni-Cr-Fe ternary phase diagram highlighting thermodynamically stable Ni-based superalloys and their approximate chemical compositions [187]

Figure 48. Important elements in Ni-based superalloys and their places within the alloys [186]

Figure 49. Unit lattice for γ -matrix (left), γ' -precipitate (center) and γ'' -precipitate phases (right) in Ni-based superalloys

Figure 50. The influence of Ni content on susceptibility to SCC in alloys stressed slightly above their yield point in 350 °C water. Ni-based superalloys used in nuclear reactors are marked in red. [213]

Figure 51. Swelling behavior of Fe-Cr-Ni alloys irradiated past 100 dpa with neutrons [215]

Figure 52. A schematic diagram illustrating the locations of the three activated Inconel superalloy components in CANDU reactors

Figure 53. Inconel X-750 annulus spacer (a) positioned for service in a fuel channel and (b) in-service photo in the hot cell

Figure 54. (a) non-optimized and (b) optimized Inconel X-750 CANDU spacers

Figure 55. Exemplary flux and temperature profile in a CANDU fuel channel

Figure 56. (a) Circumferential temperature profile of Inconel X-750 spacer in service (b) temperature gradients in non-pinched and pinched regions

Figure 57. (a) Original displacement spike model [234], (b) more detailed qualitative depiction of a displacement cascade highlighting interacting particles and point defects, (c) modern molecular dynamics simulation of the time evolution of a displacement cascade in pure, single-crystal copper at 290 °C. Defect quantities reach a maximum at ~ 0.1 ps before recombining and stabilizing after ~ 10 ps [235]

Figure 58. Elastic collision scattering process in the (a) laboratory reference frame and (b) center of mass reference frame, (c) vector diagram relating the parameters from the two reference frames after the collision

Figure 59. Illustrations of the number of displacements produced as a function of the energy transferred to the PKA: (a) Kinchin-Pease model compared to Lindhard model [240], (b) Kinchin-Pease model compared to Thompson-Wright, and NRT models [241]

Figure 60. Neutron flux spectra seen by an Inconel X-750 spacer compared to that seen in an average PWR core [197]

Figure 61. Thermal neutron absorption cross-sections for all three possible transmutation reactions involving ^{58}Ni and ^{59}Ni . The ^{59}Ni cross-sections have been scaled according to their relative maximum concentration in the CANDU core, 4%.

Figure 62. Total displacement damage and the contributions from each reaction for Inconel X-750 using the neutron flux of an average fuel bundle

Figure 63. Calculated point defect flux to dislocations at the onset of irradiation using defect sink strengths of 4×10^{14} for dislocations, 2.4×10^{13} for grain boundaries, a 30% interstitial bias for dislocations and a dpa rate in CANDU reactors of $\kappa = 10^{-7}$ dpa/s, and a 10% in-cascade survival rate

Figure 64. TEM images of the dislocation defect structures of Inconel X-750 components irradiated to 55 dpa containing 1.8 at% He. [229]

Figure 65. Calculated helium and hydrogen gas along with the total displacement damage for an Inconel X-750 spacer in a high power channel of a CANDU-6 reactor at full power assuming a mid-burn-up flux spectrum [228]

Figure 66. The effect of number of helium atoms, n , on the growth rate of a bubble, dR/dt [266]

Figure 67. Effect of dislocation-bias factor, ϵ_I , on bubble growth rate. [266]

Figure 68. BF TEM images of He bubbles in low temperature (6 o'clock) and high temperature (12 o'clock) 53 dpa ex-service Inconel X-750 spacers and their size distributions [229].

Figure 69. Equilibrium pressure of a helium bubble as a function of bubble radius

Figure 70. (a) Radiation defects in an ex-service Inconel X-750 component irradiated to 53 dpa containing 1.8 at% He at $\sim 300^\circ\text{C}$ shown through weak beam DF TEM imaging. (b) size distribution of all defects observed in components irradiated at both $\sim 180^\circ\text{C}$ (6 o'clock) and $\sim 300^\circ\text{C}$ (12 o'clock) [229]

Figure 71. Particle strengthening mechanisms as a function of particle radius. It is more energetically favorable to cut through small particles and bow around large particles.

Figure 72. Schematic of particle strengthening as a function of particle radius, r , and volume fraction, f . $f_3 > f_2 > f_1$ showing that increasing the volume fraction of the particle increases its hardening effect, in addition to increasing the critical radius, r_c , meaning particle shearing becomes more favored for particles with larger radii at higher volume fractions.

Figure 73. Applied shear stress needed to detach a dislocation from a void in pure Ni and the amount of bowing in the leading dislocation that initially encounters the void [281]

Figure 74. Diffraction patterns and DF TEM images showing the dose-evolved, irradiation-induced destruction of γ' and γ'' up to 20 dpa [283]

Figure 75. Disorder and dissolution kinetics of γ' precipitates under 300 keV Ni^+ irradiation at a dose rate of 10^{-3} dpa/s [285]

Figure 76. Irradiation temperature and dose map indicating the nature of irradiated γ' precipitates in Inconel X-750 (non-implanted and pre-implanted with 200 appm He). The irradiation was performed with 1 MeV Kr^{2+} ions at a dose rate of 10^{-3} dpa/s [274, 286, 287]

Figure 77. Diffraction patterns taken from Inconel X-750 components (a) non-irradiated and neutron irradiated to 54 dpa and 1.7 at% He at an irradiation temperature of (b) 180 °C and (c) 300 °C

Figure 78. Mechanical properties dose evolution of irradiated, precipitation hardened Ni-superalloys in three radiation environments: (a) Inconel X-750 irradiated in a fast neutron flux of 1×10^{22} n/m² in EBR-II at 420-427 °C [196], (b) Inconel 718 irradiated with 800 MeV protons up to a fluence of 3×10^{25} p/m² in LAMPF at temperatures < 250 °C [287], (c) Inconel 718 irradiated with 800 MeV protons and spallation neutrons at LANSCE [288, 289]

Figure 79. Fracture surfaces from bending specimens cut from Inconel 718 irradiated by 800 MeV protons in LANSCE at temperatures < 250 °C: (a) ~2.5 dpa, (b) ~8.5 dpa, (c) ~10 dpa [287]

Figure 80. Fracture surfaces of Inconel X-750 components: (a) non-irradiated and (b) irradiated to 23 dpa at 300-330 °C [245]

Figure 81. Engineering stress-strain curves from room temperature tensile tests on irradiated Inconel 718 from the LANSCE spallation target (800 MeV protons and spallation neutrons, $T_{\text{irr}} = 367\text{-}400$ °C) [289]

Figure 82. TEM images showing helium bubbles (a) aligning a grain boundary and matrix-precipitate interface of an irradiated Inconel X-750 component (55 dpa, 1.8 at% He, $T_{irr} = 300-330$ °C) [227] (b) enlarged portion within a grain boundary revealing a zone denuded of cavities adjacent to the boundary indicating that the boundary is a strong defect sink [228]

Figure 83. Intergranular fracture mechanisms caused by bubble coalescence within grain boundaries. (a) nano-scale dimpled intergranular fracture [293], (b) ductile dimpled intergranular fracture caused by bubbles nucleating on grain boundary precipitates, growing, and joining, leading to grain boundary decohesion. A wide precipitate free zone (PFZ) is shown in the center and a narrow one on the right. [294]

Figure 84. Examples of materials irradiated at high temperatures showing evidence of: (a) helium effected grain boundaries in Alloy 600 irradiated in HFIR to 8.5 dpa at 650 °C containing 1780 appm He fractured at room temperature [298], (b) a soft, denuded zone adjacent to a grain boundary in MA957 Fe atom ion irradiated to 500 dpa at 450 °C with large voids [299].

Figure 85. Schematic depicting a grain boundary interbubble fracture mechanism caused by overpressurized bubbles in a hardened matrix, adapted from [300]

Figure 86. (a) SEM image of two single grain boundary cracks (red arrows) that have initiated along a long coherent twin boundary (dotted line). Neither crack propagates along the entire boundary, but instead both cracks terminate in short segments in the grain interior (white circles). Fraction of grain boundary types that (b) initiate cracks and (c) propagate cracks given by the red bars in comparison to their occurrence in the material (grey bars). Twin boundaries and coincident site lattice low- Σ boundaries more easily initiate cracks, but randomly oriented high angle grain boundaries more easily propagate them in hydrogen charged Inconel 725 [309]

Figure 87. (a) Diagram depicting a brittle, intergranular fracture mechanism associated with γ' grain boundary coatings. (b) Dark field TEM image of a grain boundary lined with γ' from a Nimonic PE15 alloy irradiated at 650°C in a fast neutron fluence to ~30 dpa [310, 311]

Figure 88. Mixed mode fracture surface with flat channel facets from a 15% cold-worked 316SS flux thimble tube irradiated at temperatures 290-325 °C to 73 dpa and containing 0.07 at% He tested at room temperature [144, 295, 296, 313]

Figure 89. (a) Fracture surface of 18Cr-10Ni-Ti steel after irradiation in BOR-60 at 400-450 °C to 49 dpa tested at room temperature showing both intergranular and channel facets [314], (b) drawing illustrating the scheme of transgranular channel fracture via shearing of bridges that link up voids [313]

Figure 90. Time-temperature-transformation curves for Inconel X-750 [192]. The red dot indicates the heat treatment performed on the Inconel X-750 coils in this study.

Figure 91. Relative strain map of an Inconel X-750 coil cross-section

Figure 92. Schematic of the sectioned and polished Inconel X-750 coil and Electron Backscattered Diffraction (EBSD) areas. These areas are $250\ \mu\text{m} \times 250\ \mu\text{m}$ squares of the inner edge (IE), center (C), and outer edge (OE) regions of an Inconel X-750 flat spring. EBSD orientation map grain analysis produces an average overall grain size of $8.5 \pm 2.9\ \mu\text{m}$ and indicates grain elongation in the tangential direction.

Figure 93. Some common precipitates found in Inconel X-750 including η -phase Ni_3Ti and M_{23}C_6 carbides (left) and the ordered strengthening nanoprecipitates, γ' (right) [193]

Figure 94. Displacement damage and gas production in the ex-service Inconel X-750 material used for micro-mechanical testing

Figure 95. Pressure tube temperature profiles and neutron flux profiles ($E_n > 1\ \text{MeV}$) associated with the Inconel X-750 spacers extracted for micro-mechanical testing

Figure 96. Sectioning of Inconel X-750 link from a non-irradiated coil

Figure 97. Foil extractions from a representative ex-service spacer. (a) Cross-section of an Inconel X-750 spring showing FIB milled foils of material taken from both edge and center regions of the spacer, higher magnification images of the (b) Center A foil, (c) Center B foil, and (d) Edge foil. The grain boundary revealed along the top surface by the etching process is highlighted.

Figure 98. 77 dpa, 2.4 at% He Inconel X-750 foils extracted from bulk samples at CCEM for micro-mechanical testing: (a) pinched and (b) non-pinched

Figure 99. Bulk crush testing of Inconel X-750 annulus spacers. (a) modified MTS Insight 50 testing apparatus, (b) post-test coil, (c) close-up view of testing rig pre-test depicting the loading direction

Figure 100. (a) resulting bending beam structures cut into the large lift-out foil which has already been removed from the bulk spring (b) side view of a finished three-point bend specimen (c) top view of a completed three-point bend specimen, (d) and (e) FIB ion channeling contrast images depicting grain boundaries propagating approximately straight down through the thickness of the specimens, and (f) bending specimen becomes unconstrained similar to a standard three-point bend test during loading

Figure 101. Pre-test Electron Backscattered Diffraction (EBSD) on the top surface of a representative three-point bend specimen including an Inverse Pole Figure (IPF) grain orientation map in the tensile stress direction for the outer fiber of the specimen, hkl orientation of individual grains, misorientation angles across grain boundaries, grain rotation within each grain measured along a horizontal line segment left to right from point a to point b, and highest Schmid factor of the preferred slip system(s) within each grain

Figure 102. (a) push-to-pull testing device schematic depicting how it functions from Bruker [315], (b) portion of the load-displacement curve of a test post-failure of a micro-tensile specimen which has been fit to calculate the spring constant of the push-to-pull device for compliance correction

Figure 103. P2P set-up for lift-out process inside the SEM chamber

Figure 104. Sample preparation processes for micro-tensile push-to-pull specimens. (a) large lift-out foils mounted on standard 3 mm TEM grid, (b) individual lift-out foil depicting a selected micro-tensile specimen with a central grain boundary via FIB ion contrast imaging, (c) micro-tensile specimen sectioned for lift-out and mounting onto push-to-pull device, (d) top view and (e) side view of finished micro-tensile specimen

Figure 105. Shift software program user interface for DIC point tracking. (a) pre-test: Two points are selected at the ends of the gauge length of the specimen, (b) tracing the points soon after yielding, (c) tracing the points immediately after fracture, (d) Frame-by-frame analysis of the displacement of each point, which accounts for stage drift

Figure 106. Resultant displacement damage profile in an Inconel X-750 spring using an Al degrader wheel predicted by SRIM calculations. An approximately uniform ~ 3 dpa region occurs 3-11 μm deep, with the exception of two dips at 6 μm and 10 μm which are consequences of non-uniform differences in foil thicknesses of the Al degrader wheel.

Figure 107. Resultant helium implantation profile in Inconel X-750 spring using Al degrader wheel predicted by SRIM calculations. An approximately uniform amount of He, 1-1.2%, has been implanted in the region 3-12 μm deep, with the exception of two dips at 6 μm and 10 μm which are consequences of non-uniform differences in foil thicknesses of the Al degrader wheel.

Figure 108. Schematic of micro-tensile tests milled into the outer edge of non-irradiated and He implanted Inconel X-750 coils

Figure 109. (a) SEM images of a finished micro tensile specimen, EBSD analysis of a micro tensile specimen including (b) band contrast identifying grain

boundaries, (c) Euler angle orientation color, (d) inverse pole figure maps in the x, y, and z directions, (e) hkl orientations in the tensile loading direction of each grain with misorientation angles across each grain boundary, (f) Schmid factor map indicating the easiness of slip within each grain

Figure 110. Tungsten gripper for micro-tensile testing

Figure 111. Representative bulk crush testing load-displacement curves of Inconel X-750 specimens at each irradiation condition

Figure 112. Vickers indentation microhardness values (500 gf) of Inconel X-750 specimens at each irradiation condition with an insert depicting a representative indent where cracking occurred adjacent to the indent in the 67 dpa material irradiated at 300 °C. Cracks have developed around the surfaces of indents performed on material with a dose of 67 dpa.

Figure 113. Non-irradiated outer edge three-point bend specimen 1. A crack is believed to have developed along the boundaries of the smallest pink grain indicated by the red arrow after yielding occurred.

Figure 114. Non-irradiated outer edge three-point bend specimen 2.

Figure 115. Non-irradiated outer edge three-point bend specimen 3

Figure 116. Non-irradiated outer edge three-point bend specimen 4. Potential grain boundary cracks that appeared after the maximum stress value when the beam abruptly snapped are highlighted by the red arrows.

Figure 117. Non-irradiated outer edge three-point bend specimen 5.

Figure 118. Non-irradiated center three-point bend specimen 1.

Figure 119. Non-irradiated center three-point bend specimen 2.

Figure 120. Single-grained 53 dpa, $T_{irr} = 180$ °C, three-point bend specimen 1.

Figure 121. Single-grained 53 dpa, $T_{irr} = 180$ °C, three-point bend specimen 2.

Figure 122. 53 dpa, $T_{irr} = 300$ °C, three-point bend specimen 1.

Figure 123. 53 dpa, $T_{irr} = 300$ °C, three-point bend specimen 2.

Figure 124. 53 dpa, $T_{irr} = 300$ °C, notched, three-point bend specimen 3.

Figure 125. 53 dpa, $T_{irr} = 300$ °C, notched, three-point bend specimen 4. The layer of Pt on the post-test image was for the purposes of thinning the sample down for SEM-STEM investigations.

Figure 126. 67 dpa, $T_{irr} = 180$ °C three-point bend specimen 1.

Figure 127. 67 dpa, $T_{irr} = 180\text{ }^{\circ}\text{C}$ three-point bend specimen 2. What appear to be potential grain boundary cracks are highlighted in red.

Figure 128. 67 dpa, $T_{irr} = 180\text{ }^{\circ}\text{C}$ three-point bend edge specimen 1. What appear to be potential grain boundary cracks are highlighted in red.

Figure 129. 67 dpa, $T_{irr} = 180\text{ }^{\circ}\text{C}$ three-point bend edge specimen 2.

Figure 130. 67 dpa, $T_{irr} = 300\text{ }^{\circ}\text{C}$ three-point bend center specimen 1.

Figure 131. 67 dpa, $T_{irr} = 300\text{ }^{\circ}\text{C}$ three-point bend center specimen 2.

Figure 132. 67 dpa, $T_{irr} = 300\text{ }^{\circ}\text{C}$ three-point bend edge specimen 1.

Figure 133. 67 dpa, $T_{irr} = 300\text{ }^{\circ}\text{C}$ three-point bend edge specimen 2.

Figure 134. Representative flexural stress-strain curves calculated for the midpoint at the outer fiber of the (a) center and (b) edge specimens according to three-point bend theory for each irradiation condition. Loading curves plotted in terms of the critical resolved shear stress (CRSS) calculated from the matrix orientation at the highest stress point can be seen for the center specimens in (c) and edge specimens in (d).

Figure 135. Non-irradiated outer edge micro-tensile specimen 1 containing a high angle grain boundary (44° misorientation angle)

Figure 136. Non-irradiated outer edge micro-tensile specimen 2 containing a twin boundary

Figure 137. Non-irradiated center micro-tensile specimen 1 containing a high angle grain boundary (40° misorientation angle)

Figure 138. Non-irradiated center micro-tensile specimen 2 containing an upper twin boundary and a lower high angle grain boundary

Figure 139. Non-irradiated inner edge micro-tensile specimen 1 containing a twin boundary

Figure 140. Non-irradiated inner edge micro-tensile specimen 2 containing a twin boundary

Figure 141. Single-grained non-irradiated inner edge micro-tensile specimen 3

Figure 142. Single-grained non-irradiated inner edge micro-tensile specimen 4

Figure 143. Non-irradiated inner edge micro-tensile specimen 5 containing a twin boundary

Figure 144. Non-irradiated inner edge micro-tensile specimen 6 containing a high angle grain boundary (misorientation angle $\sim 39^{\circ}$)

Figure 145. Non-irradiated inner edge micro-tensile specimen 7 containing a high angle grain boundary (misorientation angle $\sim 23^\circ$)

Figure 146. 67 dpa low temperature edge micro-tensile specimen 1 containing a high angle grain boundary (misorientation angle $\sim 51^\circ$)

Figure 147. 67 dpa low temperature edge micro-tensile specimen 2 containing a high angle grain boundary (misorientation angle $\sim 54^\circ$)

Figure 148. 67 dpa low temperature edge micro-tensile specimen 3 containing a high angle grain boundary (misorientation angle $\sim 54^\circ$)

Figure 149. Single-grained 67 dpa low temperature edge micro-tensile specimen 4

Figure 150. Single-grained 67 dpa low temperature center micro-tensile specimen

Figure 151. 67 dpa high temperature edge micro-tensile specimen 1 with a high angle grain boundary (28° misorientation angle)

Figure 152. Single-grained 67 dpa high temperature edge micro-tensile specimen 2

Figure 153. 67 dpa high temperature center micro-tensile specimen 1 containing a twin boundary

Figure 154. Single-grained 67 dpa high temperature center micro-tensile specimen 2

Figure 155. 81 dpa low temperature center micro-tensile specimen

Figure 156. Single-grained 81 dpa high temperature center micro-tensile specimen

Figure 157. 81 dpa high temperature center micro-tensile specimen with a high angle grain boundary ($\sim 55^\circ$ misorientation angle)

Figure 158. Engineering stress-strain curves of all micro-tensile, push-to-pull, Inconel X-750 specimens

Figure 159. 200 nm Berkovich indents hardness profile performed on the cross-section of a non-irradiated Inconel X-750 component

Figure 160. 200 nm Berkovich indents elastic modulus profile performed on the cross-section of a non-irradiated Inconel X-750 component

Figure 161. (a) SEM images of two rows of indents at different depths from the surface. (b) profile of the elastic modulus of Inconel X-750 as a function of distance from the irradiated surface (c) hardness profile of the helium implanted Inconel X-750 as a function of distance from the surface

Figure 162. Non-irradiated micro-tensile specimen 1 that fractured in its twin boundary

Figure 163. Non-irradiated micro-tensile specimen 2 that fractured within a high angle grain boundary

Figure 164. He implanted micro-tensile specimen 1 that fractured transgranularly through its nanotwin

Figure 165. He implanted micro-tensile specimen 2 that fractured transgranularly in its upper grain

Figure 166. He implanted micro-tensile specimen 3 that fractured along a high angle grain boundary

Figure 167. He implanted micro-tensile specimen 4 that fractured within the grain interior

Figure 168. FEM mesh modelling of the (a) normal stresses along the beam axis (tensile and compressive), (b) Von Mises stresses, and (c) plastic strain at the yield point for a standard three-point bend test and a fully constrained SSMT three-point bend test

Figure 169. Graphical representation of an Inconel X-750 spacer with mechanical properties measured by push-to-pull micro-tensile testing summarized in each region: outer edge, center, and inner edge. Bar graphs depicting the failure strength, yield strength, critical resolved shear stress (CRSS) calculated from the highest Schmid factor of the grain interior where the first observable slip step appeared, and the total elongation of the specimens are provided on the right hand side.

Figure 170. Critical resolved shear stress (CRSS) values calculated from micro-tensile specimens

Figure 171. 0.2% offset yield strengths of push-to-pull micro-tensile specimens

Figure 172. Failure strengths of push-to-pull micro-tensile specimens

Figure 173. Total elongations of push-to-pull micro-tensile specimens

Figure 174. Hypothetical plot proposed by Griffiths [197, 228] depicting the mechanical properties of precipitation-hardened, irradiated Ni-based superalloys as a function of dose. All push-to-pull micro-tensile specimens either yield and fail within their grain interiors or yield first and then fail within a grain boundary, meaning the critical dose highlighted by the red arrow is > 81 dpa for Inconel X-750 if this concept holds true.

Figure 175. Grain boundary strengths of Inconel X-750 measured by micro-tensile testing

Figure 176. Resolved normal stress on high angle grain boundaries at the time of failure in push-to-pull micro-tensile specimens

Figure 177. Testing challenges during the development of in-situ, push-to-pull, micro-tensile testing. Specimens became pre-deformed prior to testing during calibration and alignment processes (left). The port positions of the Pt GIS needle and nanomanipulators do not allow for much flexibility within the SEM/FIB chamber. The Pt needle is shown blocking the P2P testing site (right).

Figure 178. Helium bubble size and density distribution for Inconel X-750 irradiated to 53 dpa (1.8 at% He) at 120-280 °C and 300 °C [227]

Figure 179. Proposed testing geometries for future in-situ, push-to-pull micro-tensile testing

Figure 180. A newly proposed lift-out micro-tensile test for highly activated nuclear material

Publications

Howard, C., et al. "A novel in-situ, lift-out, three-point bend technique to quantify the mechanical properties of an ex-service neutron irradiated Inconel X-750 component." *Journal of Nuclear Materials* 498 (2018): 149-158.

C. Howard, et al. "In-Situ SEM Push-to-Pull Micro-Tensile Testing of Ex-Service Inconel X-750." *The 18th International Conference on Environmental Degradation of Materials in Nuclear Power Systems – Water Reactors*. August 13-17, 2017.

C. Howard, et al. "The influence of microstructure on the cyclic deformation and damage of copper and an oxide dispersion strengthened steel studied via in-situ micro-beam bending." *Materials Science and Engineering: A* 687 (2017): 313-322.

C. Howard, et al. (2016). "Investigation of specimen size effects by in-situ microcompression of equal channel angular pressed copper." *Materials Science and Engineering: A*, 649: 104-113.

C. Howard, et al. (2015). "Characterization of Neutron Irradiated CANDU-6 Inconel X-750 Garter Springs via Lift-Out Three-Point Bend Tests," In *HOTLAB 2015 – Annual Meeting on hot laboratories and remote handling*.

H. Vo, A. Reichardt, C. Howard, et al. (2015). "Small-Scale Mechanical Testing on Proton Beam-Irradiated 304 SS from Room Temperature to Reactor Operation Temperature." *The Member Journal of The Minerals, Metals, and Materials Society*, 67: 1-5.

Reichardt, A., Lupinacci, A., Frazer, D., Bailey, N., Vo, H., Howard, C., & Hosemann, P. (2017). Nanoindentation and in situ microcompression in different dose regimes of proton beam irradiated 304 SS. *Journal of Nuclear Materials*, 486, 323-331.

A Iyengar, E.B. Norman, C. Howard, et al. (2013). "Distinguishing fissions of ²³²Th, ²³⁷Np, and ²³⁸U with beta-delayed gamma rays." *Nuclear Instruments and Methods in Physics Research B*, 304: 11-15.

Hull, K. L., Abousleiman, Y. N., Han, Y., Al-Muntasheri, G. A., Hosemann, P., Parker, S. S., & Howard, C. B. (2017). Nanomechanical Characterization of the Tensile Modulus of Rupture for Kerogen-Rich Shale. *SPE Journal*.

Abousleiman, Y. N., Hull, K. L., Han, Y., Al-Muntasheri, G., Hosemann, P., Parker, S., & Howard, C. B. (2016). "The granular and polymer composite nature of kerogen-rich shale." *Acta Geotechnica*, 1-22.

Hull, K. L., Abousleiman, Y. A., Han, Y., Al-Muntasheri, G. A., Hosemann, P., Kendall-Still, E., & Howard, C. B. (2016, June). Modernized Mechanical Testing of Kerogen-Rich Shales (KRS) By Monitoring in Situ Microscale Tensile Failures. In *50th US Rock Mechanics/Geomechanics Symposium*. American Rock Mechanics Association.

Hull, K. L., Abousleiman, Y. N., Han, Y., Al-Muntasheri, G. A., Hosemann, P., Parker, S. S., & Howard, C. B. (2015, November). “New Insights on the Mechanical Characterization of Kerogen-Rich Shale”, KRS. In *Abu Dhabi International Petroleum Exhibition and Conference*. Society of Petroleum Engineers.

Acknowledgements

I would like to thank the Meyerhoff Scholarship program at the University of Maryland Baltimore County led by Freeman Hrabowski for paving the way for me to pursue my PhD at the University of California Berkeley by surrounding me with a diverse and brilliant group of young and aspiring scientists and engineers and a healthy environment to grow. Support from the late Lamont Tolliver, Keith Harmon, and Mitsue Wiggs while I was discovering how to be a student, how to get involved with research, and how to mentor younger students as I became more senior was vital in this process.

I greatly appreciate my research advisor, Prof. Peter Hosemann, for having his door open and allowing me to come in and ask about getting involved with hands on experimental nuclear materials research at a time when I was burned out from physics and looking for a refreshing change. Peter's mentorship and friendship throughout my research projects remains invaluable to my growth as a nuclear materials scientist engineer. By allowing me to the opportunity to travel and perform research abroad through the Marshall Plan program in Austria and EAPSI program in Australia, Peter has kept my mind and spirit healthy and fresh during the marathon that is graduate school as a PhD student.

Many thanks to Daniel Kiener my advisor and Reinhard Fritz, Markus Alfreider, Michael Reisinger, Stefan Bigl, Megan Cordill, Ross Economy, Rachel Schoepner, Jakub Zalesak, Kristian Stephens, and David Roper for lending guidance and being great co-workers, friends, and the closest part of the Erich Schmid Institute (ESI) family while I worked at the institute at Montanuniversität Leoben and for the many adventures together.

The same can be said for EAPSI program director Shannon Owen, my advisor Dr. Dhriti Bhattacharyya at the Australian Nuclear Science and Technology Organisation (ANSTO), colleagues Dr. Alan Xu, Yadu Krishnan, and Arun Khuttan, and friends Thom Epps, Ryan Loe, Adrian Figg, and Austin Schwarz for making my time down under in Australia so enjoyable. I would like to thank Mihail Ionescu for performing the helium implantation on Inconel X-750 material at ANSTO.

I would like to thank Dr. Malcolm Griffiths, former radiation damage branch manager at Canadian Nuclear Laboratories (CNL), for his insistence in sending neutron irradiated ex-service components across the border from Canada to our lab in Berkeley because he recognized the value in performing new, in-situ mechanical tests on active material in order to watch intergranular failure in the electron microscope and get quantitative mechanical properties previously inaccessible. Malcolm has been a continual mentor throughout this process even as he has retired from CNL and transitioned to a position at Queen's University.

Dr. John Jackson along with Dr. Colin Knight at Idaho National Laboratory (INL) are recognized for facilitating this work as part of the U.S. Department of Energy's Rapid Turnaround Post-Irradiation Experiment (DOE RT-PIE). Dr. Brandon Miller and microscopist Jim Madden are thanked for their help in sample preparation and extraction for the foils sent to Berkeley.

I want to commend Dr. Colin Judge from CNL for reaching out and bringing his years of experience in studying the microstructure of ex-service Inconel X-750 to the discussion and pushing so hard to link the helium bubbles he saw lining the grain boundaries to the mechanics. Colin has been vital in extending the breadth of this work beyond that of a purely academic nature into the nuclear industry by sharing it with the CANDU Owners Group (COG) and Ontario Power Group (OPG) from which the first industrial contracts involving SSMT on reactor components have been born.

Dr. Grant Bickel, Don Metzger, Marc Paulseth, Rob Beiers, Andrew Buyers, Heygaan Rajakumar, Dr. Vineet Bhakri, Mike Stewart, Chris Dixon, and Clinton Mayhew from Canadian Nuclear Labs are recognized for their discussions and work and contributions involving temperature estimates, bulk crush testing and microhardness data, and in helping with my work during my visit up to CNL.

I appreciate the support and guidance given from my thesis committee: Prof. Peter Hosemann, Prof. Per Peterson, and Prof. Andrew Minor and funding provided in part through the Nuclear Energy University Program.

Finally, I would like to express gratitude towards all those who were willing to listen, lend a hand (often times at little or short notice), and teach me and give me perspective during my time in Berkeley: Scott Parker (When you were a tech, you were willing to take time out of your schedule and give the new bending tests a shot while things were in transition. You taught me a lot about the experimental process and what it means to be an organized, prepared, and thorough experimentalist.), David Frazer (for SEM/FIB and Hysitron items and seemingly never saying no to any project), David Krumwiede (for being the computer whiz in our group), Mitch Loff, Chloe Rose, Evan Still (taking the shale project full on as an undergrad after training), Hi Vo, AJ Gubser (machining sample holders), Ashley Reichardt, Amanda Lupinacci, Joey Kabel, Dr. Mehdi Balooch, Dr. Bill Choi, Dr. Ruslan Valiev, Daniel Valella, Christina Zaccaro, Lucas Brouwer, Ross Barnowski, Ryan Pavlovsky, Maria Simanovskaia, Priscila Amorim, Lawrence Liu, Elliot Chang, Brent Batas, Lina Aoyama, Kevin Doxzen, Josh Ceribelli, and countless others.

1 Motivation

1.1 The Need for Current and Future Clean Nuclear Energy

Although the political climate and public appeal of nuclear energy remains unstable, due in part to the recent accident in Fukushima, clean nuclear power has prevented 1.84 million air pollution related deaths and 64 gigatonnes (Gt) of CO₂ greenhouse gas emissions that otherwise would have resulted when burning fossil fuels. Predictions indicate that it could prevent an additional 420k-7.04 million deaths and 80-240 Gt of CO₂ emissions by 2050 [1]. All other non-carbon energy sources including photovoltaics (PV), biomass, hydroelectricity, wind, and solar thermal combined still experience challenges in meeting the total world energy requirements, most importantly due to the intermittent nature with which they produce their energy [2]. Nuclear power is unique in that it produces a large, stable baseline quantity of energy that can compete with fossil fuels. Energy demands predict an amount of baseline power > 100 EJ (10¹⁹ Joules) is needed by 2050 in order to combat greenhouse gas emissions [3, 4]. Fossil fuel production could be dramatically reduced this century (down to 9.4%) if nuclear fission renewables were to account for slightly more than half of the total world supply of energy (52%), and all other aforementioned renewables combined (38.6%) [5].

Nuclear power is the most effective instrument for effective climate change mitigation. The principal limitations on increasing total nuclear energy output revolve around societal acceptance, public anxiety, and fiscal and political inertia.

Sustaining and increasing clean nuclear power can be done in two ways: building new reactors or performing reactor lifetime extension programs. Both are vital and equally important for obtaining healthy energy futures, and both involve understanding radiation damage effects on materials at much higher doses and more extreme environments than have ever been experienced in order to allow for safe operations. However, building new reactors incurs a capital cost of approximately \$2 billion in addition to new licensing costs for all next generation designs, whereas reactor lifetime extension programs employ and adapt existing research and development programs already needed to ensure safe operations.

Currently operating generation II and generation III reactor materials function at temperatures between 100 °C and 350 °C and experience radiation damages between 0 and 90 displacements per atom (dpa)¹. Nuclear power plants in commercial operation are predominantly pressurized water reactors (PWRs), which comprise 65% of the global nuclear fleet. These reactors in combination

¹ Displacements per atom (dpa) as a unit of radiation damage is discussed in detail in Section 3.3

with boiling water reactors (BWRs) comprise the class of light water reactors (LWRs) that use normal water as both a coolant and neutron moderator. Other reactors that provide energy via thermal neutron fissions, instead moderated by graphite, that also require enriched uranium oxide fuel include light water graphite reactors (RBMK and EGP) and gas-cooled reactors (AGR). Canadian deuterium uranium reactors (CANDUs) fall into a subset of pressurized heavy water reactors (PHWRs) that use heavy water coolant, D₂O, as opposed to H₂O in LWR designs, as both a moderator and coolant. The increased efficiency of heavy water as a neutron moderator allows for the use of natural uranium fuel forms. CANDU-type reactors make up approximately 11% of the global fleet and provide 60% of the energy of the province of Ontario in Canada where they originated.

If the lifetimes of these reactors are to be extended, performing research and development on nuclear materials in the high dose regime, 50-100+ dpa, where there is currently a dearth of knowledge and limited amount of material irradiated to these doses, is a must. Material irradiated to these high doses in conventional power reactors would be most valuable because it has the same radiation damage dose rate and neutron flux, unlike accelerated tests conducted in liquid metal fast research reactors that had damage rates an order of magnitude higher.

Next generation fission and fusion reactor concepts require materials to operate at higher temperatures between 300 °C and 1000 °C, sometimes to doses that exceed 200 dpa. In the case of the Traveling Wave Reactor (TWR) doses are expected to reach 600 dpa. Figure 1 produced in [8] maps out the temperature and dose requirements for all 8 proposed generation IV advanced reactor concepts.

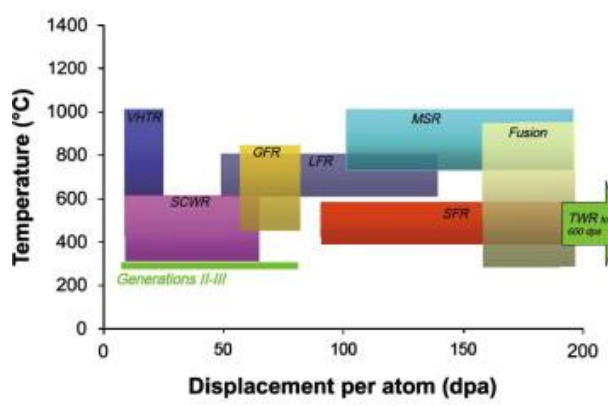


Figure 1. The temperature and dose range requirements for in-core structural materials that will operate in each of the 8 next generation reactor design concepts [8].

According to Nuclear Energy Institute World Statistics, as of last year, 60 new generation III/III+ light water plants are in construction in 15 countries. It is promising that the majority of these reactors are being built in nations with the highest and largest growing energy needs, and in places which currently emit some of the highest gross CO₂ emissions and/or the highest per capita CO₂ emissions. China leads the way with plans to build 19 new reactors, India second with 6 new plants, Russia with 5, and the United Arab Emirates with 4. By no means will the construction of only these 60 new power reactors solve the clean energy crisis, but hopefully it is the first step in the right direction, and with safe operations, gained experience, and an improved social and political climate, more plants will follow.

To supplement the design and construction of new current and next generation reactors, reactor lifetime extension is needed because simply put, the current fleet of nuclear reactors are getting old. 30 nations operate 449 nuclear power reactors, and this global fleet has an average age of 29.3 years old as of 2016, with the oldest being 47 years old [6]. Most, if not all, of these reactors are commissioned for a 40-50 year lifetime. The first generation of power reactors have already gone offline and began their decommissioning processes. This reveals itself in the fact that in 2000, the amount of global energy produced by nuclear power was 18%, and has since decreased to 10.9% [7]. New reactors cannot be built fast enough to replace the old ones. In order to curb this trend of decreasing nuclear energy, the current fleet of reactors must safely operate for a total lifetime of 80-100+ years.

1.2 CANDU Life Management Surveillance Programs

Nuclear power station operators of Canadian Deuterium Uranium (CANDU) reactors periodically remove pre-selected, activated material from in-service structures, systems, and components (SSCs) considered to be critical to the reactors operation but replaceable as part of their routine surveillance and inspection programs. Among this class of critical but replaceable SSCs are the fuel channels, consisting of high temperature Zircalloy pressure tubes (Zr-2.5%Nb), cool Zircalloy-2 calandria tubes, and Inconel X-750 internal spacers that maintain an insulating gap filled with CO₂ gas between the two tubes. These Inconel X-750 garter spring components prevent contact between the two tubes that would otherwise generate a large heat sink and compromise the thermodynamic integrity of the reactor, in addition to causing eventual hydride blistering and rupturing of the pressure tube that could ultimately result in failure and a local loss of coolant accident (LOCA). A depiction of a CANDU fuel channel can be seen in Figure 2.

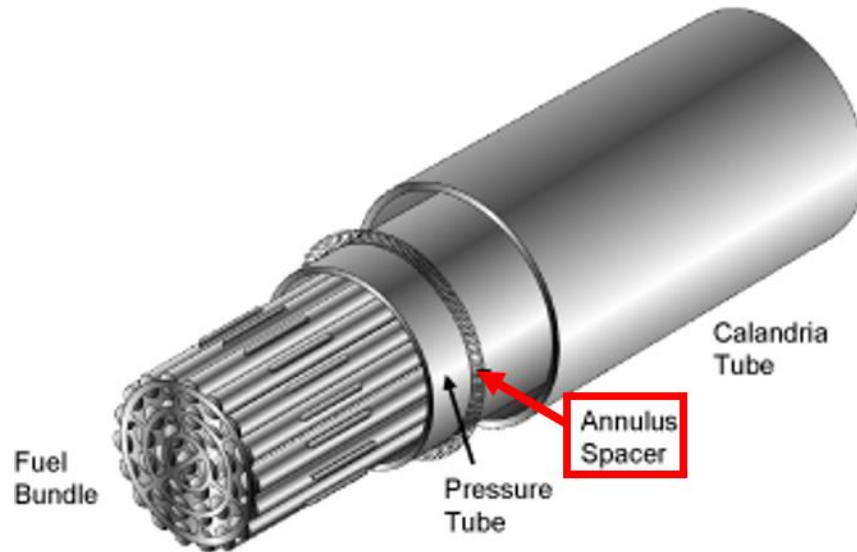


Figure 2. CANDU fuel channel with Inconel X-750 spacer coil highlighted [9]

Upon removal of a fuel channel in 2010, it was found that the Inconel X-750 spacer had become embrittled following irradiation. Although spacers were never found to have failed in-service, upon handling for inspections inside of hot cells for post irradiation examination experiments, they abruptly fractured as seen in Figure 3. Therefore, a new spacer research and development program was launched in order to investigate the primary degradation mechanisms and ensure to the Canadian Nuclear Regulatory Commission (CNRC) that the component remains fit for service, meaning that it can safely maintain its load bearing capacity, as part of the industry's ongoing plant life management plan. The SSMT work in this thesis is part of the R&D work for the spacer program. Inconel X-750 spacers are expected to remain in service for 25-30 years, when a scheduled refurbishment outage will occur and all aged SSCs undergo a thorough assessment and upgrades, whether that means replacing components, overhauling systems, reclassifying system boundaries, and/or updating plant codes. This includes fuel channel replacement. This refurbishment period also provides the insight, research, and planning needed in order to apply for reactor lifetime extension, usually an additional 25-30 years of service operating with the new refurbished components.

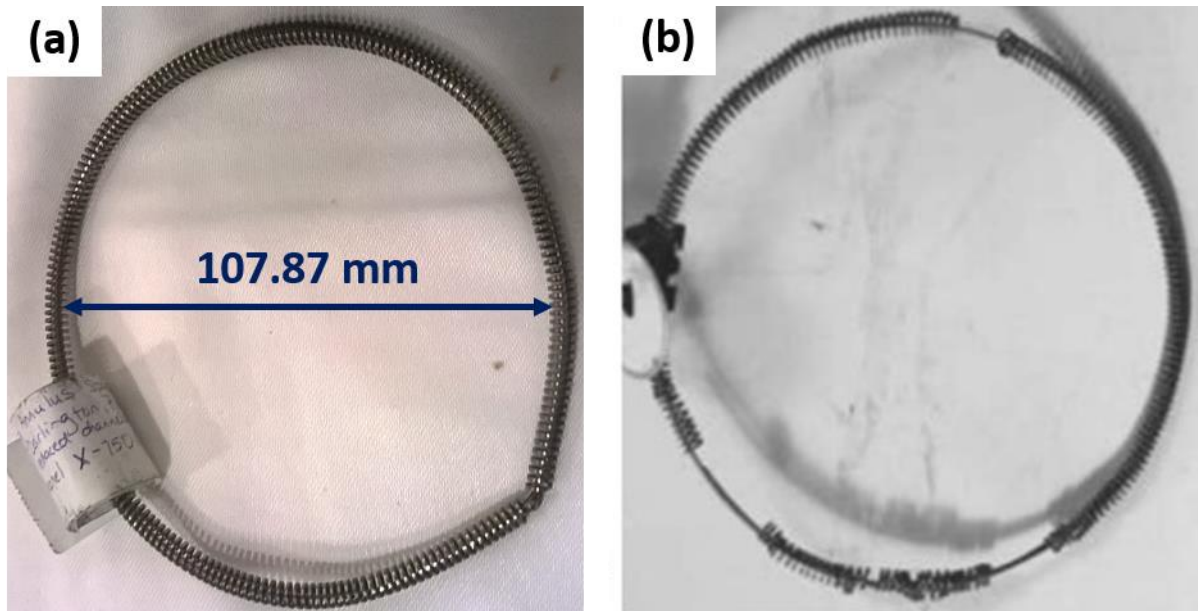


Figure 3. Inconel X-750 spacer (a) before service and (b) ex-service view while handling for post-irradiation examinations inside the hot cell [226]

1.3 Relevance to Reactor Lifetime Extension Programs

In addition to the necessity to investigate the degradation mechanisms of Inconel X-750 ex-service components as part of the Canadian nuclear industry's spacer program to ensure safe function of CANDU reactors, these components have a unique relevance to general reactor lifetime extension programs. Unlike typical light water reactor (LWR) active components whose damage microstructures saturate at low doses, typically less than or equal to 10 displacements per atom, the microstructure of Inconel X-750 garter springs continually evolves with dose. Nickel transmutation reactions occurring in the high thermal flux environment of the CANDU reactor produce enhanced radiation damage and unprecedented amounts of internal helium and hydrogen in the material, as high as a few atomic percent He. The microstructure and mechanical properties of the material investigated in this study irradiated in a power reactor to 53, 67, and 80 dpa with 1.6-2.4 at% He has not been mechanically tested before using conventional means or SSMTs, and with such high dose and He content could serve as a model material for end of life conditions experienced after reactor lifetime extensions. In many cases, the displacement damages and He contents in ex-service Inconel X-750 components will greatly exceed those achieved by core components in LWRs, even after 80-100 years of service. Therefore, they will provide valuable insights into potential core component material degradation mechanisms only achieved after lengthy service times and can be used in predictive models that would comprise part of a future license renewal application. In addition, they can provide a look ahead into what may be in store

for those reactors that have already been granted license renewals and are even looking forward to a second lifetime extension phase.

1.4 The Need for SSMTs

Bulk component mechanical properties measurements for the ex-service coiled components pictured in Figure 3 are practically impossible to measure by common standardized testing methods due to their complex geometries and non-conventional sizes. The high activity components are only 0.7-0.8 mm in thickness, so the R&D spacer program had to develop a non-conventional and non-standardized first-of-its kind bulk component “crush test” for use inside of the Fuel and Material Cells (FMC) at Canadian Nuclear Laboratories (CNL) in order to estimate the load-bearing capabilities of the high dose components. This test design which will be further explained in a subsequent section within the experimental chapter required large sections of material, approximately 20 coils, so there was only sufficient material to perform one or two tests for each component from each irradiation temperature and dose. Due to high dose rates that would be received by a worker handling even this smaller section of the component, all work is constrained to take place within hot cell facilities. A dose rate estimate for a section of component used for one bulk crush test is shown in Figure 4.

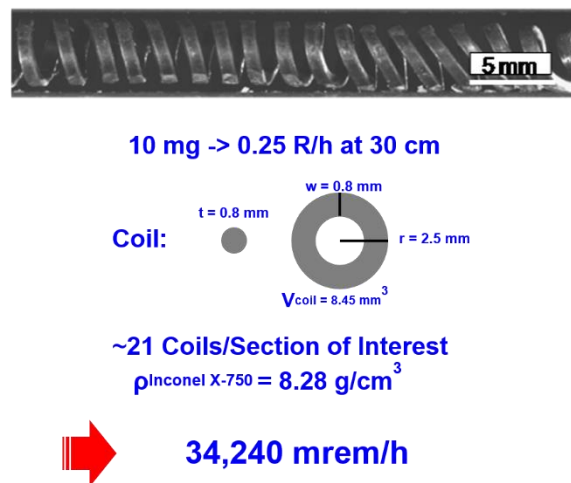


Figure 4. Dose rate estimate for a full length, load-bearing portion of an Inconel X-750 component. The material produces an approximate dose rate of ~37 R/h for a radiation worker working 30 cm away from the material.

The University of California Berkeley Radiation Safety manual’s administrative guidelines set by the Radiation Safety Committee (RSC) limit a radiation worker to 5000 mrem/yr of dose to the skin and extremities. Even if safe work practices were to be performed during bulk component testing outside of the hot cells, annual dose limits would be reached in less than 9 minutes. Obviously, sample

volumes must be reduced in order to work on this material in a safe allowable manner and abide by the As Low As Reasonably Achievable (ALARA) policy. The SSMTs performed in this study use maximum sample volumes of $\sim 500 \mu\text{m}^3$ and a maximum of 4 specimens were handled on their sample grid at one time. Even if a worker were to remain within 30 cm of the sample grid for an entire year, he/she would only receive 3.6 mrem of dose.

Besides the immense benefits from sample volume reduction with regards to performing work outside of the hot cells and reducing the cost, time, and space needed for sample manufacturing and testing, SSMT provides the added benefit of obtaining common metallurgical stress parameters such as yield strength, failure strength, and total elongation to be obtained via direct observation and straightforward calculations from sample measurements. Simpler testing stress states than those of bulk crush testing can be employed so that analytical formulations can be used. In addition, a plethora of specimens can be manufactured from each extracted component and through systematic studies which take into account their microstructures, enhanced statistics can be obtained from multiple tests on the same component. Performing testing in-situ inside of the SEM chamber allows for real time observations of deformation mechanisms, and SSMT methods development. The novel in-situ tests invented and implemented here are the first attempted on active nuclear components with a complex geometry.

1.5 Research Goals

1.5.1 Research Question

Can the novel SSMT techniques implemented on an active, ex-service Inconel X-750 component provide quantitative measurements of its mechanical properties that will provide insight into its degradation mechanisms for the nuclear industry?

1.5.2 Research Plan

- Obtain baseline mechanical properties characterization of non-irradiated Inconel X-750 components via novel SSMTs
- Develop a method of best extracting component material from bulk specimens by creating a working infrastructure between Canadian Nuclear Laboratories (CNL), the Nuclear Science User Facilities (NSUF) program in the United States, and the University of California Berkeley nuclear materials group
- Assess deformation initiation mechanisms and quantify yield strengths and yield strength differences for high dose components operating in-service at 180 °C and 300 °C

- Assess failure mechanisms, failure strengths and ductility of the high dose components at their two operating temperatures
- Perform methods development of novel SSMTs

1.5.3 Hypothesis

A novel, in-situ, SEM, lift-out, three-point bending test can quantify relative yield strength differences between non-irradiated components, active low temperature-high dose components, and active high temperature-high dose components, but it is limited in assessing absolute mechanical properties and quantifying plastic deformation, although it is able to allude to failure mechanisms. A novel, in-situ, SEM, lift-out, push-to-pull, micro-tensile test can quantify yield and failure strengths of active components, their relative differences due to irradiation conditions, and provide insight into ductility. This newest SSMT directly elucidates information on both potential deformation initiation mechanisms and failure mechanisms, and it has the most room for growth, adaptation, and expansion in the nuclear materials community.

2. Background: A Review of Small Scale Mechanical Testing (SSMT) Applied to Nuclear Materials

2.1 Introduction

Efforts to reduce sample sizes for testing irradiated materials below those required for American Society for Testing and Materials (ASTM) standardized testing extend back approximately four decades. The use of non-bulk or miniaturized test pieces is certainly not new. The limited amount of nuclear material extracted from operating power reactors only allows for one to two standard scale or component sized mechanical tests, providing a rather poor statistical confidence of mechanical properties. With the limited number of materials test reactors worldwide, space is limited for materials testing programs and adaptations of test specimen sizes resulted. Small scale test specimens inserted into test reactors are also necessary in order to avoid unwanted neutron flux variations and minimize the effects of gamma heating. Reduced sized specimens decrease dose to radiation workers and allow core components which were previously too active to handle to be investigated in post-irradiation testing. Safer activity levels associated with smaller active nuclear material allows it to be removed from the hot cells and analyzed via x-ray diffraction (XRD), scanning electron microscopy (SEM), electron backscattered diffraction (EBSD), electron dispersive spectroscopy (EDS), and transmission electron microscopy (TEM) in order to couple microstructural effects of radiation damage with the way radiation damage changes the mechanical properties and failure mechanisms of the material. Ultimately, the extraction of a minimal amount of active material for small scale tests with a minimally invasive approach can more thoroughly

characterize in-service components and reduce time, space, and cost. Coupled with non-destructive examinations, small scale testing performs localized assessments for component monitoring and material degradation projections.

With the advent and commercialization of the focused ion beam (FIB) and dual beam (SEM and FIB combined) capabilities of the 1990s, micro-sized specimens from nuclear material could be fabricated such that radiation effects on specific regions of interest like microstructural gradients, specific grain orientations, phase boundaries, grain boundaries, and new radiation induced phases could be investigated. Grain boundary strengths and interface strengths can be extracted via micro-machined samples. Fundamental defect-dislocation and defect-boundary/interface interaction studies are now possible. Irradiated components with complex geometries that do not lend themselves to standardized testing can now be fabricated to make specimens tested under uniaxial stress states. In-situ testing inside of the dual beam chamber at high vacuum allows for real time observations of deformation mechanisms to be observed and recorded. Size effect studies on irradiated materials tested at the micro-scale, millimeter scale, and bulk scale allow for correlations between mechanical properties to be made. With a plethora of specimens manufactured from the same component and tested in a systematic way which accounts for the microstructure of each specimen, enhanced statistics can be obtained from multiple tests on the same component. Common metallurgical stress parameters such as yield strengths and failure strengths can be obtained via direct observation and straightforward calculations from sample measurements due to these simpler stress states from which formulations have been analytically derived. New candidate alloys proposed for fusion reactor programs and next generation/generation four nuclear fission concepts can be ion irradiated with beam spot sizes of a maximum size $\sim 1 \text{ cm}^2$ and penetration depths on the order of microns, and small scale specimens can be fabricated from the irradiated regions and tested. Mechanical properties can be profiled over varying ion dose and implantation regimes. This data can then be used to help improve ion beam conditions to better simulate neutron radiation damage. Candidate fusion material irradiated in a neutron spallation source can be evaluated in a similar fashion.

This background chapter covers a broad range of small scale mechanical testing techniques. It begins with more rudimentary techniques including small shear punch tests/miniaturized disk bend tests [10-12, 14-16, 18-20, 27, 29, 30], miniaturized Charpy tests [38-44, 46, 47, 48], microhardness tests [54], and nanoindentation tests [62, 78, 79, 81, 88-90, 93, 95]; progresses to micro-pillar compression [116, 124, 134], micro-tensile testing [141-144], micro-bending [150-152] (cantilevers, three-point bend specimens and fatigue specimens), including the most recent, novel, in-situ, lift-out small scale mechanical tests: three-point bending and push-to-pull micro-tensile testing work, performed on material relevant to the Canadian Nuclear Industry. It will also touch on in-situ

mechanical testing techniques at the smallest scale performed within the transmission electron microscope (TEM) meant for observing dislocation motions and interactions and understanding deformation primarily from a mechanistic viewpoint.

2.2 Small Shear Punch Tests (SPT)/Miniaturized Disk Bend Test (MDBT)

One of the earliest small scale mechanical tests developed for use on nuclear materials is the small shear punch test (SPT), otherwise known as the miniaturized disk bend test (MDBT). This test originally introduced by Manahan et al. in [10] proved convenient because the disks are the same diameter and thickness ($d = 3 \text{ mm}$, $t = 250 \text{ }\mu\text{m}$) as standard disks prepared for Transmission Electron Microscopy (TEM). Simple, already established sample preparation techniques used for the TEM disks can be used. Cut the sample down to a thickness of $300\text{-}500 \text{ }\mu\text{m}$ with a high speed diamond saw blade, thin it down to $250 \text{ }\mu\text{m}$ using established mechanical grinding and polishing techniques, and use a commercially available disc punch system or ultrasonic disc cutter, and the samples are ready to test. In the test, the disc is simply supported in a cylindrical die and pressed into a cavity as shown in Figure 5a. Environmental controls ensure proper alignment and minimize drift as seen in Figure 5b, and with the introduction of an induction heating coil, specimens can be tested at elevated operating temperatures.

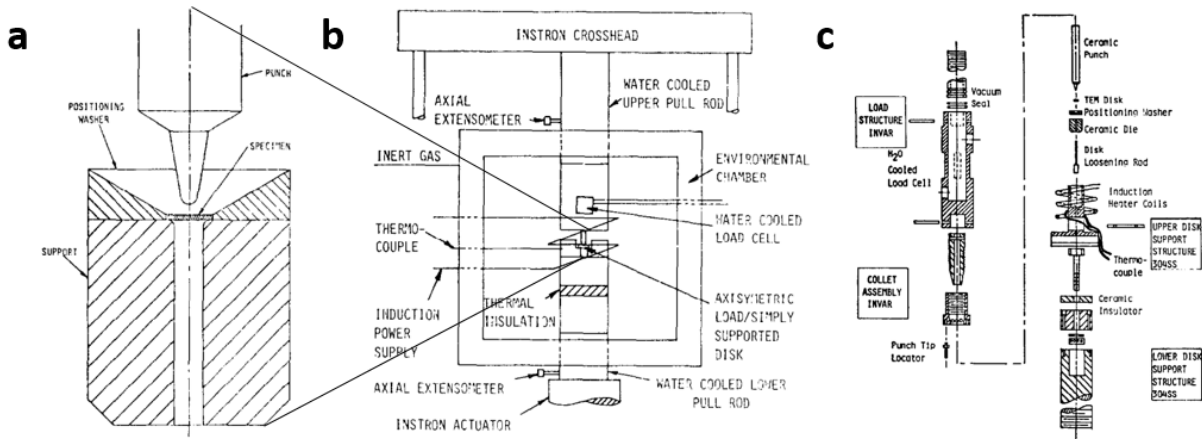


Figure 5. Schematic of miniaturized disk bend test (MDBT) taken from [10]. The irradiated specimen is housed in a cylindrical die and pressed into a cavity as seen in (a). This set up is under an enclosed environment with temperature control as seen in (b). Performing tests at elevated temperature is also an option using an induction heating coil as seen in (c).

The test can be performed in one of two ways: constant displacement rate or constant load. The load versus time is recorded from the load cell and the deflection is measured using the axial extensometer outside of the environmental chamber seen in Figure 5b in order to generate load versus displacement curves of the type shown in Figure 6.

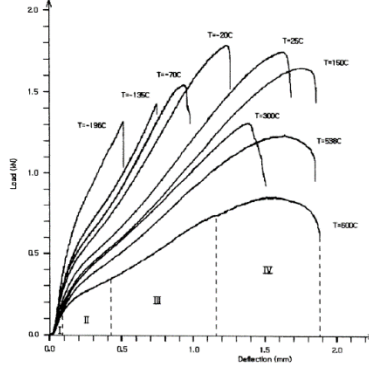


Figure 6. Representative shear punch test load-displacement curves for austenitic 12Cr-1Mo steel taken from [11]

As shown in Figure 2 and further described in [11] and [12], the load-displacement curves can be divided into four regimes: (I) elastic bending deformation, (II) plastic bending deformation, (III) membrane stretching, and (IV) plastic instability leading to failure. Regimes (III) and (IV) associated with necking and severe plastic deformation normally only occur during high temperature testing, especially for embrittled post-irradiated metals.

Shear punch/MDBT tests generate a biaxial stress/strain response. For the elastic deformation occurring in regime (I), the following analytical expressions developed by Roarke and Young in [13] for the deflection at the center of the disk, w , and peak stress, σ_r , at the outer fiber in the radial and hoop directions can be applied:

$$w = \frac{pa^2(3+v)}{16\pi D(1+v)} \quad (1)$$

$$\sigma_r = \sigma_\theta = \frac{3p}{2\pi t^2} \left[(1+v) \ln\left(\frac{a}{r_o} + 1\right) \right] \quad (2)$$

where p is the applied load, a the disk radius, r_o the radius of the punch-disk contact area, D the plate constant given by equation (3)

$$D = \frac{Et^3}{12(1-\nu^2)} \quad (3)$$

and ν the Poisson ratio of the material. From equation (1), assuming the disk is spherical, the strain during elastic deformation can be expressed as follows:

$$\varepsilon = \frac{tw}{a^2+w^2} \quad (4)$$

where t is the thickness of the disk and all other variables are listed above. More commonly, the shear stress, τ , is plotted against the normalized displacement, δ , which are given by the following expressions:

$$\tau = \frac{p}{2\pi r_o t} \quad (5)$$

$$\delta = \frac{d_c}{t} \quad (6)$$

with d_c being the displacement of the punch.

Once the deformation escalates beyond the elastic regime, deriving analytical expressions to calculate stress and strain becomes complex. Some approaches to do this can be found in [14-17]. An approach to take into account regime (III), membrane stretching, can be found in [18]. Alternative methodologies for determining the plastic stress-strain behavior of shear punch tests involve finite element analysis modelling (FEM) first suggested by [10] and later expanded by [19] and [20]. After extensive testing on a plethora of alloy systems, linear correlations between uniaxial bulk tensile yield strengths, σ_y , and SPT shear yield strengths, τ_y , and uniaxial bulk tensile engineering strain to failure, ϵ_f , and normalized displacement of the SPT, δ , were determined [17, 19-26]. An early example of these correlations on multiple metals and alloys from [17] can be seen in Figure 7.

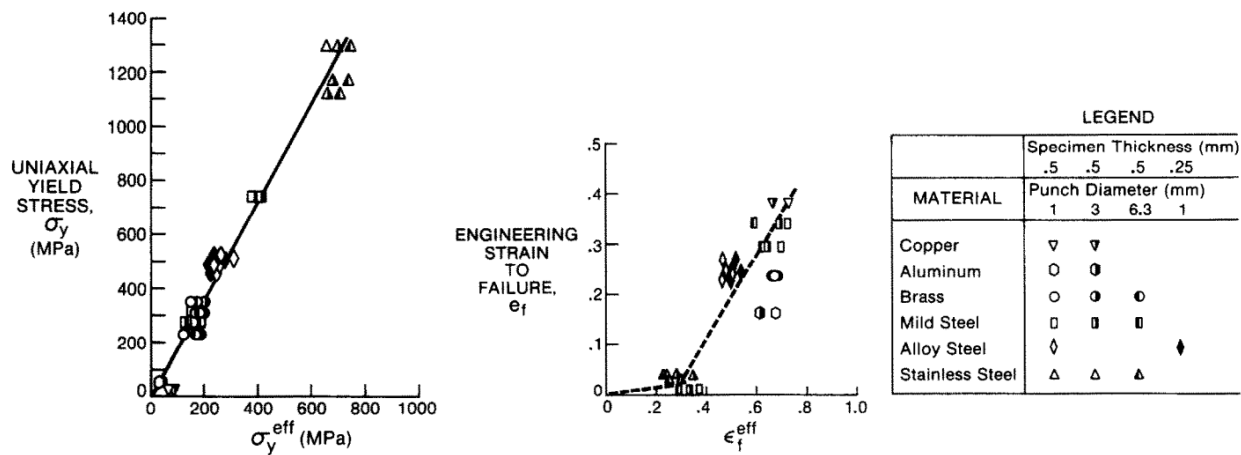


Figure 7. Plotted linear correlations between uniaxial yield stress and total elongation and shear punch test effective yield stress and total elongation [17]

Due to inexact knowledge of the stress state within the disk during the punching operation and no standard procedures for determining the yield point of a SPT test along with inherent material differences, there exists noticeable variations in the reported yield stress correlations. The ratio of the uniaxial to shear stress in the Von Mises yield criterion (critical distortional energy) for a state of pure shear, $\sigma_y/\tau_y = \sqrt{3} \approx 1.73$ can be considered an estimate for the empirical ratio. The Tresca yield criterion (critical shear stress) suggests the ratio $\sigma_y/\tau_y = 2$. However, SPT tests do not create a state of perfect pure shear. Experimental data on individual alloy sets in [27] shows that the ratios are somewhat different as shown in Table 1, noting a broad range of values between 1.7 and 2.9.

Table 1: Ratio of Yield Strength to Shear Strength for Alloys with Indicated Base Element

Base Alloy Element	σ_y/τ_y
Fe (FCC)	1.7
V	2.8
Al	2.6

When all data points are combined and plotted as one family of *fcc* alloys, a ratio of 2 is reported in [27]. FEA modelling performed in [19] determines the ratio $\sigma_y/\tau_y = 1.77$.

In addition to yield stress correlations, ductility correlations involving total elongations and strain hardening exponents were also developed. Assuming the definition of power law strain hardening (PLSH) exemplified in equation (7) for the portions of the stress-strain curves between the yield point and failure point and a 0.2% offset from linear elasticity for the yield point, equations were developed for ratios between ultimate stresses and yield stresses in equations (8) and (9).

$$\sigma = K \varepsilon_{pl}^n \quad (7)$$

$$\left(\frac{n_\sigma}{0.002}\right)^{n_\sigma} = \frac{\sigma_{UTS}}{\sigma_y} \quad (8)$$

$$\left(\frac{n_\tau}{0.002}\right)^{n_\tau} = \frac{\tau_{UTS}}{\tau_y} \quad (9)$$

where σ_{UTS} is the ultimate tensile stress, σ_y is the yield stress, K is a strength index, ε_{pl} is plastic strain, n_σ is the strain exponent of the tensile specimen, n_τ is the strain exponent of the shear punch specimen, τ_{UTS} is the shear punch maximum stress, and τ_y is the shear punch yield stress. Using the calculated strain hardening exponents n_σ and n_τ , the true uniform elongation of the tensile test ε_{u-true} , and the measured strain hardening exponent of the tensile test, n , ductility correlations were determined in [24], the most useful being $\varepsilon_{u-true}/n_\tau$ so that a uniform elongation can be estimated from the SPT. This ratio $\varepsilon_{u-true}/n_\tau$ was found to lie between 2.1 and 2.8 depending on the selected alloy system, but when all alloys are included $\varepsilon_{u-true}/n_\tau = 2.26-2.35$, and the authors suggest that a single linear correlation may be able to be applied for a variety of materials, heat treatments, and irradiation-induced microstructures based on [24] and [28].

The original, primary application of the SPT test was to pre-fabricate disks from new candidate alloys manufactured for proposed fusion reactor programs that were placed into small capsules and inserted in test reactors for irradiations where space for these capsules was extremely limited such that full tensile specimens could not be inserted. The advantages of SPT/MDBT are that the

sample preparation is quick and easy, requiring only a standard metallography grinding and polishing lab and a TEM disc punch. Testing can be performed by adapting a bulk scale Instron or similar type load cell in a relatively simple way. Reasonable correlation ratios were developed in order to estimate yield stress, strain hardening, and uniform elongation of candidate materials and track ductility loss in ex-service steels due to tempering and irradiation embrittlement [11, 12, 29]. The sample sizes are large enough to represent bulk material behavior at the millimeter scale because they contain a sufficient amount of all microstructural elements considered to be strength determining features.

However, the biaxial stress state that occurs during shear punch tests makes the determination of the mechanical properties of the discs a rather complicated matter. Improvements have been made to the test set up in [30] to reduce the compliance of the test fixture and help generate more accurate yield points that can be measured by applying 0.2% offsets and more representative loading curves with some deformation details, but a full fundamental understanding of the stress state on the disc is lacking. In addition, no direct links can be made between deformation mechanisms and mechanical properties. The sample volumes of the shear punch discs most likely require all work to maintain inside of the hot cell for highly active ex-service components which is time, space, and cost expensive.

2.3 Miniaturized Charpy Subsize Fracture Tests

Subsize fracture specimens in the form of Charpy-V-Notch (CVN) specimens are meant to track the shift in ductile to brittle transition temperature (DBTT) in reactor pressure vessel (RPV) low-alloy ferritic steels as a function of in-service time and dose. A secondary application involves placing non-irradiated, candidate structural materials for fusion reactors in the form of mini CVN specimens into irradiation facilities where in core space is at a premium and sample sizes must be kept small. A photograph of a representative subsize CVN specimen next to an ASTM CVN specimen can be seen in Figure 8 taken from [17].

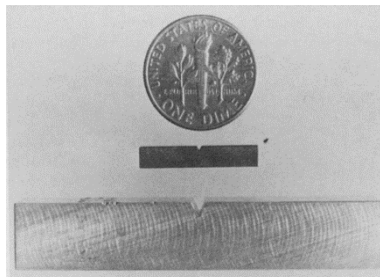


Figure 8. Representative subsize CVN specimen (center) with dimensions 3.33 mm x 3.33 mm x 16.7 mm in comparison to a standard CVN specimen (bottom) with dimensions 10 mm x 10 mm x 55 mm [17]

Even when the concept of subsize fracture tests was conceived by Myers et al. in [31], there existed an understanding that the specimens would not yield direct engineering data, but instead could serve as a more fundamental study to monitor differences caused by radiation effects and new insights on basic fracture at an unexplored length scale. It was quickly discovered that miniaturization of CVN specimens causes a decrease in Upper Shelf Energy (USE) as well as a reduction of DBTT compared to standard sized CVN specimens [32-37]. This is exemplified here in Figure 9 taken from [36] where a 9Cr-2W-0.1C ferritic steel was Charpy impact tested.

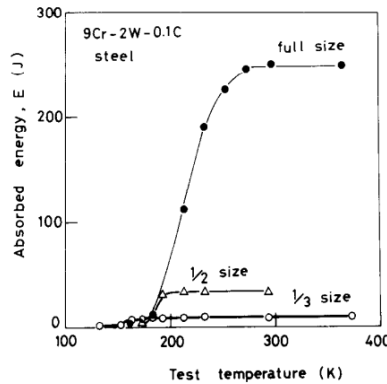


Figure 9. The absorbed energy as a function of test temperature for full sized ASTM (10 mm x 10 mm x 50 mm) CVN specimens compared against half-sized and one-third sized CVN specimens for a 9Cr-2W-0.1C ferritic steel [36]

Subsequent research introduced empirical and geometric normalization factors in order to correlate mini CVN specimen testing with standardized testing. Because the sub-sized testing was not standardized, various correlations resulted for correlating both USE and DBTT.

For USE, the European methodology [38-42] was simple: perform a large number of tests and determine one empirical ratio $USE_{full-size}/USE_{subsize} = C$, where C is a constant. The methodology in North America and Japan consisted of taking ratios of physical geometric parameters in order to determine the most suitable normalization factor (NF) as shown in equation (10).

$$\frac{USE_{full\ size}}{USE_{subsize}} = \frac{f(\text{geometric parameters})_{full\ size}}{f(\text{geometric parameters})_{subsize}} = NF \quad (10)$$

In order to assist with the explanations of the various geometric normalization factors investigated, Figure 10 depicts the specimen dimensions of any CVN test, where L is the span length, R the notch radius, θ the notch opening angle, W the specimen height, B the width of the ligament below the notch, and b the depth of the ligament below the notch, and a the notch depth.

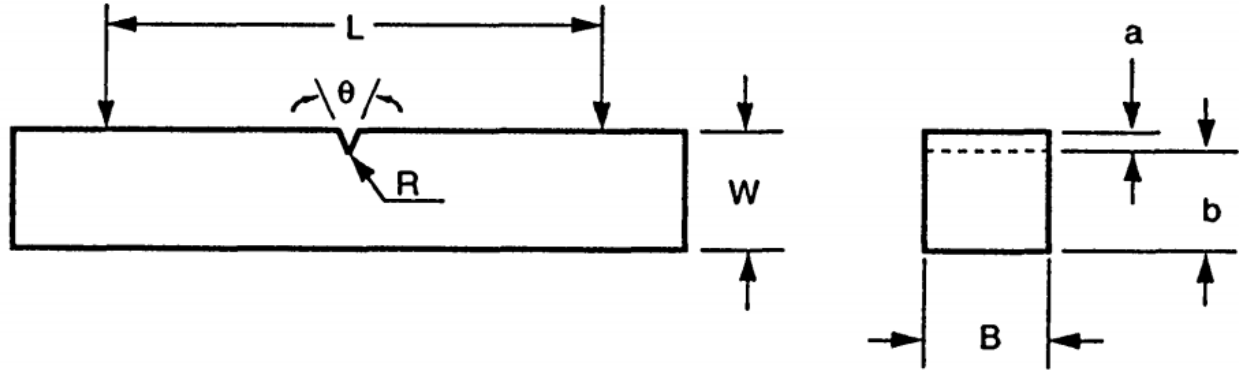


Figure 10. CVN test specimen dimensions

The first geometrical parameter was the ratio of the fracture areas of the two specimens proposed in [32] and [35], equal to Bb . Then, ratios were developed based on the nominal fracture volumes of the two specimens: Bb^2 in [37, 43] and $(Bb)^{1.5}$ in [32, 35]. Louden adjusted the ratio based on fracture volumes to also take into account specimen dimensions, and produced a new geometrical parameter Bb^2/LK_t in [44], where K_t is an elastic stress concentration factor described in [45]. Next, Kayano in [46] proposed two new geometrical parameters, $GP_1 = Bb^2/QK_t$ and $GP_2 = (Bb)^{1.5}/QK_t$ that also took into account the notch angle θ of the specimens via a plastic stress concentration factor Q expressed in equation (11), where the notch angle θ is expressed in radians.

$$Q = 1 + \frac{\pi - \theta}{2} \quad (11)$$

However, because Q is a plastic stress concentration factor based on slip-line field theory that assumes perfect elastic-plastic behavior and neglects work hardening, it will obviously not hold completely true for most materials. Slip-line field theory also requires fracture at the load where yielding occurs, which only happens at one temperature for any material during Charpy CVN testing.

Specimen size effects on the DBTT can be explained as follows. As test temperature increases, the initiation of plasticity is aided and yielding occurs at lower stress. This can be expressed as an Arrhenius relationship in equation (12), where A and c are constants and T is temperature.

$$\sigma_y = Ae^{c/T} \quad (12)$$

Weibull statistics have found that the brittle fracture stress of a specimen is determined by the value of the local stress at its weakest location where a critical structural defect sits. Thus, there exists a dependence on the volume of the specimen and a probability for sampling a specimen with a size sufficient enough to contain this weakest link. Decreasing specimen size increases scatter. The brittle fracture stress can be given according to equation (13), where Z and m are material constants and V is sample volume.

$$\sigma_f = ZV^{-1/m} \quad (13)$$

The temperature $T = DBTT$ can be considered the point at which $\sigma_y = \sigma_f$ such that equations (12) and (13) equal one another. Thus, the DBTT is a function of sample volume as follows in equation (14) where R and S are material constants.

$$DBTT = \frac{1}{R-S \ln V} \quad (14)$$

However, because subsized CVN specimens were not standardized, a variety of different notch geometries were fabricated, which equation (14) does not take into account. Thus, an empirical correlation to calculate a universal temperature shift correlation constant, T_{shift} , was adopted as the common approach, reflected in equation (15).

$$DBTT_{full\ size} = DBTT_{subsize} + T_{shift} \quad (15)$$

Normalizations for the DBTT by similar geometrical factors as described in [32, 37, 44, 46] for use in normalizing the USE proved effective such that the shifts in the DBTT caused by irradiation on the subsized specimens could equate to shifts caused in full sized specimens expressed in equation (16).

$$\Delta DBTT_{normalized\ full\ size} = \Delta DBTT_{normalized\ subsize} \quad (16)$$

Both Sokolov and Nanstead at Oak Ridge National Laboratory (ORNL) in the US [47] and Lucon et al. at SCK-CEN in Belgium [48] generated large databases of data on many ferritic steel alloys in an attempt to validate proposed mini to full sized CVN specimen correlations. The ORNL database generated in [47] investigated four types of RPV steels using five different mini CVN geometries from 11 material conditions and found that the most accurate estimation of USE involved the following ratio in equation (17).

$$\frac{USE_{full\ size}}{USE_{subsize}} = \frac{Bb^2_{full\ size}}{Bb^2_{subsize}} \quad (17)$$

The ORNL study [47] also produced an overall temperature shift combined empirical/geometrical formulation for the temperature shift T_{shift} in equation (18).

$$T_{shift} = 98 - 15.1 \ln(Bb^2) \quad (18)$$

The SCK-CEN study in [48] created a database performing a round-robin with 232 full size and 333 sub-size CVN specimen tests fabricated from 19 alloys, 8 non-irradiated and 11 irradiated, and came up with the following empirical universal normalization constants: $NF_{USE} = 21.56 \pm 2.64$, $T_{shift} = 65 \pm 15$ °C.

Through tedious efforts of generating large material databases and many attempts with a variety of geometric normalization factors, miniaturized Charpy-V-Notch specimens were able to be correlated to the full-sized standard specimens. The data and application of a Charpy test is most valuable for investigating reactor pressure vessel (RPV) steels which become embrittled after service time in order to monitor the shift in DBTT and ensure safe operations. The application of this specific SSMT is unique to investigating this component

in Light Water Reactors (LWRs). Due to lugubrious geometrical calculations and the large databases that would need to be obtained for application to other alloy systems, mini CVN is most likely not the preferred SSMT to be used to investigate other reactor components. Other SSMTs provide more straightforward determinations of mechanical properties with much simpler stress states and allow for more mechanistic information regarding deformation pathways and failure mechanisms.

2.4 Microhardness Tests

Microhardness testing involves indenting a sample surface with a diamond or hard ceramic indenter using a known applied test load between 1 and 1000 gf. Typical forces are approximately 2 N \approx 200 gf and produce indents about 50 μ m wide. Hardness measurements are measured by dividing the applied force by the surface area of the indent. There are two common testing methods: Vickers hardness testing (HV) and Knoop hardness testing (HK).

Microhardness tests are a robust, fast, and simple method of categorizing radiation-induced hardening/softening of any reactor core internals or structural materials. Because they are permanent impressions into the material, the measured hardness values can then be empirically correlated to predictive changes in yield stresses and ultimate tensile stresses as a function of irradiation dose, dose rate, or temperature. A piece of material thicker than a few hundred microns and at least a few mm² in surface area polished to a smooth finish is all that is required. Commercially available microhardness testers can easily go inside of the hot cell and perform the work in an automated fashion. However, because microhardness is an indentation technique, it creates a triaxial loading stress within the material, and it is difficult to analytically determine the exact plastic zone size around each indent. In addition, no quantitative information regarding changes in ductility or brittleness can be obtained, although qualitative information can be inferred based on post-test observations in the SEM or by extracting TEM lamella from deformed regions of material beneath the indents. Because the plastic zone sizes are quite large for microhardness indents (> 100 μ m), it may struggle to accurately characterize changes in materials produced by ion irradiation simulation studies, since the penetration depth of these irradiations is limited to 4-100 μ m. Also, good statistics may be difficult to obtain on components and materials with limited sample surface areas and thicknesses to investigate. Smaller length scale SSMTs are needed to investigate these materials.

Vickers hardness tests are the more versatile and favored of the two techniques. They indent with a pyramidal diamond punch with a 136° opening angle between opposite faces and conveniently use one hardness scale to test all materials. The Vickers hardness of a material is calculated according to equation (19)

$$HV = \frac{F}{A} = \frac{2 \sin 68^\circ F}{d^2} \quad [kgf/mm^2] \quad (19)$$

where d is the average length of the diagonals of the surface indent and F is the load. The contact area, A , can also be taken as the ratio of the area of the base of the pyramid to the area sides of the pyramid such that Vickers hardness can be given more simply as (20), where P is the stress normal to the indenter tip.

$$HV = 0.927 P \quad (20)$$

Sample thickness should be kept 2.5 times larger than the indent diameter. The indent depth can be calculated by equation (21).

$$h = \frac{d}{2\sqrt{2}\tan\frac{\theta}{2}} \quad (21)$$

Minimum distances between indents and the distance between any indent and the edge of the sample should be at least 2.5 times larger than the average indent diagonal length.

Plastic flow of the metal around the indenter tip must be examined in two dimensions, along and perpendicular to the axis of the indenter tip because the tip surface is not parallel to the sample surface. Plastic deformation occurs when the Huber-Mises criterion is met, when the maximum shear stress reaches a critical value, k , according to equation (22)

$$2k = 1.15\sigma_y \quad (22)$$

where σ_y is the yield stress. Prantl mapped plastic flow around the pyramidal wedge punch in [49]. The stress normal to the top surface of the indenter, P , can be given by equation (23)

$$P = 2k(1+\pi/2) \quad (23)$$

Combining equations (21) and (22) produces

$$P = 1.15\sigma_y(1+\pi/2) \approx 2.96\sigma_y \quad (24)$$

Combining equations (20) and (24) produces the material independent analytical correlation between Vickers microhardness and yield strength as (25)

$$\sigma_y = 3.55 HV \quad [MPa] \quad (25)$$

The first empirical correlations were performed on austenitic stainless steels with varying amounts of cold work by Bruemmer [50] and Kodama and Suzuki [51] from which the following correlation was fit to the data:

$$\sigma_y = 2.5(HV - 68) \quad [MPa] \quad (26)$$

Toloczko repeated the experiment in [52] and arrived at a quite similar correlation equation:

$$\sigma_y = 2.7HV - 125 \quad [MPa] \quad (27)$$

By Vickers hardness testing irradiated and non-irradiated 300 series steels, Higgy and Hammad empirically verified a linear relationship between changes in HV and changes in σ_y [53]:

$$\Delta HV = K \Delta \sigma_y \quad (28)$$

where $K = 2.82$ for 316 SS and $K = 3.00$ for 347 SS. J. Busby ultimately compiled the work of many independent projects correlating changes in Vickers microhardness to changes in yield strength on austenitic stainless steels and RPV ferritic steels under irradiation shown in Figure 11 and arrived at master correlation equations [54]:

$$\Delta HV = 3.03 \Delta \sigma_y \quad (fcc) \quad (29)$$

$$\Delta HV = 3.06 \Delta \sigma_y \quad (bcc) \quad (30)$$

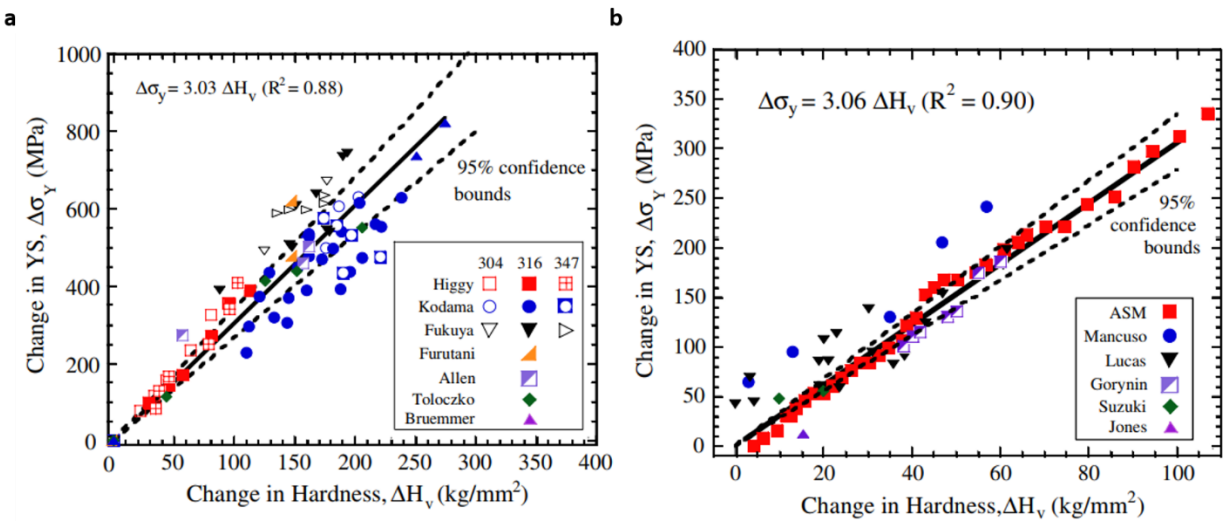


Figure 11. Master empirical correlation curves plotting change in uniaxial tensile yield stress versus change in Vickers microhardness for austenitic stainless steels (a) and ferritic steels (b). [54]

Because the correlation factors are nearly identical for austenitic and ferritic steels, these results strongly suggest that the correlation is independent of alloy type, crystal structure, and operating conditions. This concept is also supported by Tabor in [55] who derived a theoretical correlation factor between the changes in the two mechanical properties of 3.33 MPa/kg/mm^2 and experimentally measured correlation factors for two alloy systems to be $K_{C \text{ steel}} = 3.44 \text{ MPa/kg/mm}^2$ and $K_{Cu} = 3.33 \text{ MPa/kg/mm}^2$. However, irradiation effects may slightly reduce the correlation constant and account for the $\sim 0.3 \text{ MPa/kg/mm}^2$ difference, or this difference is simply statistically insignificant.

Knoop hardness tests are meant for brittle materials and thin sheets or thin effected areas, be they by irradiation, welding, or other processing, where a shallow indentation depth is required to avoid unwanted effects of cracking and compliance. An elongated pyramidal diamond punch with a length to width ratio of 7:1 and a larger opening angle of 172.5° and smaller opening angle of 130°

indents the polished sample surface. The indentation depth can be approximated as 1/30 of the longer dimension of the punch. Knoop hardness is given in equation (23), where F is the load, $C_p = 0.070279$ is a shape factor, and L is the length of the longest indent diagonal [329].

$$HK = \frac{F}{C_p L^2} \quad [kgf/mm^2] \quad (31)$$

Knoop hardness tests have been applied to investigate irradiation effects on ceramics in the nuclear industry such as nuclear graphite in [56] which serves as a moderator, reflector, and structural material, especially in gas-cooled reactor designs and boron carbide power proposed as an absorber in fast reactor control elements in [57]. Knoop hardness also served as an effective tool for remote measurements in the hot cell on thin neutron irradiated Zircaloy cladding tubes investigating all six planar directions of the tube. The results of [58] indicated a reduction in anisotropy of the Zircaloy cladding with an increase in neutron fluence. Similarly in [59], the effect of differing texture in Zircaloy cladding tubes impacting its mechanical properties was investigated via Knoop hardness. Because of its advantage in investigating the mechanical properties of thin sheets, Knoop hardness was also used to study the radiation stability of ZrN, which serves as a proposed inert matrix material to house transuranic fuel in next generation reactor designs as well as a surrogate material for characterizing transuranic nitride metallic fuels [60]. Knoop hardness was effective at profiling the changes in mechanical properties across the heat effected zone (HAZ) of a weld in V-4Cr-4Ti candidate fusion reactor first wall and structural material [61].

2.5 Nanoindentation Tests

Nanoindentation tests extract the elastic modulus and hardness of a specimen while only indenting it to a maximum depth of a few microns. This SSMT was specifically developed for measuring the mechanical properties of samples that have a minimal volume. Thus, nanoindentation is the ideal quick and robust mechanical testing technique used to study the effect of ion irradiations and determine their validity as a surrogate irradiation technique to in-service irradiations. Nanoindentation has been proven to accurately profile ion irradiated zones of material and the transition interface between irradiated and non-irradiated material where injected interstitials sit, in good agreement with Stopping Range of Ions in Matter (SRIM) software [62]. Nanoindentation can also generate larger statistics than microhardness due to its smaller plastic zone (< 50 μm); more indents can be taken from the same sample surface. In cases where the preservation of components and/or candidate materials is a must, nanoindentation can be considered an effectively non-destructive testing technique. It lends itself well as a potential non-destructive, portable SSMT technique which can be brought to the component or material on site while it is in-service or while service has been halted without needing to remove it. For

expensive, one-of-a-kind, new alloys developed for next generation reactor technologies, nanoindentation is the best technique to obtain some mechanical information and preserve sample material.

The punch penetration depth beneath the surface of the specimen is measured as the load is applied to the indenter to produce load versus displacement curves. By knowing the exact geometry of the indenter tip, the contact area can be determined; the elastic modulus can be determined by measuring the slope of the unloading portion of the load versus displacement curve.

A popular, widely accepted method for determining the mechanical properties of hardness, H , and elastic modulus, E , through experimental methods is given by Oliver and Pharr in [63]. Depictions of typical loading-unloading nanoindentation curves highlighting important physical parameters can be seen in Figure 12.

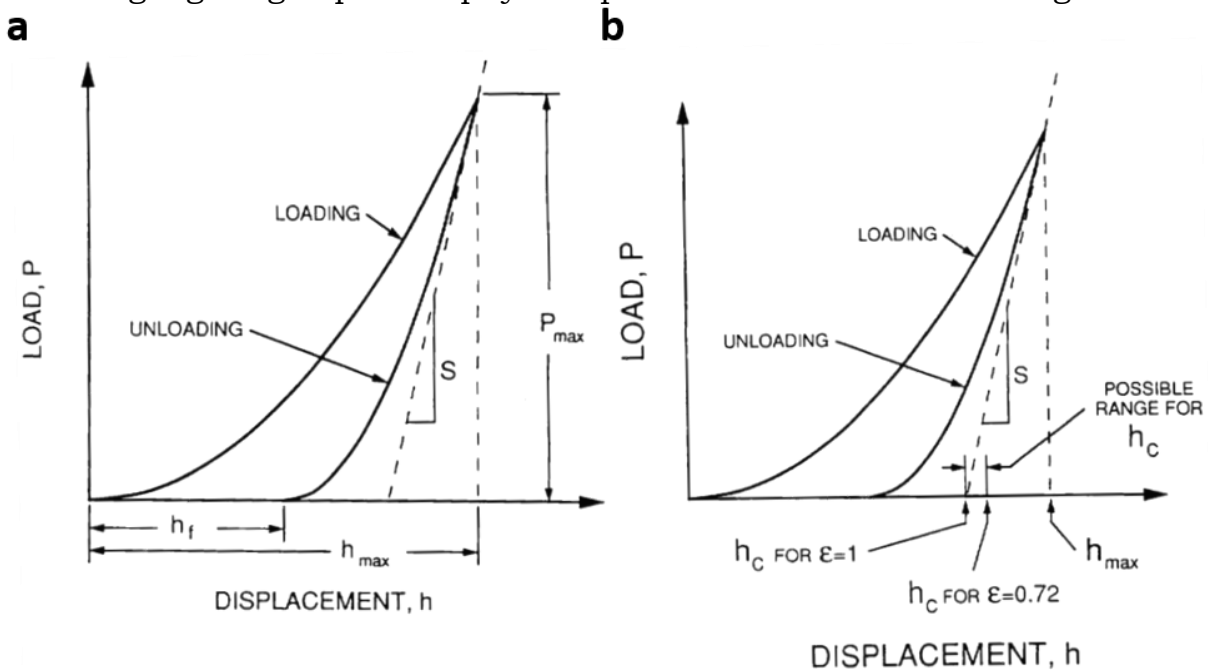


Figure 12. Nanoindentation load versus displacement curves, indicating the peak load, P_{max} , displacement at peak load, h_{max} , and final contact depth after unloading, h_f in (a). The initial unloading stiffness, S , shown in both (a) and (b), determines the contact depth, h_c , along with a geometric constant, ϵ , as shown in (b) [63].

The earliest load-displacement studies performed by Tabor [64, 65] confirmed that the impression formed in metals takes the shape of the indenter punch, but with a slightly larger tip opening angle. Since elastic contact solutions existed for both spherical and conical punches, the effect of plasticity in the elastic unloading data could be accounted for by taking into account the shape of the indented surface in this elastic analysis. The shape of the unloading curve and amount of recovered displacement can be related to the elastic modulus.

Because the indenter is not a perfectly rigid body, this is accounted for by introducing a reduced modulus, E_r , which is a superposition of the moduli of the indenter and indented material according to equation (32)

$$\frac{1}{E_r} = \frac{(1-\nu^2)}{E} + \frac{(1-\nu_i^2)}{E_i} \quad (32)$$

where ν_i and E_i are the known Poisson's ratio and elastic modulus of the indenter punch and ν and E are the Poisson's ratio and elastic modulus of the indented material. A stiffness parameter, S , as shown in Figure 8 was related to the reduced modulus and contact area, A_c , of the indent in [66-70] by equation (33) and shown to hold true for any indenter tip that can be analytically modelled by a smooth function in [71].

$$S = \frac{dP}{dh} = \frac{2}{\sqrt{\pi}} E_r \sqrt{A_c} \quad (33)$$

The total displacement, h_{max} , can be divided into the contact depth and the displacement of the sample surface at the perimeter of contact, h_s .

$$h_{max} = h_c + h_s \quad (34)$$

Surface deflection, h_s , is dependent on indenter geometry according to equation (35) derived in [72], where ϵ is a geometric constant spanning the range $\epsilon = 0.72$ for conical indenters and $\epsilon = 1$ for flat punches, P_{max} is the maximum load, and S is the stiffness calculated according to (33).

$$h_s = \epsilon \frac{P_{max}}{S} \quad (35)$$

Experimentally, the Oliver and Pharr method [63] utilizes the fact that the deformation of the indenter during nanoindentation is minimal and creates an area function as described in [73] and [74]

$$A = F(h) \quad (36)$$

where the contact area is

$$A_c = F(h_c) \quad (37)$$

The two most commonly used indenter tips are the Berkovich three-sided pyramidal diamond punch with an opening angle equal to 142.3° and the spherical nanoindenter. The three-sided pyramidal Berkovich indenter tip makes a sharper point (tip radius 50-100 nm) than the four-sided Vickers microhardness punch allowing for more precise shallow nanoindents. Its mean contact pressure is determined from measuring its contact depth, h_c , such that the perfect projected contact area is:

$$A_{c-perf-Berk} = 3\sqrt{3}h_c^2 \tan^2\theta \approx 24.5 h_c^2 \quad (38)$$

with θ being the half-opening angle equal to 65.27° . For spherical nanoindenters, the perfect contact area is given by:

$$A_{c-perf-sphere} = \pi (2R_i h_c - h_c^2) \approx 2\pi R_i h_c \quad (39)$$

where R_i is the radius of the sphere punch. The approximation is valid for indentation depths much smaller than the radius of the indenter. The Oliver and Pharr method [73] begins with a perfect contact area function, A_{perf} , as a first estimate and applying an iterative process indenting the material to be studied to large depths to in order to correct for tip blunting and load frame compliance where C_i are fitting constants:

$$A_{c-real} = A_{c-perf} + C_1 h_c + C_2 h_c^{1/2} + C_3 h_c^{1/4} + \dots + C_8 h_c^{1/128} \quad (40)$$

The hardness, H , is then computed from the maximum load, P_{max} , and contact area by evaluating (40) at the contact depth, h_c , as

$$H = \frac{P_{max}}{A_c} \quad (41)$$

The slope of a fraction of the initial unloading portion of the curve in Figure 8, normally the highest 70-80% up to the maximum load, can be fit to a straight line to measure the stiffness, S , if the peak load is held to minimize creep effects. Standard nanoindentation loading can be load controlled or displacement controlled and employs a 5-2-5 three segment sequence. Loading occurs for 5 seconds during the first segment, the peak load is held for 2 seconds during the second segment, and unloading occurs for 5 seconds in the third segment. In [73], Oliver and Pharr developed a power law relation

$$P = C(h - h_f)^m \quad (42)$$

to describe the unloading portion of the curve seen in Figure 8 by expressing the load, P , as a function of the displacement, h , final displacement after unloading, h_f , and material constants C and m . The stiffness, S , is determined by differentiating (42) and evaluating it at the peak load and displacement, P_{max} and h_{max} after determining materials constants C and m via linear regression least squares fitting. After the stiffness value, S , is determined by either of the above procedures, the reduced modulus can be calculated by rearranging (33), and the elastic modulus can be solved for using (32).

The primary application for nanoindentation in the nuclear materials community has been to probe shallow ion irradiated and implanted sample regions and map out relative changes in hardness for candidate reactor structural materials. The reasons for this are twofold: first to determine if materials with certain inherent properties such as crystal structure, microstructure, etc. are more susceptible to irradiation hardening; and second to fine tune ion irradiation techniques such that they better simulate radiation environments the components experience in service. This can be done by performing the same nanoindentation studies on the same ion and neutron irradiated material and control material so that a one-to-one comparison can be made without having to be concerned with heat-to-heat processing variations. Nanoindentation of ion irradiated materials can be

performed either parallel to the incoming ion beam or perpendicular to the incoming ion beam. This is depicted in Figure 13 adapted from [75].

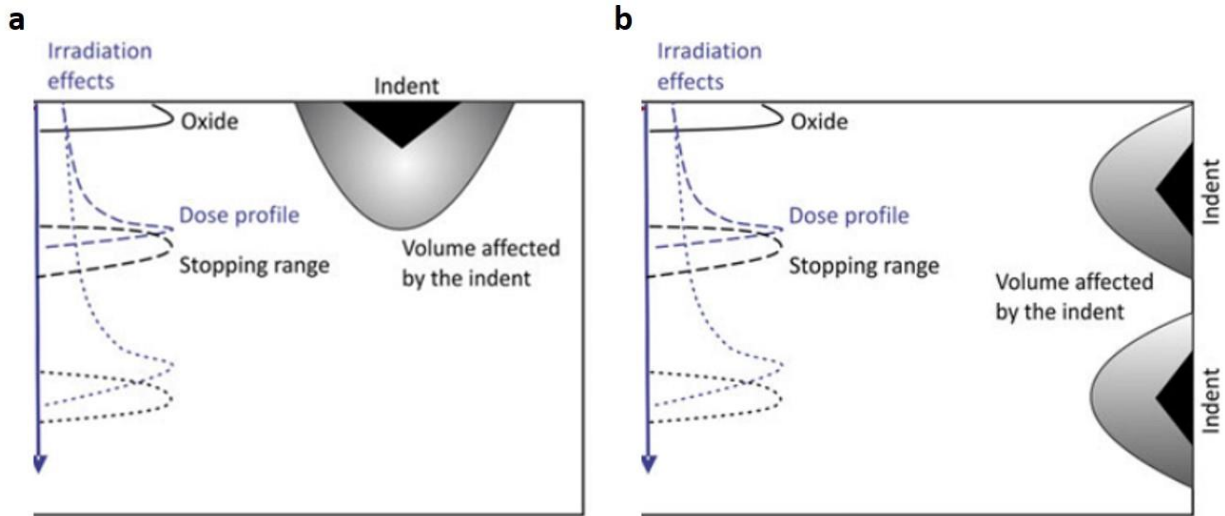


Figure 13. Schematic depiction of nanoindentation performed on ion irradiated materials (a) parallel to the incident ion beam and (b) perpendicular to the incident ion beam. Shallow ion irradiated samples are exemplified by the dashed line and deep ion implanted samples by the dotted line [75]

If nanoindentations are performed into the sample surface in the beam direction as in Figure 13a, the materials properties are sampled over a wide dose range in a non-uniform manner. Because each nanoindent brings with it a plastic zone size approximately five times the indentation depth [76], indenting in parallel to the beam direction convolutes the measurement into sampling a broad range of doses and dose rates, especially if the plastic zone were to include the stopping peak region. For example, if a 200 nm deep indent were made in an ion irradiated sample, all material in a 1 μm radius around that indent would contribute to its hardness value. Plastic zone sizes, c , associated with individual indents can be calculated according to the Johnson model from [77], knowing the yield strength of the material, σ_y , elastic modulus of the material, E , half-opening angle of the indenter punch, θ , and radius of the indent, r , according to:

$$c = r \sqrt[3]{\frac{E}{3\sigma_y \tan\theta}} \quad (43)$$

This also raises the importance of indent spacing; any two indents' plastic zones should not overlap. Thus, as a safe rule of thumb, indents should be spaced apart roughly 10 to 20 times their indentation depth. Therefore, individual hardness measurements cannot be associated with individual SRIM dose calculations for specific depths if the indentation is performed as shown in Figure 9a. Instead, only a global hardness change can be associated with the entire dose range of the ion implantation. For all of these reasons, the preferred method of nanoindentation on ion irradiated materials is the one depicted in Figure 13b,

often referred to as cross-section nanoindentation. Load-controlled nanoindentation set to a maximum load of ion irradiated material should also be avoided because the non-uniformity of the irradiation will cause indents in the harder/softer irradiated region to go to a shallower/deeper depth and appear harder/softer than they really are. This will overestimate the effects of radiation hardening/softening. Cross-section nanoindentation in constant displacement-controlled mode most accurately samples individual dose regions of ion implantation, and when an optimal indentation depth is chosen, can profile the hardness changes in the material in a way that almost mirrors the predicted SRIM profile of the ion irradiated material, except for the stopping peak region. An example of effective 200 nm depth, cross-section nanoindentation on 10 dpa proton irradiated 304 SS with its overlaid SRIM profile adapted from [78] can be seen in Figure 14.

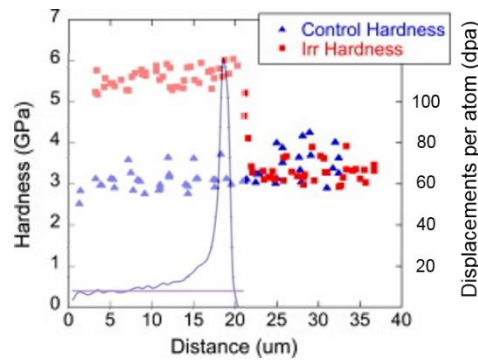


Figure 14. 200 nm deep cross-section nanoindentation of 10 dpa proton irradiated 304 SS with overlaid SRIM dose profile [78]

It is well documented that an indentation size effect (ISE) exists where the measured hardness increases with decreasing indentation depth [62, 79]. Nix and Gao have modelled the ISE based on the volumetric density of geometrically necessary dislocations (GND) contained within the hemispherical plastic zone beneath the visible indent [80]:

$$\frac{H}{H_o} = \sqrt{1 + \frac{h^*}{h}} \quad (44)$$

H is the hardness of the material at a given depth h , H_o is the hardness of the material at an “infinite depth,” effectively the bulk hardness value, and h^* is the characteristic depth where the material produces bulk hardness values when indented. By performing indents at many depths and measuring their hardness values, the ISE can be accounted for by plotting the data as $(H/H_o)^2$ vs. $1/h$ to determine the characteristic depth, h^* .

Krumwiede performed nanoindentation studies on 8 neutron irradiated nuclear alloys (T91, HT9, NF616, F82H, EuoFer97, MA956, MA957, and 14YWT) [81] in order to correlate nanohardness values from indents outside the size-effected

zone, H , with tensile yield strengths, σ_y , by adapting the Busby correlation in [54] to nanoindentations

$$\Delta\sigma_y = 289.17 \Delta H \quad (45)$$

and also applying the following correlation adapted from [82] between the absolute values of nanoindentation hardness and tensile yield strength.

$$\sigma_y = 266.5 H - 114 \quad (46)$$

The results indicate that utilizing the correlation that predicts the absolute tensile properties, equation (46), is more accurate. Krumwiede also points out that when correlating nanoindentation indents to stress values, the value calculated in equation (46) is a more accurate representation of the 8% flow stresses of non-irradiated materials, whereas it more accurately predicts the yield strengths of irradiated materials. Evidence of this is displayed in Figure 15 and can be attributed to the fact that nanoindentation produces sufficient plastic strains to create strain hardening, which is more prevalent in non-irradiated materials.

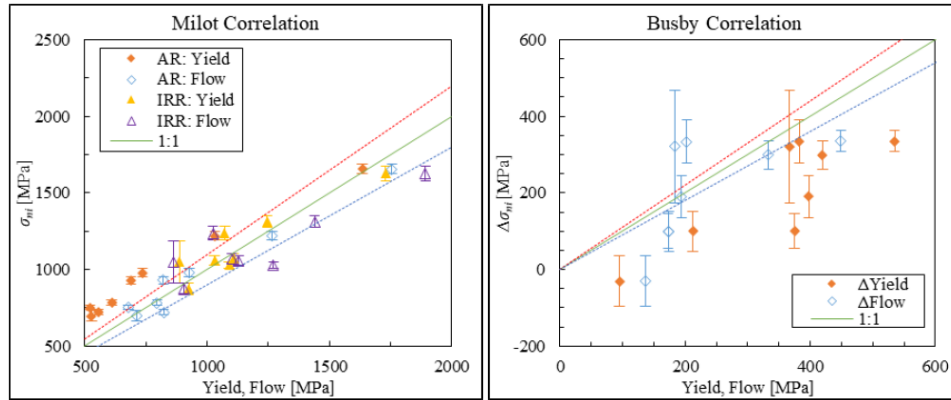


Figure 15. Measured tensile properties plotted against stress values calculated from two nanoindentation hardness-stress correlations: an absolute correlation (left) and change in stress correlation (right). The absolute correlation provides more accurate predictions of a non-irradiated material's flow stress and an irradiated material's yield stress. [81]

In order to select the optimal depth for nanoindentation which both samples a uniform dose in the ion implanted region and which either completely avoids, minimizes, or corrects for the size-effect regime of the material, continuous stiffness measurement (CSM) nanoindentation of ion irradiated material proves to be a useful tool. CSM superimposes a cyclic load onto the monotonic loading sequence of standard nanoindentation and provides hardness and modulus values as a continuous function of the indenter punch depth during one indentation cycle [83]. Thus, CSM cross-section nanoindentation can more efficiently measure and correct for ISE in both the ion implanted region and non-irradiated region and compare the two as exemplified in [84] on an ion irradiated T91 ferritic/martensitic steel alloy, 800H austenitic steel alloy, and Fe-10% Cr steel alloy as shown in Figure 16.

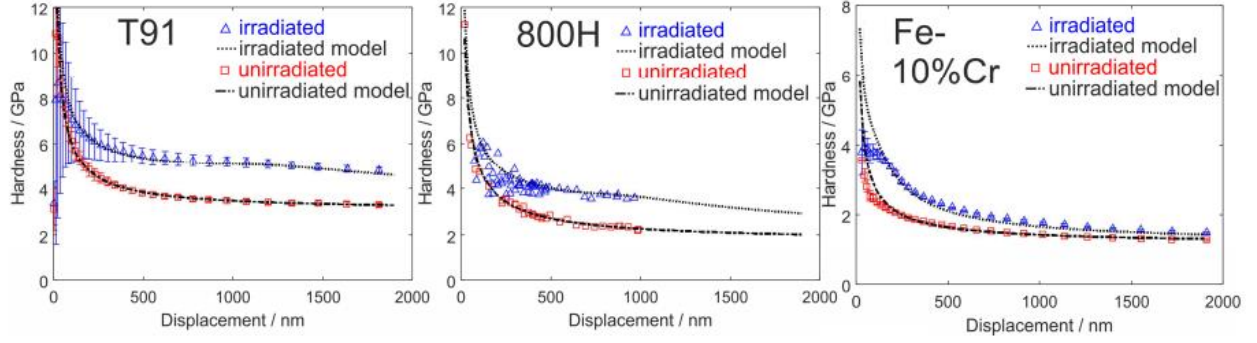


Figure 16. Continuous stiffness measurement (CSM) nanoindentation technique applied to three advanced engineering alloys depicting their hardness vs. depth profiles [82]

Spherical nanoindentation has been explored in an attempt to model an irradiated material's complete elastic-plastic response under contact loading and produce relevant stress-strain curves using Hertz's theory for frictionless contact between two isotropic elastic solids [85] and recasting it into linear relationships for indentation stress, σ_{ind} , and indentation strain, ϵ_{ind} [86, 87]:

$$\sigma_{ind} = \frac{P}{\pi a^2} \quad (47)$$

$$\epsilon_{ind} = \frac{a}{R_{eff}} \quad (48)$$

P is the indenter load, a is the contact radius, and R_{eff} is the effective radius of the indent. The contact radius and effective indent radius can be expressed as:

$$a = \sqrt{2h_c R_i - h_c^2} \quad (49)$$

$$\frac{1}{R_{eff}} = \frac{1}{R_i} + \frac{1}{R_s} \quad (50)$$

R_i is the radius of the indenter and R_s the radius of the indent, and the contact depth, h_c , for a spherical indenter can be approximated as:

$$h_c = h_{max} - \frac{3P}{4S} \quad (51)$$

the maximum displacement h_{max} minus three-fourths times the ratio of the load, P , over the stiffness, S . A new formulation for indentation strain, ϵ_{ind} , born from establishing effective zero-load and zero-displacement points based on a refined idealized primary indentation zone presented in [88] has proven to more accurately capture a material's mechanical properties:

$$\epsilon_{ind} = \frac{4h}{3\pi a} \quad (52)$$

Spherical nanoindentation has been applied to ion irradiated tungsten, studied as a candidate plasma facing component in nuclear fusion reactors in [89, 90] due to tungsten's incredibly high strength, making it difficult to investigate with traditional mechanical tests or other SSMTs where load limits of testing devices would be reached before yielding of the material. The indentation stress-strain curves for the irradiated tungsten candidates can be seen in Figure 17.

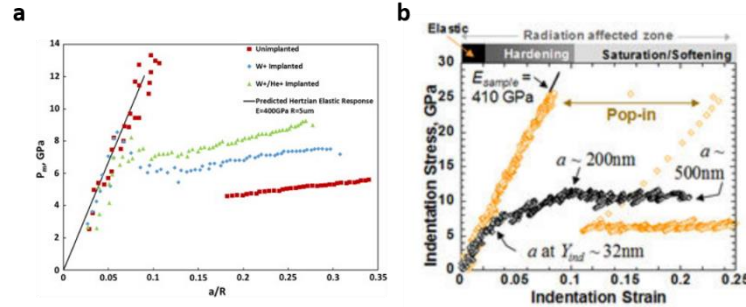


Figure 17. Indentation stress-strain curves calculated from spherical nanoindentation experiments performed on ion irradiated tungsten [89, 90]. Non-irradiated tungsten, red in (a) and orange in (b), shows behavior much like its predicted Hertzian elastic response up until yield. The irradiated yield and flow stresses, blue and green in (a) and black in (b) have increased noticeably.

An artifact of spherical indentation stress-strain curves is the pop-in event, seen as a strain burst in Figure 17. These jumps in displacement are attributed to the indenter suddenly experiencing a large jump in penetration depth simultaneous to the onset of significant plastic deformation [91]. Pop-in events can generate noticeably high stresses close to the theoretical limit $G/2\pi$ [92], where G is the shear modulus of the material, as seen in the stress-strain curves shown in Figure 17. This is attributed to dislocation starvation; the spherical indenter punch is comparable or smaller than dislocation-networks in the sample, so it is much more difficult to activate a dislocation source. Of course, this can be counteracted by using a larger spherical indenter, which would be effective for neutron irradiated material with a uniform irradiation field. However, for ion implanted materials, the irradiated zone is limited to $\sim 100\text{s nm} - 10\text{s }\mu\text{m}$, so in order to sample this zone only and measure changes in mechanical properties due to irradiation without having the plastic zone of the indent extend into non-irradiated material, small spherical indenters and shallow depths must be employed. Performing the spherical indentation in cross-section would be the preferred method, but often times pop-in events are unavoidable. Therefore, for the case of pop-ins, Bushby has developed a methodology [93] for calculating the effective indentation yield strength according to [94] by projecting the plastic portion of the stress-strain curve backward to intersect the elastic loading portion before the pop-in and taking this intersection point as the yield stress. This work in [93] was performed on an ion-irradiated Fe-12%Cr fusion candidate structural alloy. The indentation work hardening coefficient which quantifies the change in plastic flow stress with increase in strain is a much more

straightforward calculation and can be done in the same way as for a standard stress-strain curve.

More recently, spherical nanoindentation has been compared against more advanced SSMT techniques, which will be the future discussions of this review, all performed on single-grained proton irradiated 304 SS specimens [95]. The results indicate that although the absolute values of the yield stresses deviate significantly depending on the technique employed, the changes in yield stress, flow stress, and failure stress are in good agreement.

Because spherical nanoindentation is a time inexpensive SSMT requiring minimal sample preparation beyond a well-polished sample surface and minimal total sample volume, it may be a promising technique to obtain an initial understanding of a neutron irradiated material's elastic-plastic stress-strain behavior and relative changes in mechanical properties. However, the stress-strain curve formulations are much different than those of traditional uniaxial mechanical tests, so some extrapolation is still required in order to make that link and assess its accuracy.

Nanoindentation fracture toughness methods have been applied to nuclear ceramics based on the following formulation from [96]

$$K_{IC} = \alpha \sqrt{\frac{E}{H} \frac{P}{c^{3/2}}} \quad (53)$$

which assumes rapid crack growth which has concluded by the time unloading of the indenter is complete, meaning no slow crack growth effects. The parameters are defined as α , an indenter tip shape factor, E elastic modulus, H indentation hardness, P applied load, and c total measured crack length from the center of the indent to the end of the crack. Specifically, the SiC coating layer meant to prevent fission product release on tristructural isotropic (TRISO) ceramic advanced nuclear fuel forms was indented in [97] and the cracks associated with the 200 nm deep indents ($H = 30\text{-}42$ GPa) seen in Figure 18 were measured and applied to equation (53) in order to arrive at a fracture toughness values between 1.0 and 3.6 $\text{MPa}\sqrt{m}$ for the SiC coating.

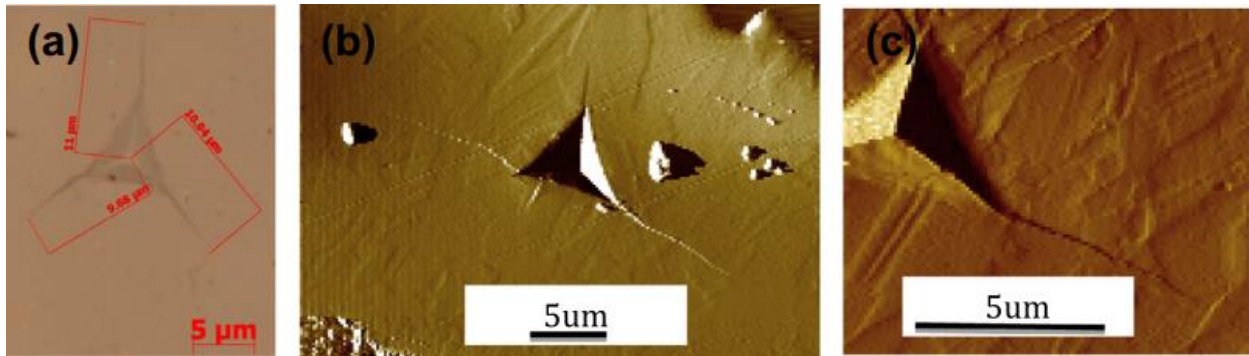


Figure 18. Nanoindentation in SiC coating shell of TRISO advanced nuclear fuel form inducing cracking. (a) optical image (b) scanning probe microscopy (SPM) image of an indent with surrounding cracks, (c) high resolution image revealing the transgranular nature of the crack [97]

Nanoindentation has also been used more recently to evaluate the mechanical properties of irradiated materials at elevated reactor operating temperatures. High temperature indentation tests requires precise, independent temperature matching of sample and indenter tip in order to avoid thermal drift issues [98-101]. Further complications with high temperature experiments include optimizing the indenter tip material to the material to be studied [102-104] and ensuring that the sample surface of the material to be studied does not become oxidized. Diamond degrades rapidly in high temperature environments, especially in air and in contact while indenting. Cubic boron nitride (CBN) is a better choice, but growing large crystals of it and mounting it to a holder that it used in a commercial nanoindenter is challenging. Flooding the assembly with an inert, protective gas such as argon or performing high temperature studies in high vacuum [105] counteracts sample surface oxidation effects. An example of successful high temperature cross-section nanoindentation studies up to reactor operation temperature on proton irradiated 304 SS from [106] is shown in Figure 19.

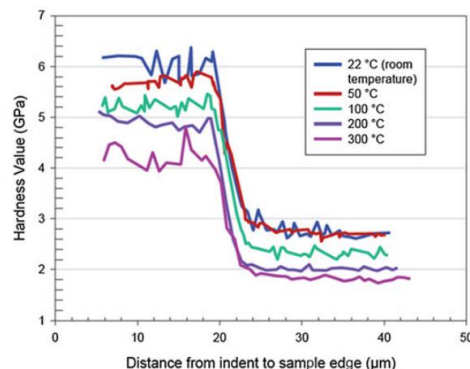


Figure 19. High temperature cross-section nanoindentation hardness profiles of proton irradiated 304 SS indicating clear sharp transitions between irradiated and non-irradiated material [106]

Higher temperature nanoindentation up to 1000 °C is desired to evaluate the mechanical properties of in-service fuels and structural materials to be used in next generation reactor concepts, and cryogenic nanoindentation on irradiated materials which has been recently developed [107] could provide a pathway for a new SSMT to investigate DBTT effects.

Ex-situ nanoindentation creep studies on post-irradiated reactor structural materials have also been explored. In this case, the indenter punch is held at a pre-determined load for an extended period of time and changes in displacement as a function of time are measured. Corrections are made for thermal drift between the sample and tip, and the standard creep equation:

$$\dot{\epsilon} = A \left(\frac{\sigma}{E}\right)^n e^{\frac{-Q}{RT}} \quad (54)$$

must be modified to take the form:

$$\frac{\Delta h}{\Delta t h_o} = A \left(\frac{H_{max}}{E}\right)^n e^{\frac{-Q}{RT}} \quad (55)$$

to be applied to indentation studies. $\dot{\epsilon}$ is the creeping strain rate, A is a material constant, n is the stress exponent, E the elastic modulus, Q activation energy, R the universal gas constant, and T temperature. The applied stress σ is replaced by the maximum hardness H_{max} and the creeping strain rate $\dot{\epsilon}$ is expressed as the change in indenter displacement over time. Equation (55) holds true for stage II steady state creep when the strain rate is assumed to be constant after the indentation is held for sufficient time. Primary stage creep during nanoindentation when dislocations are first formed, initial work hardening occurs, and dislocations are annihilated until dislocation interactions reach a steady state occurs too rapidly in nanoindentation experiments to be studied. A depiction of this nanoindentation creep study on proton irradiated PM 2000 ODS steel is shown in Figure 20 [108].

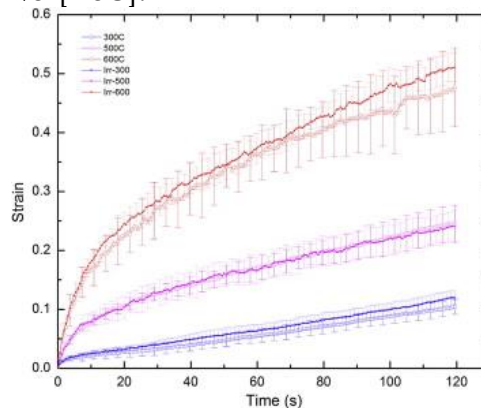


Figure 20. Nanoindentation creep curves depicting the strain rate as a function of holding time for a proton irradiated and a non-irradiated PM 2000 ODS steel [108]

Performing CSM nanoindentation creep studies on irradiated materials may be able to extend the creep time from several minutes as seen in [108] to several hours by reducing drift as demonstrated in [109] on model engineering alloys.

Because of its relative ease of required sample preparation, use, and high degree of automated instrumentation when obtaining a large amount of information from a small volume, nanoindentation has the broadest scope of applications when it comes to characterizing radiation-induced changes in mechanical properties. Many nanoindentation techniques have already been fully developed, but the bandwidth of techniques is ever growing to include new methodologies just in their infancy stages.

2.6 Micro-pillar Compression Tests

By using the Focused Ion Beam (FIB), miniaturized micro- and nano- sized specimens can be fabricated such that they have nominally uniaxial stress states throughout the entire sample. Unlike in the case of nanoindentation where there are inherent strain gradient effects associated with the three-dimensional stress state in the bulk material, deformation occurs at a specific location contained to a well-defined volume. There is no uncertainty with regards to the plastic zone size. It is a straightforward task to take the measured load-displacement curve recorded in the test and using only sample measurements, calculate engineering stress-strain curves. Using analytical solutions for a rigid flat punch compressing a pillar into bulk material [110], modifying it for non-cylindrical pillars [111], and assuming no volume change in the pillar during compression, one can arrive at true stress and true strain formulations where the inputs are the measured force in μN , $F_{\mu\text{N}}$, the measured displacement in nm, d_{nm} , the Poisson ratio of the material, ν , the measured cross-sectional area of the micropillar in m^2 , A , the measured height of the micropillar in m, h , and the elastic modulus of the material in Pa, E .

$$\sigma_{true} [MPa] = \frac{\pi 10^{-12} F_{\mu\text{N}}}{4A} \left(1 + \frac{10^{-9} d_{nm} - 10^{-6} F_{\mu\text{N}} \frac{1-\nu}{E \sqrt{\frac{4A}{\pi}}}}{h} \right) \quad (56)$$

$$\varepsilon_{true} = \ln \left(1 + \frac{10^{-9} d_{nm} - 10^{-6} F_{\mu\text{N}} \frac{1-\nu}{E \sqrt{\frac{4A}{\pi}}}}{h} \right) \quad (57)$$

Micropillar compression was first introduced by Uchic in 2004 [112] who discovered associated size effects in single crystal nickel. Over the course of the next decade, many size-effect studies on the plasticity of various metallic systems occurred and have been well documented in the review in [113]. The most notable trend is that specimen yield strength increases with decreasing characteristic length for single-grained specimens, as depicted in Figure 21 for *fcc* materials

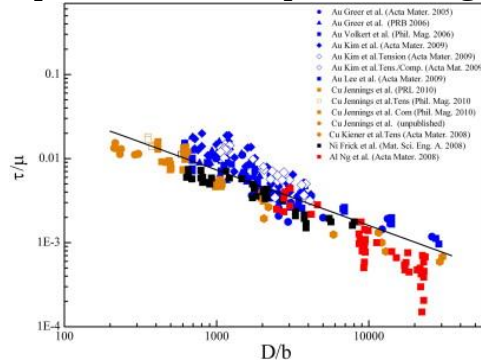


Figure 21. Size effect strengthening in single-grained *fcc* micropillars. Normalized shear flow stress is plotted against specimen characteristic length (diameter normalized by Burgers vector) [113]

which obey a simple power law correlation between their yield strength, σ_y , and diameter, d , with scaling exponent $n \approx 0.6$:

$$\sigma_y \sim d^{-n} \quad (58)$$

The concept of dislocation starvation again rules supreme; extremely small micropillars do not contain enough moveable dislocations so they must first be nucleated, requiring much higher applied stresses. When a few dislocation sources are present, the stress to activate these sources scales inversely with the size of the source and the spacing of the defects. For polycrystalline micropillars, however, there is an intermediate size regime between that of the single crystal strengthening effect and bulk behavior where specimens become weakened due to the formation of a near surface zone, where grain boundaries near the surface have less of a strengthening effect because dislocations can easily propagate to free surfaces and annihilate without forming dislocation pile-ups near these grain boundaries. Eventually, when enough grain boundaries are present in a micropillar such that the majority are in its interior, it will behave like a bulk specimen [114]. For high defect density materials, such as severely plastically deformed (SPD) materials or irradiated materials, the grain boundaries are no longer the strongest strength determining feature, and this intermediate soft size region does not exist [115, 116]. This size scaling behavior of polycrystalline specimens can be summarized in Figure 22 adapted from [117].

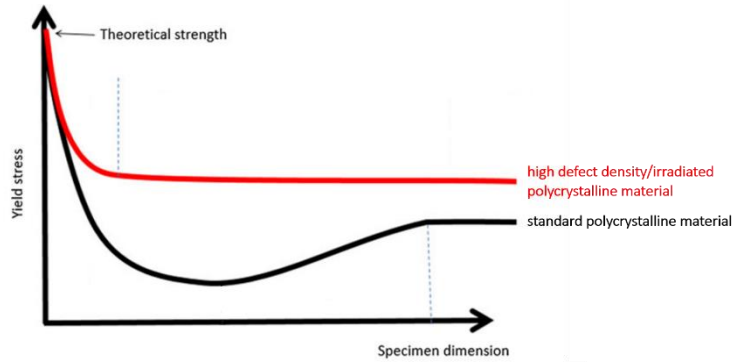


Figure 22. Schematic of size effects in polycrystalline micro-specimens, with a standard material shown in black and a high defect density/irradiated material shown in red. Adapted from [117].

Using the FIB, large batches of micropillars can be fabricated in order to obtain good sampling statistics as exemplified in the schematic in Figure 23. The schematic in Figure 23 represents a simple three step process used to manufacture square micropillars along the edge of a well-polished bulk sample with a sharp edge.

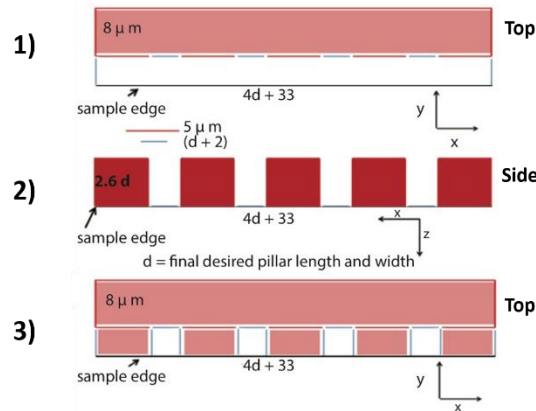


Figure 23. Three-step process developed at UC Berkeley to efficiently fabricate batches of 4 square micropillars along the sample edge in preparation for in-situ SEM testing, where d is the final desired pillar length and width. The process is described as follows:

- 5) A rough trench is milled out at high current (1-15 nA) behind the edge region where the pillars will be made looking down onto the top surface of the sample.
- 6) The sample is viewed looking down onto the side surface, and rough pillar shapes are milled into the “wall” of material at high current (1-7 nA). Note that in this step, the maximum height of the micropillar is determined. For accurate mechanical properties measurements, the final pillar height should be 2-3 times the pillar width [118].
- 7) The sample is viewed from the top again and final polishing/ cleaning of the front and back pillar surfaces is performed at low currents (1.5-100 pA). Counter tilting of 1° is performed to reduce taper.
- 8) Similar cleaning is performed on the pillar side and top surfaces at low currents with the sample oriented as seen in step 2.

In general, simple step-by-step machining procedures can be followed in a semi-automated fashion using standard commercial patterning tools. First, “rough cuts” are performed at higher milling currents, usually 1-15 nA, in order to carve out the general micropillar shape from the bulk. After, “polishing/cleaning” is performed at lower currents, usually 1.5-100 pA, at a glancing angle in order to remove most of the FIB damage during the “rough cutting” stage as well as reduce the taper of the pillar. Knowing the exact, optimal current for each material to be studied requires FIB operational experience. This method of fabricating pillars along the edge of the polished sample is most convenient for performing the compression testing in-situ at high vacuum inside of the SEM

chamber and allows for near perfect alignment during testing in all three axes using the Hysitron PI 85 Picoindenter.

Removing all FIB damage from micropillars is impossible. Kiener has done a study in [119] showing that the FIB damaged region of the micropillar for Cu, a soft material, is within the first 10-40 nm closest to the free surface and depends on the crystallinity, current, and cutting angle used. It can be speculated that the FIB impacted region of other micropillars would be similar, and perhaps for harder or denser materials would be even less. In order to minimize the effect of FIB damage, micropillars should be much larger in width than twice the FIB affected region. Kiener has also suggested that this damage could be annealed out of the smallest nanopillars in [120], but this annealing process also alters the material's microstructure and could change how it mechanistically deforms.

The first studies examining ion irradiated and neutron irradiated materials were mostly performed on candidate engineering alloys, notably ferritic ODS steels [121] and ferritic/martensitic steels [62, 122]. The main focus was to evaluate and compare the uniaxial compressive yield strengths of non-irradiated and irradiated material. The use of micropillar compression testing as a way to sample site specific regions of a material was employed in [123] to fabricate pure ferrite pillars and pure martensite pillars out of a ferritic-martensitic steel, determine their individual mechanical properties, and knowing the phase composition of the bulk alloy, accurately predict its bulk mechanical behavior from the micropillar data.

The possibility of in-situ microcompression testing in order to ensure perfect alignment through positioning of the indenter with aid of the SEM, observe the real-time deformation of the micropillars and record test videos, and couple deformation with quantitative mechanical properties has recently greatly expanded the testing scope. In-situ microcompression was performed in different dose regimes of proton irradiated 304 SS [124] in order to investigate the radiation-induced changes in deformation mechanisms and mechanical properties of the material in multiple dose regimes within the same grain of the sample. Micropillars in the stopping peak dose region (~100 dpa) were found to be much stronger than those in the more uniformly irradiated region (~10 dpa). In addition, radiation deformation mechanisms were quantitatively investigated and compared for the two irradiated conditions and the non-irradiated condition. Calculations for total energy dissipation, energy dissipation per load drop, number of dislocations per observable slip step, and average slip step were made. A depiction of the experimental method and representative test curves is shown in Figure 24.

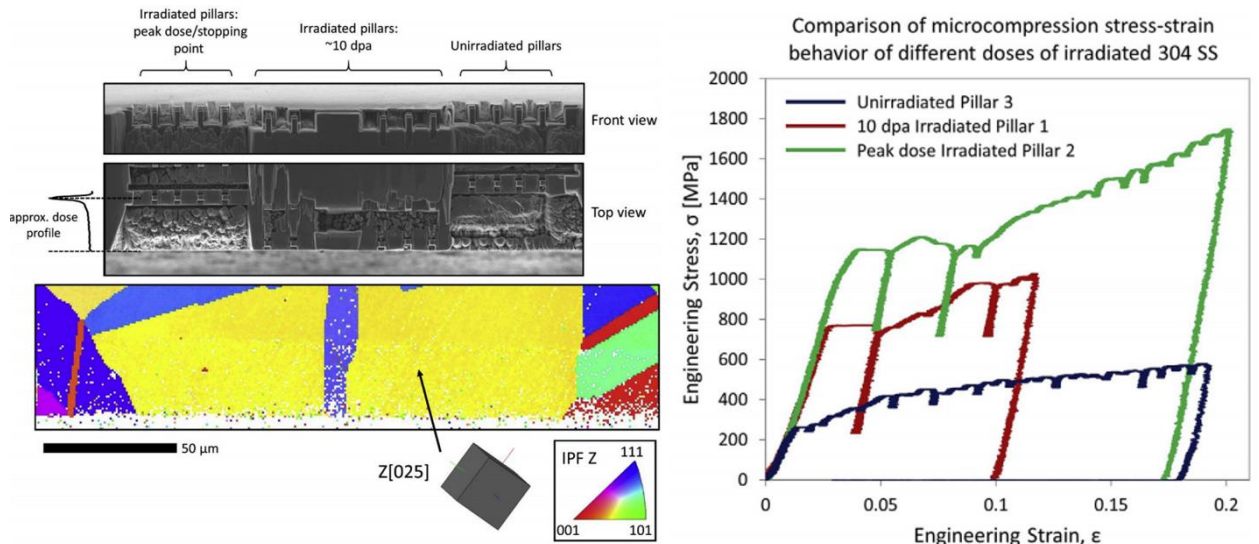


Figure 24. Experimental set up for fabricating micropillars in three distinct irradiation regions from the same grain of a proton irradiated 304 SS specimen and the resultant microcompression engineering stress-strain curves indicating the relative differences in mechanical properties [124]

In-situ microcompression has also been applied to investigate the interface properties of SiC/SiC matrix-fiber composites, considered as accident tolerant fuel cladding material for next generation high temperature reactors [125-127]. Specifically, by varying the interface angle, θ , through the micropillar, between 8° and 84° , and plotting the resolved shear stress versus the resolved normal stress, the debonding shear stress and internal friction coefficient of the composite were determined according to the Mohr-Coulomb criterion. A schematic and exemplary pillar from this experiment can be seen in Figure 25.

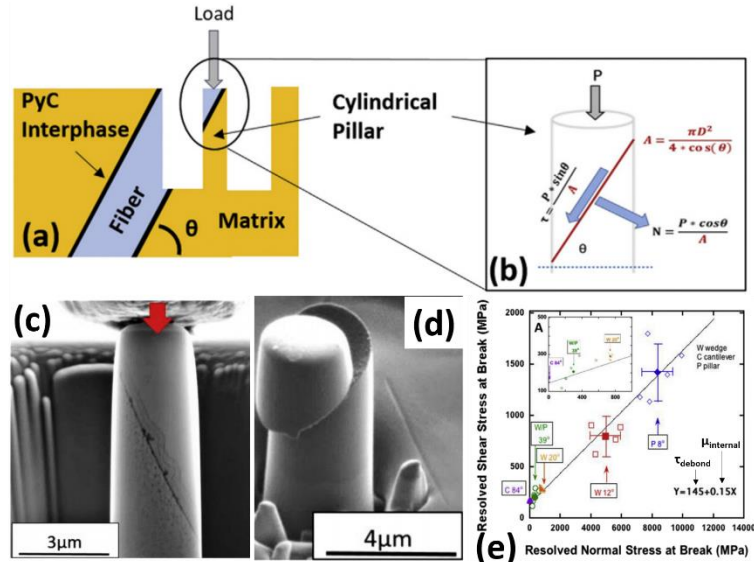


Figure 25. Micropillar compression of SiC/SiC matrix-fiber composites: (a) pillar fabrication schematic, (b) resolved stresses under compression, (c) representative pillar pre-testing, (d) representative pillar with fractured interface post-test, (e) determination of debonding stress and internal friction coefficient according to the Mohr-Coulomb criterion [126]

Micropillar compression testing performed on model materials at cryogenic temperatures in [128] and elevated temperatures [129-132] show promise in developing micropillar compression as a technique to evaluate DBTT on nuclear materials and evaluate reactor components at operating temperatures. Similar issues exist as would for developing nanoindentation for these applications: thermal drift between the pillar and flat punch, indenter punch material selection to resist degradation, and oxidation of the micropillar free surfaces. In addition, for ex-situ micro compression testing, which is the most common for elevated temperature testing, the alignment is difficult and must be done either using a goniometer to evaluate the imprint of the flat punch on the sample and ensure its symmetric [133] or measuring the location of the sample in different areas and tilting it until its straight. Recently, these difficulties have been overcome on irradiated 304 SS by Vo et al. [134], where microcompression testing was performed ex-situ at elevated temperatures up to reactor operation temperature, 300 °C, as shown in Figure 20. Correlations between micropillar data and nanoindentation data at elevated temperature over the range of test temperatures were also developed.

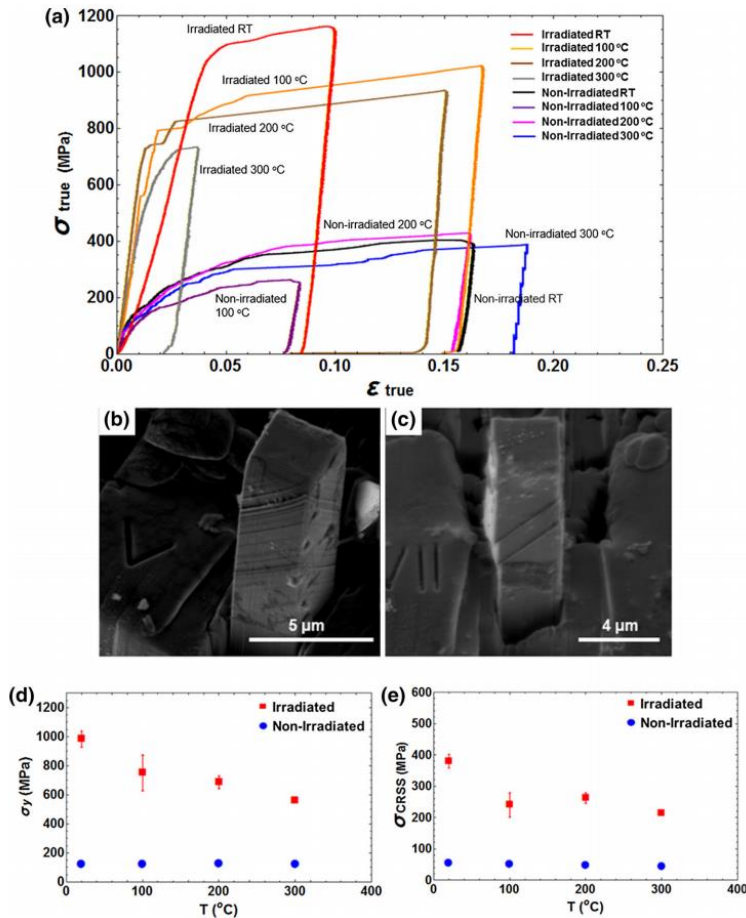


Figure 26. Microcompression testing of irradiated and non-irradiated 304 SS at elevated temperature. (a) micropillar compression true stress-true strain curves, post-test SEM images of a representative (b) non-irradiated micropillar (many small dislocation slip steps) and (c) irradiated micropillar (few large dislocation slip step channels), and yield strength, (d), and critical resolved shear stress, (e), versus temperature [134]

A recently developed, in-situ, irradiation creep study involving micropillar compression testing has been developed using a custom designed spring loaded transducer positioned in line with the ion beam [135]. Although this was performed on a bulk metallic glass and not a nuclear material, the results show clear evidence of irradiation induced creep. There is certainly reason to investigate irradiation creep for materials relevant to the nuclear community and industry by holding them at load under irradiation in a similar fashion.

For highly activated neutron irradiated materials, it would be of great advantage to not have to perform the microcompression test with the bulk sample still attached underneath. Lifting out smaller amounts of material to fabricate a lift-out pillar would greatly reduce the total dose. Lift-out techniques employ nanomanipulators inside high resolution systems, most commonly SEMs, to

locate, attach, transfer, and manipulate small volumes of material using piezoelectric materials combined with inertial drive mechanisms in multiple degrees of freedom, often times three coordinate axes, rotation, and tilt. The actuators obtain nanometer resolution by exploiting differences in static and dynamic friction coefficients, and they can achieve total travel distances of several centimeters. Operating these nanomanipulators close to their range limits should be avoided in order to eliminate drifting of the probe. Needle point probes typically made of tungsten electropolished to $\sim 1 \mu\text{m}$ thickness that can also be re-sharpened in-situ via FIB after blunted due to heavy use harvest tiny specimens and handle them with minimal damage. A gas injection system, typically a platinum organic gas, attaches the specimen to the probe and the specimen to its desired location. The hydrocarbons are stripped from the gas via FIB and the remaining platinum “glues” the specimen to the probe and testing site.

A technique has been developed at UC Berkeley where large lift-out foils approximately $30 \mu\text{m} \times 3 \mu\text{m} \times 8 \mu\text{m}$ from a non-irradiated and irradiated MA957 oxide dispersion strengthened (ODS) steel were removed from the bulk, and rough pillars approximately $3 \mu\text{m} \times 3 \mu\text{m} \times 8 \mu\text{m}$ were cut from the large foil and mounted on top of hard, stiff, flat Si stubs using a Pt gas injection system (GIS) system. These pillars were then polished to remove FIB damage and surface roughness to final sizes of $1.75 \mu\text{m} \times 1.75 \mu\text{m} \times 4 \mu\text{m}$. A small load controlled pre-stress was performed to ensure good surface alignments between the diamond flat punch and the pillar top as well as no gap and good surface alignment between the pillar bottom and the top of the Si stub. The pre-stress was entirely within the linear elastic regime. Corrections were made in order to account for displacing the silicon atom probe stub below the lift out pillars by taking SEM micrographs of 9 tips and measuring the opening angles, widths, and lengths of the tips and developing an analytical expression using geometrical relationships. A comparison between corrected and uncorrected data shows that this effect is almost negligible. Yield strength values changed by 6 MPa or less. Successful tests were performed on two non-irradiated pillars and one irradiated pillar, and the yield strength values were in good agreement with the literature: $\sigma_{y\text{-non-rad}} \approx 1100 \text{ MPa}$ and $\sigma_{y\text{-rad}} \approx 1300 \text{ MPa}$. Figure 27 summarizes this experiment.

A parallel, lift-out, micropillar compression approach also developed at UC Berkeley involves lifting-out a large foil of the material to be studied and mounting it on top of a FIB flattened post of a standard Mo 3 mm TEM disk for in-situ SEM testing. Mo grids are chose due to their high stiffness and robustness in handling as opposed to soft Cu grids which may cause more noticeable compliance issues and which easily bend upon handling. The advantage of this method over the previous method is the fact that individual specimens can be thinned for ion irradiation and helium implantation using the Zeiss Orion Helium Ion Microscope (HIM) which is limited to a penetration depth

of ~300 nm. However, the larger foil may generate a detectable radiation field due to its larger sample volume as opposed to the first method which only involves individual pillars. An example foil can be shown in Figure 28.

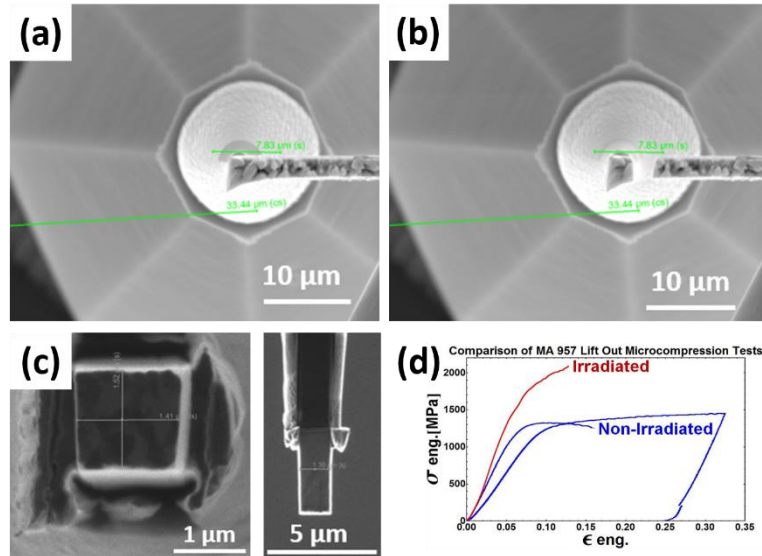


Figure 27. Lift-out pillar compression technique: (a) large lift-out foil positioned over top of a flat Si stub, (b) a rough lift-out pillar mounted on top of the Si stub with a Pt GIS, (c) top and side images of a finished, cleaned lift-out pillar, (d) engineering stress-strain curves for irradiated and non-irradiated MA 957 lift-out pillars. Enhanced from [136]

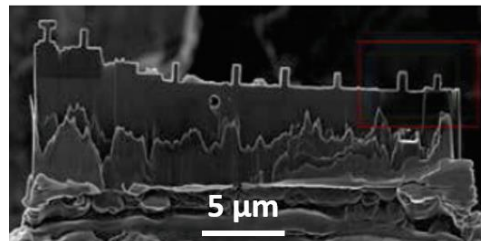


Figure 28. Helium Ion Microscope (HIM) image of an array of micropillars manufactured on a lift-out foil sitting on top of a Mo TEM grid post. The pillars boxed in red have been implanted with a flux of 10^{18} He ions/cm². [137]

Instruments associated with the SEM/FIB that are not designed for irradiation now become accessible for use on highly irradiated lift-out micropillars that have seen high doses and dose rates because their sample volume is so small that no residual activity can be measured by standard radiation detectors. Lift-out microcompression also seems to be more FIB time efficient because trenching is only performed once from one orientation to extract the large foil instead of twice from two orientations in order to fabricate a batch of micropillars in a bulk

specimen. Several lift-out micropillars can be manufactured from one large lift-out foil.

2.7 Micro-tensile Tests

Although micropillar compression testing has a wide breadth of applications in the nuclear materials community and allows for the convenience of a uniaxial stress state to obtain quantitative yield stress values, and with in-situ testing, a limited look into changes in deformation pathways caused by irradiation, ductile metallic specimens cannot be tested to failure and no mechanical information regarding ductility can be obtained. Microtensile testing has the advantage of obtaining uniform and total elongation of a specimen tested in a uniaxial stress state in addition to obtaining yield stress and work hardening rates which can also be obtained from micropillars. The results produced are by far the easiest to analyze of any SSMT and match directly to the most commonly used ASTM test in practice in industry.

As is the case for most SSMTs, micro-tensile testing originated in the fields of more basic materials science research as a way to investigate the synthesis of materials with reduced dimensions, such as thin coatings, nanostructured materials, and thin films. This has helped experimental techniques advance to commercial availability with controlled instrumentation. The development of micro-tensile techniques in the non-nuclear fields is well reviewed by Giancola and Eberl [138]. Highlights include the availability of easy-to-use non-contact strain measurement systems such as interferometric strain displacement gauges and digital image correlation (DIC), small-scale actuators using cantilevers or produced by lithographic masking and microelectronics (MEMS), and the improvement of high fidelity dynamic range transducers, positioning stages, and sensors.

Micro-tensile specimens fabricated for in-situ SEM testing using a gripper-based pulling design emerged first on model materials in [139, 140]. The gripper is FIB manufactured from either an unfinished diamond flat punch or a tungsten nanomanipulator probe and threaded on the backside to be screwed into an in-situ SEM nanoindenter. Careful attention to the gauge length to sample width aspect ratio should be paid; aspect ratios smaller than 2:1 show significant size effect strengthening due to the limited free glide of dislocations over the sample cross-section resulting in dislocation pile-up. Gripper based, in-situ SEM micro-tensile testing has since been expanded to irradiated, single-grained specimens on the order of $1.3 \mu\text{m} \times 1.3 \mu\text{m} \times 4.5 \mu\text{m}$ fabricated from the bulk of a well-polished sample surface in [140] on proton irradiated 304 SS. Clear differences in strength: critical resolved shear stress (CRSS) and yield stress, and plasticity/ductility: total elongation, total plastic energy released, the associated number of load drop events in the stress-strain curves, the average energy released per load drop, and the associated number of dislocations needed to form individual slip step channels were well documented. Post-irradiation annealing

at 500 °C indicated significant recovery of ductility as well as reduction in radiation strengthening. This can be seen in Figure 29 adapted from [141].

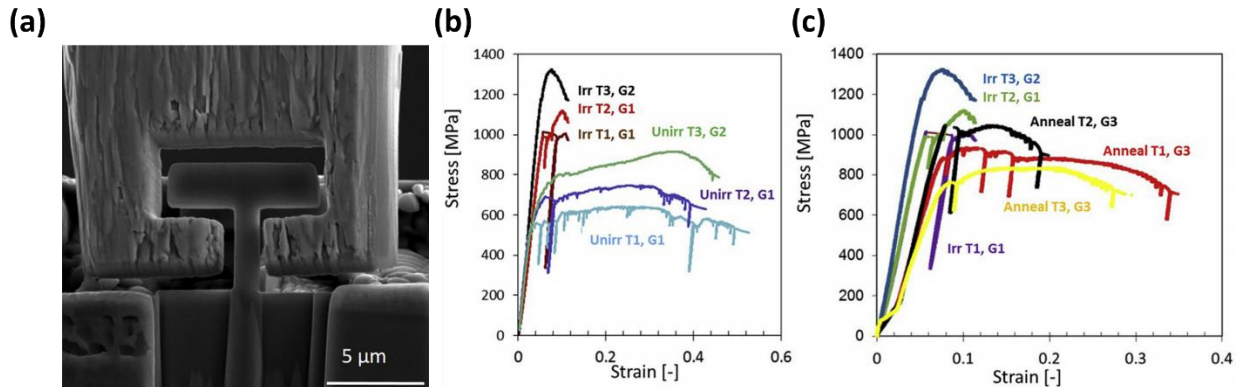


Figure 29. Bulk micro-tensile testing of proton irradiated 304 SS. (a) SEM image of pre-test experimental set up depicting tungsten gripper aligned to pull a test specimen. (b) Engineering stress-strain curves of irradiated and non-irradiated micro-tensile specimens. (c) Post-irradiation annealed micro-tensile specimens indicate some recovery of ductility and reduction in yield strength increase. [141]

Similar to the gripper method of pulling a micro-tensile specimen fabricated from larger electropolished needles in [139, 140] or from the well-polished bulk sample surface, a hook-based technique (micro-test rig MTR-3 developed by MicroTesting Solutions in Hilliard, OH, USA and operated at the Institute of Materials Engineering in ANSTO) has been used to pull larger 10 μm width x 13 μm thickness x 25-30 μm gauge length micro-tensile specimens, experimental design shown in Figure 30, cut out of a thin pre-prepared foil or wedge of the material of interest [142].

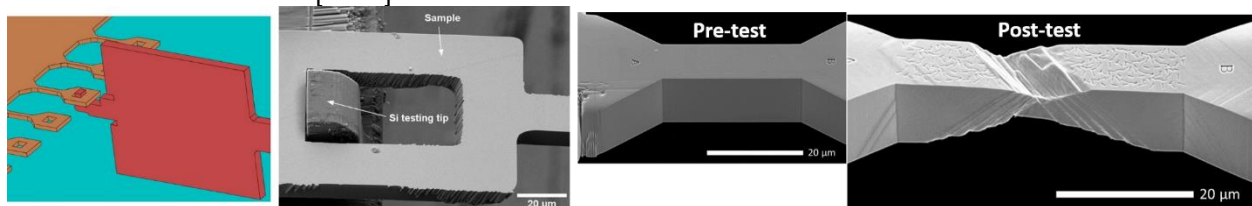


Figure 30. Hook-based micro-tensile testing design which allows for larger sized specimens up to maximum approximate size 15 μm x 15 μm x 30 μm to be tested in-situ in the SEM. An example single-crystal nickel specimen from [142] is depicted.

An interesting caveat of the work of [142] reveals that the stopping peak region produced by ion irradiation blocks dislocations. Traditionally, well prepared foils or wedges are ion irradiated and subsequently micro-tensile specimens are fabricated in the ion irradiated region, but if neutron irradiated material could be prepared in the form of a foil or wedge, there is no reason the same testing methodology could not be used.

The second type of in-situ, micro-tensile testing performed on nuclear materials involves extracting individual specimens from regions of interest using lift-out techniques employing micro- and nano- manipulators and mounting them on a pre-fabricated testing device. Because nuclear material is often highly activated in the case of neutron irradiation or limited to μm^3 of uniform volume dose in the case of ion irradiation, lift-out micro-tensile testing is preferred for examining specific microstructural features of irradiated materials. This technique can assess interfacial and grain boundary strength properties as well as isolate radiation nucleated phases, such as δ -phase zirconium hydrides which only average 1 μm in thickness. Fujii and Fukuya [143] first used a cantilever-based technique on FIB notched, 45° angled, oxidized grain boundary micro-tensile specimens extracted from Alloy 600, a material commonly used in light water reactors (LWRs) that becomes susceptible to irradiation assisted stress corrosion cracking (IASCC). This technique involves pulling the micro-tensile specimen that is attached to a cantilever and calculating the load applied to the specimen from the displacement of the cantilever by simple beam mechanics according to equation (59).

$$F = \frac{Ewt^3d}{4l^3} \quad (59)$$

E is the Young's modulus and l , w , and t are the length, width, and thickness of the cantilever and d is the displacement of the cantilever during loading. They were able to induce grain boundary failure on two specimens, and grain boundary strength measurements indicated weakening caused by increased phosphorous segregation in one boundary compared to the other. Miura and the previous authors then expanded this lift-out, micro-tensile, cantilever technique to assess the effects of helium on the grain boundary fracture of 316 SS [144]. They placed the grain boundaries perpendicular to the loading direction in a debonding stress state and notched them such that the grain boundary line length was approximately 300 nm and line thickness was 2 μm . Specimens fractured within their grain boundaries when total helium concentrations in the material were higher than 2 at%, the spacing between bubbles on the boundaries was less than or equal to 5 nm, and the matrix hardness was greater than 4.6 GPa. Grain boundary failure strength is noted to trend inversely with helium concentration. Figure 31 depicts the methodologies of these lift-out, micro-tensile, cantilever based tests.

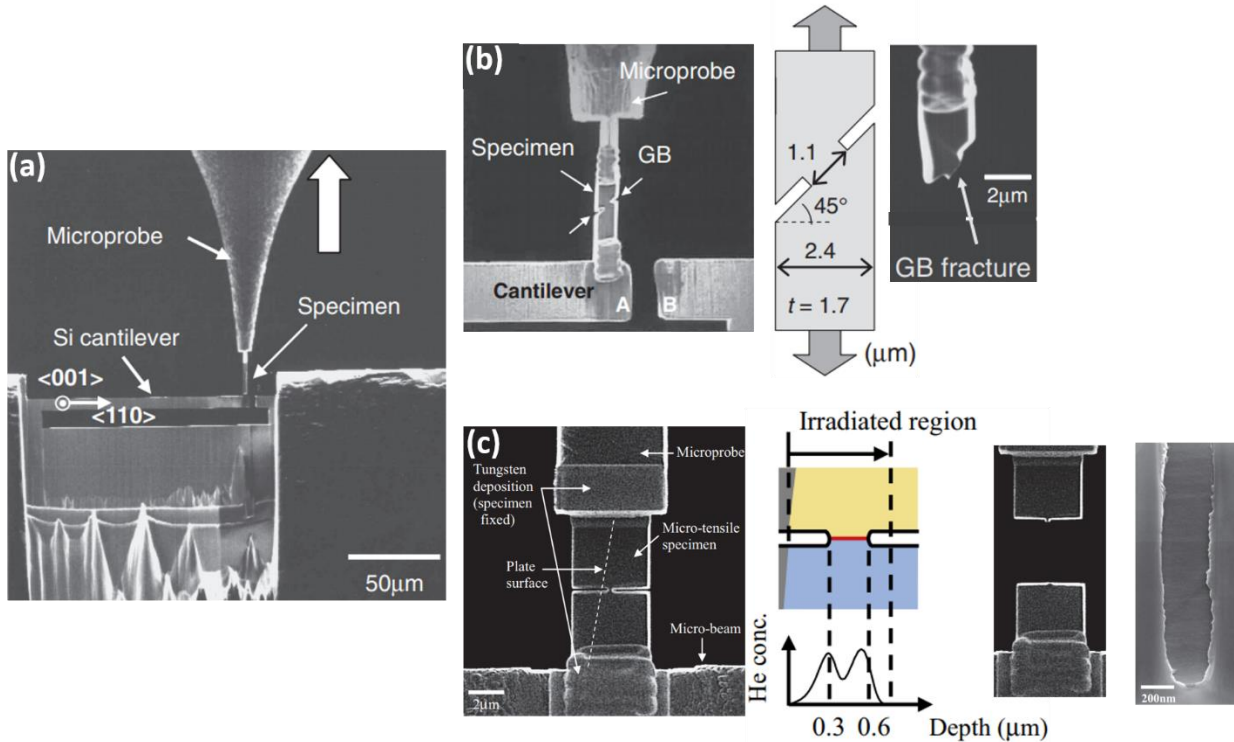


Figure 31. A lift-out, micro-tensile, cantilever-based, in-situ SSMT: (a) View of the complete experimental set up, (b) grain boundary oxidized Alloy 600 specimen notched and tested in a mixed-mode state producing grain boundary failure [143], (c) helium implanted 316 SS notched grain boundary tested in a pure debonding stress state inducing brittle grain boundary fracture [144]

2.8 Micro-Bend Tests

Because almost all commercial indenter systems operate in compression mode only, and due to the fact that the sample preparation, manufacturing, and testing requires complicated lengthy and expensive techniques for the case of micro-tensile testing, micro-bend testing has been developed as an alternative. Micro-bend testing has the capability to directly evaluate more mechanical properties information than nanoindentation, elastic modulus and yield strength, and can be performed with easier alignment than is required for micro-pillar compression. Two commonly used micro-bend tests are in practice today: micro-cantilever testing where a bending beam remains fixed to a bulk substrate at one end and is loading from the opposite end, and micro-three-point bending in which a beam is fixed at its two ends and is pressed in its center. Although both the elastic modulus and yield point can be easily accessed, evaluating any post-yield plastic mechanical properties in a quantitative manner is rather difficult and requires FEM modelling. The bending beams also experience complex stress states; in the case of cantilevers tension on top and compression at the bottom highest at its anchored base and in the case of three-point bending

beams tension at the bottom and compression at the top, highest at its center under the indenting punch. There is also a neutral axis in the center of the beams that remains unstrained. Obvious strain gradients result so analysis of continuous slip channels becomes difficult because the driving forces for dislocation motion change as a function of length along the beams. The energetic approach can be taken, but knowledge of exact crack geometries, lengths, and opening displacements is needed in addition to the recorded load-displacement data. Obtaining this is only possible through in-situ TEM testing due to the high resolution required. At this length scale, testing becomes almost purely mechanistic in nature.

2.8.1 Micro-Cantilever Tests

The first micro-bending method, micro-cantilever testing, was introduced by Di Maio and Roberts [145] to measure the fracture toughness, K_{IC} , of a thin chemically vapor deposited (CVD) tungsten carbide based coating. House-shaped cantilevers were FIB milled from the bulk as pictured in Figure 32 and the plane stress fracture toughness relation

$$K_{IC} = \sigma_c \sqrt{\pi a} F\left(\frac{a}{b}\right) \quad (60)$$

with K_{IC} as the fracture toughness, σ_c the fracture stress, a , the crack length, and $F(a/b)$ a dimensionless shape factor dependent on cantilever geometry. Cutting the cantilevers into the smoothly polished surface of the specimen in arrays like seen in [89] in Figure 33 allows them to be precisely located and loaded accurately, avoiding misalignment issues, using scanning probe microscopy (SPM) to identify the center point of the cantilever at its tip with an ex situ nanoindenter.

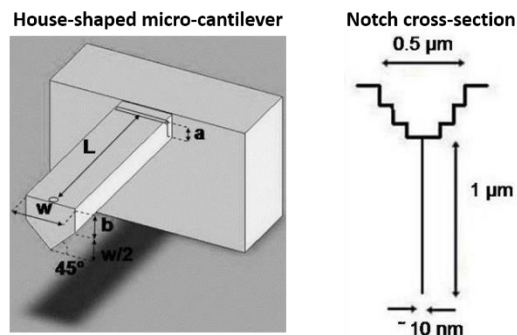


Figure 32. Notched house-shaped micro-cantilever [145]

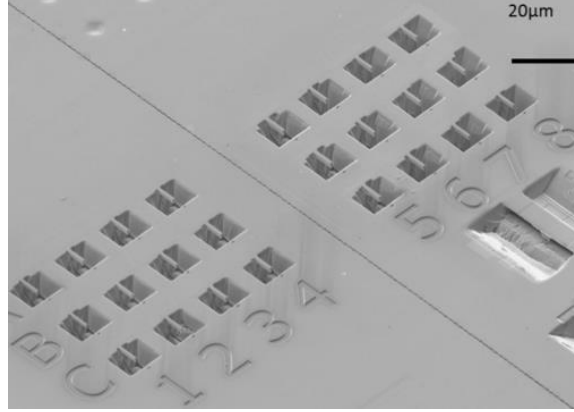


Figure 33. Array of micro-cantilevers milled into a well prepared surface of irradiated Fe-12% Cr. Accurate testing with good alignment can be performed easily ex-situ using scanning probe microscopy (SPM) to identify the loading point in the center of each cantilever [89].

Assuming that only small deflections occur in the material, the stress, σ , can be calculated as

$$\sigma = \frac{PLy}{I} \quad (61)$$

Where P is the applied force of the indenter, L is the length of the cantilever, y is the vertical distance between the neutral axis and the top of the cantilever, and I is the inertia of the cantilever. For the house-shaped cantilevers, the inertia, I , and neutral axis offset parameter, y , are derived as function of the cantilever's width, w , and thickness before taper, b , shown in Figure 32 as follows:

$$y = \frac{\frac{wb^2 + w^2}{2} \frac{(b+w)}{4} \frac{6}{6}}{bw + \frac{w^2}{4}} \quad (62)$$

$$I = \frac{wb^3}{12} + (y - \frac{b}{2})^2 bw + \frac{w^4}{288} + (\frac{7b}{6} - y)^2 \frac{w^2}{4} \quad (63)$$

The shape factor, $F(a/b)$, for house-shaped beams was calculated for crack length, a , to sample thickness before taper, b , ratios $0.3 \leq a/b \leq 0.5$ by applying the boundary element method (BEM) in [146] to relate the applied load to the specimen/crack geometry.

$$F\left(\frac{a}{b}\right) = 1.85 - 3.38\frac{a}{b} + 13.24\left(\frac{a}{b}\right)^2 - 23.26\left(\frac{a}{b}\right)^3 + 16.8\left(\frac{a}{b}\right)^4 \quad (64)$$

This methodology was validated on silicon and measured $K_{IC} = 1.1 \pm 0.016$ MPa/ \sqrt{m} , very close to the bulk fracture toughness values 0.83-0.95 MPa/ \sqrt{m} [147, 148]. The WC coating was then assessed and found to have $K_{IC} = 3.2 \pm 0.3$ MPa/ \sqrt{m} . Because these cantilevers were machined in the center of the bulk specimen, the loading was performed ex-situ. Careful attention should be paid to using FIB milled notches that serve as crack initiators with regards to the FIB

damage created and ensuring an acceptable notch geometry with its appropriate shape factor is produced. House-shaped cantilevers in the bulk were also used to assess the fracture toughness properties of oxidized Alloy 600 exposed to pressurized water at 325 °C at a pressure of 30 kPa [149]. Non-oxidized and oxidized boundaries exposed for 1500 hours were not found to fracture in a brittle manner, but oxidized boundaries exposed for 4500 hours were found to fracture with a toughness 0.73-1.82 MPa/ \sqrt{m} . It is also worthy to note from [149] that no correlation was found between fracture toughness and oxidized grain boundary misorientation angle. This is shown in Figure 34. A concurrent micro-cantilever study on oxidized grain boundaries in Ni alloys subjected to pressurized water reactor (PWR) environments was performed in [150].

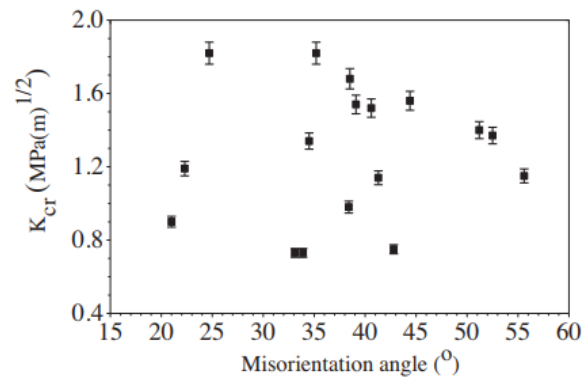


Figure 34. Evidence of no correlation between grain boundary misorientation angle (boundary type) and fracture toughness of the associated fractured grain boundary in an oxidized Alloy 600 material exposed to pressurized water reactor primary water for 4500 hours [150]

Cantilever geometries similar to those proposed in [145] also investigated the mechanical properties of silicon carbide (SiC) coating layers around spherical, tristructural isotropic (TRISO) particles considered to be a likely candidate next generation fuel form [97]. Because this SiC coating is only 30-50 μm thick, it could not be investigated by conventional means, so five notched microcantilevers were attempted as shown in Figure 35. These specimens produced slightly inflated fracture toughness values, 3.79-7.99 MPa/ \sqrt{m} , compared to fracture toughness values determined through an independent indentation fracture toughness technique, 1.0-3.6 MPa/ \sqrt{m} . This was attributed to blunt notches milled in the cantilevers. FIB milling sharp notches using the line patterning tool at low currents, 5 pA at 30 keV for example [151], can alleviate this issue. Post-test SEM microscopy of the fractured surface of the cantilever can then be used to determine initial crack length, a .

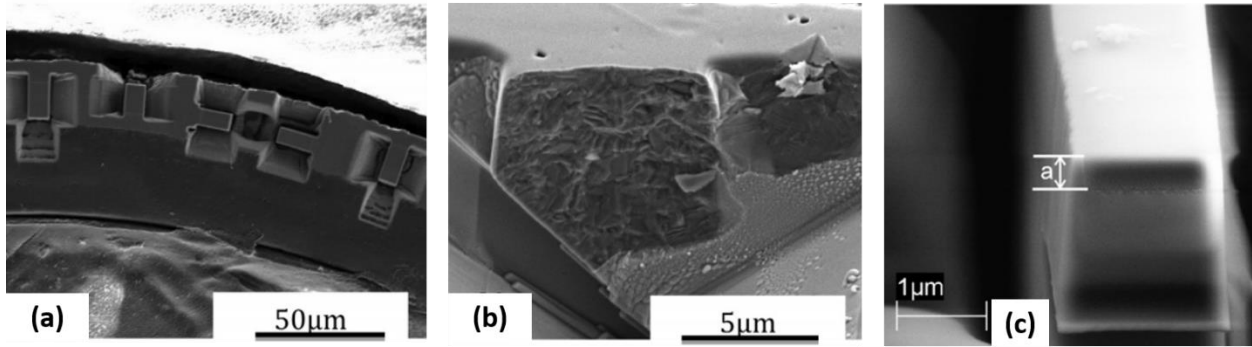


Figure 35. Micro-cantilever testing of SiC coating layer encasing TRISO fuel material: (a) Batch of cantilevers milled into outer SiC coating in a polished cross-section of TRISO fuel material, (b) Fractured SiC micro-cantilever with blunt notch [97], (c) Fractured silicon oxide cantilever with sharp notch. The initial crack length, a , generated by the sharp notch can be easily measured [151].

Micro-cantilevers served useful in investigating the mechanical properties of multiple passive oxide layers grown on HCM12A ferritic-martensitic steel in a liquid lead-bismuth corrosive environment. This steel is considered a promising candidate for generation IV lead-cooled fast reactors (LFRs). By precise FIB milling at the edge of the specimen, the two oxide layers could be investigated independently as shown in Figure 39, and it was found that the outer layer fractured in an intergranular manner, whereas the inner layer fractured in a transgranular fashion. Through micro-cantilever testing of the beam milled across both oxide layers, “cross-section” in Figure 36, a region of nano-pores in the inner oxide was discovered to be the primary crack initiation site [152].

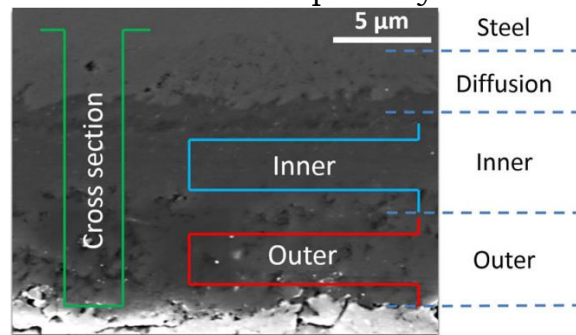


Figure 36. Schematic of edge micro-cantilevers FIB milled into two passive oxide layers formed on a F/M steel exposed to a high temperature liquid metal environment. Testing of the micro-cantilever cut in cross-section revealed the existence of a high porosity region within the inner oxide serving as a fracture initiation point [152].

Because these cantilevers were milled into the edge of the specimen, in-situ bending could be performed using electron and ion imaging to perfectly align a custom diamond flat pillar punch at the tip of the beams, and videos could be recorded to observe real time deformation.

The bonding strength and failure of next generation metallic fuel forms (U-Mo) to zirconium coatings was investigated using micro-cantilevers as well [153]. This fuel concept is desired for burning low enriched uranium in test reactors and protecting it with a Zr diffusion barrier. Cracks and porosity of the interface caused by the plasma deposition process could be investigated, and a fine Zr grain structure (5-30 nm) adjacent to the fuel was found to provide high interfacial strengths. The mechanical properties of traditional UO₂ fuel forms have also been investigated via micro-cantilevers as presented in [117].

Lift-out microcantilevers have also been produced for in-situ testing in both the SEM and TEM to reduce activity levels in a similar way to the methodology explained for micro-pillars, where a large bulk foil is lifted out and mounted on top of the post of a 3 mm Mo TEM disc. An image of a lift-out micro-cantilever fabricated from neutron irradiated 304 SS can be seen in Figure 37 [117]. In-situ testing can allow for DIC which can serve as an input for FEM modeling of stress states to help understand plastic deformation.

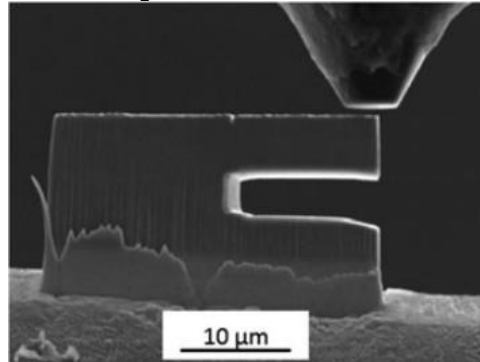


Figure 37. SEM image of a lift-out 304 SS neutron irradiated micro-cantilever about to be tested [117]

2.8.2 Micro-Fatigue Tests

Low-cycle fatigue testing involves a simple adjustment of micro-cantilever testing where the indenter punch pushing the cantilever and bending it is replaced by a gripper much like the one described for micro-tensile testing that moves the cantilever back and forth in a cyclic loading cycle with a prescribed frequency. Testing to date has studied model materials and non-irradiated engineering alloys due to the fact that micro-fatigue bending beams are often electro-etched from millimeter sized rods of material using acids and liquid radioactive contamination is undesirable shown in Figure 38. This is done in order to allow plenty of space for the fatigue gripper, fabricated from a tungsten wire, to grab and deform the sample with no interference from surrounding material. However, FIB trenching around a fabricated micro-beam could also clear space for safe operation of the fatigue gripper if micro-fatigue testing were to be desired for irradiated materials. Alternative lift-out sample preparation techniques as previously discussed for micro-pillar compression and micro-bending where a

large foil is lifted out and mounted on a post with free space around it for the micro-fatigue specimen to be fabricated from could also be done.

Initially, single crystal copper micro-beams were cyclically deformed [154] in an exploratory study. This methodology was then applied to investigate the microstructural and mechanical instabilities of ultrafine grained (ufg) copper severely plastically deformed (SPD) via high pressure torsion (HPT) [155] and equal channel angular pressing (ECAP) [156].

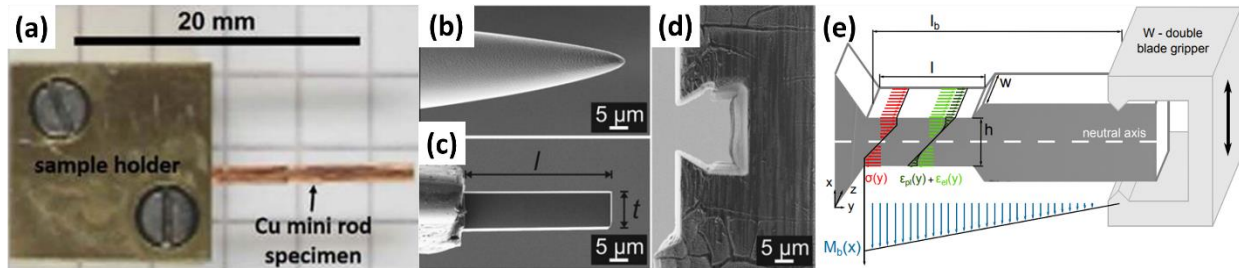


Figure 38. (a) sample holder machined for holding mini rod specimens to be electropolished, (b) electro-chemically sharpened needle tip, (c) FIB machined micro-bending beam, (d) SEM image of a tungsten wire with a FIB fabricated dove-tailed slit for gripping, (e) schematic depicting a micro-fatigue specimen with its labelled dimensions width, w , length, l , bending length l_b , and thickness t/h . Relative intensities of the elastic, $\epsilon_{el}(y)$, and plastic, $\epsilon_{pl}(y)$, strains and stress, $\sigma(y)$, along the y -axis, and the normalized bending moment $M_b(x)$ along the x -axis are drawn. [154-156]

An example of a typical loading cycle can be seen in Figure 39. There is typically a “zero force gap” because the gripper is wider than the micro-beam in order to properly align it to perform the test without damaging the specimen, so there is some dead time before the gripper contacts the beam and bends it on either side. Typically cyclic loading is performed with a displacement ratio $R = u_{min}/u_{max} = -1$ and a sinusoidal displacement loading frequency.

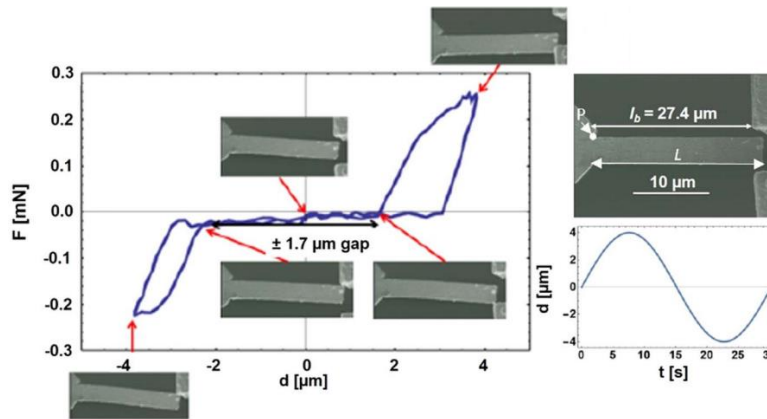


Figure 39. Measured raw load vs. displacement data with insets showing SEM images recorded in-situ during a loading cycle to depict the contact between beam and gripper using to correct for compliance. The aligned beam before testing is shown with its measured length, L , and bending length, L_b . The sinusoidal loading cycle, displacement vs. time, is shown on the lower right. [156]

In order to characterize the microstructural instability of the samples, testing is paused after a pre-determined number of cycles at an associated strain amplitude. The grains of ufg SPD copper have been shown to follow three pathways during low cycle fatigue testing shown in Figure 40: large grains grow at the expense of small grains that vanish, a suddenly appearing grain continuously grows, and misorientation gradients between subgrains in large grains are erased [155].

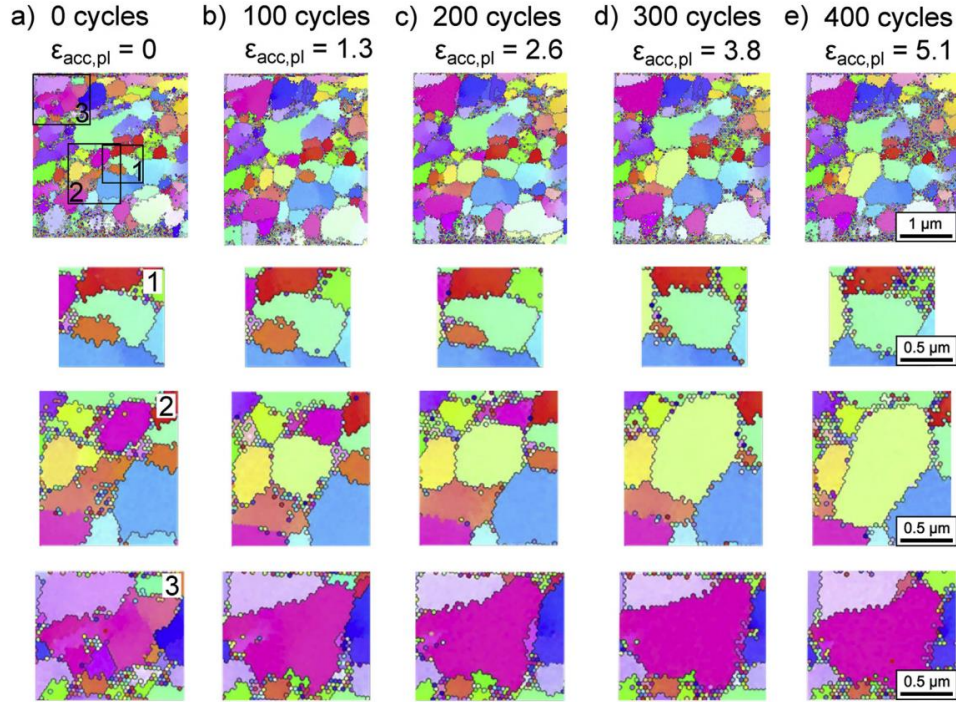


Figure 40. EBSD maps depicting the microstructural evolution of HPT Cu during cyclic loading after a specified number of cycles and strain amplitude. In location 1, the small orange grain is eaten by the larger green grain which grows to take its place. In location 2, the yellow-green grain is created and grows, and in location 3, the subgrains within the magenta grain are erased. [155]

To quantify the mechanical properties and mechanical changes in the micro-fatigue specimens, the following stress and strain equations derived from linear elastic beam theory for rectangular cross-sectioned cantilevers are applied where ε is the strain, σ the stress, u the measured displacement, h the thickness, b the width, L the length of the bar, l_b the bending length of the bar, and F the measured force.

$$\varepsilon = \frac{uh}{2Ll_b} \quad (67)$$

$$\sigma = \frac{6Fl_b}{bh^2} \quad (68)$$

Applying these equations, the cyclic yield strength can be traced out as a function of cycle number for each strain amplitude investigated. In addition, if the strain amplitudes are sequentially increased, the cyclic stress-strain curve can be created, and by integrating the area inside of each cycle, the energy dispersed per cycle can also be mapped out. An example of this mechanical properties assessment can be seen in Figure 41.

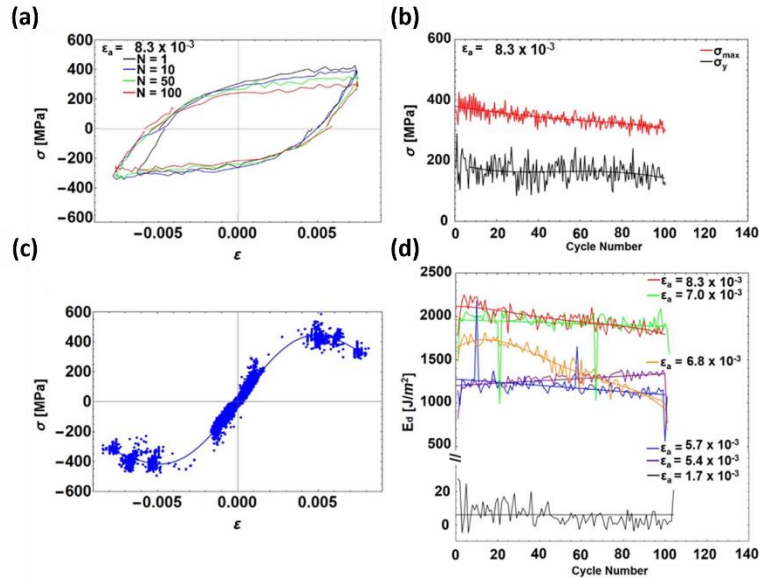


Figure 41. (a) Selected stress-strain curves at cycles number 1, 10, 50, 100 for the plastic strain amplitude $\epsilon_a = 8.3 \times 10^{-3}$, (b) yield strength and maximum stress as a function of cycle number, (c) cyclic stress-strain curve, (d) energy dissipated per cycle as a function of cycle number at selected strain amplitudes [156]

This type of full load reversal cyclic bending of micro-beams was also applied to a PM 2000 oxide dispersion strengthened (ODS) steel and the cyclic stress-strain curve and stress as a function of cycle number at comparable plastic strain amplitudes were in good agreement with large scale fatigue experiments performed on a similar ODS Eurofer 97 steel in [157]. This is exemplified in Figure 42.

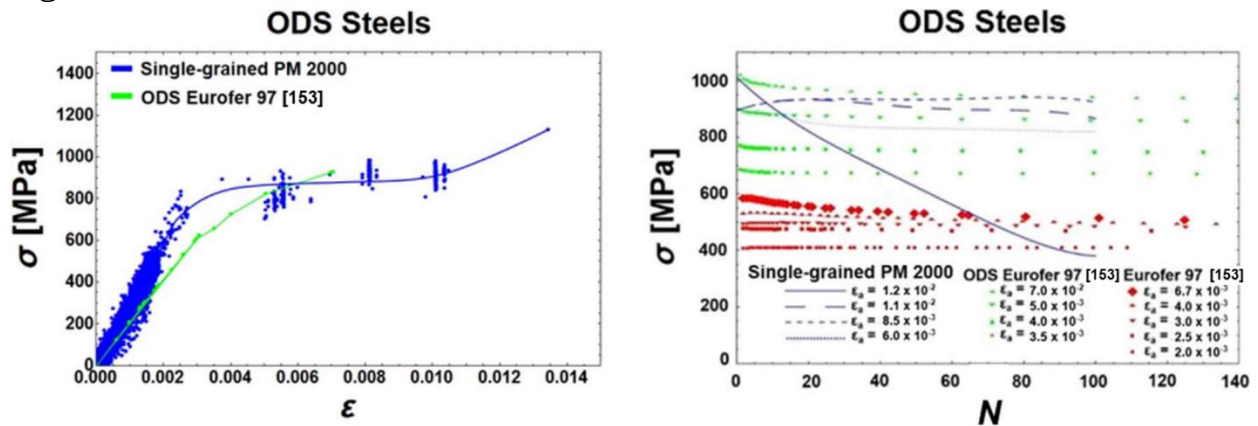


Figure 42. Comparison of micro-fatigue (sample dimensions $4.7 \mu\text{m} \times 2.1 \mu\text{m} \times 23.9 \mu\text{m}$) and macroscopic fatigue cyclic stress-strain curves and maximum stress values as a function of cycle number for similar ODS steels: PM 2000 in the case of micro-fatigue and Eurofer 97 in the case of macroscopic fatigue. The data strongly agrees. [156]

Gripping-based micro-fatigue studies are well suited for in-situ investigations involving low cycle fatigue testing because the nanoindentation systems often experience drift issues after long periods of time in use and must be stopped and corrected so that proper alignment is ensured. It is suggested that this method be used for test plans where a few hundred cycles or less are desired at each plastic strain amplitude in order to not compromise sample-gripper alignment and to ensure testing is carried out in a timely fashion. A more robust, large, specialized ex-situ micro-fatigue actuator was built in [158] in order to perform a larger number of cycles, on the order of 2×10^5 cycles, on a Ni-P amorphous alloy. An increased number of cycles with their mechanical properties is obtained in a trade off with losing the ease of observing deformation mechanisms in real time while performing the test in the SEM. Only post-test fracture surface images can be obtained.

High cycle micro-fatigue testing vibrates the micro-cantilever using a resonant frequency device such that the total deflection is precisely controlled. This methodology allows for measuring the fatigue lifetimes of thin films/interfaces by testing to $\geq 10^8$ cycles using an array of micro-cantilevers as demonstrated in [159, 160]. Scanning the reflectivity of the thin layer to detect the damage front and back calculations of stress states via FEM is required. Although this method is somewhat indirect, it does allow for plotting high cycle lifetime diagrams rapidly simply as the damage front position versus cycle number. Figure 43 illustrates the controlled frequency sweeping mechanism using a piezoelectric actuator to produce the desired fatigue amplitudes.

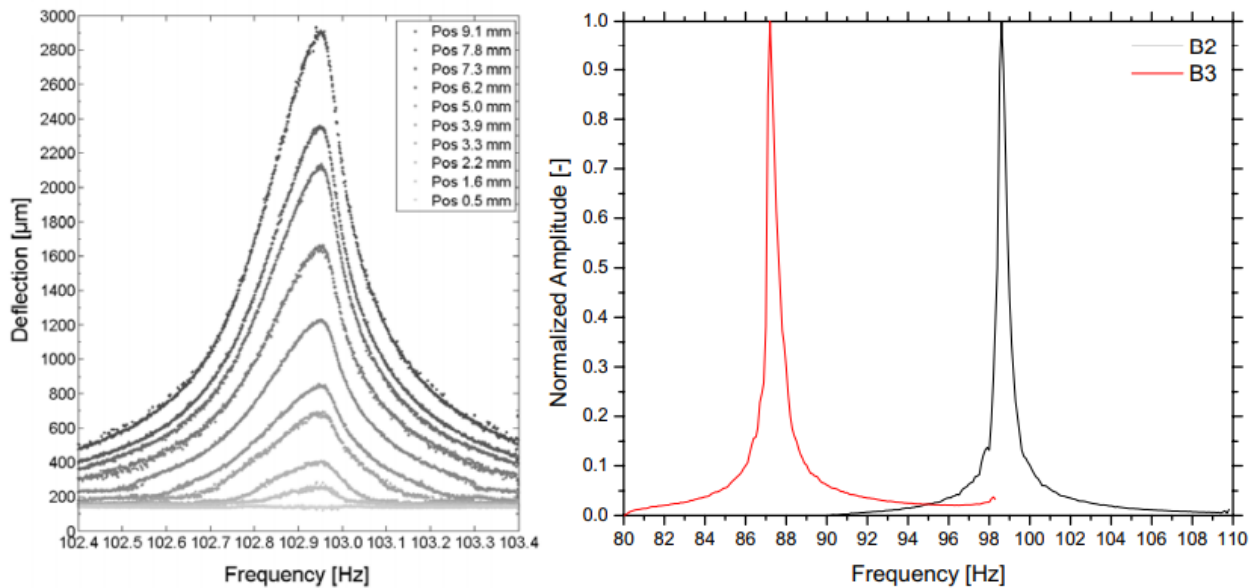


Figure 43. Controlled frequency sweeping mechanism, left, used to measure the specific deflections of the vibrating cantilevers as a function of their positions and a frequency sweep plot on the right indicating the resonant frequencies producing maximum strain amplitudes of two tested cantilevers [160]

High temperature micro-fatigue testing incurs the same challenges as other high temperature SSMTs with regards to degradation of the bending apparatus and oxidation of the specimens, maintaining a non-reactive atmosphere, and eliminating specimen-indenter thermal drift. This has been achieved on the model materials Si [161], CrN [162], and a candidate fusion reactor material, ion irradiated tungsten [163] and shows promise for future advancement to more nuclear materials with the increased availability of high temperature testing systems.

2.9 In-Situ Transmission Electron Microscope (TEM) Tests

When the length scale of small scale mechanical testing (SSMT) is reduced from the mini-scale (millimeters) and micro-scale (micrometers) down to the nano-scale (nanometers), dislocation nucleation, multiplication, and movement can be observed in real time as the specimens are deformed in the TEM. Because these specimens are tens to a few hundred nanometers in thickness, they are clearly in the size effect dominated area, meaning stress-states are clearly different from those observed in the bulk. Making the link between quantitative mechanical properties such as yield strength, ultimate tensile strength, ductility, and work hardening rate becomes increasingly difficult. However, valuable information in nuclear materials regarding deformation initiation and dislocation interaction with radiation-induced defects such as dislocation loops and helium bubbles, radiation effected grain boundaries, and radiation produced phases such as zirconium hydrides can be learned. The propagation of deformation from the onset of yielding up until failure can be tracked by simply watching it as it happens. In-situ TEM mechanical studies can take the form of most SSMTs when applied to nuclear materials.

In-situ TEM SSMTs were made possible by the design of a sample holder compatible with widely used JEOL TEMs first reported by Wall and Dahmen [164, 165] and adapted by Stach [166]. An independent three-axis inertial positioner built by Bobji [167] was also effective in studying deformation behaviors. The commercially available instrumentation is depicted in Figure 44.

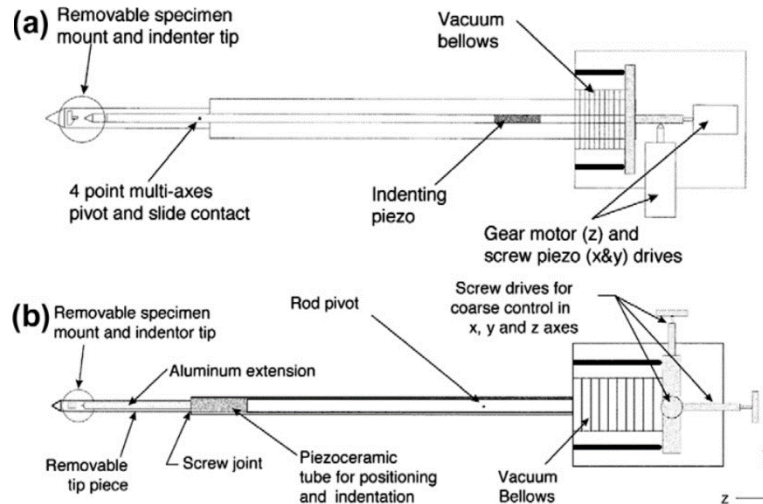


Figure 44. Commercially available in-situ TEM SSMT holders: (a) adapted version of the initial design in [164, 165] and (b) JEOL holder [168]

In-situ TEM nanoindentation has been used to observe the onset of plasticity [169-172], dislocation-grain boundary interactions in many materials [173] including ones relevant to the nuclear industry like martensitic steel [174], and in order to observe specific work hardening mechanisms [175]. This technique has also been used to characterize the mechanical behavior of 50 nm sized nanoparticles [176] and could be considered for similar investigations of oxide dispersion strengthened (ODS) nano-oxides in nuclear alloys. The observation of crack growth of composites in [177] could be performed on SiC/SiC nuclear composites.

In-situ TEM nano-pillar compression testing has been performed on ion irradiated specimens, most notably proton irradiated Cu [108] and helium irradiated/implanted Cu [178, 179] and Fe [180] with success in both revealing more about microstructural deformation and relative changes in mechanical properties through their stress-strain curves. In the case of proton irradiated Cu, a remarkable discovery was made; the size effect strengthened regime became greatly reduced and all nanopillars with diameters greater than ~400 nm exhibited the same yield strength in single-crystal (100) oriented Cu. The increased density of radiation created defects reduces the size needed to cause dislocation-defect interactions that reflect bulk like behavior [108]. In the case of the irradiated iron nanopillar, helium bubbles form herring-bone-like arrangements parallel to the {110} planes throughout the pillar [180]. Helium irradiation of Cu nanopillars was found to cause the formation of a He bubble superlattice and subsequent deformation revealed a twinning-like transformation of this lattice as a competing deformation mechanism with more traditional superlattice disordering via dislocation slip [179].

In-situ TEM nano-tensile testing has investigated engineering alloys and both helium implanted and self-ion irradiated materials: He implanted Cu [181] and self-ion irradiated zirconium pressure tube alloys [182]. Nano-tensile testing has been performed at both elevated and cryogenic temperatures. In the case of the helium implanted Cu, during the tensile tests, the helium bubbles were observed to first elongate and narrow. Then, if there was a low density of helium bubbles, the bubbles were found to fragment into a few narrow bubbles and finally cleave into many small spherical bubbles. This leaves a bubble-free channel for shear localization to occur. If a high density of bubbles exists and the bubble spacing is small, bubbles will tend to coalesce and form larger bubbles which ultimately fail. This concept along with in-situ TEM evidence is presented in Figure 45 [181].

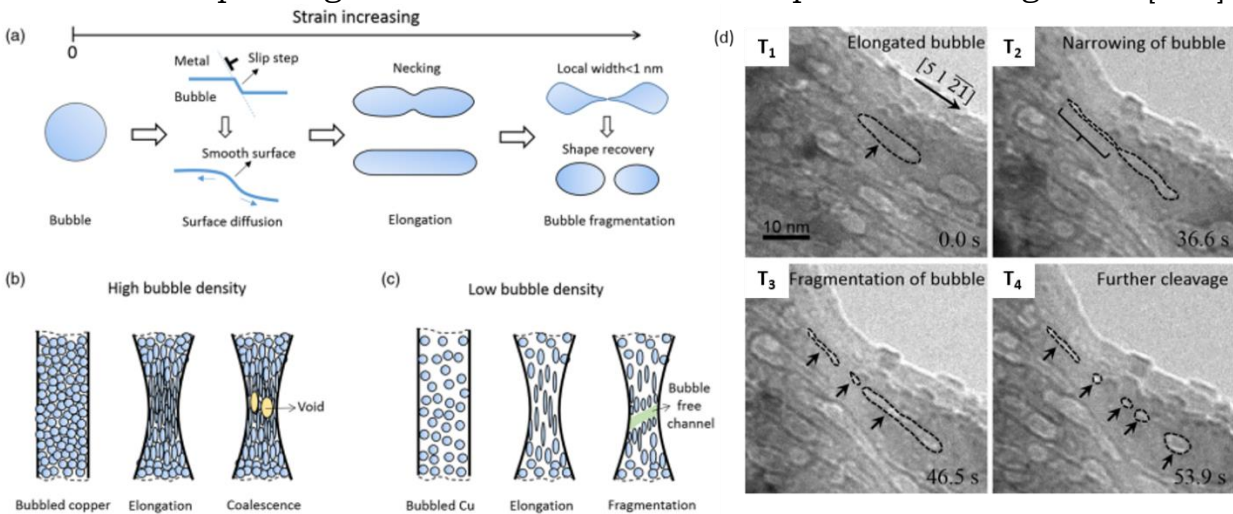


Figure 45. Schematic of deformation evolution in a material with high and low bubble densities. (a) general dislocation-bubble interaction inducing bubble cutting, (b) high bubble density specimen failing via bubble coalescence, (c) low bubble density specimen failing via bubble fragmentation leading to a bubble free channel where shear localization occurs. (d) in-situ TEM evidence of bubble elongation and fragmentation [181]

In-situ tensile tests performed at elevated temperature, 350 °C, on self-ion irradiated Zircaloy 4 in [182] observed the interactions between radiation induced dislocation loops and mobile dislocations, revealing real time evidence of dislocation pinning that could be matched with radiation hardening, and pre-existing dislocation loops becoming incorporated into gliding dislocations and eventually cleared out by larger dislocation channels. At the other end of the test temperature range, in-situ tensile testing at cryogenic temperatures revealed deformation-induced martensitic phase transformations in 304 SS via the formation of stacking faults to ϵ -martensite and through direct transformations to α' -martensite [183].

Due to the complexities in both designing bending tests that accurately measure mechanical properties and designing successful in-situ TEM experiments, in-

situ TEM bending studies on engineering alloys relevant to the nuclear industry are the rarest. One study has been performed to assess the fracture toughness of a notched 100 nm thick metallic thin film by performing a crack opening test on a doubly-fixed three-point bend specimen [184]. The experimental set up is shown in Figure 46.

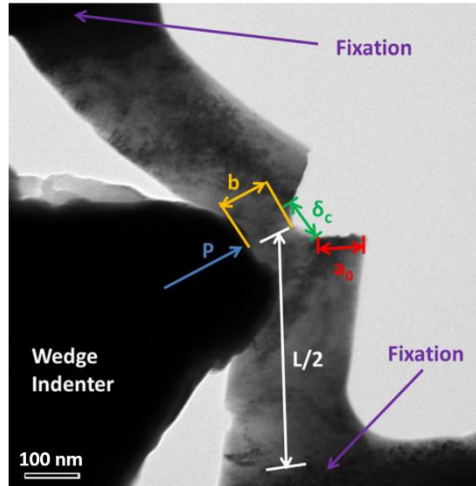


Figure 46. TEM image depicting a three-point bend specimen tested in-situ with its measurable dimensions labelled: P being applied load, $L/2$ half of the bending span, b the ligament thickness, a_0 the initial crack length, and δ_c the crack tip opening displacement [184]

This methodology gives clear visibility of the crack tip as it is loaded and opens and also allows for techniques like transmission EBSD in the TEM to be performed between loading cycles. The crack tip opening displacement (CTOD) can be measured via DIC software and used to calculate the stress intensity factor, but corrections must be made for the fixed ends of the specimen and the plasticity occurring during deformation.

3 Materials and Radiation Effects Theory

3.1 Nickel-Based Superalloys

Pure nickel is a silvery-white metal that forms a face-centered-cubic (*fcc*) crystal lattice. Chemical, physical, as well as known mechanical properties of conventional pure nickel can be found in Table 2 [185]. Elemental nickel (along with iron and cobalt) forms the basis for a group of alloys that are high temperature materials resistant to mechanical and chemical degradation up until temperatures approaching their melting points known as superalloys [186].

Table 2 Room Temperature Properties of Commercially Pure (99.6%) Ni

Atomic Number	28
Standard Atomic Weight	58.6934 amu
Density	8.89 g/cm ³
Melting Point	1435-1446 °C
Thermal Conductivity	60.7 W/m°C
Bulk Tensile Strength	317 MPa
Total Elongation	30%
Young's Modulus	207 GPa
Shear Modulus	76 GPa
Poisson's Ratio	0.31
Hardness	800 MPa
Lattice Type	Face-centered cubic (fcc)
Burgers vector	0.249 nm
Stacking fault energy	90 mJ/m ²

High nickel content (usually $\geq 70\%$ Ni), *fcc* based superalloys have a γ matrix phase consisting of three main alloying elements: Ni, Cr, and Fe. A ternary phase diagram highlighting the thermodynamically stable regions where Ni-based superalloys form is shown in Figure 47 [187].

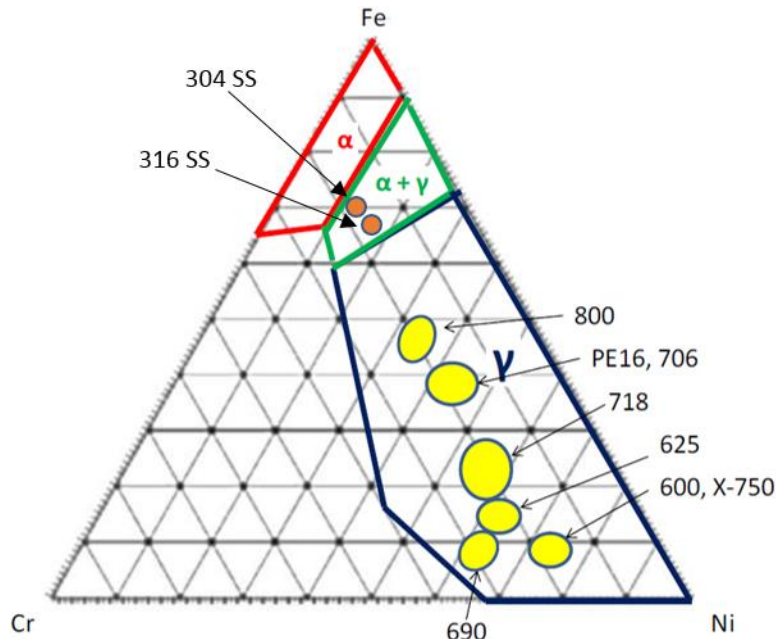


Figure 47. Ni-Cr-Fe ternary phase diagram highlighting thermodynamically stable Ni-based superalloys and their approximate chemical compositions [187]

In addition, a wide range of elements including Al, Ti, Nb, and Mo are soluble in Ni, creating a large range of possibilities for solid-solution strengthening and precipitation-hardening. The likelihood of these elements ending up in solution as opposed to forming secondary precipitate phases can be predicted by comparing their relative atomic sizes and electron vacancy numbers (N_v) to Ni. All elements of importance composed in Ni-based superalloys and their common places in the alloys are shown in Figure 48 [186].

Two possible ordered precipitate phases produce the most significant contribution to the strengthening of nickel-based superalloys: γ' and γ'' . Alloys containing these secondary precipitate phases maintain constant or increasing yield strengths and creep resistances with increasing temperature up until 800 °C [186]. The ordered phase strengthening effects are a function of the volume fraction and size distribution of the precipitate phase.

The γ' phase takes the stoichiometry Ni_3X and forms a fine array of 5-20 nm spherical coherent precipitates with an $L1_2$ ordered phase. The secondary element X is either Ti or Al and occupies the cube corners of the *fcc* lattice, whereas the Ni atoms occupy the face centers. Depictions of the γ phase and γ' phase are given in Figure 49. There is a slight lattice mismatch of 0.5% between the γ -matrix and γ' -precipitates, and Ti or Al solute aggregates can cause minor solid-solution hardening, but the ordered structure is the major strengthening feature [188]. Normal slip in *fcc* systems occurs along the family of $\{111\}$ planes in the set of $\langle 110 \rangle$ directions and has 12 pathways, but the ordered precipitates

impede these pathways at an increasing rate at elevated temperatures. This is because shear on the $\{111\}$ planes creates an antiphase boundary (APB) since there is a layer of misplaced atoms. Either a Ni atom is forced into the Al/Ti site or an Al/Ti atom is forced into the Ni site. If slip were to avoid forming the APB it would have to occur on $\{100\}$ planes, but the activation energy for these slip pathways is four times greater than normal $\{111\}\langle 110\rangle$ slip occurring in the γ -matrix. This phase is thermodynamically stable up to 800 °C after which it transforms into a η -hcp phase if overaged at elevated temperatures.

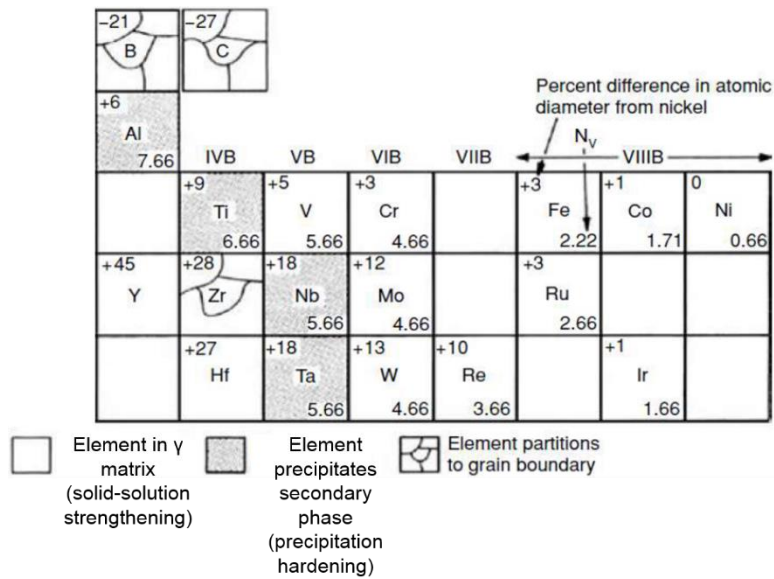


Figure 48. Important elements in Ni-based superalloys and their places within the alloys [186]

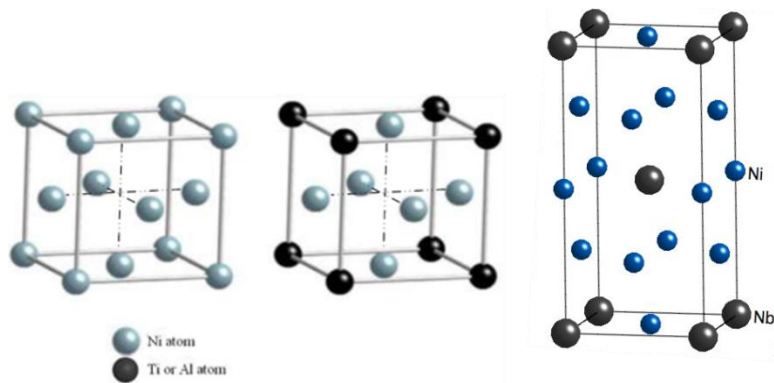


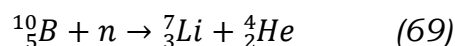
Figure 49. Unit lattice for γ -matrix (left), γ' -precipitate (center) and γ'' -precipitate phases (right) in Ni-based superalloys

If Nb is included as an alloying element in the Ni-based superalloy, the γ'' semi-coherent, ordered phase taking the stoichiometry Ni_3Nb can be produced in the

form of body centered tetragonal (BCT) discs. These 60 nm x 10 nm discs arrange themselves such that their (001) plane is parallel to the {001} family of planes in the γ -matrix and their [100] direction is parallel to a set of $\langle 100 \rangle$ directions in the γ -matrix. Order hardening occurs in a similar fashion to γ' and coherency strain hardening also exists due to the larger lattice mismatch between the BCT and FCC phases. This phase is thermodynamically stable up to 650 °C after which it transforms into a δ -orthorhombic phase if overaged at elevated temperatures and is pictured at the right of Figure 49.

The overaged η and δ precipitates do not strengthen the alloys because they have lost coherency, are much larger, and do not exist in high density. However, when segregated to grain boundaries in limited amounts, they restrict grain growth, but ultimately as brittle, needle-shaped inclusions are detrimental to the mechanical properties.

Carbides frequently nucleate on the grain boundaries of Ni-based superalloys during heat treatments, and they are effective for very high temperature turbine blade applications because they prevent the grain boundaries from sliding and the grain size from increasing [186]. However, they may enhance stress corrosion cracking (SCC) issues and are unwanted in nuclear applications [186]. Borides operate in a similar fashion but are even more detrimental in irradiated materials in causing high temperature stress corrosion cracking (HTSCC) and low temperature crack propagation (LTCP) at concentrations larger than 20 wt ppm [189]. Because boron-10 comprises 20% of all boron isotopes and has an extremely high affinity for thermal neutrons, transmutation effects produce helium and lithium through the reaction



that degrade the fracture toughness of the superalloy and increase its SCC rates. Because boron is a trace element, less than 100 appm He is produced in most superalloys.

Five generic heat treatments are used to create the desire microstructure of a specific Ni-based superalloy:

1. Homogenization: A heat treatment close to the melting temperature of the alloy (~1400 °C) that diffuses out gross solidification microchemical gradients and brings carbides into solution.
2. Solution Anneal (SA): A heat treatment between 890 °C and 1100 °C used to bring secondary ordered strengthening phases into solution but precipitate out some carbides on grain boundaries.
3. Direct Age (DA): Hot working and immediate ageing at 704-746 °C to precipitate out the ordered strengthening phases

4. Single Step Ageing: Single ageing treatment at 704-746 °C following a SA.
5. Double Step Ageing: A two-step ageing treatment after the SA. The first step occurs at 885 °C to improve the alloy's stress rupture properties by precipitating out grain boundary carbides to limit grain boundary sliding. The second step at 704-746 °C precipitates out the ordered strengthening phases.

Specific thermo-mechanical treatments and cooling rates control each alloy's phase stability and transformation kinetics and determine the shape, size, and spacing of the strengthening nanoprecipitates, which ultimately determine high temperature creep and yielding properties [190].

3.2 Nickel-Based Superalloys in Nuclear Reactors

Nickel based alloys provide excellent strength and ductility [196, 197], corrosion resistance at elevated temperatures [196, 197], and good creep properties [198] beneficial for use in nuclear power systems. In LWRs, this has led to their use as reactor internal structural components, including fasteners (bolts) [199], centering pins [200], jet pump restraints [201], and tie-rods and cladding for absorber rods [202, 203]. Currently, these components are either used in fuel assemblies that are limited to less than six years of in-core service [204], or they exist as peripheral components operating for the lifetime of the reactor. Thus, doses to these components remain limited, and the only reported evidence of failure in-service occurred in the late 1980s in Inconel X-750 bolts that ruptured as a result of intergranular stress corrosion cracking (IGSCC) after approximately 11.5 years in the French Chooz PWR [199]. This failure was attributed to a poor heat treatment, and the bolts were replaced with new ones which underwent an improved two-stage heat treatment similar to the one described in Table 4 in order to promote homogeneous carbide precipitation in grain boundaries and homogeneous γ' distribution that resists IGSCC.

In addition, Inconel 600 and 690 are the most common steam generator materials [205], and they are highly susceptible to SCC and irradiation assisted SCC (IASCC). The initiation of SCC in nickel based alloys involves an incubation period dependent on temperature, residual stresses in the components left by fabrication processes, and material susceptibility in its operating environment [206]. Coolant hydrogen concentration and temperature play a strong role in determining the maximum possible SCC susceptibility of a given material [207, 208]. Inconel 690 resists high temperature corrosion effects more than Inconel 600 due to its higher Cr content, and in general heat treatments that can homogeneously distribute Cr near grain boundaries are preferred since Cr

depletion at grain boundaries sensitizes them to corrosive attacks [209-211]. These heat treatments usually involve a high temperature SA followed by a lower temperature ageing step much like in Table 4.

Alloy 800 has been used as steam generator tubing in CANDU as well as German PWRs with relatively good success to date. Despite a large number of operating years accumulated on the components, degradation has seldom been reported, although a recent ageing study has detected boron precipitation on grain boundaries that requires further investigation in order to determine its impact on tube integrity [212].

High temperature, primary water effects on SCC have also been well documented in [213], and for Alloy 600, it again proves crucial to perform a secondary heat treatment at 700-750 °C for 10+ hours after SA in order to mitigate these effects because it has a Ni content above 70%, making it most susceptible. The influence of Ni content in the alloy on SCC susceptibility can be seen in Figure 50.

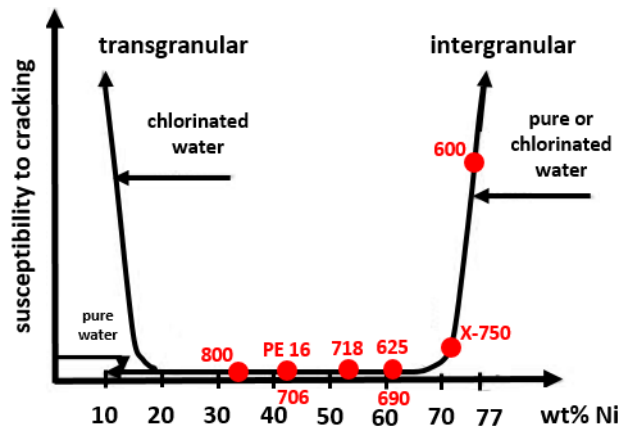


Figure 50. The influence of Ni content on susceptibility to SCC in alloys stressed slightly above their yield point in 350 °C water. Ni-based superalloys used in nuclear reactors are marked in red. [213]

Nickel-based superalloys have also been considered in future generation IV concepts because of their superior high temperature strength and general corrosion resistance [214]. In addition, Ni-based superalloys with intermediate Ni contents are resistant to swelling, even at doses past 100 dpa of neutron irradiation, as shown in Figure 51 [215].

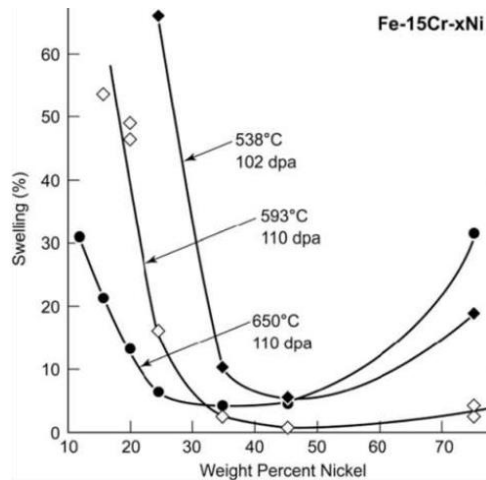


Figure 51. Swelling behavior of Fe-Cr-Ni alloys irradiated past 100 dpa with neutrons [215]

These properties make Ni-based alloys (Ni content ~35-55%) ideal for use in the supercritical water reactor (SCWR) where thermal neutron flux/fluence is low and keeps helium production at a minimum such that corrosion and swelling are the major degradation issues.

However, there is a lack of information on high dose effects and helium embrittlement caused by high thermal neutron fluxes at lower temperature ranges relevant to generation IV designs, 300-550 °C because most data has been obtained from neutron irradiations in fast breeder reactors in order to achieve high dose. This radiation environment is not representative of Ni-alloys that would be in-service in high thermal neutron fluxes and incur significant helium production in their lifetimes.

Another study on Alloy 617 and Alloy 800H performed at irradiation and test temperatures between 580-700 °C up to 1.5 dpa in the High Flux Isotope Reactor (HFIR) revealed significant ductility losses in Alloy 800H, although for Alloy 617 it retained around 10% total elongation. In both cases, radiation strengthening of the alloys occurred. [216]

The precipitation hardened Ni-based superalloys Nimonic PE-16 and Inconel 706 have also seen use in sodium cooled fast reactors in the UK and US [217] because of their strength, creep resistance, and lower swelling rates compared with other structural alloys. Helium embrittlement caused by transmutations producing large quantities of helium and phase instability are the two major issues of concern in this system [214, 218]. Hastelloy N, another Ni-based alloy, is considered the primary candidate for the structural material that will be the primary loop of the molten salt reactor (MSR) because of its chemical compatibility with molten fluoride salts [219, 220].

The internals, piping, and heat exchangers proposed for high-temperature gas cooled reactors (HTGR) are also Ni-based superalloys, Inconel 617 for operation temperatures up to 950 °C and Incoloy 800H for temperatures up to 850 °C [221] because of their excellent high temperature properties, and a database has been developed for both alloys [221, 222]. Hastelloy XR is also being developed for HTGR applications. For all Ni-based alloys operating in a high temperature helium gas environment, impurities in the He gas creating corrosion issues have been of primary concern, and secondary issues concerning thermal ageing have arisen [223-225].

3.2.1 Inconel X-750 in CANDU Reactors

Inconel superalloy components in currently operating CANDU reactors consist of cable sheathing and core wires in flux detector assemblies and tensioning springs for reactivity control systems that reside at the core periphery as well as fuel channel annulus spacers in the core that maintain an insulating gap between the hot Zr-2.5% Nb pressure tube and the cool Zircalloy-2 calandria tube. Figure 52 illustrates the CANDU reactor core and periphery and points out these components.

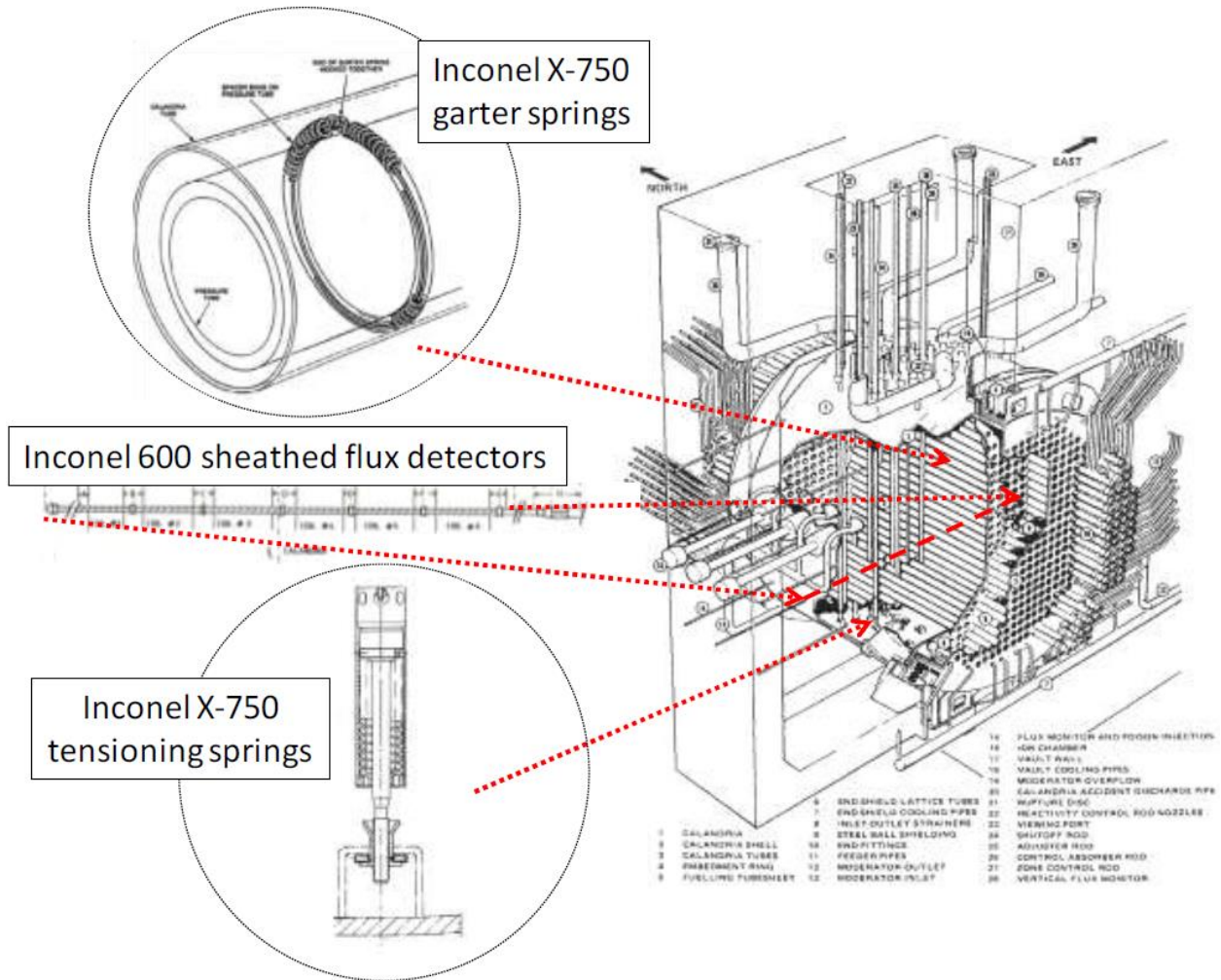


Figure 52. A schematic diagram illustrating the locations of the three activated Inconel superalloy components in CANDU reactors

There are between 380 and 480 horizontal fuel channels that comprise the CANDU core, and four spacers separated by approximately 1 m span the length of each fuel channel between fuel inlet and outlet positions. In total, between 1520 and 1920 Inconel X-750 spacers are in service in each CANDU reactor. Pictures of a garter spring positioned for service, and a picture through the hot cell of springs in service can be seen in Figure 53. In-service components roll along the length of the pressure tube because it expands during operation; they sometimes end up overlapping as seen in Figure 53b.

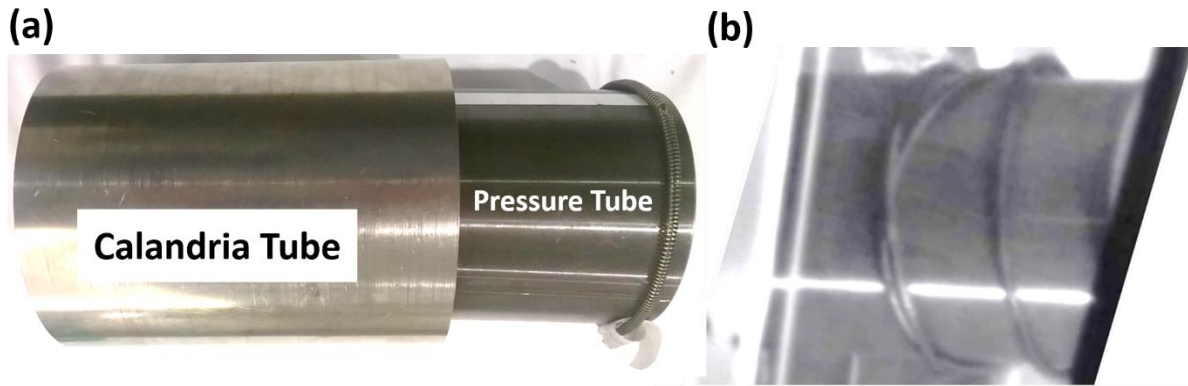


Figure 53. Inconel X-750 annulus spacer (a) positioned for service in a fuel channel and (b) in-service photo in the hot cell

Two different spring designs exist. The non-optimized springs have a tighter pitch, meaning the coils are spaced closer to one another, and are coiled from a heavier gauge wire (1 mm x 1 mm cross-section). The optimized springs have a looser pitch, meaning the coils are a bit more spaced out, and are coiled from a lighter gauge wire (0.7 mm x 0.7 mm cross-section). However, both designs seen in Figure 54 come from Inconel X-750 processed with the same chemical composition and heat treatments found in Table 4.

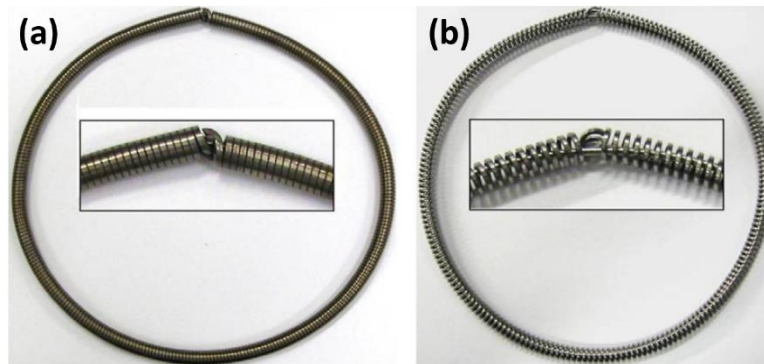


Figure 54. (a) non-optimized and (b) optimized Inconel X-750 CANDU spacers

Each design has a hooked end designed to sit at the top of the pressure tube as seen in Figure 53a and Figure 54, and a Zr girdle wire runs through the center of the coil as can be seen in Figure 54b. All spacers operate in a dry carbon dioxide gas environment. Noticeable temperature and flux differences exist in the axial direction within an individual fuel channel. Spacers at the center of the channel experience the highest neutron flux and operating temperature, whereas spacers close to the inlet and outlet experience the lowest neutron flux and operating temperature. The neutron flux and temperature profile of the components in operation can be seen in Figure 55.

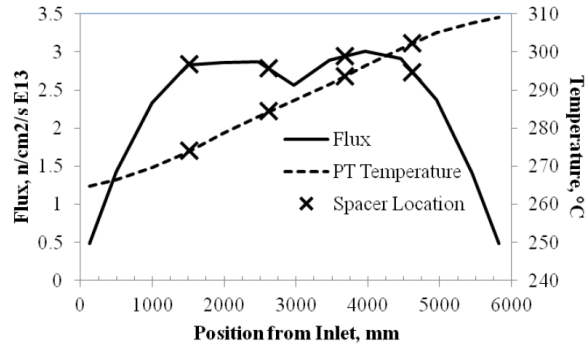


Figure 55. Exemplary flux and temperature profile in a CANDU fuel channel

After time in-service, due to the combined weight of the fuel bundle and heavy water coolant, the pressure tube creeps and sags with respect to the calandria tube, “pinching” the spacer between the hot pressure tube and cool calandria tube [197, 226-233]. This creates a circumferential temperature variation around the spacer where the pinched material (6 o’clock position) operates at 120-280 °C and the non-pinched material (12 o’clock position) operates at 302-306 °C. Variability in the pinched material results from local contact points at the bottom of the fuel channel; locations in direct contact with the pressure tube operate close to the higher bound temperature, 280 °C, and locations in direct contact with the calandria tube operate close to the lower bound temperature, 105 °C. Because the pressure tube moves in-service, this creates more uncertainty in the exact operating temperature since the springs are designed to roll along the length axis of the tube and accommodate axial expansion. Figure 56a shows the circumferential temperature profile and Figure 56b shows the temperature gradients within the pinched and non-pinched regions.

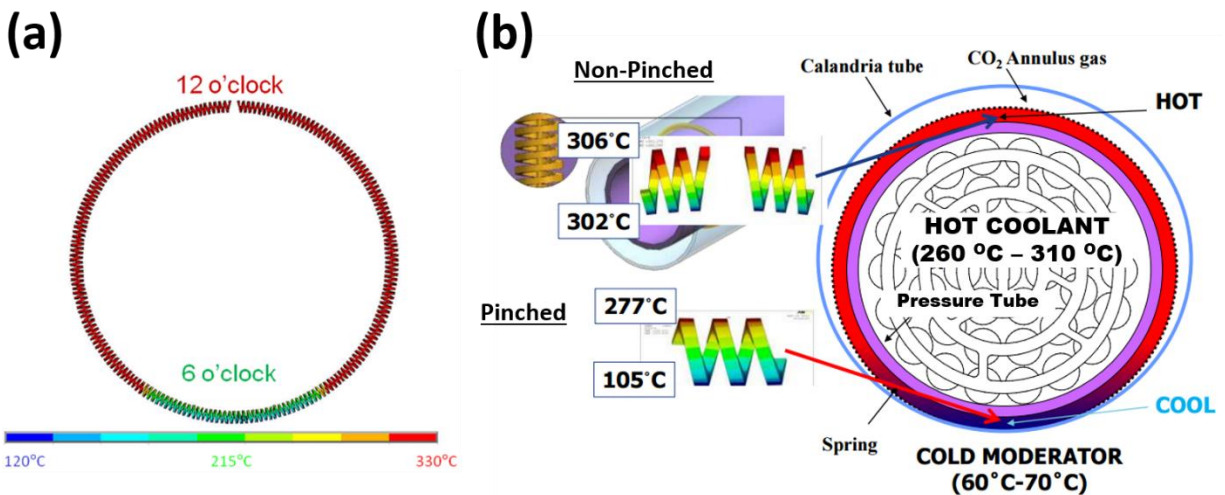


Figure 56. (a) Circumferential temperature profile of Inconel X-750 spacer in service (b) temperature gradients in non-pinched and pinched regions

It is crucial that these spacers maintain their load bearing capacities for the lifetime duration of reactor operation because they prevent hydride blistering that would otherwise occur if the hot pressure tube and cold calandria tube were to contact one another. If hydride blistering were to occur with the hot and cold legs in contact, pressure tube rupture could result, leading to a local loss of coolant accident (LOCA).

3.3 Radiation Damage Basics

Structural materials of a nuclear reactor including fuel cladding, core internals, the reactor pressure tube/vessel, and supporting framework are predominantly metal components, so the focus of radiation damage will be centered on the effect of ionizing radiation on metals with crystallography.

Displacement Damage

Energetic particles emitted either from nuclear reactions, such as nuclear fission, or ion accelerators with sufficiently high energy interact with structural materials via ionization and electronic stopping through Coulombic interactions above a threshold energy, E_c . Below this threshold energy, direct collisions between the energetic particle and an atom in the matrix lattice occur until the particle loses so much energy that it is below the displacement energy, E_d . During these collisions, the atoms displaced from their original lattice sites may also gain sufficient energy to cause further displacements, resulting in a displacement damage cascade, shown in Figure 57.

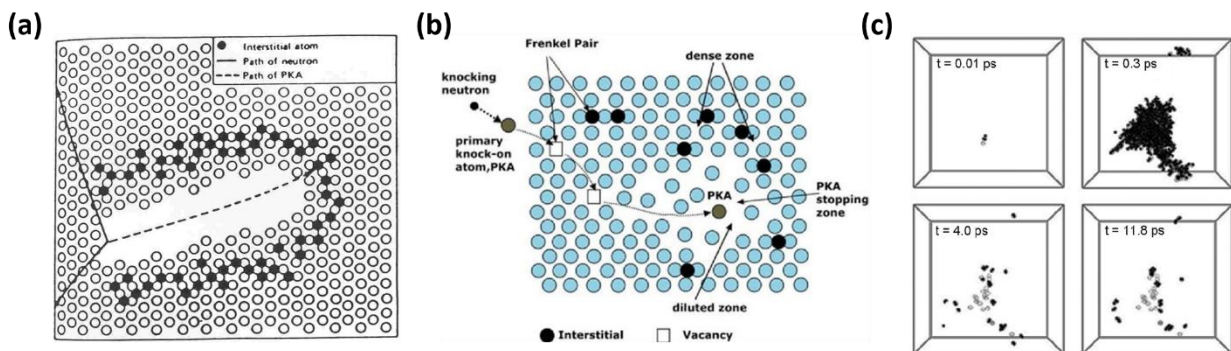


Figure 57. (a) Original displacement spike model [234], (b) more detailed qualitative depiction of a displacement cascade highlighting interacting particles and point defects, (c) modern molecular dynamics simulation of the time evolution of a displacement cascade in pure, single-crystal copper at 290 °C. Defect quantities reach a maximum at ~ 0.1 ps before recombining and stabilizing after ~ 10 ps [235]

In this case, the initially displaced matrix atom, the primary knock-on atom (PKA), displaces a secondary atom in the matrix. This atom becomes a secondary

knock-on atom and may displace a tertiary knock-on atom and so on until the amount of energy dissipated causes all displaced atoms to have energies below the energy needed to overcome the energy barrier that holds an atom in place in the lattice. At low energies below E_d , the displaced atoms do not displace any more atoms and either fill a pre-existing vacancy in a lattice site or become an interstitial point defect in the material. Pre-existing vacant lattice sites exist due to thermal agitations of the crystal that allow atoms to overcome their energy barriers and become kicked out of a lattice site. Each material has a pre-existing equilibrium vacancy concentration at any given temperature, but in the presence of radiation, due to displacement cascades, excess point defects (vacancies and interstitials) are created. When a collision produces both an interstitial atom displaced from its lattice site along with that vacant lattice site, these two coupled defects are referred to as a Frenkel pair. In order to become a substitutional atom and occupy a lattice site, the atom must have a similar atomic radius ($\leq 15\%$ difference), produce a similar crystal structure when combined with atoms the same as itself, and have a similar number of valence electrons and electronegativity.

The common metric used to quantify radiation damage is displacements per atom (dpa). Radiation damage equal to one displacement per atom means that every atom in the irradiated material has been displaced from its original lattice site one time. The simplest model used to calculate the number of displacements caused by a displacement cascade, ν , is the Kinchin-Pease model [236]. This model is based on binary elastic collisions that employ classical mechanics, namely the conservation of momentum and kinetic energy. An energetic particle with mass M_1 and velocity v_{10} impacts a stationary particle in the lattice with mass M_2 . After the collision, the particles exit at angles ϕ_1 and ϕ_2 with velocities v_{1F} and v_{2F} . This description depicted in Figure 58a explains things from the laboratory reference frame. When things are transformed to the center of mass (CM) reference frame shown in Figure 58b, the equations become more simplified. The CM has the equivalent mass of the whole system $M_1 + M_2$, and from conservation of momentum, the CM velocity is given as:

$$v_{CM} = \frac{M_1}{M_1 + M_2} v_{10} \quad (70)$$

Considering a time well before the collision and a time well after the collision and applying conservation of both momentum and energy:

$$M_1 u_{10} + M_2 u_{20} = M_1 u_{1F} + M_2 u_{2F} \quad (71)$$

$$M_1 u_{10}^2 + M_2 u_{20}^2 = M_1 u_{1F}^2 + M_2 u_{2F}^2 \quad (72)$$

In the CM frame, the initial velocities are given as:

$$u_{10} = v_{10} - v_{CM} \quad (73)$$

$$u_{20} = v_{CM} \quad (74)$$

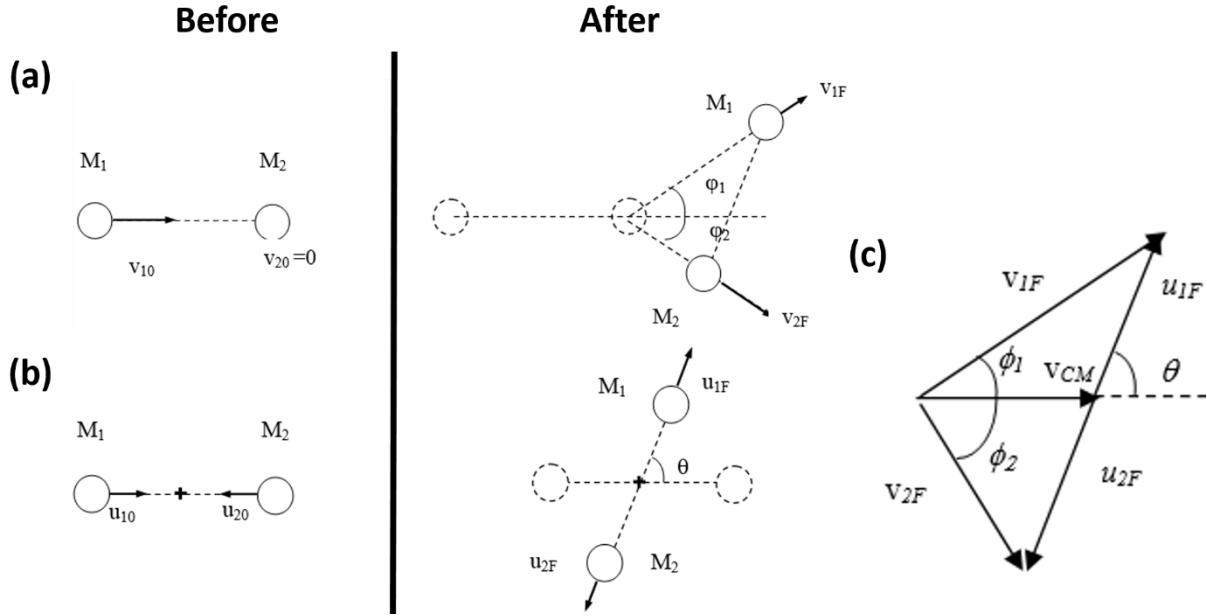


Figure 58. Elastic collision scattering process in the (a) laboratory reference frame and (b) center of mass reference frame, (c) vector diagram relating the parameters from the two reference frames after the collision

Because (71) and (72) must be satisfied,

$$u_{1f} = u_{10} = v_{10} - v_{CM} \quad (75)$$

$$u_{2f} = u_{20} = v_{CM} \quad (76)$$

Following Figure 62c, the final velocities can be written as:

$$v_{1F} = u_{1F} + v_{CM} \quad (77)$$

$$v_{2F} = u_{2F} + v_{CM} \quad (78)$$

By using the law of cosines:

$$v_{2F}^2 = v_{CM}^2 + u_{2F}^2 - 2v_{CM}u_{2F}\cos\theta \quad (79)$$

and then substituting (76) into (79):

$$v_{2F}^2 = 2v_{CM}^2(1 - \cos\theta) \quad (80)$$

Multiplying both sides by $M_2/2$ and substituting for v_{CM} , the kinetic energy of the impacted particle can be expressed as a function of the incident particle

$$E_{2F} = \frac{2M_1M_2}{(M_1+M_2)^2} E_{10}(1 - \cos\theta) \quad (81)$$

This expression can then be further simplified. The incident particle energy E_{10} will be denoted E , the energy transferred to the impacted particle E_{2F} expressed as T , and the pre-factor mass ratio as Λ , given by:

$$\Lambda = \frac{4M_1M_2}{(M_1+M_2)^2} \quad (82)$$

The simplified energy transfer equation is:

$$T = \frac{\Lambda E}{2}(1-\cos\theta) \quad (83)$$

A head on collision ($\theta = 180^\circ$) will transfer the maximum amount of energy:

$$T_{max} = \Lambda E \quad (84)$$

and considering all possible collisions, the average energy transfer will be $T_{max}/2$ or $\Lambda E/2$.

The rate of atomic displacements, R_d , meaning the number of atomic collisions per unit time per unit volume, can be calculated as the product of the atomic density of the material, N , scattering cross-section which is a function of energy, $\sigma_d(E)$, and flux of the incident energetic particles, $\phi(E)$:

$$R_d(E) = N\sigma_d(E)\phi(E) \quad (85)$$

The standard radiation damage unit, dpa, then arrives by dividing the collision rate by the atomic density of the material and multiplying by the irradiation time, t :

$$dpa = \frac{R_d(E)t}{N} \quad (86)$$

In order to consider the impact of the full neutron energy flux spectrum occurring in a reactor, all neutron energies that displace atoms must be included to determine a total neutron irradiation displacement damage dose. Neutrons in a reactor will have a maximum energy, E_{max} , and the minimal energy a neutron must have in order to displace an atom from its lattice site is E_d/Λ . Therefore, the total dpa in reactor is:

$$dpa = t \int_{\frac{E_d}{\Lambda}}^{E_{max}} \sigma_d(E_n)\phi(E_n) dE_n \quad (87)$$

The total scattering cross section, $\sigma_d(E_n)$, can be expressed by adding all displacements caused by PKAs ($E_d < E < \Lambda E_{max}$) and incorporating the probability of interaction of the neutron to create the energetic PKA through a differential energy transfer cross section, $\sigma_n(E_n, T)$ as:

$$\sigma_d(E_n) = \int_{E_d}^{\Lambda E_{max}} \sigma_n(E_n, T) v(T) dT \quad (88)$$

The Kinchin-Pease (KP) model assumes all collisions are elastic and uses the hard sphere model, considers all PKA energies above the threshold energy, E_c , to only dissipate energy through electronic stopping and Coulombic interactions that strip off electrons from matrix atoms without generating any atomic displacements, and ignores the crystal structure of the material being irradiated. In addition, point defect annihilation is not considered. Thus the number of displacements as a function of energy transferred in the Kinchin-Pease model is given by:

$$v(T) = \begin{cases} 0 & T < E_d \\ 1 & E_d < T < 2E_d \\ \frac{T}{2E_d} & 2E_d < T < E_c \\ \frac{E_c}{2E_d} & T > E_c \end{cases} \quad (89)$$

Using (89) and knowing the energy spectrum of the neutrons in reactor, and cross-sections and displacement energy of the irradiated material, displacement damage can be quantified in terms of dpa. More advanced methods to calculate the number of displacements from collisions, $v(T)$, have been developed by Lindhard [237], Thompson and Wright (TW) [238], and Norgett, Robinson, and Torres (NRT) [239]. Figure 59 adapted from [240, 241] shows a comparison of the various models. The more advanced models depart from the hard sphere model and consider highly energetic interactions that cause displacements and more smooth transitions between the electronic stopping and nuclear stopping regime based on weighted damage efficiencies as functions of particle energy and atomic number.

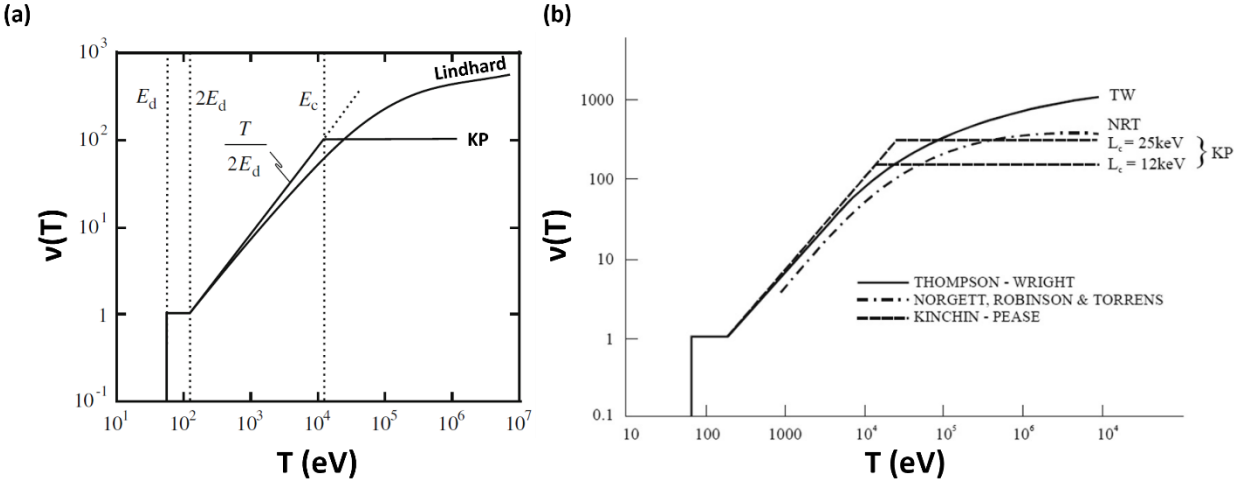


Figure 59. Illustrations of the number of displacements produced as a function of the energy transferred to the PKA: (a) Kinchin-Pease model compared to Lindhard model [240], (b) Kinchin-Pease model compared to Thompson-Wright, and NRT models [241]

A prominent computer modelling code called *The Stopping and Range of Ions in Matter* (SRIM) [242] uses Monte Carlo techniques to trace the collisions of an incident high energy particle through a solid, so that displacement damage (dpa) can be calculated as a function of particle penetration depth. The program begins with selecting an ion projectile of known density and energy and a target material. The ion travels through a free flight path between two large scattering angle collisions while the code tracks angular deviations of grazing collisions. After a small angle collision, the new energy of the projectile is calculated as

$$E' = E_o - T_{small} - E_{ion} \quad (90)$$

where E' is the remaining energy of the projectile, T_{small} is the energy transferred in small angle collisions, and E_{ion} is the ionization energy losses from electronic stopping of the target atoms given as

$$E_{ion} = k\sqrt{E} \quad (91)$$

where k is a material constant of the target. The energy transferred during a large angle collision, T , is also calculated along with the new projectile energy E'' using a Monte Carlo impact parameter, the classical scattering integral (88), and the universal interatomic potential to determine the scattering angle θ . The energy transferred is then calculated using (83) and the new projectile energy is

$$E'' = E' - T \quad (92)$$

After a large angle collision, there are two paths that can be taken in SRIM. The first faster path uses a quick calculation employing standard defect production

theory and the NRT model to determine the total number of displacements (vacancies) produced. The slow path follows the full damage cascade and traces the recoil atoms and the secondary displacements they produce and iterates until all recoil atoms have energies lower than the target displacement energy and no further displacements will occur. Both pathways follow the injected projectile until its energy is below $\frac{E_d}{\Lambda}$ and it can no longer displace target atoms. The method is repeated for as many initial projectile atoms as is selected by the user. [243]

Although the initial impact of a high energy neutron or ion creates a displacement cascade, the generated Frenkel pairs are clustered in a small region as seen in Figure 57c. Also seen in Figure 57c, after a short period of time, over 90% of the initial Frenkel pairs are annihilated as a vacancy finds a self-interstitial. However, the remaining point defects that do not recombine evolve; vacancies coalesce into small clusters which can turn into stacking fault tetrahedron (SFT) in *fcc* metals and nanovoids in *bcc* metals. If the clusters grow, larger voids or cavities result. Remaining interstitials coalesce into dislocation loops. The evolution of these surviving residual point defects and extended defects is responsible along with radiation induced/enhanced diffusion, precipitation, and segregation is responsible for mechanical properties effects such as radiation hardening and embrittlement, creep, swelling, and/or physical properties changes. The specific radiation damage effects most pertinent to Inconel X-750 components will be discussed in more detail in subsequent sections.

Transmutation

In special cases, the incident energetic particle, in most cases a neutron, interacts with a target atom that has a high affinity for it, a large absorption cross-section, and a nuclear reaction occurs. In one case, the nucleus of the target atom becomes energized and it emits a gamma ray when it returns to its ground state. In other cases, the energetic particle will be absorbed by the target nucleus and transmute into a different element and/or isotope. When this occurs, a second energetic particle (electron, positron, proton, or alpha particle) is also emitted with significant energy capable of causing additional displacement damage through collisions with lattice atoms.

If the transmutation reaction emits a proton or alpha particle, these particles will quickly capture electrons from the surrounding metal matrix and become hydrogen and helium. Both are known to have significant effects on the mechanical properties of nuclear structural materials. Although in many cases hydrogen easily escapes materials, helium is completely insoluble in metals and forms bubbles which alter the microstructure of the material and compromise

its mechanical properties. Nuclear transmutation reactions are prominent in nickel superalloys which have a high affinity for thermal neutrons, and (n,p) and (n, α) reactions will greatly enhance the materials displacement damage as well as cause radiation embrittlement and additional mechanical properties effects which will be discussed in further detail in the subsequent sections of this chapter for the Inconel X-750 garter spring components.

3.3.1 Radiation Damage in the CANDU Core

The neutron flux spectrum in CANDU reactor cores is much higher in the thermal and epi-thermal energy regime and slightly lower in the fast energy regime compared to light water reactor (LWR) core averages, seen in Figure 60 [197]. Maximum fast neutron fluxes, $E_n > 1$ MeV, within CANDU fuel assemblies are on the order of 4×10^{13} n/cm²/s. Each fuel bundle is contained in its own pressurized tube, so fast fission neutrons emitted by the fuel rods can interact first with uranium and oxygen atoms in the fuel itself, second in the heavy water D₂O coolant, third in the Zr-2.5Nb pressure tube, fourth in the Inconel X-750 annulus spacer, and last with the Zircaloy-2 calandria tube moving radially outward within the CANDU core. If a neutron collides only once with any structure within the fuel channel, subsequent collisions will almost always occur within the heavy water coolant as the neutron is moderated down to thermal energies. Therefore, an increased number of thermal neutrons will interact with Inconel X-750 spacers compared to fast neutrons. The total thermal neutron flux impinged on an annulus spacer averaged over all locations within the CANDU core is $\sim 1.4 \times 10^{14}$ n/cm²/s.

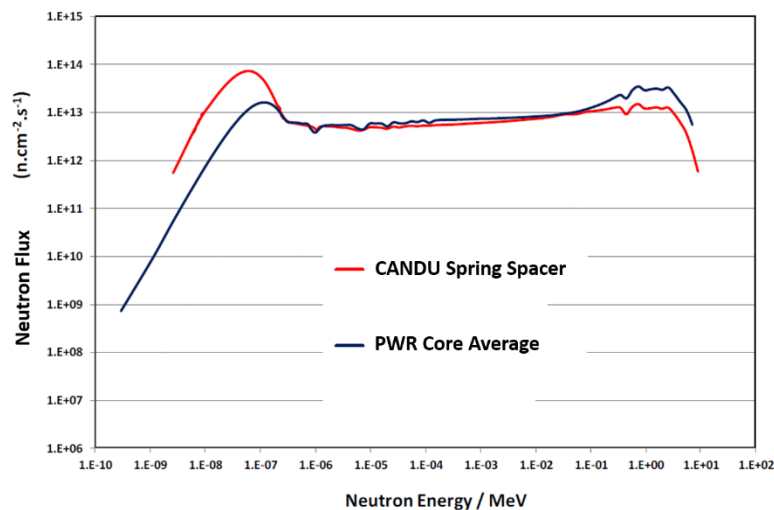


Figure 60. Neutron flux spectra seen by an Inconel X-750 spacer compared to that seen in an average PWR core [197]

The primary source of core displacement damage usually comes from fast neutrons colliding with core component atoms and producing displacement cascades, but due to the high thermal neutron flux in CANDU cores and the positioning of the spacers, indirect thermal neutron displacement damage via transmutation reactions with the nickel atoms in Inconel X-750 contributes an impactful quantity of displacement damage. This indirect thermal neutron displacement damage comes primarily from the recoil of the nucleus and secondarily from collisions of the emitted β and α particles with other matrix atoms.

3.3.1.1 Fast Neutron Damage

Direct collisions between fast neutrons and atoms in garter spring Inconel X-750 spacers (70% nickel atoms) generate displacement cascades because they greatly exceed the threshold energies needed to remove an atom from its lattice site. The displacement energy of Ni atoms is $23 \text{ eV} \leq E_{d-Ni} \leq 40 \text{ eV}$ [244].

The minimum neutron energy needed to displace a Ni atom from its lattice, given by ΔE_{d-Ni} , is between 347 eV and 603 eV. When neutrons within this energy range displace a Ni atom, that Ni atom will then have a recoil energy approximately equal to its displacement energy, just enough to create one PKA. Neutrons with greater energies can create PKAs even at glancing angle collisions, but neutrons with energies below this range cannot displace a Ni atom but instead only cause it to vibrate within its lattice site and emit phonons.

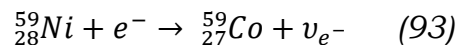
High energy fast neutrons create displacement cascades and high energy PKAs above the Coulomb energy, E_c , of the ionized atom. These highly energetic, charged PKAs are predominantly slowed by electronic stopping and produce heat before they collide with many more nearby nuclei that also recoil and make secondary collisions. Cascades have the potential to displace hundreds of atoms if the initial neutron energy is in the MeV range. The transfer of energy occurs in the initial 10^{-6} ps. Then, the PKA begins slowing down in the first 0.2 ps. This is the time period when the maximum number of point defects exists and is referred to as the cascade efficiency. A thermal spike is observed between 0.2-3.0 ps where internal electrical forces among defects and interstitial diffusion can be enhanced such that mobile interstitials find nearby lattice vacancies and annihilate. Within 3-10 ps the region where the cascade occurs begins cooling down to the bulk solid temperature as thermally enhanced recombination lessens but still continues. After 10 ps has passed, further migration and recombination of the newly created point defects can occur, but this microstructural evolution now becomes a function of steady-state parameters: irradiation temperature, point defect migration energy, defect sink strength, and the fraction of defects free for long-range migration. This steady-state microstructural evolution leads to long term radiation effects.

Irradiation temperature is a key parameter in determining whether long term point defects evolve in a recombination-dominated environment or a sink-dominated environment. Recombination is favored at low reactor operating temperatures or when pre-existing point defect sinks exist in the material at high densities. This is the *recombination-dominated regime*. When reactor temperatures are high enough during normal operating conditions, individual interstitials and vacancies born during displacement cascades have the opportunity to migrate to separate defect sinks in the material such as grain boundaries and inclusions. In this case, the microstructure continually evolves and the material is considered to be in a *sink-dominated regime*.

The initial neutron energies, which span approximately 11 orders of magnitude (0.0001 eV-10 MeV) as shown in Figure 60, control how much accumulated radiation damage is created. Each location within the CANDU core has a slightly different percentage of neutrons within each energy group, but using an average CANDU fuel channel power profile, it can be estimated that Inconel X-750 spacers receive 1 dpa/year in service from fast neutrons. Because they remain in service for 25-30 years before planned refurbishment, they will receive 25-30 dpa from fast neutrons in their lifetime in the reactor. However, this fast neutron damage is not the total displacement damage or the only type of radiation damage seen by the components before they reach their end of life.

3.3.1.2 Thermal Neutron Damage: (n,p) and (n, α) Transmutations

The Inconel X-750 components contain 70 wt% Ni atoms, and 68% of these Ni atoms are ^{58}Ni . The ^{58}Ni isotope has a high affinity for absorbing thermal neutrons and then emitting a gamma ray, meaning it has a large thermal (n, γ) reaction cross-section (Figure 65). The resultant ^{59}Ni isotope will reach a maximum concentration of ~4% of the ^{58}Ni concentration after it has been exposed to thermal neutrons in the CANDU core for 5-10 years depending on its position [245, 246]. This will occur in thermal neutron fluences ($E_n < 0.5$ eV) of approximately $\sim 3.5 \times 10^{22}$ n/m² [245], whereas all naturally occurring isotopes of other engineering alloys only have significant neutron reaction cross-sections under fast neutron fluence. Naturally occurring ^{59}Ni only exists in trace amounts and is a long-lived cosmogenic radionuclide with $t_{1/2} = 76,000$ years. It decays by an electron capture (EC) reaction to cobalt-59, a stable isotope:



However, in a reactor environment, ^{59}Ni has a high probability of absorbing a thermal neutron and producing hydrogen and helium via (n,p) and (n, α) reactions (Figure 61), leading to enhanced atomic displacement damage, mostly from recoils of the heavier nucleus with minor contributions from energetic p and α particles, in addition to large amounts of H and He gas production. Once

the concentration of ^{59}Ni has reached its maximum in the CANDU core, the radiation damage produced per neutron caused by thermal neutrons can exceed the radiation damage caused by fast neutrons (Figure 66). Table 3 provides the ^{59}Ni transmutation reactions along with the average number of displacements each reaction produces and the thermal neutron cross-section of ^{59}Ni for each reaction.

Table 3. ^{58}Ni and ^{59}Ni transmutation reactions and their associated $\sigma_{a\text{-th}}$ and displacement damage

Ni transmutation reactions:	# Displacements [247,248]	$\sigma_{a\text{-th}}$ (barns) [231]
$^{58}\text{Ni} + n \rightarrow ^{59}\text{Ni} + \gamma$		100
$^{59}\text{Ni} + n \rightarrow ^{56}\text{Fe} + ^4\text{He}$	1762	50
$^{59}\text{Ni} + n \rightarrow ^{59}\text{Co} + \text{H}$	222	5
$^{59}\text{Ni} + n \rightarrow ^{60}\text{Ni} + \gamma$	5	100

The (n, α) reaction creates the largest amount of displacement damage (total damage energy 176.2 keV) and has a high cross-section over a range of neutron energies as shown in Figure 61. The ^{59}Ni effect will be the most significant contribution to radiation damage in Inconel X-750 components (~35 dpa after 25 years of service) as shown in Figure 62 because the thermal neutron flux is high everywhere in the CANDU core. Direct collisions from neutrons with $E_n > 600$ eV contribute ~25 dpa in 25 years of service.

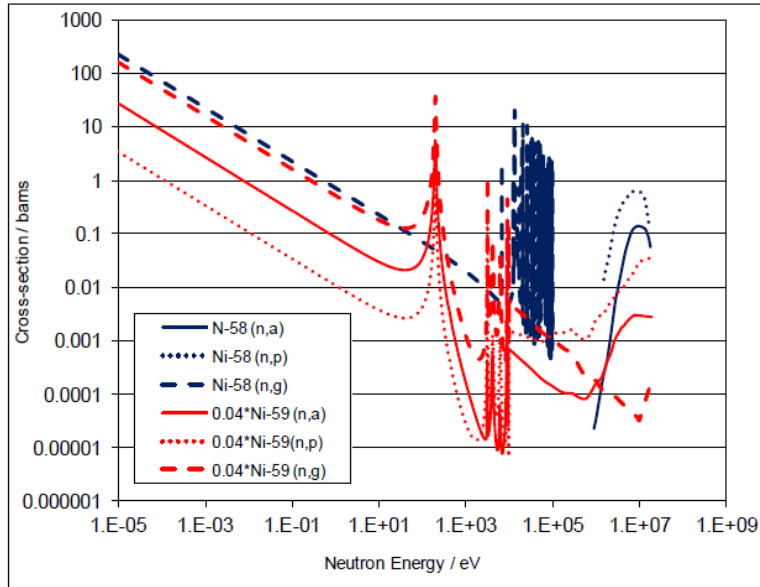


Figure 61. Thermal neutron absorption cross-sections for all three possible transmutation reactions involving ^{58}Ni and ^{59}Ni . The ^{59}Ni cross-sections have been scaled according to their relative maximum concentration in the CANDU core, 4%. [197]

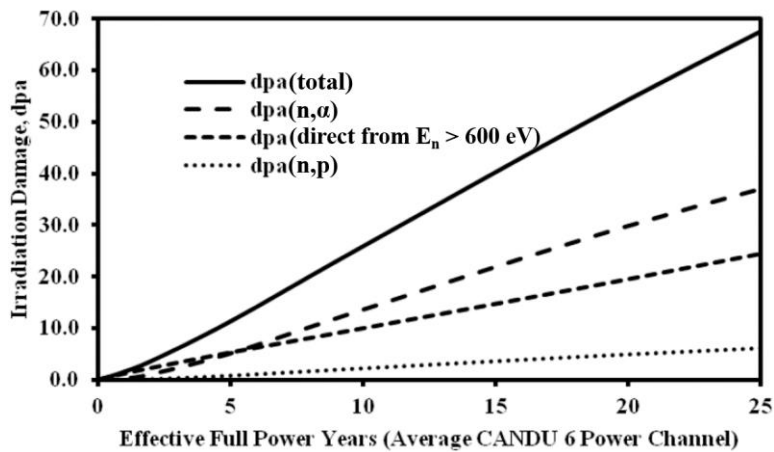


Figure 62. Total displacement damage and the contributions from each reaction for Inconel X-750 using the neutron flux of an average fuel bundle [226]

3.3.1.3 Point Defects

Inconel X-750 components operate under two distinct irradiation temperatures, $T_{\text{pinched}} = 120\text{-}280\text{ }^{\circ}\text{C}$ and $T_{\text{non-pinched}} = 300\text{-}330\text{ }^{\circ}\text{C}$. Irradiation responses are highly dependent on the mobility of newly created vacancies and interstitials, which is strongly influenced by irradiation temperature. Using rate theory point defect concentration equations for vacancies, C_v , and self-interstitials, C_i :

$$\frac{\partial C_v}{\partial t} = G_v - RC_i C_v - D_v C_v \sum_{j=1}^n S_{vj} \quad (94)$$

$$\frac{\partial C_i}{\partial t} = G_i - RC_i C_v - D_i C_i \sum_{j=1}^n S_{ij} \quad (95)$$

the flux of point defects to pre-existing defect sinks in the component can be calculated. The variables in the point defect equations are defined as follows. The total point defect generation rates, G , from both displacement cascades and transmutations are given by:

$$G = f\kappa(1 - \varepsilon) + G_T \quad (96)$$

where f is the in-cascade recombination survival fraction, κ is the dpa rate, ε is the clustering fraction, and G_T is the thermal neutron generation rate. The long-term recombination rate parameter, R , is a function of the recombination radius, r_o , and point defect diffusion coefficients, D_i and D_v , and is given as:

$$R = 4\pi r_o (D_i + D_v) \quad (97)$$

The sink strength of a pre-existing sink such as a dislocation, grain boundary, cavity, void, or inclusion, is denoted S_i for interstitials and S_v for vacancies. Typical Inconel X-750 garter springs have a dislocation density $\sim 3 \times 10^{14} \text{ m}^{-2}$ [228] and equiaxed grains that average 8.5 μm in diameter. Using this pre-existing microstructure, and knowing the vacancy migration energy in nickel is between 1 eV [249] and 1.4 eV [250], calculations can be made to plot the flux of point defects to selected defect sinks as illustrated in Figure 63.

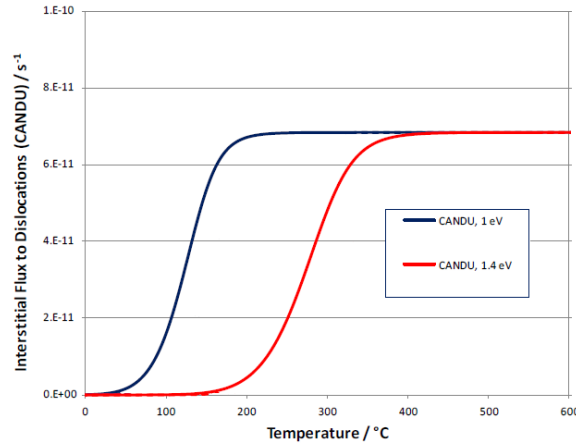


Figure 63. Calculated point defect flux to dislocations at the onset of irradiation using defect sink strengths of 4×10^{14} for dislocations, 2.4×10^{13} for grain boundaries, a 30% interstitial bias for dislocations and a dpa rate in CANDU reactors of $\kappa = 10^{-7} \text{ dpa/s}$, and a 10% in-cascade survival rate [249, 250]

When considering a freely-migrating point defect density towards the higher end of the range, the pinched material at the 6 o'clock position falls into a recombination dominated regime, whereas the non-pinched material comprising most of the rest of the spring falls into a sink dominated regime. Figure 67 illustrates the fact that the temperature range within the garter springs most likely encompasses the transition expected between complete recombination and complete absorption by pre-existing sinks. As the microstructure of the component evolves with dose and time, the transition region may shift, and the net point defect flux to sinks will vary because new defect sinks are being born and existing defect sinks are changing.

TEM observations of the microstructures of the high dose materials irradiated at the two irradiation temperatures shown in Figure 64 [229] are in good agreement with the red curve in Figure 64. The microstructures appear much cleaner in the pinched components, providing evidence of recombination, but the microstructure of the non-pinched components appears littered with a higher density of defects.

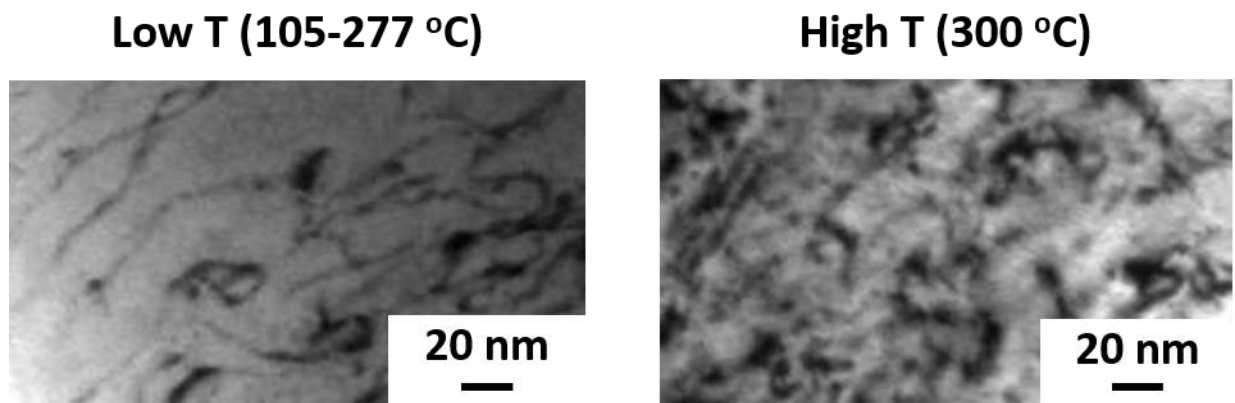


Figure 64. TEM images of the dislocation defect structures of Inconel X-750 components irradiated to 55 dpa containing 1.8 at% He. [229]

3.3.1.4 Helium and Hydrogen Gas Production

Displacement damage and point defect evolution is not the only contribution to radiation effects that alter the mechanical properties and microstructure of Inconel X-750 annulus spacers. As previously noted, (n,p) and (n, α) two-step transmutations produce significant quantities of hydrogen and helium gas over the course of a spacer's lifetime. Hydrogen is soluble and extremely mobile as an interstitial, but helium is completely insoluble. Helium atoms will find small vacancy clusters or pre-existing defect sinks such as dislocations, grain boundaries, and matrix-carbide interfaces, and bubbles will nucleate and grow. This process accelerates the onset of void swelling and may contribute to grain boundary embrittlement [227, 251-264].

Figure 61 depicting the neutron absorption cross-sections as a function of energy reveals that helium production is favored when thermal and slow neutrons interact with Ni atoms, whereas hydrogen production is favored when fast neutrons more energetic than 1 MeV interact with the material. Formulas for calculating the amounts of hydrogen and helium produced from the two-step transmutation reactions shown in Table 3 have been developed by Greenwood in [248] using the ENDF library [265] as a cross-section database:

$$\frac{N_H}{N_{o-58Ni}} = \frac{\sigma_p}{\sigma_T} + \frac{\sigma_p e^{-\sigma_y \phi t}}{\sigma_y - \sigma_T} - \frac{\sigma_y \sigma_p e^{-\sigma_y \phi t}}{\sigma_T (\sigma_y - \sigma_T)} \quad (98)$$

$$\frac{N_{He}}{N_{o-58Ni}} = \frac{\sigma_\alpha}{\sigma_T} + \frac{\sigma_\alpha e^{-\sigma_y \phi t}}{\sigma_y - \sigma_T} - \frac{\sigma_y \sigma_\alpha e^{-\sigma_y \phi t}}{\sigma_T (\sigma_y - \sigma_T)} \quad (99)$$

The parameters are as follows: N_H is the number of hydrogen atoms produced, N_{He} is the number of helium atoms produced, N_{o-58Ni} is the initial number of ^{58}Ni atoms in the Inconel X-750 component, σ_α is the spectral averaged (n, α) cross-section, σ_p is the spectral averaged (n,p) cross-section, σ_T is the total absorption cross-section of ^{59}Ni , σ_y is the spectral averaged (n, γ) cross-section, ϕ is the total neutron flux, and t is the total irradiation time.

Greenwood's gas production equations indicate that when the neutron spectrum is heavily thermal as is the case in a CANDU core, ^{59}Ni is quickly produced from ^{58}Ni and subsequent H and He gas will be produced in a non-linear fashion as the concentration of ^{59}Ni increases to its maximum of 4% after between 5 to 10 years of time in service. When the amount of ^{59}Ni has already reached its stable maximum concentration, gas production continues in a linear fashion. More helium will be produced in predominantly thermal neutron spectrums, whereas more hydrogen will be produced in predominantly fast neutron spectrums. A mixed spectra environment will produce elevated levels of both H and He. Figure 65 plots the calculated H and He gas along with the total displacement damage for an Inconel X-750 spacer in a high power channel of a CANDU-6 reactor at full power assuming a mid-burn-up flux spectrum [228]. The values plotted in Figure 65 should be considered to be the maximum amounts of gas able to be produced in the component and the upper bound for displacement damage because all spacers do not operate in high power channels at full power for their entire time in service.

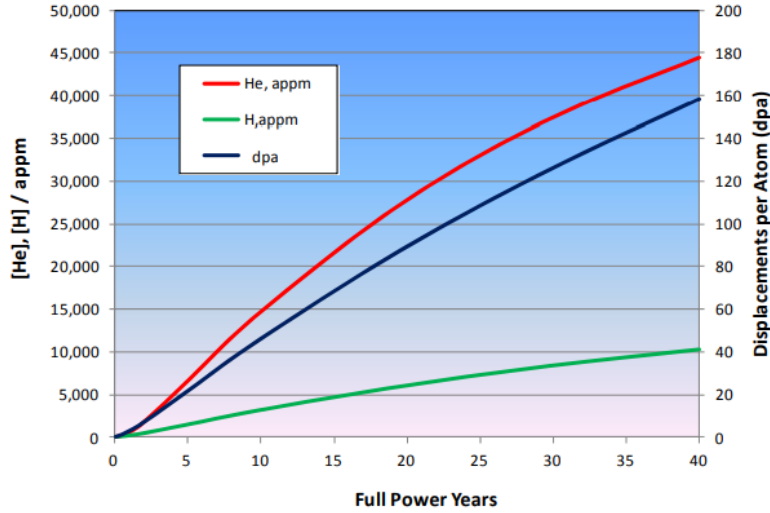


Figure 65. Calculated helium and hydrogen gas along with the total displacement damage for an Inconel X-750 spacer in a high power channel of a CANDU-6 reactor at full power assuming a mid-burn-up flux spectrum [228]

3.3.1.5 Helium Bubble Nucleation and Growth

Helium atoms produced by (n, α) transmutation reactions and vacancies produced by displacement damage cascades are absorbed by small di-vacancy void embryos in nucleation and growth processes that produce helium bubbles. Nucleating a spherical bubble requires overcoming the excess surface area interfacial free energy the bubble requires in order to form (equation 100). The additional interfacial free energy can be reduced if the bubble nucleates at a pre-existing interface in the material: either a grain boundary, matrix-carbide interface, or other matrix-precipitate interfaces in the Inconel X-750 springs. This process of heterogeneous nucleation is more energetically favorable compared to homogeneous nucleation of bubbles within the clean γ -matrix due to the reduction of free energy required expressed as the last term of equation (100).

$$\Delta G = -\frac{4}{3}\pi r^3 \Delta G_V + 4\pi r^2 \gamma - A_{interface} \gamma_{interface} \quad (100)$$

Equation (100) expresses the change in free energy of the material required to nucleate a spherical bubble where ΔG is the overall change in free energy, r is the radius of the bubble, ΔG_V is the volume free energy, γ is the surface tension of the bubble, and $A_{interface}$ and $\gamma_{interface}$ the surface area and surface tension of a pre-existing interface in the material.

The critical radius for nucleating a bubble can be given by differentiating (100).

$$r_{crit} = \frac{2\gamma}{\Delta G_V} \quad (101)$$

In a continual radiation environment, the critical radius depends on the vacancy supersaturation, SS , expressed as a ratio of the irradiated vacancy concentration, c_v , and the equilibrium vacancy concentration, c_{v-eq} :

$$SS = \frac{c_v}{c_{v-eq}} = e^{\frac{G_v - G_{v-eq}}{kT}} \quad (102)$$

where G_v and G_{v-eq} are the Gibbs free energies of the supersaturated material and the material at equilibrium respectively, k is Boltzmann's constant, and T is the irradiation temperature. A critical number of vacancies required to form a stable cavity can be determined by differentiating the difference in free energies of the supersaturated material and equilibrium material and setting the expression equal to zero. The critical number of vacancies that form a stable cavity is given by:

$$n_{critical} = \left(\frac{2B\gamma}{3kT \ln(SS)} \right)^3 \quad (103)$$

where B is a constant based on the atomic volume, Ω , given by:

$$B = 4\pi \left(\frac{3\Omega}{4\pi} \right)^{2/3} \quad (104)$$

Although cavities do not have a preference for absorbing vacancies over interstitials, the stress fields created by dislocations preferentially attract interstitials. This dislocation-bias can induce a vacancy flux to the cavities which is greater than the thermal emission of vacancies leaving the cavities. In this case, cavity growth will occur. When insoluble helium atoms produced by transmutation reactions are introduced, they help to stabilize and grow cavities as shown in Figure 66. With no helium atoms, a perfect void, there is one critical radius. Below this value, the void shrinks until vanishing; above this value, the void undergoes continuous growth. As a small number of helium atoms are added to the cavity to form a bubble, it obtains two stable critical radii. Tiny overpressurized bubbles above points B and D in Figure 66 will grow at a decreasing rate until reaching the smaller critical radius. A bubble between points A and B, for example, will shrink until it reaches the smaller critical radius at point B. Bubbles with larger critical radii at points A and C are metastable. Slight perturbations will cause them to either continually shrink to the smaller critical radius if a few helium atoms are lost or continually grow if a few helium atoms are gained. If a high enough amount of helium atoms are in the bubble, it enters an eternal realm of continuous growth, the region labelled III in Figure 66.

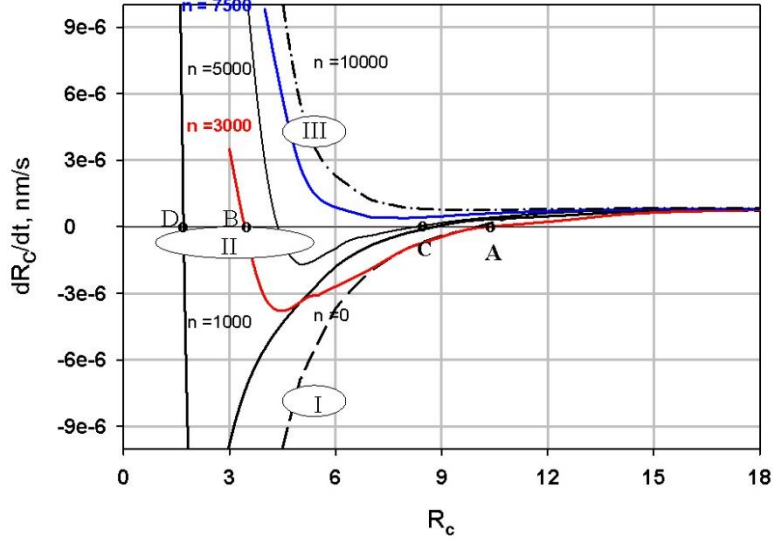


Figure 66. The effect of number of helium atoms, n , on the growth rate of a bubble, dR/dt [266]

Olander has developed an expression to describe the time dependence of the radius of the bubbles, dR/dt , as a function of the diffusion coefficients of vacancies and interstitials, D_v and D_I , the supersaturated and equilibrium concentration of vacancies, c_v and c_{v-eq} , the equilibrium concentration of interstitials, c_I , the atomic volume, Ω , the surface tension of the bubble, γ , Boltzmann's constant, k , the irradiation temperature, T , the radius of the bubble, R , the number of helium atoms, n , a dislocation-bias factor, ϵ_I , a helium atom transmutation production rate, G , the dislocation density, ρ_d , the density of vacancy dislocation loops, ρ_{VL} , the number density of cavities, N_C , and the average length of a dislocation, d .

$$\frac{dR}{dt} = \frac{\Omega}{R} \left[D_V c_V - D_V (c_V^{eq})_o \exp \left\{ \frac{2\gamma\Omega}{k_B T R} - \frac{3\Omega n}{4\pi R^3} \right\} - D_I c_I \right] + \frac{\frac{1}{4}\epsilon_I G \Omega}{\pi R^2 N_C + d(\rho_d + \rho_{VL})} \quad (105)$$

Performing a sensitivity study on the parameters reveals that increasing the production rate of helium atoms, G , and net flux of vacancies, $D_V c_V - D_I c_I$, both greatly increase bubble growth. Increasing defect densities (ρ_d and ρ_{VL}) will slightly reduce bubble growth rate because there are more competing defect sinks for newly produced helium atoms to find. Greatly increasing the cavity density, N_C , will have a similar effect because more cavities will be competing with one another for helium atoms. The dislocation-bias factor, ϵ_I , has the strongest effect on increasing bubble growth rates as shown in Figure 67. A 1% interstitial absorption bias, $\epsilon_I = 0.01$, moves the curve up into a regime of complete continuous growth. [266]

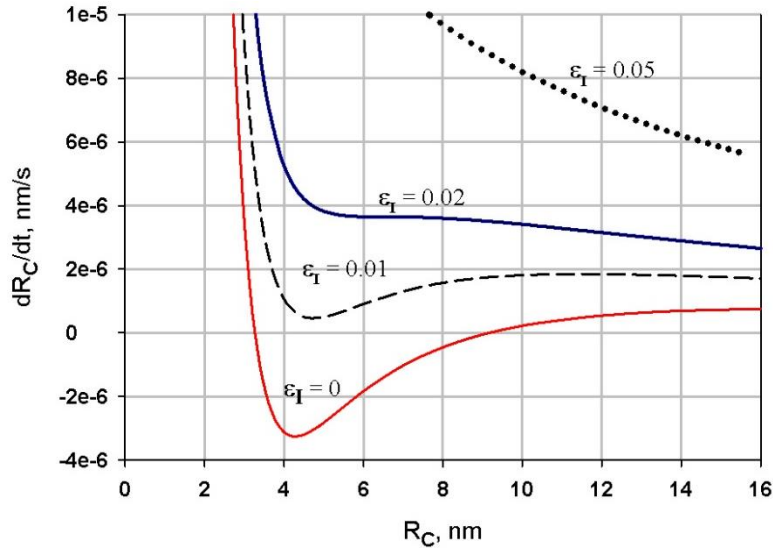


Figure 67. Effect of dislocation-bias factor, ϵ_I , on bubble growth rate. [266]

It is well established that helium bubbles form in irradiated Ni-based components. Direct TEM images of He bubbles in 53 dpa irradiated Inconel X-750 components along with their size distributions for low temperature and high temperature material can be seen in Figure 68 [229]. The average size of a helium bubble in low temperature components is ~ 2 nm, whereas in high temperature components it is approximately double, ~ 4 nm. He atom migration tendencies mirror that of point defects, such that the low temperature material contains a much higher density of much smaller bubbles, but the high temperature material contains a larger range of helium bubble sizes and a larger mean bubble size.

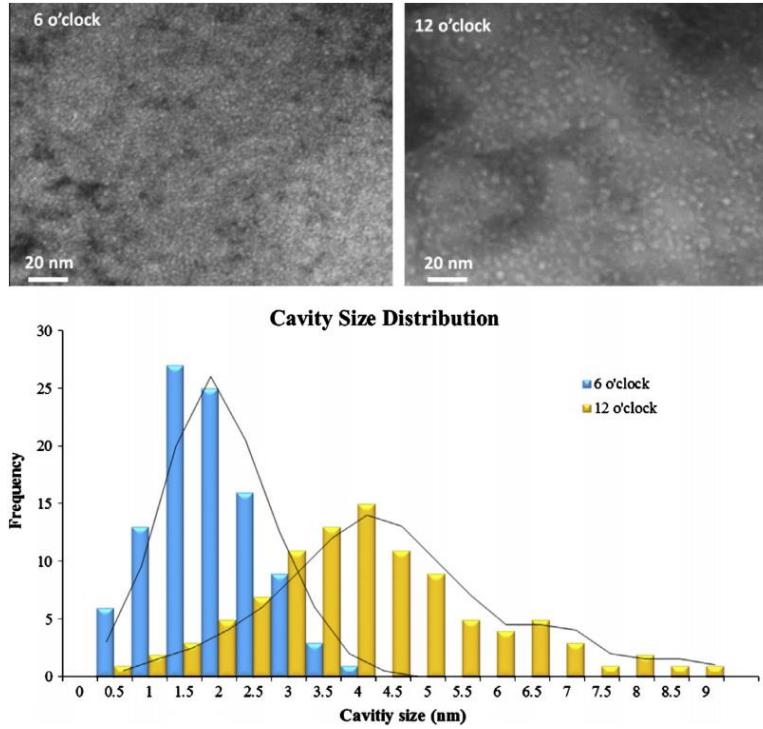


Figure 68. BF TEM images of He bubbles in low temperature (6 o'clock) and high temperature (12 o'clock) 53 dpa ex-service Inconel X-750 spacers and their size distributions [229].

3.3.1.6 Helium Bubble Pressure

The state of the helium atoms within each bubble strongly influences how the bubble changes the mechanical properties of the surrounding matrix or interface in which it lies. The mechanical stress balance for a bubble is given as:

$$P + \sigma_r(R) = \frac{2\gamma}{R} \quad (106)$$

A bubble is considered to be in mechanical equilibrium when it imposes no residual stress, $\sigma_r(R) = 0$, on the surrounding material, such that

$$P_{eq} = \frac{2\gamma}{R} \quad (107)$$

Pressure deficit bubbles, otherwise termed as underpressurized bubbles, have pressures $P < 2\gamma/R$, and pressure excess bubbles, otherwise termed as overpressurized bubbles have pressures $P > 2\gamma/R$. Using the surface tension of Ni, $\gamma = 1.89 \text{ N/m}$, the pressure of the helium bubbles can be estimated as a function of bubble radius as shown in Figure 69.

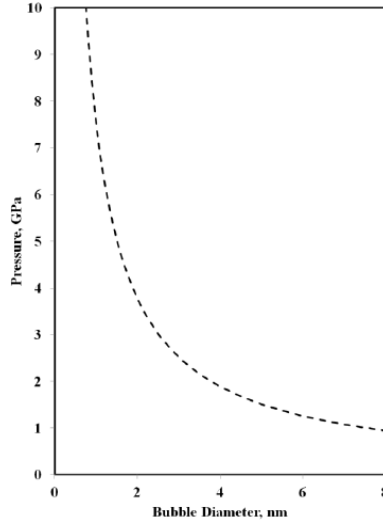


Figure 69. Equilibrium pressure of a helium bubble as a function of bubble radius

It is recognized that for the high pressures seen in Figure 68 in nanometer sized helium bubbles in irradiated Inconel X-750 components, helium does not behave as an ideal gas because it becomes incompressible. The pressure in the bubbles is larger than that of an ideal gas, so equations of state (EOS) for high pressure helium should be used to more accurately determine bubble pressures.

A common approach is to use a hard sphere EOS to calculate the compressibility, Z , of helium. Carnahan and Starling developed a closed form expression for the compressibility in terms of the packing fraction of He, y [267]:

$$Z = \frac{P}{NkT} = \frac{1+y+y^2+y^3}{(1-y)^3} \quad (108)$$

where y is given as:

$$y = \frac{\pi d_{HS}^3}{6} N \quad (109)$$

and $d_{HS} = 0.20$ nm [266] is the hard sphere diameter of a helium atom and N is the number density of He atoms in the bubble. Thus, the pressure of a helium bubble can be determined from measuring the helium atom density and diameter of the bubble.

3.3.2 Mechanical Properties Evolution of Irradiated Nickel Superalloys

Radiation damage in the form of displacement damage and the production of hydrogen and helium gas in Inconel X-750 garter springs dramatically alters their mechanical properties. This section details irradiation effects on nickel superalloys. It begins with general effects such as radiation hardening mechanisms via induced defects and transitions to effects more specific to Ni superalloys, such as loss of γ' phase stability and grain boundary embrittlement

mechanisms including hydrogen embrittlement and helium bubble embrittlement.

3.3.2.1 Radiation Hardening Mechanisms

Metals become hardened under irradiation due to two causes: source hardening and friction hardening. Source hardening is the increase in the initial stress required for a dislocation to begin moving. It can be expressed as:

$$\sigma_s = \frac{k}{\sqrt{D}} \quad (100)$$

where D is the spacing between two sources and k is a material specific strengthening coefficient. Source hardening is also thought of as an increased unlocking or unpinning stress required to release a dislocation into its preferred slip system. In irradiated fcc alloys like the Inconel X-750 components, irradiation-induced defect clusters nearby Frank-Read sources increase the stress needed to allow source multiplication and loop expansion [268]. Once the source has been unlocked and the applied stress is sufficient enough for dislocations to begin moving, moving dislocations are predominantly effected by friction hardening.

Friction hardening is the sum of all obstacles' resistance stress experienced by dislocations when they move in the lattice. Friction hardening can be divided up into short-range hardening mechanisms and long-range hardening mechanisms.

$$\sigma_{fr} = \sigma_{SR} + \sigma_{LR} \quad (101)$$

Short range hardening mechanisms are caused by the interaction of the moving dislocation with obstacles that lie in the slip plane where it is moving. These increased stresses arise when the dislocation comes very close to or in some case contacts the obstacle. Each obstacle, whether it be a dislocation loop, precipitate, void, or helium bubble, has its own short range hardening stress, so the total short range hardening can be expressed as the sum of each individual defect's short range hardening factor.

$$\sigma_{SR} = \sigma_{loops} + \sigma_{precipitates} + \sigma_{bubbles} + \dots \quad (102)$$

$$\sigma_{SR} = GbT (\alpha_l \sqrt{2r_l N_l} + \alpha_{prec} \sqrt{2r_{prec} N_{prec}} + \alpha_{bubble} \sqrt{2r_{bubble} N_{bubble}} + \dots) \quad (103)$$

The shear modulus, G , Burgers vector, b , Taylor factor for fcc alloys, $T = 3.06$ [267], dispersive barrier strength of each defect, α_i , mean radius of the defect, r_i , and mean atomic number density of the defect, N_i , are the parameters that determine the degree of hardening of each defect. Each type of defect will have a different barrier strength, and the size, density, and spacing of the defects will change their relative barrier strengths. A perfect barrier would have a dispersive

barrier strength of $\alpha = 1$. This type of hardening known as the Orowan mechanism [270] is founded on the understanding that dislocations overcome defect barriers by bowing around obstacles, and it can be derived using standard dispersive barrier models [269-273].

Long range hardening mechanisms involve repulsive interactions between the moving dislocation and the forest dislocation network within the matrix of the material. Local stress fields arise from long range dislocation-dislocation interactions such that the total long range friction hardening can be expressed as:

$$\sigma_{LR} = \alpha Gb\sqrt{\rho} \quad (103)$$

where α is the overall dispersive barrier strength of the dislocation network, G is the shear modulus, b is the Burgers vector, and ρ is the dislocation density of the material.

Traditional radiation defects created by displacement damage cascade collapses that contribute to hardening in Inconel X-750 components primarily include stacking fault tetrahedrals (SFTs), interstitial/vacancy dislocation loops, and voids. Visible dislocation loops seen at irradiation temperatures 120-330 °C consist of faulted/Frank loops and perfect loops which are born from faulted loops. Loops indicate that a plane of atoms has either been inserted or removed from the matrix, causing an extrinsic or intrinsic stacking fault. Faulted loops lie on the $\{111\}$ close packed planes and are immobile. They can be turned into perfect loops if an $a_0/6 \langle 112 \rangle$ Shockley partial dislocation sweeps through them and atomically shears one layer of atoms. The new perfect loop has an $a_0/2 \langle 110 \rangle$ Burgers vector on $\{111\}$ habit planes. When the loop unfaults, its habit plane gradually changes to $\{110\}$ and a pure, mobile, edge loop is born. As perfect loops are further irradiated, clustered dislocation networks arise which increase long range friction hardening. In *fcc* transition metals, many vacancies become trapped by immobile vacancy clusters, either SFTs, sessile loops, or small voids created during displacement cascades, so the observed dislocation loops in *fcc* alloys are interstitial loops [252].

Stacking fault tetrahedrons in close packed *fcc* alloys are generated from small $a_0/3 \langle 111 \rangle$ faulted loops that dissociate into $a_0/6 \langle 110 \rangle$ stair rod dislocations and an $a_0/6 \langle 112 \rangle$ Shockley partial dislocation [274]. The three-dimensional tetrahedron shape arises from the six stair rod dislocations that bind it [275].

The largest contributors to radiation hardening are the high densities of radiation produced immobile defect clusters because they have the highest barrier strengths and the strongest resistance to dislocation motion. However, at a critical dose, the density of these defects is known to saturate and reach an

equilibrium: when the quantity of new defects nucleated is cancelled out by an equal quantity of existing defects being annihilated. Therefore, irradiation hardening from defects such as dislocation loops reaches a maximum value. Assuming moving dislocations will bow around loops using the approach described by equation (103), the barrier strength of the sessile loops is ~ 0.1 . They are weak barriers.

The defect structures and size distributions (SFTs and dislocation loops) for the high dose Inconel X-750 components irradiated to 53 dpa with 1.8 at% helium at irradiation temperatures of both ~ 180 °C and ~ 300 °C investigated here have been well studied by Zhang in [229, 274] and are displayed in Figure 70.

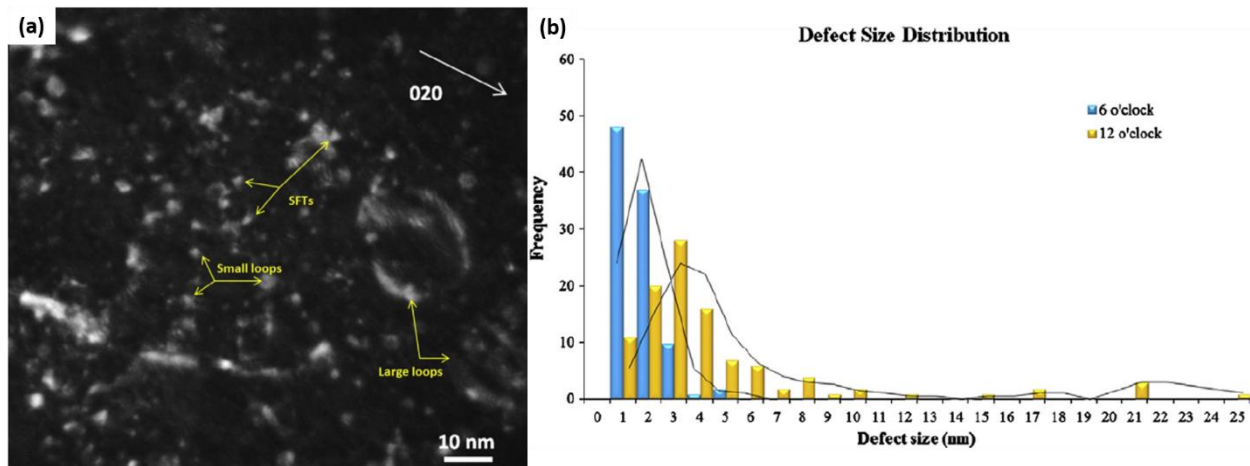


Figure 70. (a) Radiation defects in an ex-service Inconel X-750 component irradiated to 53 dpa containing 1.8 at% He at ~ 300 °C shown through weak beam DF TEM imaging. (b) size distribution of all defects observed in components irradiated at both ~ 180 °C (6 o'clock) and ~ 300 °C (12 o'clock) [229]

The high densities of small defects in ex-service material irradiated at both temperatures can be attributed to displacement cascade collapse [275, 276]. Clearly, a significant amount of larger defects are observed in the high temperature material as evidenced by the long tail in Figure 70b, but not in the low temperature material. This provides direct evidence for the fact that many defects in the 6 o'clock material recombine and remain small (recombination dominant regime), whereas in the 12 o'clock material, they migrate, find each other at a defect sink, and are able to form larger interstitial dislocation loops (sink dominated regime). Based on equation (103), it is expected that more radiation hardening will be present in the material irradiated at the higher temperature with larger defects that produce a higher short range hardening factor. It is more difficult for dislocations to bow around larger loops compared to smaller ones.

An alternative hardening mechanism to dislocations bowing around obstacles is that the moving dislocation may instead shear precipitates, bubbles, or voids by a length equal to the Burgers vector of Inconel X-750. Shearing increases the exposed surface area and requires additional work. When the ordered γ' nanoprecipitates are sheared by native $a_0/2 \langle 110 \rangle$ dislocations, an antiphase boundary (APB) is created, and the energy required to bypass this resultant configuration is extremely high. This is what gives Ni superalloys like the Inconel X-750 components intrinsically high strength. The strength required to cut a precipitate or bubble is a function of its radius, r , surface energy, γ , Burgers vector of the matrix, b , and the average spacing of the precipitate or bubble, d .

$$\sigma_{cutting} = \frac{\pi r \gamma}{bd} \quad (104)$$

Particle/bubble shearing and Orowan bowing are competing mechanisms. It is more energetically favorable for moving dislocations to cut through small precipitates and bubbles, whereas they prefer to bow around larger ones. Figure 71 plots the radius of the defect versus the strength required to move a dislocation past it via the two mechanisms. The critical radius where maximum strengthening effects occur (neither mechanism is energetically favorable) is typically between 5 nm and 30 nm.

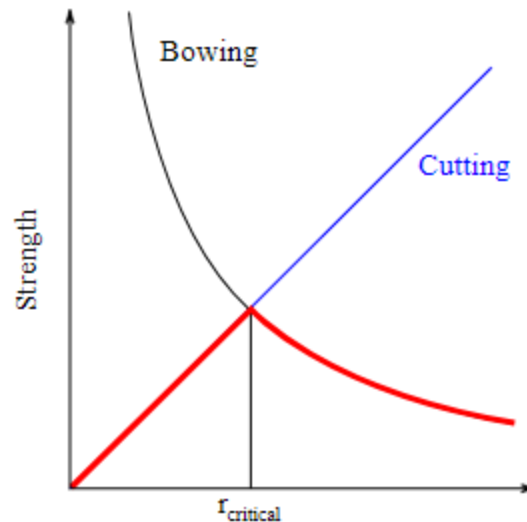


Figure 71. Particle strengthening mechanisms as a function of particle radius. It is more energetically favorable to cut through small particles and bow around large particles. [330]

The volume fraction of the precipitates/bubbles also plays a key role as shown in Figure 72. Increasing the volume fraction increases the overall strengthening effects, while also increasing the critical radius.

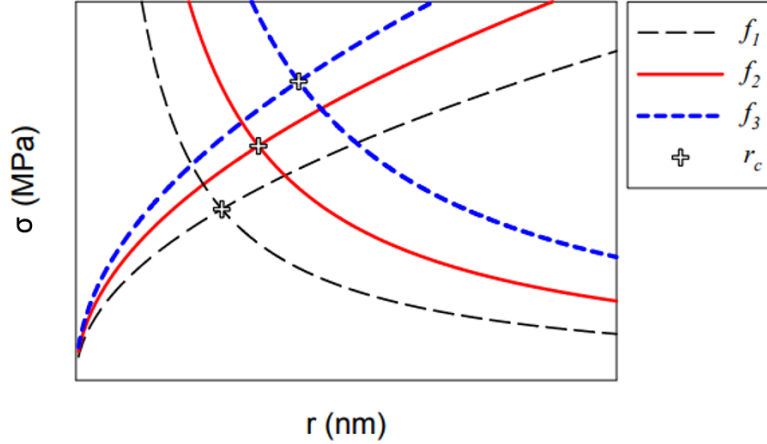


Figure 72. Schematic of spherical defect strengthening as a function of spherical defect radius, r , and volume fraction, f . $f_3 > f_2 > f_1$ showing that increasing the volume fraction of the spherical defect increases its hardening effect, in addition to increasing the critical radius, r_c , meaning shearing becomes more favored for spherical defects with larger radii at higher volume fractions. [331]

Determining the effects of helium bubbles on hardening and mechanical properties depends on their relative barrier strength and how they interact with moving dislocations. Bubble size and density/volume fraction along with the internal pressure of the bubbles influences how they inhibit dislocation motion. If the standard dispersive barrier model [269-273] is applied to helium bubbles assuming they impede dislocations as expressed in (103), an effective dispersive barrier strength, $\alpha_{\text{He bubble}}$, can be found.

The Friedel-Kroupa-Hirsch dispersive barrier model for dislocations encountering weak spherical obstacles, which takes into consideration the less extensive bowing of dislocations prior to obstacle breakaway, is a more refined approach to correlating radiation hardening (change in yield strength) with helium bubble diameter and helium bubble number density [278, 279]:

$$\Delta\sigma_y = \frac{1}{8} M\mu b d N^{2/3} \quad (105)$$

The parameters are the Taylor factor for fcc metals, $T = 3.06$, the shear modulus, μ , the Burgers vector, b , the average bubble diameter, d , and the number density of bubbles, N .

More recent in-situ TEM studies coupled with molecular dynamics (MD) simulations have revealed a difference in the hardening mechanism of helium bubbles depending on their internal pressure. If a helium bubble is underpressurized, a dislocation bypass mechanism allows the dislocation to shear the bubble by a length of the Burgers vector of the γ -matrix. The dislocation can annihilate when it hits the matrix-bubble interface at the front

of the bubble and re-form at the back of the bubble as it continues moving. The stress required to bypass underpressurized bubbles was not much larger than the critical resolved shear stress (CRSS) of the matrix, implying that these void-like bubbles with low pressures are weak barriers [280]. An effective dispersive barrier strength of $\alpha = 0.16$ has been suggested in [268]. Overpressurized bubbles containing more He atoms than vacancies disturb the *fcc* matrix by producing self-interstitial clusters and punching out dislocation loops near the bubble-matrix interface. These additional defects form a strong barrier.

Further MD simulations on pure Ni performed in [281] propose a critical void size in nickel where a transition from small voids with weak barrier strengths transition into larger voids with stronger barrier strengths. This critical void size was found to be 2 nm; voids larger than this cause substantial bowing in the leading dislocation entering the void, but voids smaller than this pass through in a relatively straight fashion as shown in Figure 73. For voids > 2 nm, the leading dislocation becomes pinned and the trailing dislocation is temporarily repelled. This is reflected in the rapid increase of stress required for the dislocation to detach from the larger voids and continue its motion shown in Figure 73.

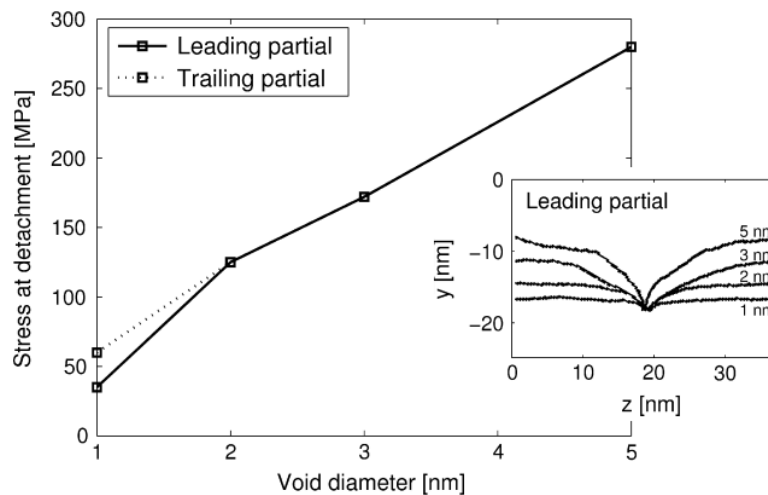


Figure 73. Applied shear stress needed to detach a dislocation from a void in pure Ni and the amount of bowing in the leading dislocation that initially encounters the void [281]

For the Inconel X-750 components studied here, the critical bubble size may be slightly different since this model was developed for voids in pure Ni, but it serves as a good approximation. More helium bubble hardening is predicted in the high temperature components with larger bubbles. Overall, high densities of large bubbles will produce the greatest amount of hardening in Ni-based alloys.

3.3.2.2 γ' Disordering and Dissolution

The coherent and semi-coherent, ordered, secondary phase precipitates γ' and γ'' give the Ni-based superalloys Inconel X-750 and Inconel 718 their high strength at high temperature [196, 197] and excellent creep resistance [198]. During service in reactor, irradiation-induced mixing will destroy the order of the second phase nanoprecipitates. In the γ' phase in Inconel X-750 spacers, Ni_3Ti and Ni_3Al , the Ti and Al solute atoms will be knocked off of their corner atom lattice sites and settle into temporary residence at an interstitial site or a vacant lattice site. At this point, the γ' and γ'' phases are considered disordered; the antiphase boundary contribution to their hardening has been erased. Depending on the irradiation temperature and helium content of the material, ballistic effects may either simultaneously dissolve the precipitates by ballistic effects as they become disordered, or the total dissolution of the secondary ordered phases will be delayed and occur at a higher dose after complete disordering has concluded in a two-step process as thermodynamics drive the atoms to stable lattice positions. Neutron irradiation induced effects on the secondary precipitates in Inconel 718 at an irradiation temperature of 288 °C are depicted in Figure 74. The original γ' becomes distorted at 3.5 dpa and is hard to discern after 20 dpa [282].

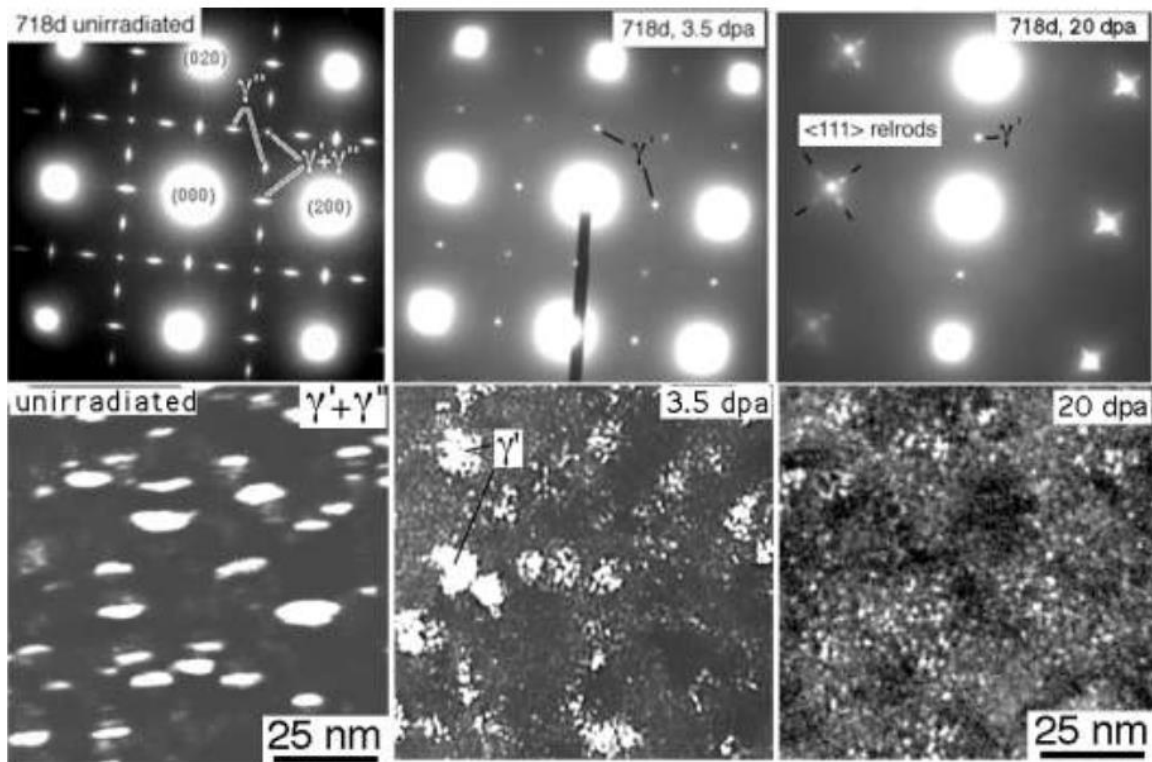


Figure 74. Diffraction patterns and DF TEM images showing the dose-evolved, irradiation-induced destruction of γ' and γ'' up to 20 dpa [282]

Studies on the radiation stability/instability of precipitation-strengthened Ni-Al alloys have first revealed irradiation temperature and dose rate dependencies. Nelson reported that the stability of the γ' precipitates depends on an equilibrium between ballistic radiation effects and radiation enhanced diffusion. At irradiation temperatures below 300-325 °C and dose rates below 10^{-2} dpa/s, Nelson reports γ' to be disordered; at higher irradiation temperatures and dose rates, the precipitates remain intact [283]. A follow up study by Camus found that at a lower dose rate, 10^{-3} dpa/s, three temperature regimes exist. For temperatures $T_{\text{irr}} < 270$ °C, a two-step process occurs where γ' precipitates first disorder (~ 0.1 dpa) and then full dissolution occurs at a higher dose (> 1 dpa). For the temperature range 270 °C $< T_{\text{irr}} < 350$ °C, radiation enhanced diffusion is significant enough to cause reordering and slow down dissolution such that disordering and dissolution occur simultaneously at a higher dose (> 10 dpa). For the highest temperature range, $T_{\text{irr}} > 350$ °C, rather immediate complete dissolution occurs at lower doses. This is illustrated in Figure 76; Camus employed TEM imaging and field-ion microscopy (FIM) to track the progressions of γ' [284]. The measurements of [283, 284] highlight the fact that γ' disordering and dissolution are highly dependent on dose rate because high rates of radiation-induced mixing will not allow adequate time for long range thermal diffusion to occur. Thus, changes in dose rates will cause temperature shifts in the regions in Figure 75.

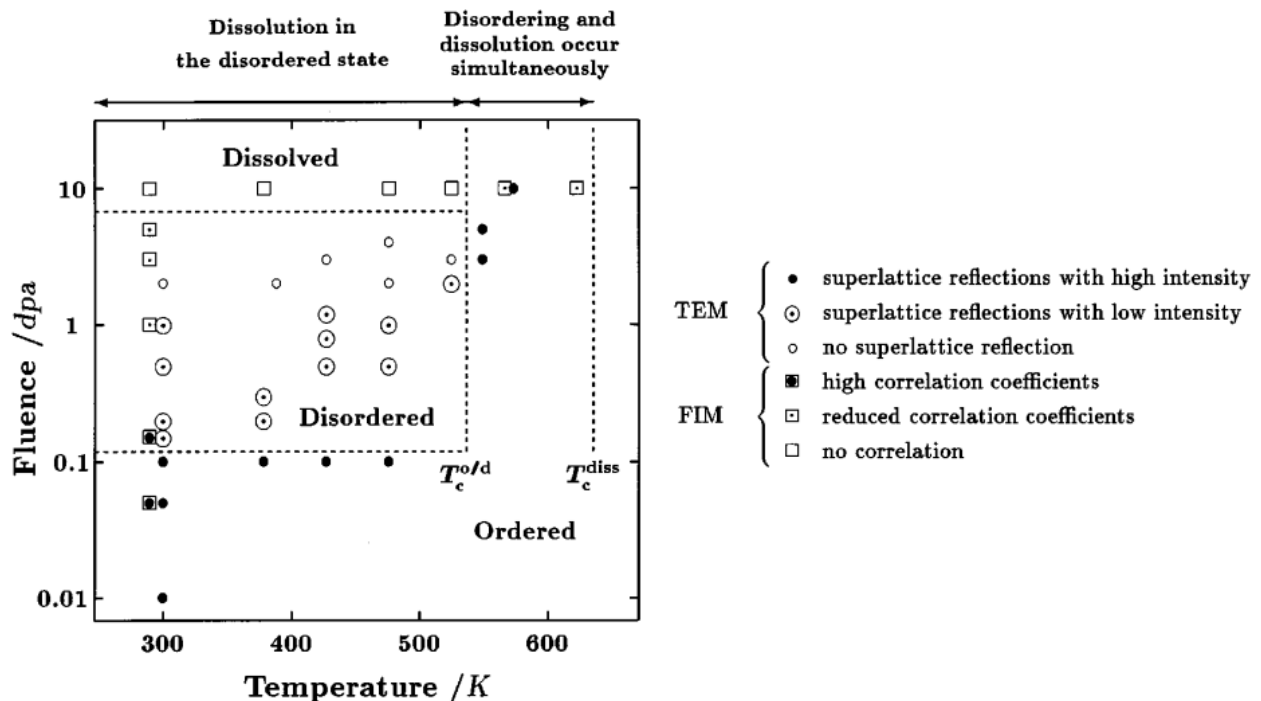


Figure 75. Disordering and dissolution kinetics of γ' precipitates under 300 keV Ni^+ irradiation at a dose rate of 10^{-3} dpa/s [284]

More recently, Zhang irradiated Inconel X-750 with Kr^{2+} ions at a dose rate of 10^{-3} dpa/s up to a maximum dose of 5.4 dpa at irradiation temperatures 60-400 °C [285], and in a subsequent investigation at 500 °C and 600 °C [286]. He then repeated these experiments with Inconel X-750 pre-implanted with 200 appm and 5000 appm helium [274]. The dose evolution of the γ' disordering was tracked by incrementally imaging its superlattice diffraction patterns in the TEM at various doses and irradiation temperatures. The results are shown in Figure 76. Material without helium irradiated at temperatures below 400 °C becomes disordered at a dose slightly below 0.06 dpa, but at higher irradiation temperatures, γ' remained stable up to 5.4 dpa. Helium was found to delay particle disordering; superlattice diffraction spots did not fully vanish until doses > 0.7 dpa for 200 appm material and > 3 dpa for 5000 appm. However, pre-implanted helium specimens maintained the same critical disordering temperature ($T_{critical} = 400$ °C) as the non-implanted specimens.

		No helium								200 appm								5000 appm							
		Temperature, °C								Temperature, °C								Temperature, °C							
		60	200	300	400	500	600			60	200	300	400	500	600			60	200	300	400	500	600		
Dose, dpa	0	•	•	•	•	•	•		Dose, dpa	0	•	•	•	•	•	•		Dose, dpa	0	•	•	•	•	•	•
	0.014	•	•	•	•	•	•			0.014	•	•	•	•	•	•			0.014	•	•	•	•	•	•
	0.058	○	○	○	○	•	•			0.058	•	•	•	•	•	•			0.058	•	•	•	•	•	•
	0.271	○	○	○	○	•	•			0.271	•	•	•	•	•	•			0.271	•	•	•	•	•	•
	0.678	○	○	○	○	•	•			0.678	•	•	•	•	•	•			0.678	•	•	•	•	•	•
	2.711	○	○	○	○	•	•			2.711	○	○	○	○	•	•			2.711	•	•	•	•	•	•
	5.422	○	○	○	○	•	•			5.422	○	○	○	○	•	•			5.422	○	○	○	○	•	•

○: no γ' superlattice diffraction observed
•: γ' superlattice diffraction observed

Figure 76. Irradiation temperature and dose map indicating the nature of irradiated γ' precipitates in Inconel X-750 (non-implanted and pre-implanted with 200 appm He). The irradiation was performed with 1 MeV Kr^{2+} ions at a dose rate of 10^{-3} dpa/s [274, 285, 286]

Investigations of neutron irradiated Inconel X-750 components (54 dpa, 1.7 at% He) studied in this thesis revealed that superlattice diffraction spots have completely vanished for material irradiated at both 180 °C and 300 °C, strongly suggesting that the γ' in the components is completely disordered and that the ordered precipitates are entirely dissolved as depicted in Figure 77 [229].

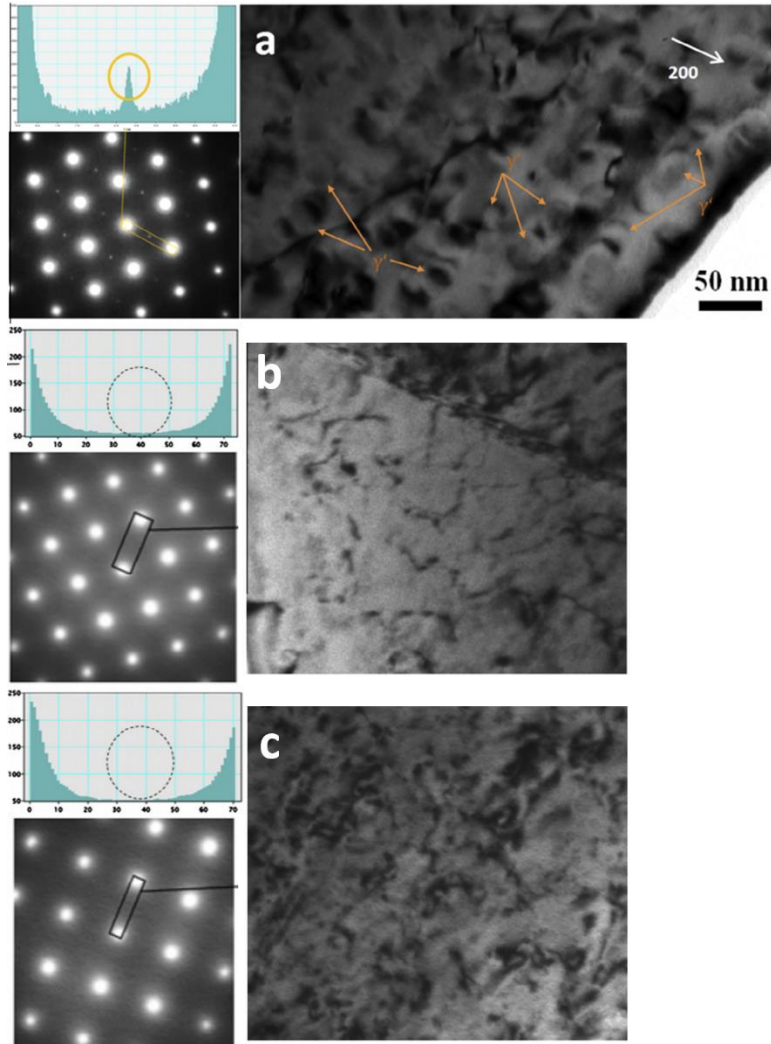


Figure 77. Diffraction patterns taken from Inconel X-750 components (a) non-irradiated and neutron irradiated to 54 dpa and 1.7 at% He at an irradiation temperature of (b) 180 °C and (c) 300 °C [229]

The disordering and dissolution of Inconel 718, precipitation hardened with both γ' and γ'' , as studied in [283] under neutron irradiation at an irradiation temperature of 288 °C and shown in Figure 73, revealed that disordering and dissolution occur separately. Precipitate disordering was noticeable at doses ~ 3.5 dpa but complete dissolution did not occur until doses > 20 dpa. The separate effects of disordering and dissolution on the mechanical properties of the material will be discussed in more detail in the next section.

3.3.2.3 Dose Evolution of Mechanical Properties

Initially, partial disordering occurs in Ni-based superalloys at low doses as the material simultaneously becomes saturated with new radiation defects (dislocation loops, SFTs, microvoids). Even though the γ' and γ'' precipitates have

lost some of their ordering, solute strengthening associated with local Al and Ti concentrations is still present. Some of the potential antiphase boundary hardening contributions are lost, but solution hardening in combination with newly created radiation defects causes an initial increase in hardness and yield strength at low doses ≤ 5 dpa [196, 287-289] as seen in Figure 78.

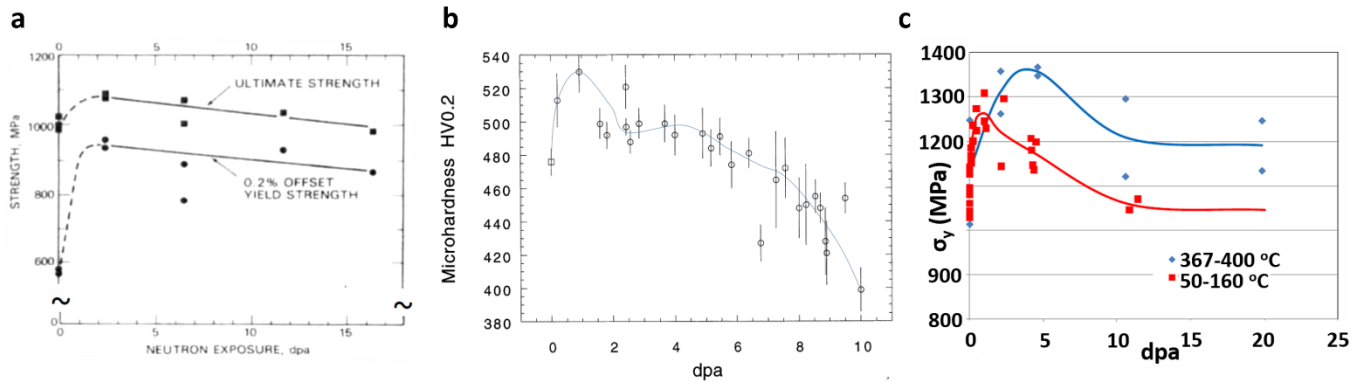


Figure 78. Mechanical properties dose evolution of irradiated, precipitation hardened Ni-superalloys in three radiation environments: (a) Inconel X-750 irradiated in a fast neutron flux of $1 \times 10^{22} \text{ n/m}^2$ in EBR-II at 420-427 °C [196], (b) Inconel 718 irradiated with 800 MeV protons up to a fluence of $3 \times 10^{25} \text{ p/m}^2$ in LAMPF at temperatures < 250 °C [287], (c) Inconel 718 irradiated with 800 MeV protons and spallation neutrons at LANSCE [288, 289]

As the Ni-based alloys are further irradiated, hardening from radiation defects has completely saturated, and the precipitates eventually become entirely disordered, leading to the first signs of radiation softening. At even higher doses, any residual solution strengthening from local concentrations of Al or Ti is erased as the precipitates are dissolved and dispersed throughout the γ -matrix, leading to the largest reductions in the strength of the alloys. Typical mechanical properties evolution of irradiated Ni-superalloys as a function of dose is shown in Figure 78.

Investigations of the mechanical properties of Inconel 718 plates and welds in fast neutron environments in irradiation temperatures 400-430 °C irradiated to doses between 1.5 and 28 dpa by Mills [290] found that any hardening and embrittlement caused by radiation defects saturated at 8 dpa. Yield stresses increased up to a maximum at 7 dpa, and ultimate tensile strengths reached their maximum at 1.5 dpa and began decreasing with increasing dose. In a separate study on the same material in a similar fast neutron environment by Mills and Mastel in [196], shown in Figure 78a, it was similarly found that yield strengths and UTS initially increase at doses ≤ 2.5 dpa, but further irradiation causes gradual decreases in strength.

At high irradiation temperatures, recovery of cold-worked dislocation structures will also play a role in radiation softening, as shown by Garner in 20% cold worked austenitic alloys. Yield strengths decreased proportionally to decreases in dislocation densities with increasing doses at irradiation temperatures > 500 °C [291]. The recovery of the network dislocation structures occurred in a gradual manner, and this decrease in strength with increasing fluence was not experienced by the exact same material in a solution annealed state. Elevated temperatures will cause any cold-worked alloy to recover its network dislocations, but radiation assisted thermal diffusion processes will enhance this process by increasing the concentration of point defects. This enhancement will be slightly offset as point defect clusters and dislocation loops form.

Post-irradiation testing of double-shelled Inconel 718 windows irradiated at the Los Alamos Neutron Science Center (LANSCE) is represented in Figure 78b and 78c [287-289]. The low temperature material depicted in Figure 78c was subjected to a mixture of protons and spallation neutrons up to a total dose of 10 dpa [288], whereas the material in Figure 78b and the material irradiated at a higher temperature in Figure 78c was exposed to the high energy proton beam up to doses of 10 dpa and 20 dpa respectively [287, 289]. Radiation softening at doses beyond several dpa is observed regardless of irradiation temperature, indicative that precipitate disordering and dissolution must factor into the effect, especially for the materials at low irradiation temperatures < 250 °C where irradiation assisted thermal recovery is not activated. Radiation softening does not occur until 5 dpa in the material irradiated at higher temperature, whereas softening begins at 1.5 dpa for the low temperature material. This suggests that saturation of radiation defect hardening does not occur until higher dose and/or some ordered γ' and γ'' is still retained until higher dose in the material irradiated at higher temperature.

Fracture surfaces from three-point bend tests performed on the same Inconel 718 material shown in Figure 78b are displayed in Figure 79. Fracture appears to transition from transgranular, to mixed-mode, to purely intergranular with increasing dose. By ~10 dpa, the irradiated material fractures in an entirely intergranular manner.

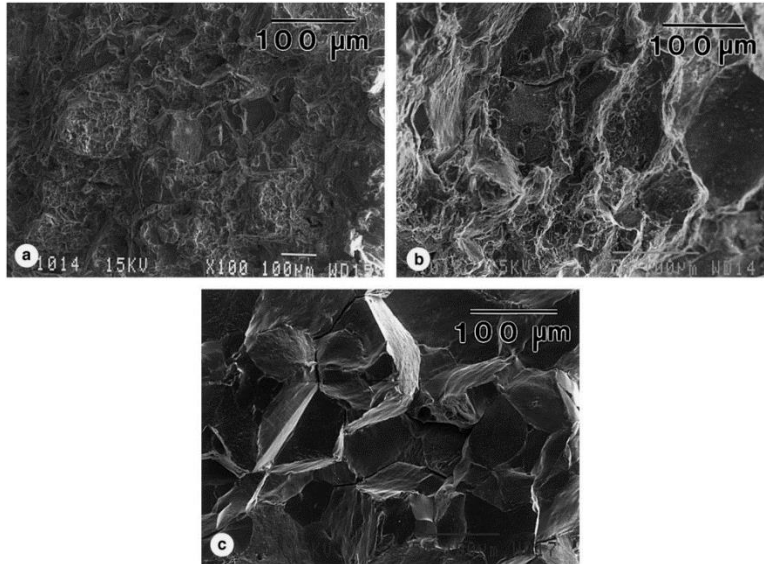


Figure 79. Fracture surfaces from bending specimens cut from Inconel 718 irradiated by 800 MeV protons in LANSCE at temperatures < 250 °C: (a) ~2.5 dpa, (b) ~8.5 dpa, (c) ~10 dpa [287]

Similar evolution in fracture behavior occurs in the Inconel X-750 components in this thesis as shown in Figure 80. A comparison of fracture surfaces from non-irradiated material and material irradiated to 23 dpa at 300-330 °C reveals textbook ductile cup-cone failure transitioning into brittle intergranular failure when tested at room temperature [245].

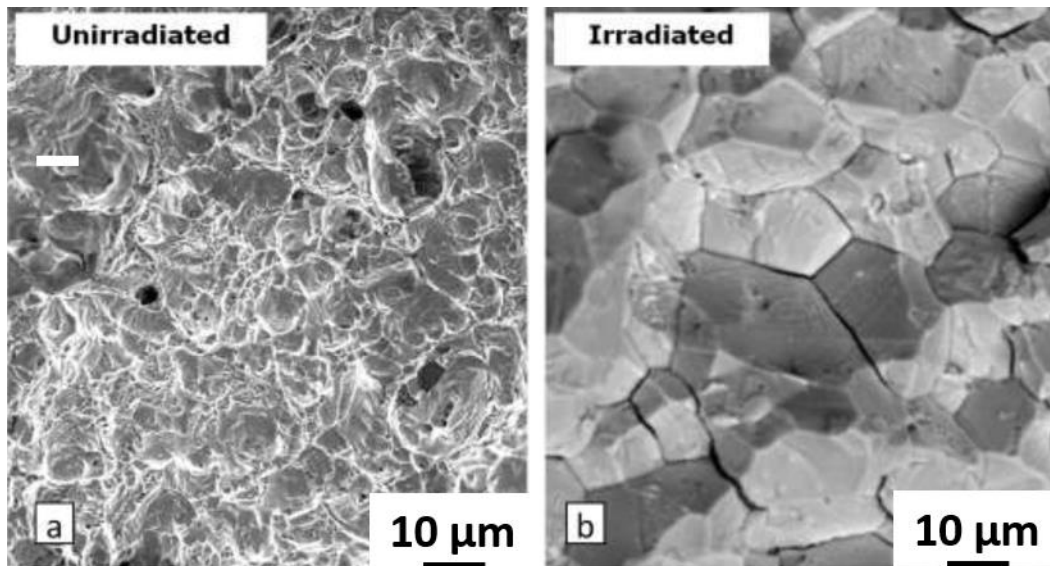


Figure 80. Fracture surfaces of Inconel X-750 components: (a) non-irradiated and (b) irradiated to 23 dpa at 300-330 °C [245]

Irradiation induced embrittlement coupled with irradiation softening is certainly an unusual phenomena. For most metals, irradiation hardening and embrittlement coincide, but as seen in Figure 78b and Figure 79, ductile transgranular failure occurred at the highest strength and lower dose, ~1 dpa, whereas brittle intergranular failure arose at higher dose, 10 dpa, but microhardness values below the hardness of the non-irradiated material [287]. Engineering stress-strain curves of Inconel 718 in Figure 81 quantify ductility reductions in material irradiated with 800 MeV protons and spallation neutrons at 400 °C in LANSCE [289]. The 20 dpa, high temperature material has become severely embrittled to the point where its total elongation is less than 1%. Much like the case of Inconel X-750 components, (p, α) transmutation reactions produce significant levels of helium (~150 appm/dpa [292]). Total helium concentrations are approximately 3000 appm for the material irradiated to 20 dpa, and hydrogen generation is estimated to be 6000 appm [292]. Hydrogen and helium embrittlement most likely play a key role in causing intergranular failure which will be discussed in more detail in the subsequent section.

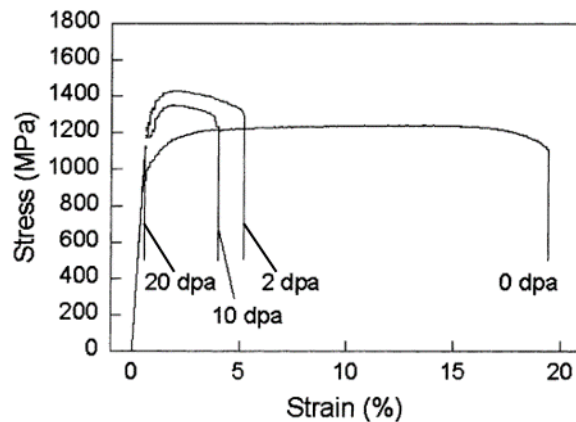


Figure 81. Engineering stress-strain curves from room temperature tensile tests on irradiated Inconel 718 from the LANSCE spallation target (800 MeV protons and spallation neutrons, $T_{irr} = 367-400$ °C) [289]

Because no data has been obtained on Ni-superalloys irradiated beyond 20 dpa, it is unclear whether the radiation softening and embrittlement effects saturate at high doses obtained before end of life conditions are reached. It can be speculated that there exists a critical dose where all ordered nanoprecipitates are completely dissolved and dispersed throughout the matrix such that softening due to their disappearance ends, but helium and hydrogen concentrations in the Inconel X-750 components are continually increasing and could also play dominant roles in mechanical properties evolution at doses beyond 20 dpa.

3.3.2.4 Mechanisms for Grain Boundary Embrittlement

Radiation embrittlement via compromised grain boundaries is a challenging degradation mechanism to manage in core structural components. The rate at which the boundaries become embrittled is difficult to predict and answering how best to quantify this embrittlement is a complex issue. Many mechanisms have been suggested as explanations for how grain boundaries become weakened under irradiation that are of great scientific and commercial interest. Those considered plausible for irradiated *fcc* nickel superalloys in non-corrosive environments like the Inconel X-750 garter springs consist of: helium bubble embrittlement, hydrogen embrittlement, and precipitate effects in and near grain boundaries, and strain localization interactions with grain boundaries.

Helium Bubble Grain Boundary Embrittlement

By far the most significant factor surmised to lead to loss of strength in combination with embrittlement in irradiated reactor core Ni-based alloys is the accumulation of helium that nucleates and grows helium bubbles with increasing dose. Ni-alloys are most susceptible to helium bubble grain boundary embrittlement because of transmutation reactions producing highly elevated levels of helium within the material.

For Ni-superalloys in a CANDU core flux environment, helium generation normally exceeds 300 appm/dpa. This generation rate allows for sufficient mass transport to accumulate helium bubbles within grain boundaries and weaken them. Once the bubbles nucleate within a boundary, additional helium will stabilize them, so it can be postulated that grain boundaries weaken with increased dose due to helium bubble accumulation. A series of helium bubbles have been shown to align the grain boundaries in high dose, 55 dpa, 1.8 at% He, Inconel X-750 components as shown in Figure 82 [227,228].

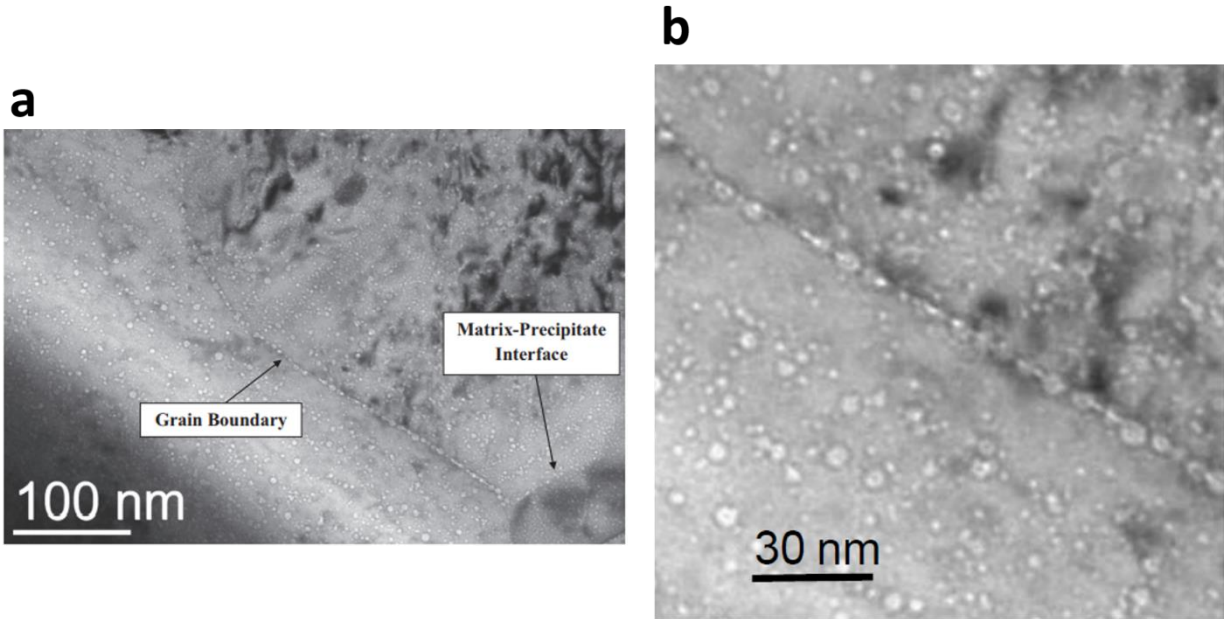


Figure 82. TEM images showing helium bubbles (a) aligning a grain boundary and matrix-precipitate interface of an irradiated Inconel X-750 component (55 dpa, 1.8 at% He, $T_{irr} = 300-330\text{ }^{\circ}\text{C}$) [227] (b) enlarged portion within a grain boundary revealing a zone denuded of cavities adjacent to the boundary indicating that the boundary is a strong defect sink [228]

Hojna has described the mechanism of brittle intergranular failure caused by helium bubble embrittlement as a bubble coalescence process in the very narrow soft zones adjacent to the boundaries as illustrated in Figure 83a [293]. For precipitate hardened alloys such as Inconel X-750, widely spaced carbide precipitates within the boundaries may cause voids/bubbles to nucleate on them, grow, and coalesce together in the precipitate free zones as shown in Figure 83b [294]. If decohesion occurs within the voids/bubbles in the boundary, dimples should exist in the fractured grain boundary. If the dimples are very shallow and difficult to resolve, fracture is more brittle, but if they are large and well defined, ductile intergranular fracture has occurred.

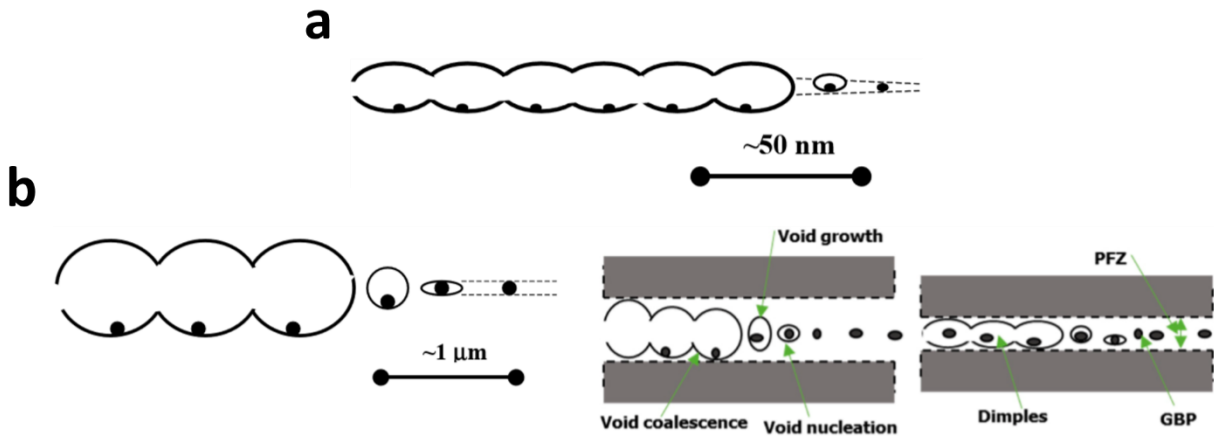


Figure 83. Intergranular fracture mechanisms caused by bubble coalescence within grain boundaries. (a) nano-scale dimpled intergranular fracture [293], (b) ductile dimpled intergranular fracture caused by bubbles nucleating on grain boundary precipitates, growing, and joining, leading to grain boundary decohesion. A wide precipitate free zone (PFZ) is shown in the center and a narrow one on the right. [294]

Several examples exist supporting the models proposed in Figure 83 with materials irradiated at low temperatures $\leq 330^{\circ}\text{C}$ containing relatively low concentrations of helium. Cavities similar to the ones depicted in Figure 82 and Figure 83 are believed to have caused intergranular failure in 20% cold-worked 316SS thimble tubes operating in LWRs irradiated at $290\text{--}325^{\circ}\text{C}$ and 3 [295, 296]. In addition, grain boundary helium bubbles appearing in a Nimonic PE16 Ni-superalloy irradiated in a fast reactor environment to 20 dpa containing 20 appm helium were linked to radiation embrittlement by Boothby [297].

Many materials irradiated at high temperatures ($T_{\text{irr}} > 400^{\circ}\text{C}$) exhibit high densities of helium stabilized bubbles or large voids. The fracture surface of Alloy 600 irradiated in HFIR at 650°C to 8.5 dpa containing 1780 appm helium fractured at room temperature accumulated so much helium on its boundaries that only thin webs of the original metal held the grains together. The helium appears as white strands seen in Figure 84a [298]. Large voids in MA957 ion irradiated with Fe atoms to 500 dpa at 450°C are evident as shown in Figure 84b. There is a soft zone denuded of voids adjacent to a grain boundary seen in Figure 84b, which may make it prone to intergranular failure [299].

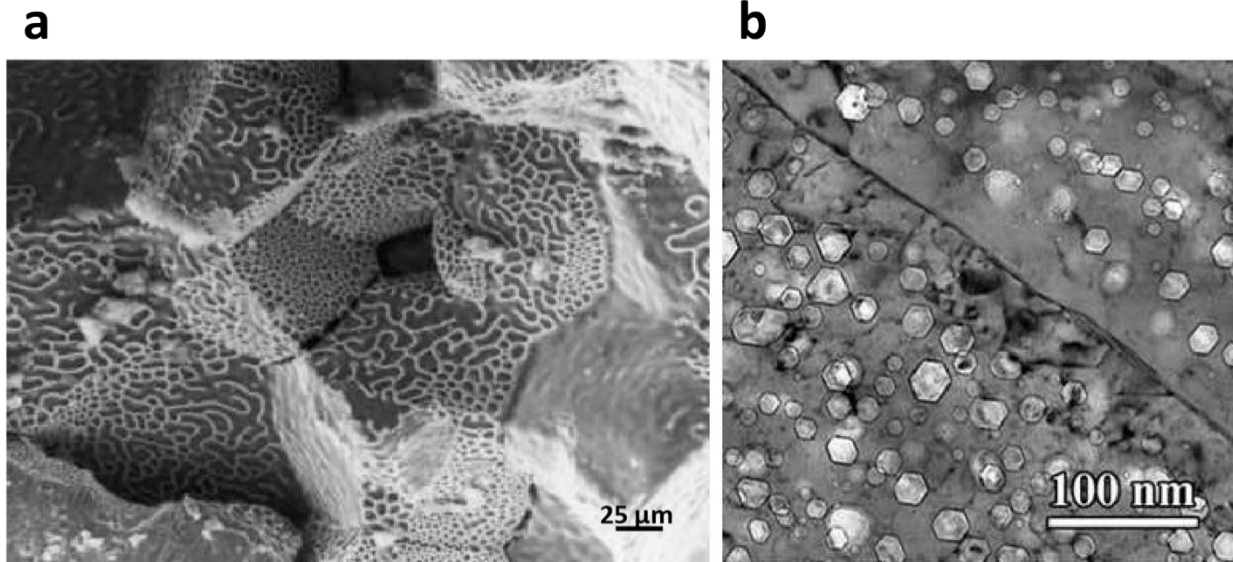


Figure 84. Examples of materials irradiated at high temperatures showing evidence of: (a) helium effected grain boundaries in Alloy 600 irradiated in HFIR to 8.5 dpa at 650 °C containing 1780 appm He fractured at room temperature [298], (b) a soft, denuded zone adjacent to a grain boundary in MA957 Fe atom ion irradiated to 500 dpa at 450 °C with large voids [299].

The pressure state of the helium bubbles can also influence how they embrittle the material surrounding them. An interbubble fracture mechanism for a plane of small, overpressurized bubbles has been developed by Evans to describe how bubbles produced by helium ion irradiation cause surfaces to delaminate [300]. If this plane of tiny bubbles with pressures in excess of equilibrium were to sit within a grain boundary, a tensile stress would be created perpendicular to the boundary. This could lead to tearing of the material along the boundary plane if the bubbles could not punch out dislocation loops or emit self-interstitial atoms due to a high density of radiation defects in the grain interiors of the material. The grain interiors, highly saturated with radiation defects, would need to interact with the overpressurized bubbles to create pressures in excess of the shear modulus of the material for parting of the grain boundary plane to occur. A schematic of the interbubble fracture mechanism along a grain boundary is depicted in Figure 85, adapted from [300]. This phenomena has occurred when hydrogen blisters form in steels, so it is hypothesized as a form of helium bubble grain boundary embrittlement.

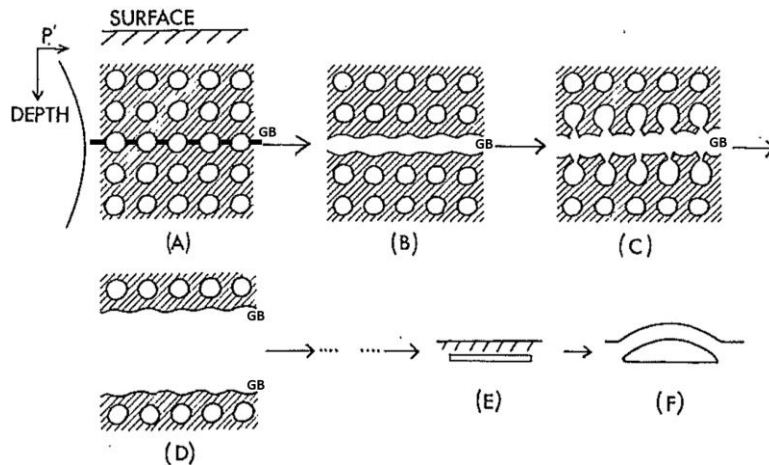


Figure 85. Schematic depicting a grain boundary interbubble fracture mechanism caused by overpressurized bubbles in a hardened matrix, adapted from [300]

Hydrogen Embrittlement

Hydrogen rapidly diffuses such that it is easily taken up from the environment by Ni-alloys. Hydrogen generated in reactor core environments by (n,p) reactions with Fe, Cr, and Ni much like the transmutation reaction previously described involving ^{59}Ni also contributes. Large quantities of retained hydrogen, ~5000 appm, have been measured in pure Ni after it was irradiated to 8.5 dpa and in Inconel 718 after it was irradiated to 10 dpa in the LANSCE facility with high energy protons and spallation neutrons [251, 301, 302]. Determining the exact conditions for hydrogen retention in any nuclear alloy proves challenging because hydrogen atoms are so easily picked up and lost to the surrounding environment. Recent measurements on Inconel X-750 components show retained hydrogen concentrations 250-1500 appm after 19 years in service, suggesting 5-30% hydrogen retention rates [303].

Retained hydrogen must be considered as a potential contributor to swelling and embrittlement. Garner proposed that in materials with a high density of voids/bubbles, the hydrogen is directly stored within the cavities in the form of molecular H_2 [304]. Carbides formed on the grain boundaries of Ni-based metals for the purposes of decreasing their susceptibility to stress corrosion cracking in reactor coolant [305] are susceptible to hydrogen embrittlement [306, 307]. Incoherent carbides are strong hydrogen trapping sites that promote hydrogen storage within grain boundaries. Elevated hydrogen levels inside grain boundaries promote intergranular fracture in Inconel X-750 [306]. Figure 69 indicates that the maximum amount of hydrogen produced by ^{59}Ni transmutations before end-of-life in Inconel X-750 components is 5000-8000 appm of hydrogen. Even though H atoms are extremely mobile interstitials, strong trap sites like grain boundary carbides and He bubbles may

locally retain 5-30% of the hydrogen produced and measured. These hydrogen concentrations may appear trace in comparison to the bulk material, but when locally concentrated have been known to compromise grain boundaries and embrittle the material [306, 307].

Hydrogen charged Inconel X-750 (~1500-3600 appm H) tested at temperatures < 150 °C in air resulted in enhanced low temperature crack propagation and intergranular cracking [308]. The material was held at low temperatures to minimize hydrogen losses, and various testing methods were employed. Non-charged, hot-worked, and aged material produced high toughness, transgranular ductile fracture. Pre-charged material had reduced fracture toughness and failed in an intergranular manner [308].

In-situ tensile testing of hydrogen charged Inconel 725 samples reveals a dual role of coherent $\Sigma 3$ twin boundaries in hydrogen embrittlement [309]. Coherent twin boundaries were found to be most susceptible to crack initiation, which seems counterintuitive considering they provide high strength and corrosion resistance in many alloys. However, coherent twin boundaries were found to be most resistant to crack propagation, indicating that crack initiation and crack propagation are governed by different mechanisms in hydrogen embrittled grain boundaries in Ni-based alloys [309]. Figure 86 shows the role of coherent twin boundaries as preferential crack initiators (single grain boundary cracks observed), whereas randomly oriented high angle boundaries are most likely to propagate intergranular failure (multiple grain boundary cracks observed).

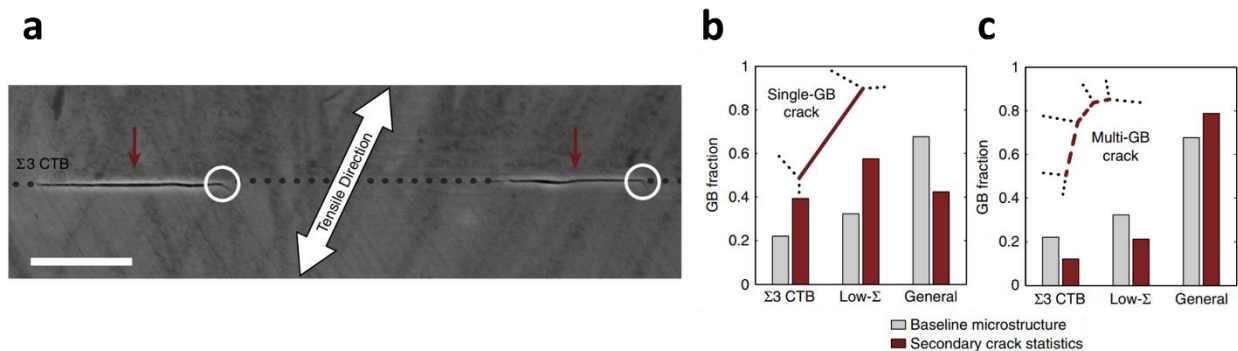


Figure 86. (a) SEM image of two single grain boundary cracks (red arrows) that have initiated along a long coherent twin boundary (dotted line). Neither crack propagates along the entire boundary, but instead both cracks terminate in short segments in the grain interior (white circles). Fraction of grain boundary types that (b) initiate cracks and (c) propagate cracks given by the red bars in comparison to their occurrence in the material (grey bars). Twin boundaries and coincident site lattice low- Σ boundaries more easily initiate cracks, but randomly oriented high angle grain boundaries more easily propagate them in hydrogen charged Inconel 725 [309]

Precipitate Grain Boundary Embrittlement

Segregation of brittle phases at grain boundaries promotes intergranular failure. In four developmental Ni-Fe based superalloys all strengthened with ordered γ' and/or γ'' precipitates as well as the γ' strengthened Nimonic PE16, the precipitates were disordered and dissolved at high irradiation temperatures ($T_{irr} = 425-650$ °C) and found to re-precipitate on and along grain boundaries [310, 311]. Subsequent tensile testing resulted in reduced ductility and intergranular fracture in the brittle phases due to radiation-induced solute segregation that formed continuous or semi-continuous coatings of γ' formed at the grain boundaries [310, 311]. Figure 87 shows a diagram of the brittle grain boundary phase, cleavage failure mechanism linked to grain boundary agglomeration of γ' particles and a dark field TEM image of a grain boundary lined with the ordered precipitates.

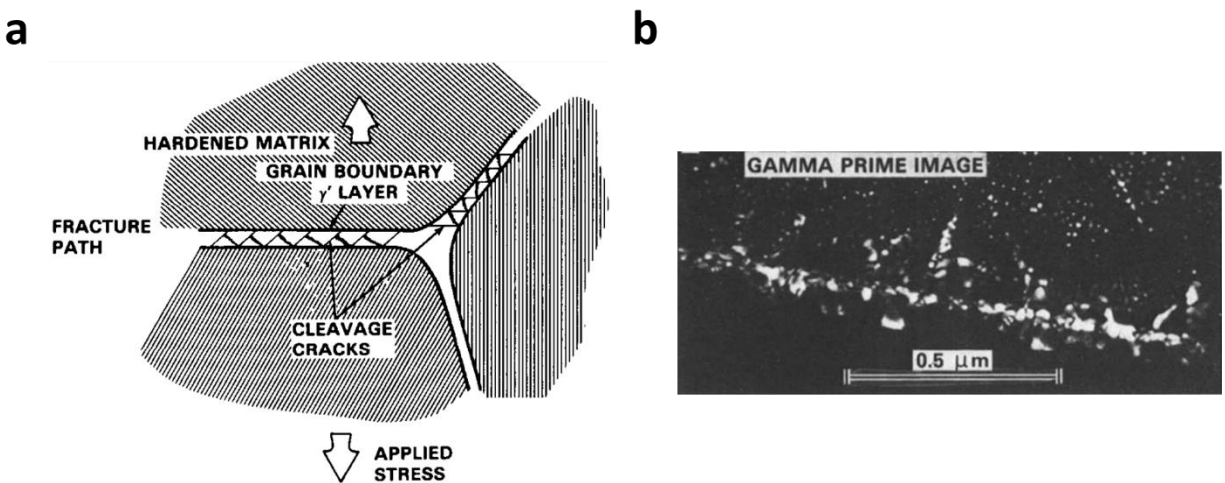


Figure 87. (a) Diagram depicting a brittle, intergranular fracture mechanism associated with γ' grain boundary coatings. (b) Dark field TEM image of a grain boundary lined with γ' from a Nimonic PE15 alloy irradiated at 650°C in a fast neutron fluence to ~ 30 dpa [310, 311]

Strain Localization Interactions with Grain Boundaries

Soft, denuded zones adjacent to grain boundaries seen in Figure 83b in highly irradiated Inconel X-750 components are cause for the consideration of strain localization within them leading to interactions with the boundaries that cause them to fail. One involves strain localization causing dislocation pile-ups at the interface between precipitates and grain boundaries, which would promote void formation in the interface and cracking in the boundary. When slip bands intersect carbides lining the grain boundaries of Ni-superalloys, they cannot easily propagate into adjacent grains and promote pile-up leading to high stress concentrations and cracking. Soft precipitate free zones have been linked to

intergranular failure of non-irradiated Inconel X-750 in the past [312], so similar phenomena are to be expected in irradiated material with denuded zones shown in [227].

Another possibility involving strain localization interaction with grain boundaries involves the formation of dislocation channels in grain interiors that intersect grain boundaries. When dislocation channels interact with grain boundaries, they are bound to produce high stress points and promote grain boundary cracking, especially within boundaries that are already compromised by helium bubbles. Hojna describes a type of mixed mode channel-intergranular fracture that occurs in austenitic steels irradiated at low temperatures $< 360\text{ }^{\circ}\text{C}$ in [313]. In this description it is carefully noted that channel fracture is a transgranular shear fracture that follows a dislocation channel with a plate-like appearance. Even though dislocation channels can exist in all grains in the material, the size of the plate-like facets they create can be comparable to the grain size when they shear, making it difficult to distinguish between channel and intergranular fractures. Figure 88 shows a mixed mode fracture surface from a 15% cold-worked 316SS flux thimble tube irradiated at temperatures $290\text{-}325\text{ }^{\circ}\text{C}$ to 73 dpa and containing 0.07 at% He tested at room temperature [144, 295, 296, 313].

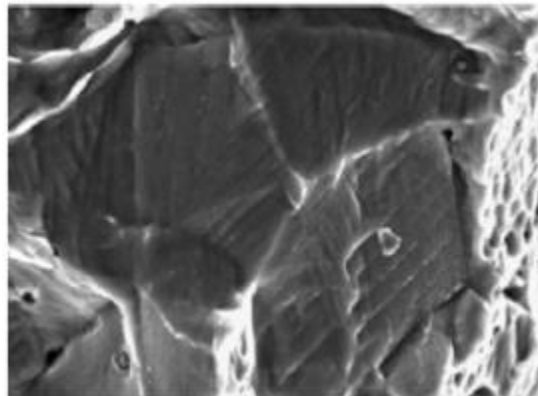
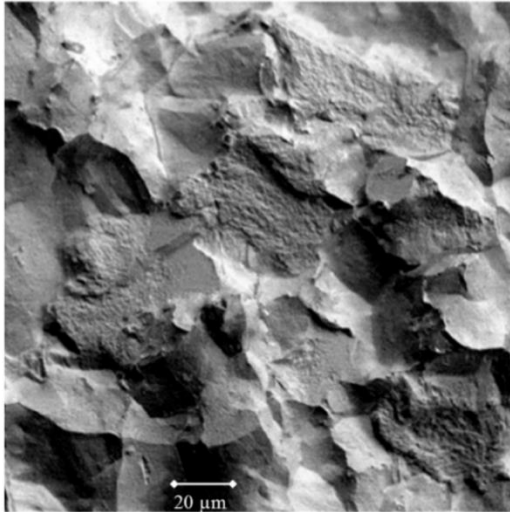


Figure 88. Mixed mode fracture surface with flat channel facets from a 15% cold-worked 316SS flux thimble tube irradiated at temperatures $290\text{-}325\text{ }^{\circ}\text{C}$ to 73 dpa and containing 0.07 at% He tested at room temperature [144, 295, 296, 313]

Intergranular fracture coupled with channel facets was also observed in Russian 18Cr-10Ni-Ti steel after irradiation in BOR-60 at $400\text{-}450\text{ }^{\circ}\text{C}$ to 49 dpa tested at room temperature [314]. The steel contained 3-13% void swelling. Its fracture surface along with a drawing illustrating the scheme of transgranular channel fracture via the shear of bridges linking voids is shown in Figure 89 [313, 314]. The helium bubbles in the grain interiors of Inconel X-750 components may

promote dislocation channeling and the linking of the shear of helium bubbles in a similar fashion until the channel reaches a grain boundary and grain boundary cracking proceeds.

a



b



Figure 89. (a) Fracture surface of 18Cr-10Ni-Ti steel after irradiation in BOR-60 at 400-450 °C to 49 dpa tested at room temperature showing both intergranular and channel facets [314], (b) drawing illustrating the scheme of transgranular channel fracture via shearing of bridges that link up voids [313]

4 Experimental Procedures

4.1 Inconel X-750 Coils

Inconel X-750 coils are precipitation hardened variants of Alloy 600 that first undergo a solution anneal (SA) followed by a single step ageing treatment. The material is deformed prior to the final heat treatment mostly near the outer surface by coiling and surface grinding operations. The nominal chemical composition and heat treatments are shown in Table 4.

Table 4. Chemical composition in wt. % and heat treatments for Inconel X-750 coils [191]

Element	Al	C	Co	Cr	Cu	Fe	Mn	Ni	S	Si	Ti	Nb + Ta
Concentration	0.4-1	.08	1	14-17	0.5	5-9	1	70	0.01	0.5	2.25-2.75	0.7-1.2
Solution Anneal (SA)						1093-1204 °C						
Single Step Ageing						732 ± 14 °C for 16.5 hrs., air cool						

The associated time-temperature-transformation curve for Inconel X-750 can be seen in Figure 90, with the specific treatment used for these coil components highlighted in red.

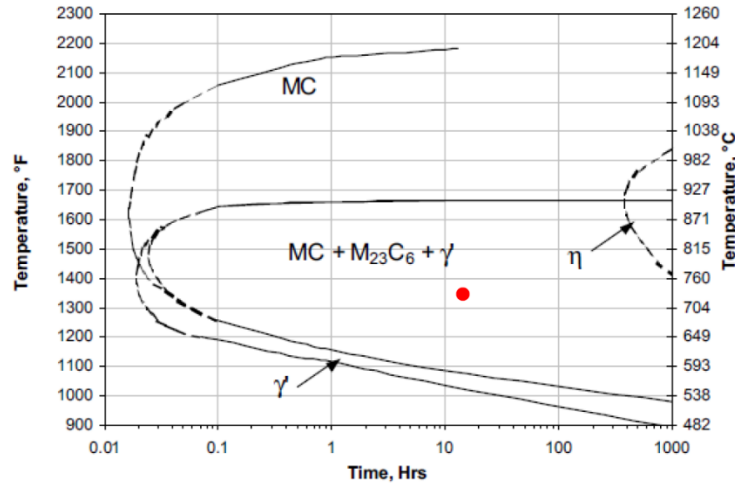


Figure 90. Time-temperature-transformation curves for Inconel X-750 [192]. The red dot indicates the heat treatment performed on the Inconel X-750 coils in this study.

An electron backscattered diffraction (EBSD) map of a cross-section of a coil shown in Figure 91 reveals clear evidence of cold-working. Residual strains on the order of 3% at the inner and outer edges exist, and the region unaffected by the cold working processes is shifted $\sim 100 \mu\text{m}$ towards the inner diameter of the coil.

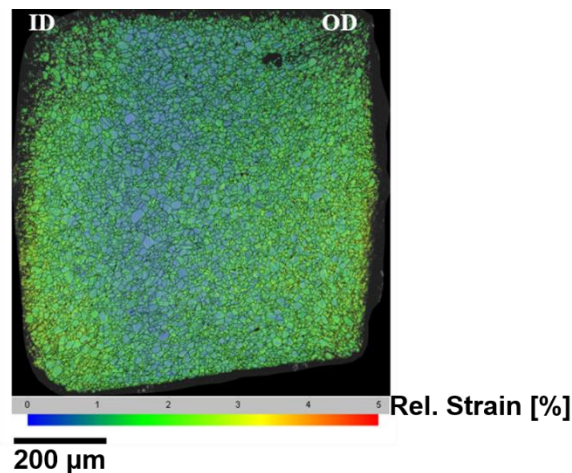
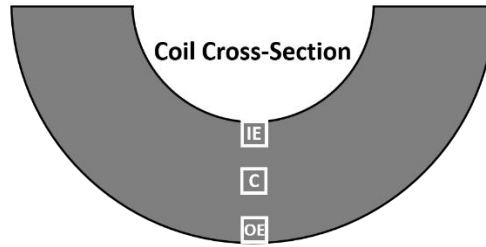


Figure 91. Relative strain map of an Inconel X-750 coil cross-section

More in depth EBSD scans were performed using a Zeiss Ultra Plus SEM with 15 keV e^- and a 300 nm step size to characterize the initial microstructure of the Inconel X-750 springs via three 250 mm x 250 mm area squares: one bordering the inner edge of the spring, one in the center of the spring, and one bordering the outer edge of the spring depicted in Figure 52. Average grain sizes for each square were calculated independently via two methods: the Planimetric method

calculating the number of grains per unit area, and the average grain intercept method using both horizontal and vertical lines, in order to differentiate average grain size in the radial and tangential directions. The overall average grain size for the entire spring via the Planimetric area method was found to be $d = 8.5 \pm 2.9 \mu\text{m}$. Grains were found to be elongated by $1.3 \pm 0.7 \mu\text{m}$ in the tangential direction and $2 \mu\text{m}$ smaller on average in the edge areas compared to the center region. Electron images, EBSD grain orientation maps, and average grain size in the radial and tangential directions can be seen in Figure 92 for all three regions.



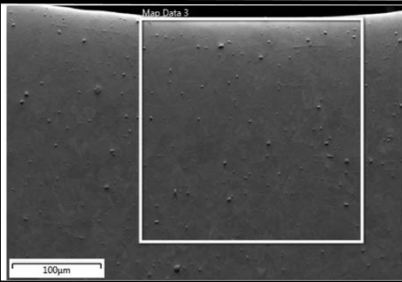
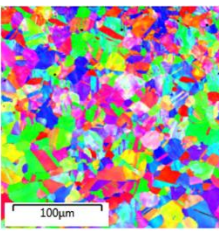
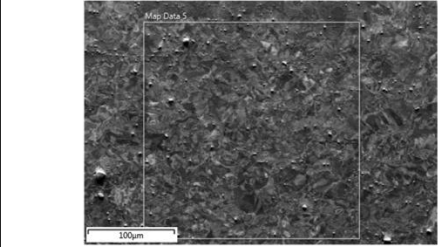
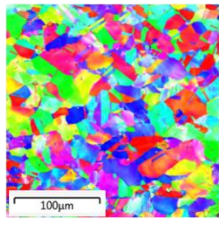
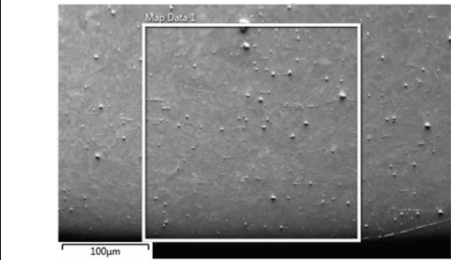
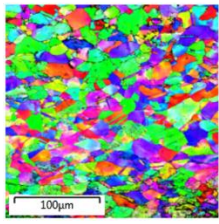
Inconel X-750 Spring Location	e ⁻ Image	EBSD Orientation Map	d _{avg.radial}	d _{avg.tangential}
Inner Edge (IE)			8.4 ± 0.9	8.9 ± 1.0
Center (C)			8.7 ± 0.9	10.4 ± 1.0
Outer Edge (OE)			6.4 ± 0.9	8.1 ± 1.0

Figure 92. Schematic of the sectioned and polished Inconel X-750 coil and Electron Backscattered Diffraction (EBSD) areas. These areas are 250 µm x 250 µm squares of the inner edge (IE), center (C), and outer edge (OE) regions of an Inconel X-750 flat spring. EBSD orientation map grain analysis produces an average overall grain size of 8.5 ± 2.9 µm and indicates grain elongation in the tangential direction.

The processing of Inconel X-750 leads to a rich microstructure. In addition to the *fcc* γ -matrix that contains many solution annealed and deformation twins as seen in Figure 52, blocky micron-sized *fcc* (Ti,Nb)C inclusions forming stringers in the extrusion direction are also evident. Smaller $M_{23}C_6$ (90 wt.% Cr) precipitates < 1 µm are found on the grain boundaries as well as in grain interiors. In addition, 15 nm sized ordered *fcc* γ' Ni_3Al strengthening precipitates

pictured in Figure 93 are non-uniformly distributed throughout the material. The lattice parameter difference between the matrix and γ' precipitates is 0.5%. An η -phased Ni_3Ti precipitate can be seen on grain boundaries as shown in Figure 93, especially near the outer surface [193].

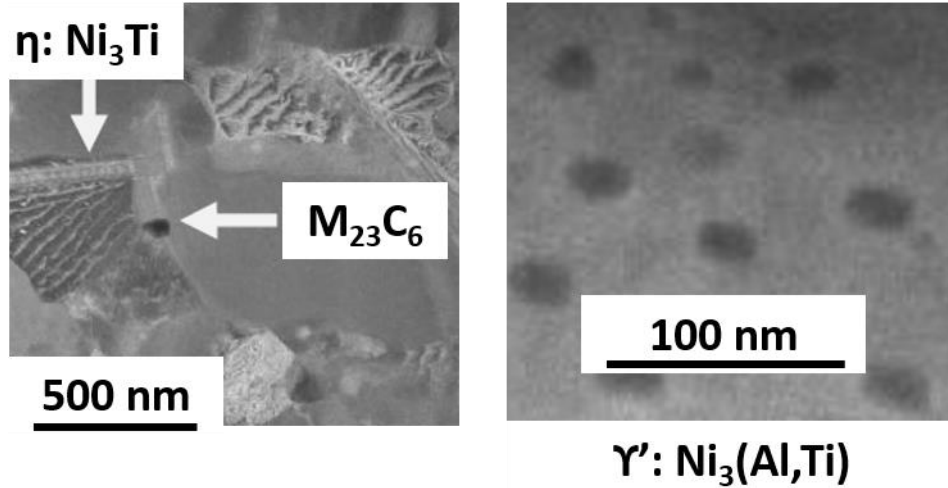


Figure 93. Some common precipitates found in Inconel X-750 including η -phase Ni_3Ti and M_{23}C_6 carbides (left) and the ordered strengthening nanoprecipitates, γ' (right) [193]

Chemical, physical, as well as known mechanical properties of Inconel X-750 wire heat treated in a similar fashion to the coiled components in this study can be found in Table 5 [191].

Table 5: Room Temperature Properties of Inconel X-750 [191]

Standard Atomic Weight	59.2323 amu
Density	8.28 g/cm ³
Melting Point	1393-1427 °C
Thermal Conductivity	12 W/m°C
Tensile Yield Strength	972-1096 MPa
Ultimate Tensile Strength	1393-1407 MPa
Total Elongation	16%
Young's Modulus	215 GPa
Shear Modulus	80 GPa
Poisson's Ratio	0.29
Hardness	1186 MPa
Lattice Type	Face-centered cubic (fcc)
Burgers vector of γ -matrix	0.252 nm [194]
Burgers vector of alloy	0.35607 nm
Stacking fault energy	40-70 mJ/m ² [195]

4.1 Ex-Service Neutron Irradiated Inconel X-750

Core Inconel X-750 material removed by station operators for routine surveillance by the utilities was shipped to Canadian Nuclear Laboratories (CNL) for a variety of post-irradiation experiments to be performed. The ex-service material was sectioned using the Fuel and Materials Cells (FMC) at CNL into pieces less than 1 mm x 1 mm x 0.25 mm with a diamond saw, mounted in epoxy holders and mechanically ground and polished to a mirror finish inside of the FMC at CNL. Two sections of two garter springs were then donated and shipped to the Nuclear Science User Facility (NSUF) sample library at Idaho National Laboratory (INL) and subsequent work was performed as part of the U.S. Department of Energy (DOE) Rapid Turnaround Post-Irradiation Experiments (RT-PIE) program with the University of California Berkeley. Three sections from two ex-service annulus spacers were shipped to the Canadian Centre for Electron Microscopy (CCEM) at McMaster University to be prepared and donated to the University of California Berkeley for PIE experiments.

Sections of the components were obtained from both low temperature pinched material ($T_{irr} = 120-280$ °C) and high temperature non-pinched material

($T_{irr} = 300-330 \text{ }^{\circ}\text{C}$) at all three unique irradiation conditions. Table 6 and Figure 94 display the specific radiation environments associated with each of the three ex-service components in terms of dose received and H and He produced via transmutations. The associated fuel channel pressure tube temperature and neutron flux profiles ($E_n > 1 \text{ MeV}$) from which the spacers were extracted are given in Figure 95. The spacer irradiated to the highest dose is a non-optimized spacer, whereas the others are optimized spacers. The non-optimized material saw a much lower total flux and the optimized coils had very similar flux and temperature profiles.

Table 6. Ex-Service Neutron Irradiated Inconel X-750

ID	Type		EFPY	dpa	He (appm)	H (appm)	$T_{irr-max} \text{ (}^{\circ}\text{C)}$
A	Optimized	LT	14.25	54	17391	3705	268
		HT					319
B	Optimized	LT	18.82	67	21381	4571	249
		HT			21283	4549	327
C	Non-Optimized	LT	22.63	81	25600	5511	244
		HT					321

***EFPY = Equivalent Full Power Years**

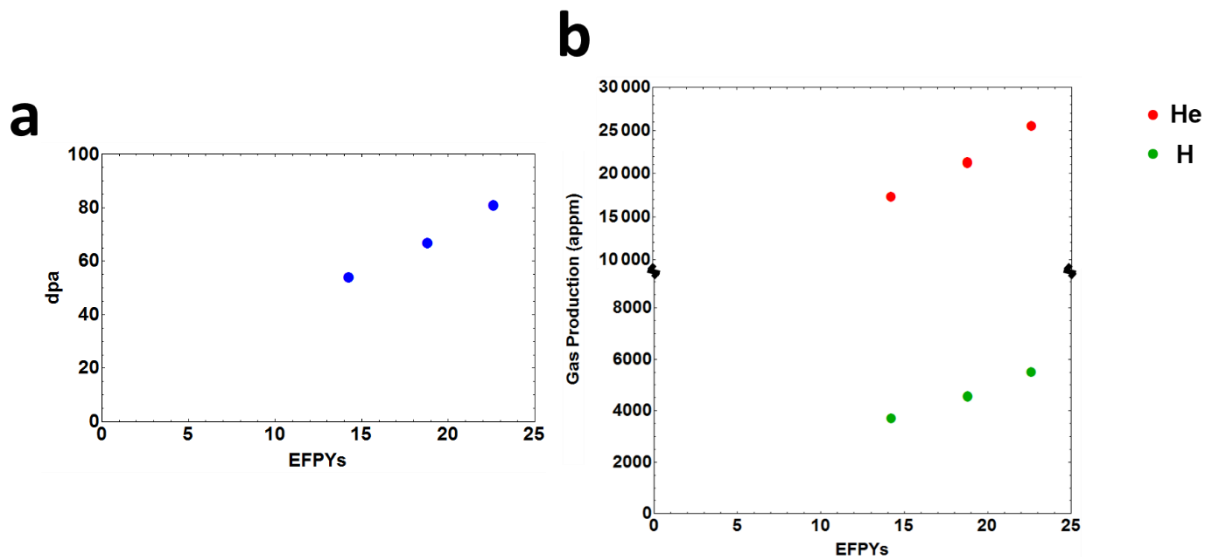


Figure 94. (a) Displacement damage and (b) gas production in the ex-service Inconel X-750 material used for micro-mechanical testing

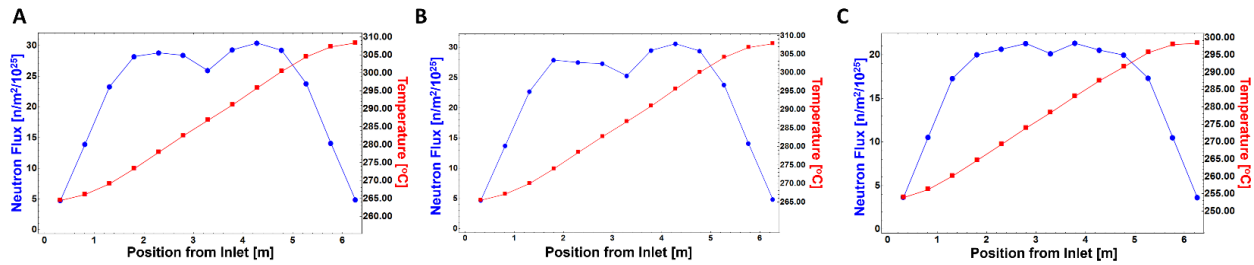


Figure 95. Pressure tube temperature profiles and neutron flux profiles ($E_n > 1$ MeV) associated with the Inconel X-750 spacers extracted for micro-mechanical testing

4.2 Sample Preparation

4.2.1 Sample Preparation of Non-Irradiated Inconel X-750

An optimized, non-irradiated Inconel X-750 coil was sent to the University of California Berkeley to be used for baseline micro-mechanical testing. A “C-shaped” link from this coil shown in Figure 93 was sectioned using a high speed diamond saw and mechanically polished flat to a mirror finish according to the Struers© recommendations given in Table 7, which was specifically developed for polishing Ni-based superalloys.

Table 7. Struers Polishing Formula for Preparing Ni-Based Superalloys

Table 1 - Contemporary Preparation Method for Superalloys

Step	Surface	Surface	DP	DP	DP	OP
Surface	SiC Paper	SiC Paper	MD-Dur	MD-Dac	MD-Dac	MD-Nap
Abrasive	SiC	SiC	DP-Suspension	DP-Suspension	DP-Suspension	OP-A
Grit Grain Size	180 grit	220 grit	9 μ m	3 μ m	1 μ m	
Lubricant	Water	Water	Green/Red	Green/Red	Green/Red	
[rpm]	240-300	240-300	150	150	150	120-150
Force [N]	25	25	25	25	25	25
Time [min]	Until Planar	1	8	6	5	3

Preparation Method for Nickel and Ni-Base Superalloys; for superalloys, one SiC step is adequate and the 1- μ m step is not needed for solution annealed and aged specimens, but may be needed for solution annealed specimens.

Ni-based superalloys are susceptible to the same etching problems as austenitic, ferritic and duplex stainless steels when polished by colloidal silica and etched with reagents containing Cl⁻ ions.

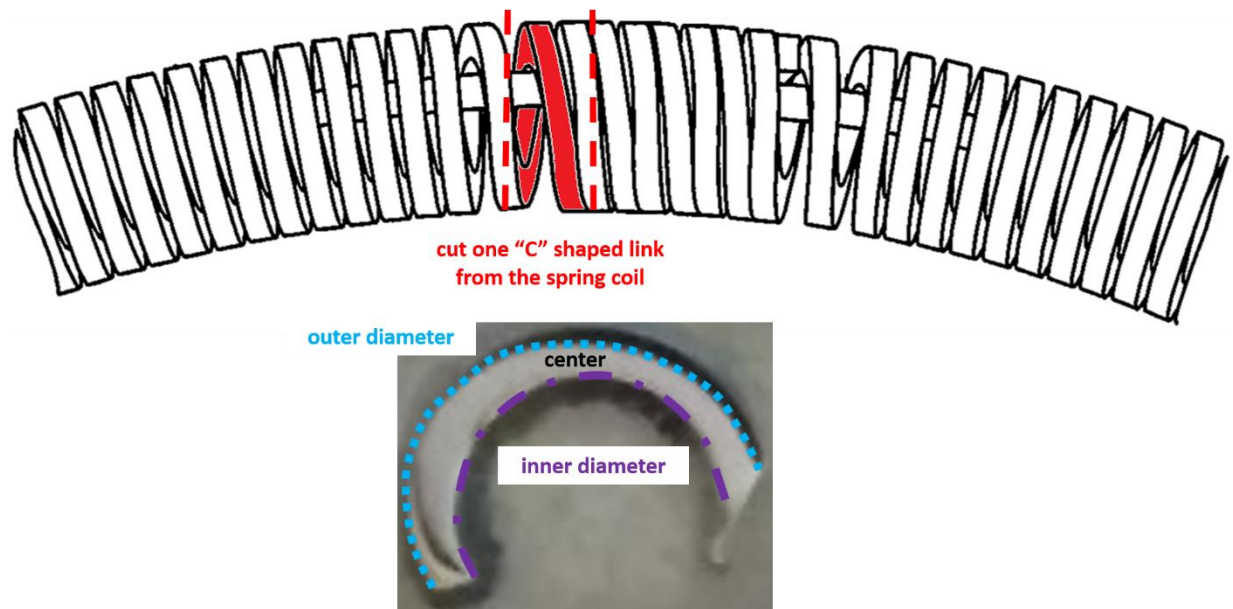


Figure 96. Sectioning of Inconel X-750 link from a non-irradiated coil

Micro-mechanical test specimens in the form of three-point bend specimens and micro-tensile specimens were taken from both edge regions within 10 μm of the inner diameter and outer diameter as shown in Figure 96 as well as from the center of the spring wire.

Non-irradiated, micro-mechanical specimens extracted from the center of the coil required a double lift-out process in order for their bottom surfaces to be perfectly flat and flush with respect to their testing sites, such that accurate stress values can be calculated. Therefore, initial lift outs using an Oxford OmniProbe nanomanipulator were performed to extract larger foils that were temporarily mounted on 3mm TEM grid posts. These larger foils are then further shaped into micro-mechanical specimens that have perfectly flat bottoms using an in house machined 90° SEM holder and the FIB, lifted out a second time, and placed onto their appropriate testing sites.

4.2.2 Sample Preparation and FIB Milling of Neutron Irradiated Inconel X-750

Sectioned spacers donated to the NSUF sample library were further prepared at the Materials Fuels Complex (MFC) in Idaho National Laboratory (INL) using an in-house etching process in attempts to reveal their grain boundary structures. A FEI Quanta 3-D Focused Ion Beam (FIB) and Oxford OmniProbe at Idaho National Laboratory (INL) were used to extract 40 μm x 20 μm x 10 μm foils with grain boundaries centered within the top surfaces of the foils. Material was taken from both the center and edge regions of the irradiated springs as shown in Figure 97. Pre-fabricated slots were cut into molybdenum lift-out grids using the FIB and the lifted-out foils were adhered to these sites using the platinum-based gas injection system (GIS). These large foils were then shipped to UC Berkeley

for further preparation unique to the type of micro-mechanical test to be performed, which will be discussed in subsequent sections.

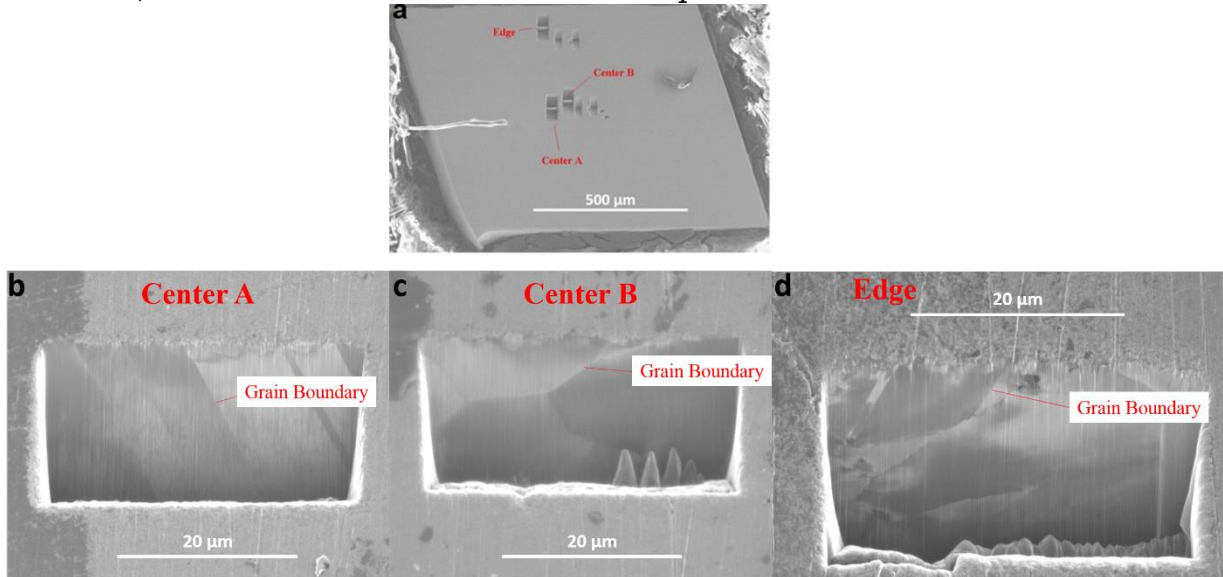


Figure 97. Foil extractions from a representative ex-service spacer. (a) Cross-section of an Inconel X-750 spring showing FIB milled foils of material taken from both edge and center regions of the spacer, higher magnification images of the (b) Center A foil, (c) Center B foil, and (d) Edge foil. The grain boundary revealed along the top surface by the etching process is highlighted.

Sections of spacers sent to the CCEM were FIB milled with a Zeiss NVision 40 to extract lamella approximately $20\ \mu\text{m} \times 20\ \mu\text{m} \times 4\ \mu\text{m}$ in size from the center of the ex-service material mounted in cross-section. The resulting lamella prepared to be lifted out are shown in Figure 98.

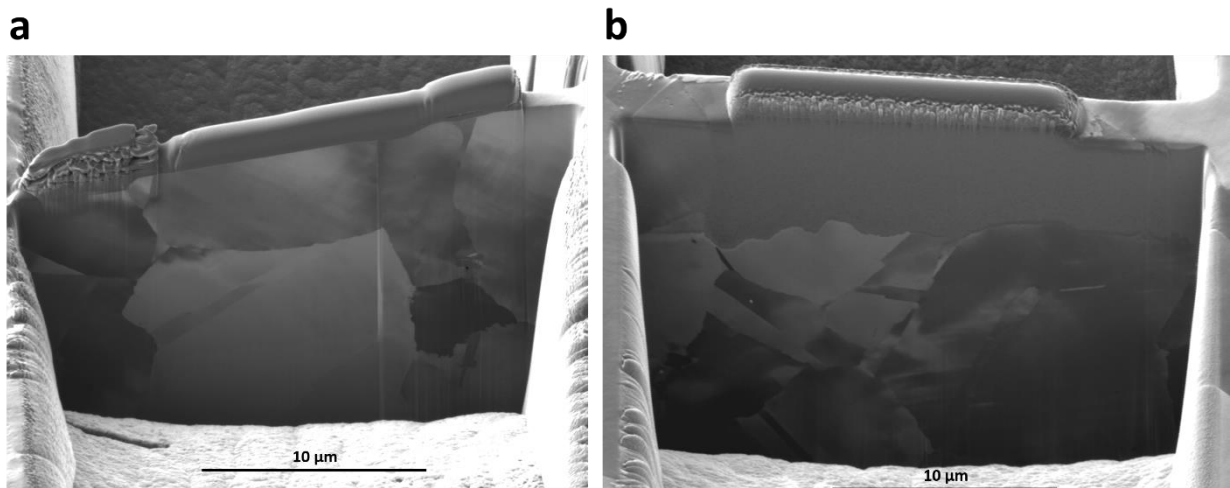


Figure 98. 77 dpa, 2.4 at% He Inconel X-750 foils extracted from bulk samples at CCEM for micro-mechanical testing: (a) pinched and (b) non-pinched

4.3 Bulk Component Crush Testing

A portion of each irradiated annulus spacer approximately 20 coils long from both the pinched, low temperature region ($T_{\text{irr}} = 120\text{-}280\text{ }^{\circ}\text{C}$) and non-pinched, high temperature region ($T_{\text{irr}} = 300\text{-}330\text{ }^{\circ}\text{C}$) was sectioned using a diamond saw inside the Fuel and Materials Cells (FMC) at CNL. A non-irradiated equivalent length of material was prepared to obtain a baseline mechanical test. A modified MTS Insight 50 device shown in Figure 99a crushed the 20 coil long sections between two hardened tool steel plates as shown in Figure 99b at a displacement controlled rate of 0.025 mm/min until they fractured. These tests were performed inside of the FMC. Load-displacement curves were generated in units of Newtons per coil versus millimeters of displacement.

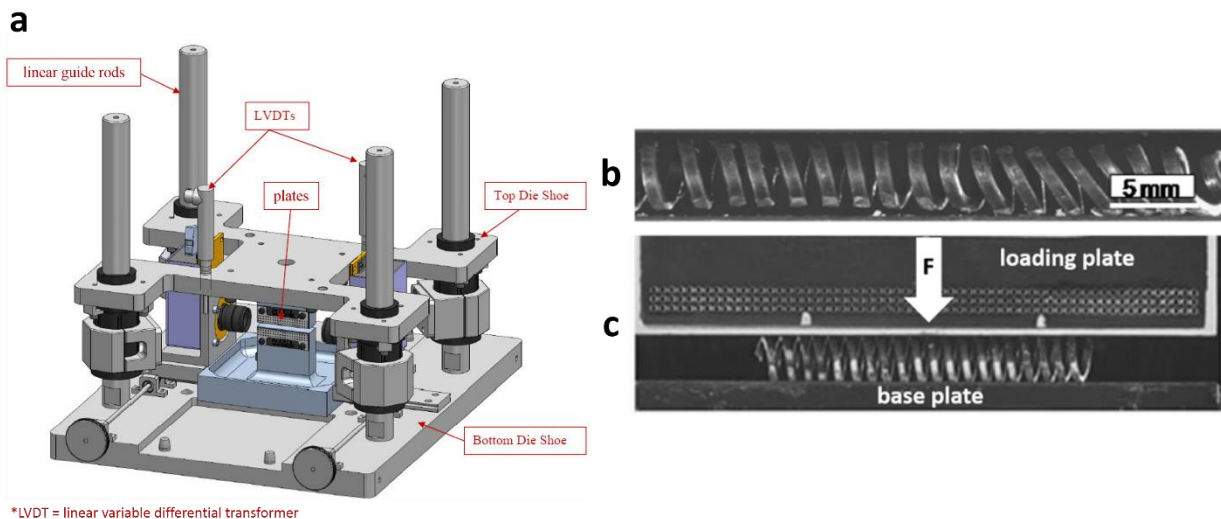


Figure 99. Bulk crush testing of Inconel X-750 annulus spacers. (a) modified MTS Insight 50 testing apparatus, (b) post-test coil, (c) close-up view of testing rig pre-test depicting the loading direction

4.4 Microhardness Testing

Vickers hardness testing was performed on the non-irradiated and ex-service material after it was sectioned into pieces less than 1 mm x 1 mm x 0.25 mm with a diamond saw, mounted in epoxy holders and mechanically ground and polished to a mirror finish inside of the FMC at CNL at a load of 500 gf. Twelve Vickers indentation microhardness values were obtained from each specimen at each irradiation condition (dose and irradiation temperature) according to ASTM standard E384, requiring that indents be spaced apart at least 2.5 times greater than their diameters and that the centers of all indents remain greater than 2.5 times their diameter in distance away from all edges of the sample.

4.5 In-Situ Micro-Three-Point Bend Testing

Micro-three-point bend specimens were fabricated from 54 dpa and 67 dpa specimens operating at average irradiation temperatures of both 180 °C and 300°C. Irradiated specimens from both the edge and center of the spacer, as shown in Figure 94a, were extracted. In addition, non-irradiated specimens were removed from both the outer edge and center of the “C-shaped” coil pictured in Figure 93. In order to obtain multiple tests for each irradiation condition and conserve material for micro-tensile tests, two to five specimens were made from material with a specific dose, irradiation temperature, and location (center or edge).

4.5.1 Micro-Three-Point Bend FIB Specimen Preparation

Three-point bend specimens were manufactured from the large foils previously prepared at the MFC at INL using an in house machined 90° SEM holder inside a FEI Quanta 3D FEG with a Ga⁶⁹⁺ FIB. Initially, larger milling currents (3-7 nA) were used to cut rough beams of approximate dimensions 20 μm x 7 μm x 7 μm. Resulting bar shapes cut into the large foil can be seen in Figure 100a.

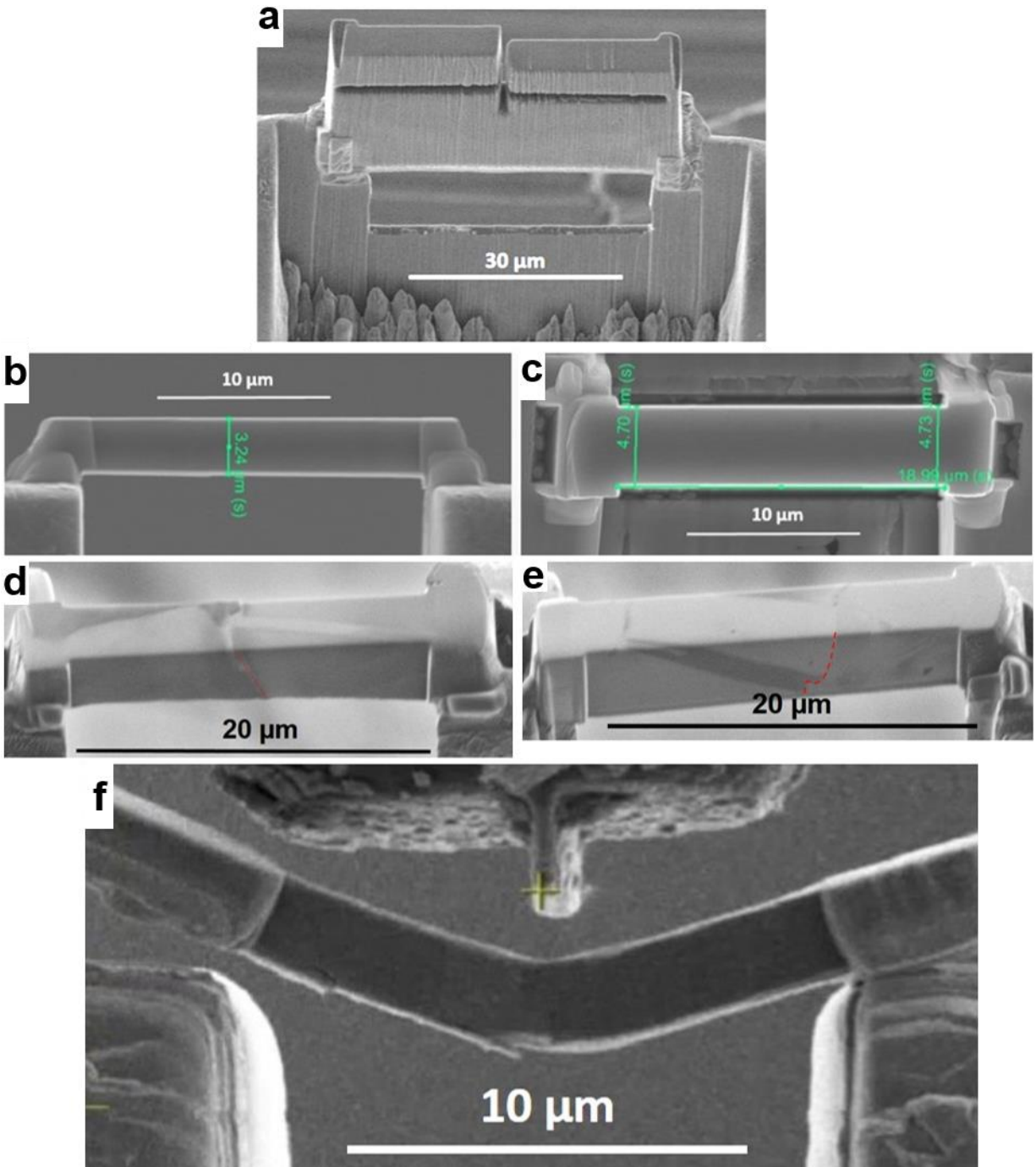


Figure 100. (a) resulting bending beam structures cut into the large lift-out foil which has already been removed from the bulk spring (b) side view of a finished three-point bend specimen (c) top view of a completed three-point bend specimen, (d) and (e) FIB ion channeling contrast images depicting grain boundaries propagating approximately straight down through the thickness of the specimens, and (f) bending specimen becomes unconstrained similar to a standard three-point bend test during loading

Each bar specimen similar to the two shown in Figure 97a was subsequently lifted out using an OmniProbe 200 Nanomanipulator and mounted on a pre-fabricated bridge test site as shown in Figure 97b. The pre-fabricated, bridge test sites were FIB manufactured from Mo 3 mm TEM grid posts by first flattening the top of the post and then milling an open valley to form a bridge for the three-point bend specimen to lie across. The lift-out bars were attached using the Pt GIS and final polishing occurred using smaller milling currents (100 pA-1 nA). The amount of Pt GIS deposition was kept to a minimum in an attempt to reduce its effect on the three-point bending stress state. However, this attachment is required in order to prevent the loss of samples during the mounting process and/or transfer between FIB milling and testing. This process and an example of a finished three-point bend specimen can be seen in Figure 97. The final three-point bend specimens were approximately 15-20 μm in bending length and 3-5 μm in width and thickness.

4.5.2 Electron Backscattered Diffraction Pre-Test Analysis

Each micro-bend specimen was analyzed using EBSD on its top surface using an acceleration voltage of 30 keV, electron current of 48 nA, and step size ≤ 50 nm in order to map each sample's initial microstructure, identify grain boundaries, and determine grain orientations. The individual specimens were found to contain between one and five grain boundaries. Grain orientations at the bottom surface of the specimens would be more accurate, but performing EBSD on the bottom surface of the specimens is impossible due to shadowing from sample supports. However, Focused Ion Beam (FIB) ion channeling contrast images of the front and back sides of the specimens were obtained in order to ensure that grain boundaries propagated approximately straight down through the thicknesses of the specimens. Representative FIB ion channeling contrast images of the sides of polished bending specimens with grain boundaries clearly visible can be seen in Figures 100d and 100e. Using these grain orientation maps, the *hkl* orientations, grain rotation, and highest Schmid factor of the preferred slip system(s) for each grain was calculated for the outward tensile stress direction at the bottom of the specimens. In addition, misorientation angles between two grains were measured. A representative depiction of the pre-test microstructural analysis can be seen in Figure 101. Nearly all grain boundaries in the specimens that were not twin boundaries were measured to be high angle grain boundaries with misorientation angles greater than $\sim 28^\circ$. Table 8 gives the root mean squared (RMS) absolute and normalized grain rotation within a single grain interior for specimens at each irradiation condition. Normalized average grain rotations exceed 1 degree/ μm in edge specimens for both non-irradiated and high dose conditions. This indicates that grains at the edges of the component are more heavily deformed (by at least 0.4 degrees/ μm)

due to cold-working and grinding manufacturing processes, whereas grains in the center of the component are much less deformed.

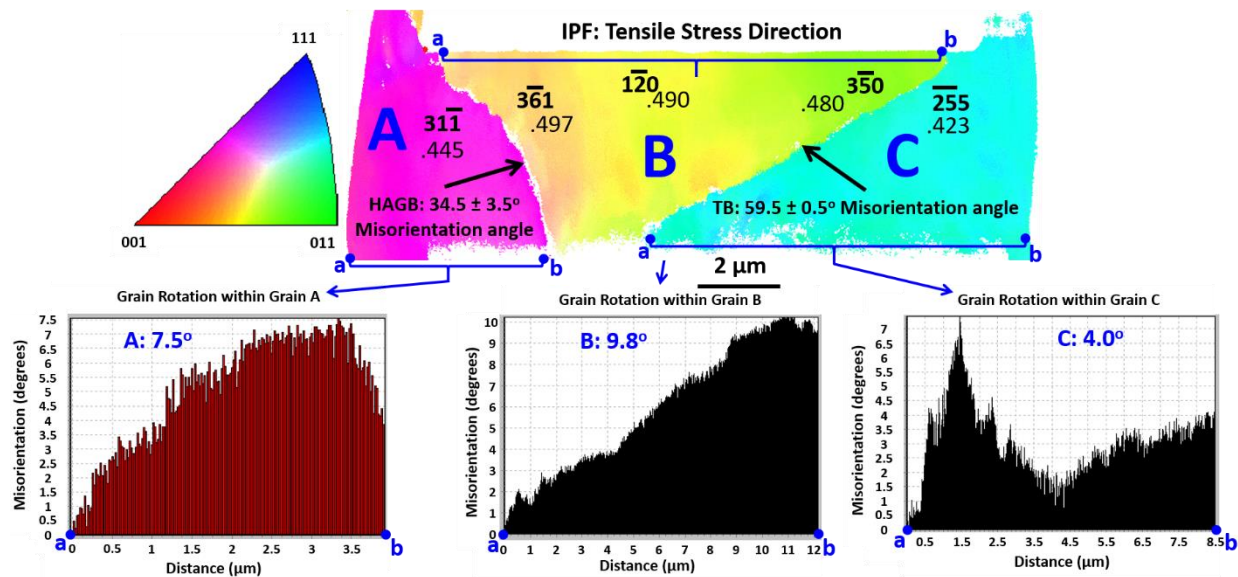


Figure 101. Pre-test Electron Backscattered Diffraction (EBSD) on the top surface of a representative three-point bend specimen including an Inverse Pole Figure (IPF) grain orientation map in the tensile stress direction for the outer fiber of the specimen, hkl orientation of individual grains, misorientation angles across grain boundaries, grain rotation within each grain measured along a horizontal line segment left to right from point a to point b, and highest Schmid factor of the preferred slip system(s) within each grain

Table 8. Root-Mean-Squared Absolute and Normalized Grain Interior Misorientations of Inconel X-750

Irradiation Condition	Non-Irradiated		53 dpa $T_{avg} = 180^\circ \text{C}$	53 dpa $T_{avg} = 300^\circ \text{C}$	67 dpa $T_{avg} = 180^\circ \text{C}$		67 dpa $T_{avg} = 300^\circ \text{C}$	
	Edge	Center	Center	Center	Edge	Center	Edge	Center
θ_{rms} (degrees)	$5.4^\circ \pm 4.5^\circ$	$5.2^\circ \pm 2.0^\circ$	$3.4^\circ \pm 1.9^\circ$	$2.5^\circ \pm 1.7^\circ$	$6.5^\circ \pm 3.2^\circ$	$2.6^\circ \pm 1.3^\circ$	$6.7^\circ \pm 2.1^\circ$	2.3 ± 0.9
θ_{rms}/L (degrees/ μm)	2.4 ± 5.2	0.6 ± 0.4	0.1 ± 0.1	0.4 ± 0.3	1.7 ± 1.4	0.5 ± 0.2	0.6 ± 0.3	0.2 ± 0.1

4.5.3 Testing Procedures

Two to five specimens made from both center and edge regions of a non-irradiated spring and 67 dpa irradiated spring, and from the center of 53 dpa springs were bent at their centers under vacuum in a FEI Quanta 3D FEG using a Hysitron PI 85 Picoindenter. The actuator was equipped with a custom made 1 μm thick and 12 μm wide diamond wedge punch. Two sets of irradiated specimens were produced and tested; the first set from material with a low irradiation temperature (180 $^\circ\text{C}$) and the second from material with a high

irradiation temperature (300 °C). Videos were recorded for all tests for further analysis using the Scanning Electron Microscope (SEM) on the FEI Quanta 3D FEG. All tests were performed in displacement controlled feedback loop mode at loading and unloading rates of 10 nm/s to maximum strains larger than 10% or until noticeable plastic deformation occurred. Equivalent strain rates were between 1×10^{-3} and 2×10^{-3} . In order to ensure proper sample to tip alignment the PI 85 was tilted inside the SEM chamber to 8-15° to allow simultaneous imaging of the sample and indenter with both the SEM and FIB beams. The recorded force vs. displacement curves were converted into flexural stress vs. flexural strain curves for the center point at the outer fiber of the beam using the following equations from standard three-point bending flexural theory:

$$\sigma = \frac{3FL}{2bd^2} \quad (106)$$

$$\varepsilon = \frac{6Dd}{L^2} \quad (107)$$

where F is the recorded displacement in N, L the length of the specimen in mm, b the specimen width in mm, d the specimen height in mm, D the recorded displacement at the midpoint in mm, σ the stress at the midpoint in MPa, and ε the strain in the outer surface at the midpoint. The linear elastic loading portions of each curve were fit to linear regression lines of the form $\sigma = Y \varepsilon + A$, where σ is stress, Y is the effective specimen stiffness parameter, ε is strain, and A is an offset parameter. A 0.2% offset from this linear elastic loading regime was applied much like in ASTM tensile testing to acquire an effective specimen yield strength (σ_y). Let it be noted that due to the Pt GIS attachments, these equations serve as rough approximations of the tensile stresses at the outer fiber midpoint. Deformation of the attachments themselves as the beams are bending create complications that cannot be easily accounted for by analytical expressions. However, as seen in Figure 97f, bending specimens do become unconstrained during testing such that they begin to parallel a standard three-point bend test.

4.6 In-Situ Micro-Push-to-Pull Tensile Testing

Inconel X-750 samples for this study have been taken from the following irradiation conditions: approximately 67 dpa and 2.1 at% helium (taken from both the center and edge regions of the component) and approximately 81 dpa and 2.6 at% helium (taken from the center of the component). Non-irradiated control material was also taken from all three regions of the component: the center, outer edge, and inner edge. Irradiated specimens operating at temperatures 120-280°C and $300 \pm 15^\circ\text{C}$ were investigated.

4.6.1 Push-to Pull Device

The push-to-pull (P2P or PTP) device used for the micro-tensile experiments in this study is a consumable, MEMS-fabricated, silicon spring device. A flat punch indenter is used to press down on the center of the knob at the top of the device. When this occurs, the 2.5 μm gap that the specimens are affixed to expands at a constant rate controlled by the in-situ indenter and performs a uniaxial tension test on the material. Depictions of the P2P testing device and the testing set-up for this study can be seen in Figure 102a. Corrections for the spring compliance of the push-to-pull device and indenter system can be made individually for each test by either loading the device with no sample on it or by continuing to load the device after sample failure and fitting this linear load-displacement curve to obtain a spring stiffness as seen in Figure 102b. The latter option is the more time efficient option because in this case the in-situ indenter only requires set up and alignment once rather than twice to obtain all the data needed for each test, so this option was chosen for this study. By employing this method, push-to-pull devices were measured to have average spring constants of $k = 462 \pm 85 \text{ N/m}$. Using this spring constant, the load required to open the P2P device without any sample on it is subtracted from the raw measured load of the system to obtain the load on the sample:

$$F_{\text{sample}} = F_{\text{raw}} - kd \quad (108)$$

The common units of measure when working with the in-situ indenter are forces in μN and displacement of the P2P gap, d , in nm, so k is converted to units of $\mu\text{N}/\text{nm}$ when applied to equation (108).

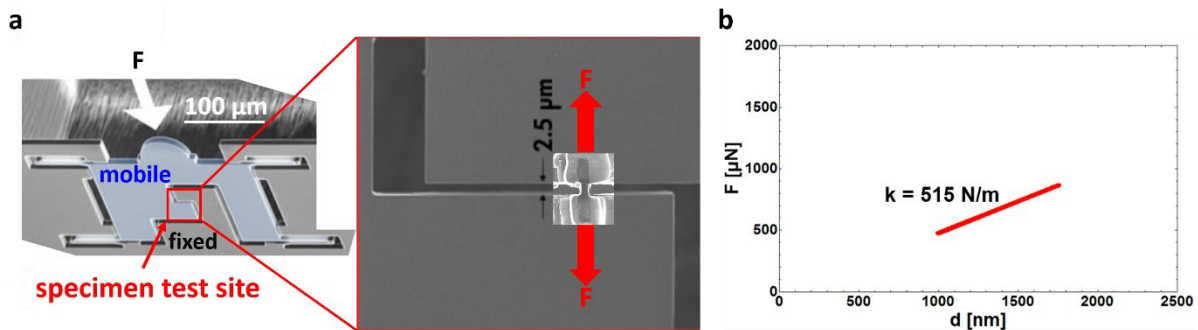


Figure 102. (a) push-to-pull testing device schematic depicting how it functions from Bruker [315], (b) portion of the load-displacement curve of a test post-failure of a micro-tensile specimen which has been fit to calculate the spring constant of the push-to-pull device for compliance correction

4.6.2 Tensile Specimen Sample Preparation

Irradiated specimens were manufactured from the large lift-out foils mounted on TEM grid posts prepared at the MFC in INL (Figure 94) to make all 67 dpa

samples and the Centre of Advanced Nuclear Systems at Mc Master University (Figure 95) to make all 81 dpa samples. Non-irradiated specimens were extracted from a “C-shaped” coil prepared as described in section 4.2.1. Specimens taken from the inner edge and outer edge could be prepared using an in house machined 90° SEM holder such that their bottom surfaces were flat when lifted out of the coil and placed directly onto their test sites. However, specimens taken from the center of the non-irradiated coil required a double lift-out process using a TEM grid post as an intermediate sample holder to shape the specimens flat before they were mounted on their test sites.

All specimens were manufactured such that they were either single-grained or contained one grain boundary using an in house machined 90° SEM holder inside vacuum in a FEI Quanta 3D FEG with a Ga⁶⁹⁺ FIB. Initially, larger milling currents (1-5 nA) were used to section individual specimens to be lifted out of the large foils and attached to a Bruker silicon push-to-pull device using ion beam assisted chemical vapor deposition (CVD) of a platinum precursor organometallic gas. Figure 103 depicts the required geometry inside the chamber required for successful sample mounting across the gap of the P2P device.

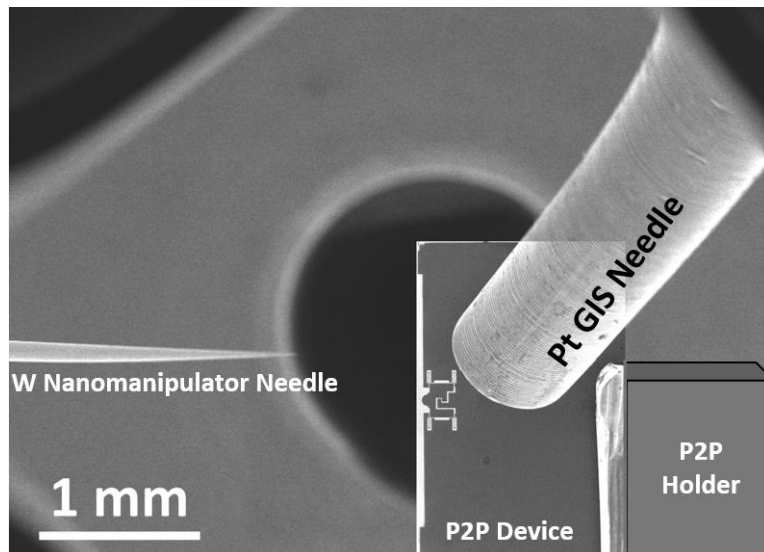


Figure 103. P2P set-up for lift-out process inside the SEM chamber

After specimens were secured to the testing device, they were FIB polished to smooth average final dimensions of $\sim 1.3 \mu\text{m} \times \sim 1.3 \mu\text{m} \times \sim 2.5 \mu\text{m}$ at currents of 50-100 pA. The sample fabrication processes can be seen in Figure 104.

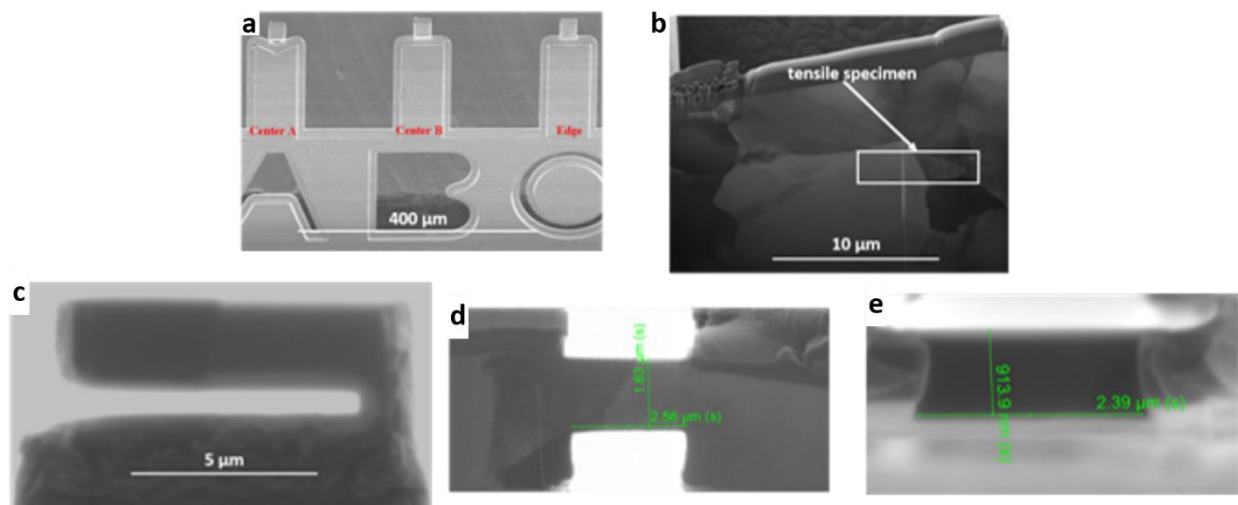


Figure 104. Sample preparation processes for micro-tensile push-to-pull specimens. (a) large lift-out foils mounted on standard 3 mm TEM grid, (b) individual lift-out foil depicting a selected micro-tensile specimen with a central grain boundary via FIB ion contrast imaging, (c) micro-tensile specimen sectioned for lift-out and mounting onto push-to-pull device, (d) top view and (e) side view of finished micro-tensile specimen

4.6.3 Electron Backscattered Diffraction Pre-Test Analysis

Completed specimens similar to those shown in Figure 103d and 103e were analyzed using EBSD on their top surfaces using an acceleration voltage of 20 keV, electron current of 48 nA, and step size ≤ 50 nm in order to map the misorientation angle between their two grains, hkl orientations of each grain, and highest Schmid factor of the preferred slip system(s) for each grain in the tensile loading direction.

4.6.4 Testing Procedures

A total number of 23 micro-tensile specimens have been fabricated and tested: two each from the non-irradiated outer edge and center regions, 7 from the non-irradiated inner edge region, 5 from 67 dpa material irradiated at 180 °C, 4 from 67 dpa material irradiated at 300 °C, one from 81 dpa material irradiated at 180 °C, and two from 81 dpa material irradiated at 300 °C. Testing was performed in vacuum in a FEI Quanta 3D FEG using a Hysitron PI 85/88 Picoindenter. Push-to-pull testing operates such that a 5 μm flat punch was used to press down on the push-to-pull device with a 2.5 μm wide gap as shown in Figure 102a, which then pulls the micro-tensile specimen to failure. Depictions of the testing set-up can be seen in Figure 102a. All tests were performed in displacement controlled feedback loop mode (piezoelectric load sensors) at loading rates of 10 nm/s until failure. Equivalent strain rates for these tests are between 1.5×10^{-3} and 5.2×10^{-3} . In order to ensure proper

sample to tip alignment between the flat punch and push-to-pull device in three dimensions (x, y, and z), simultaneous imaging of the sample and indenter was performed with both the SEM and FIB beams. Corrections for the spring compliance of the push-to-pull device were made individually for each test as described in Figure 102b.

In order to more accurately measure the strain values to obtain total elongation to failure, a digital image correlation (DIC) software program written in Python called *Shift* was used to analyze each test video frame by frame. Figure 105 shows the user interface of the *Shift* DIC program at three segments of the test video: (a) pre-test, (b) soon after yielding, and (c) immediately after fracture. Using a point tracking algorithm to trace selected points at each end of the gauge length on a frame by frame basis, the displacement is calculated as shown in Figure 105d. From this data, a text file is exported and the strain is then calculated. By matching the times of the video and the load-displacement text file, appropriate strain values are assigned to each load data point.

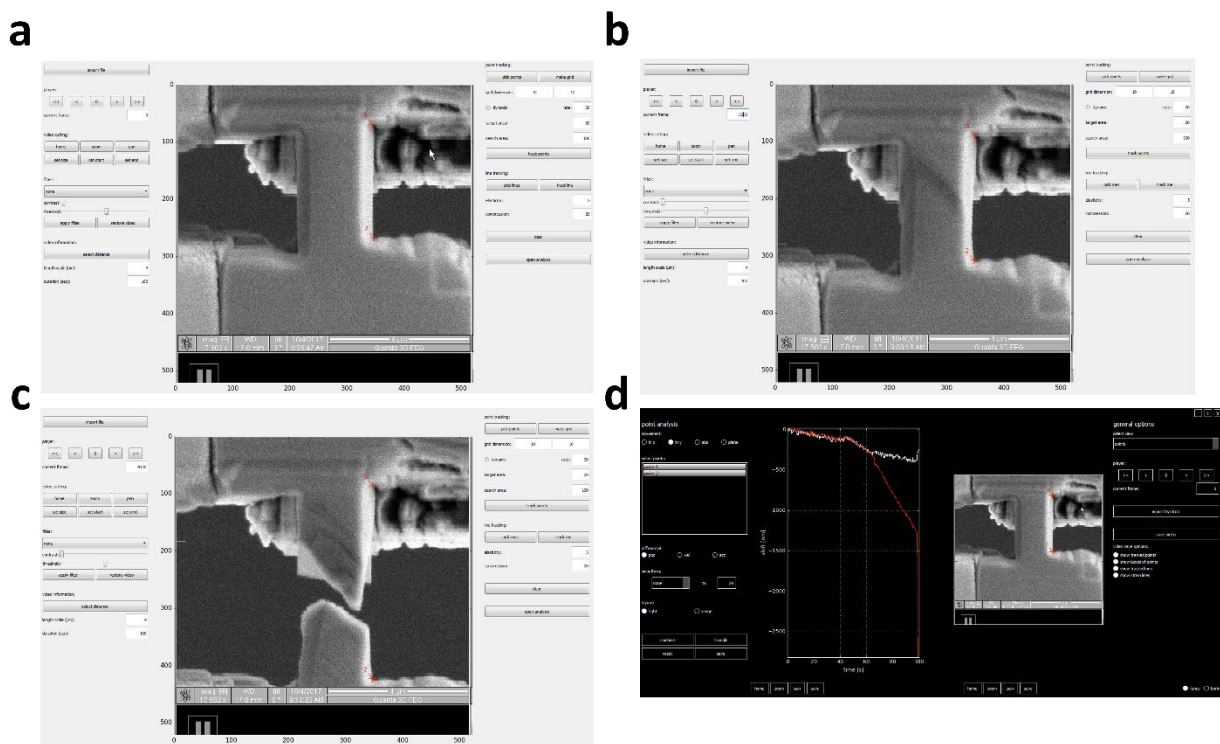


Figure 105. Shift software program user interface for DIC point tracking. (a) pre-test: Two points are selected at the ends of the gauge length of the specimen, (b) tracing the points soon after yielding, (c) tracing the points immediately after fracture, (d) Frame-by-frame analysis of the displacement of each point, which accounts for stage drift

Engineering stresses were calculated by dividing the recorded load by the measured area of the specimens in order to generate stress vs. strain plots for each test. Yield stresses were calculated for specimens that underwent plasticity by applying a linear fit to the elastic portions of the curves and applying a standard 0.2% offset. Failure stresses were also determined for each test; in cases where fracture occurred along the grain boundary, they are deemed to be the grain boundary strength of the material. Resolved normal and shear stresses on the grain boundaries at the yield point and failure point of the specimens were calculated. An effective grain boundary area factor (A/A_{GB}) was multiplied by the stresses in the tensile loading direction and resolved along the normal and shear directions as presented in Table 11.

4.7 Nanoindentation: Non-Irradiated Inconel X-750

In order to investigate the cold-working effects seen in the non-irradiated spring coil cross-section in Figure 51, lines of nanoindentation experiments were performed across the polished sample surface from the inner edge to the outer edge. Berkovich indents with a depth of 200 nm spaced 4 μm apart using a Hysitron TI 900 TriboIndenter were performed in order to obtain a hardness profile map as a function of distance from the center of the coil to correlate cold-working residual strain with mechanical properties. Unfortunately, due to high radiation fields which exceed dose limits, full cross-sections of high dose irradiated material could not be investigated using nanoindentation.

4.8 Room Temperature Ion Irradiation Studies

Ion irradiation studies of Inconel X-750 components at the Australian Nuclear Science and Technology Organisation (ANSTO) were made possible through an East Asia and Pacific Summer Institutes (EAPSI) research fellowship. The goal of these studies was to isolate the effects of helium on the mechanical properties of the material by implanting U-shaped slices of non-irradiated Inconel X-750 components prepared via the methods described in section 4.2.1. Helium ion implantation in order to simulate the radiation effects of helium transmutation reactions in the material provides the added benefits of investigating larger sample volumes of material through micro-mechanical tests without activating it. However, it requires much higher dose rates to implant comparable levels of helium to that seen in the ex-service material. In addition, in reactor elevated temperature effects over long time periods are difficult to simulate.

The ion beam irradiation of two U-shaped spring slices was performed using the 2MV Tandetron STAR accelerator at ANSTO. Two additional polished coils were preserved for non-irradiated control micro-mechanical experiments. The irradiation was performed with 6 MeV He^{2+} ions and the flux of these ions was 5.6×10^{17} ions/cm². The irradiation temperature was approximately room

temperature (20 ± 5 °C) as monitored with a thermocouple mounted close to the sample on the aluminium sample clamp. An energy degrader wheel with 14 aluminium foil thicknesses between $0.8 \mu\text{m}$ and $22 \mu\text{m}$ was used in an attempt to create a flat irradiation profile with helium uniformly implanted. Table 9 shows the resultant exit energies and stopping peak depths from SRIM calculations, and Figure 106 shows a graphical depiction of the dose-depth profile.

Table 9. He²⁺ Ion Energies Exiting the Degrader Wheel and Their Associated Stopping Peak Depths in the Inconel X-750 Spacers

Al Foil Thickness (μm)	He ²⁺ Exit Energy (MeV)	Stopping Peak Depth (μm)
0	6	12.20
0.8	5.9 ± 0.05	11.60
1.6	5.75 ± 0.05	11.20
3	5.55 ± 0.05	10.70
6	5.05 ± 0.05	9.38
7	4.90 ± 0.05	9.02
9	4.60 ± 0.05	8.29
10	4.40 ± 0.05	7.84
12	4.05 ± 0.05	7.05
15	3.45 ± 0.05	5.79
16	3.28 ± 0.05	5.59
18	2.85 ± 0.05	4.63
20	2.30 ± 0.05	3.66
22	1.85 ± 0.05	2.85

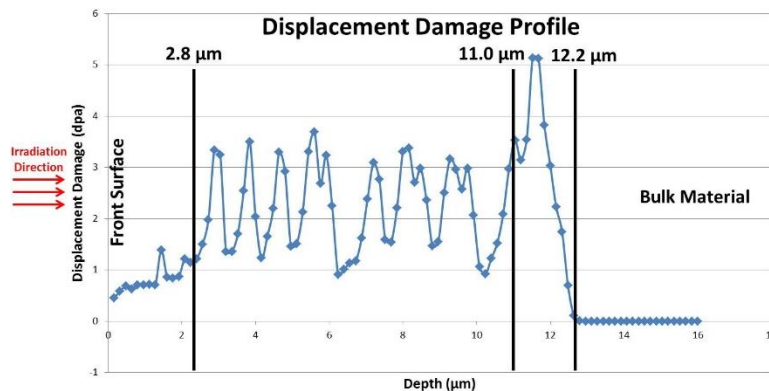


Figure 106. Resultant displacement damage profile in an Inconel X-750 spring using an Al degrader wheel predicted by SRIM calculations. An approximately uniform ~ 3 dpa region occurs $3\text{--}11 \mu\text{m}$ deep, with the exception of two dips at $6 \mu\text{m}$ and $10 \mu\text{m}$ which are consequences of non-uniform differences in foil thicknesses of the Al degrader wheel.

There is an initial surface region less than 3 μm in depth with total displacement damage less than 1 dpa, a uniform ~ 3 dpa region occurs 3-11 μm deep, with the exception of two dips at 6 μm and 10 μm which are consequences of non-uniform differences in foil thicknesses of the Al degrader wheel, a final stopping peak region 12 μm deep reaching 5 dpa, followed by non-irradiated bulk material at greater depths. A helium concentration distribution can be seen in Figure 107.

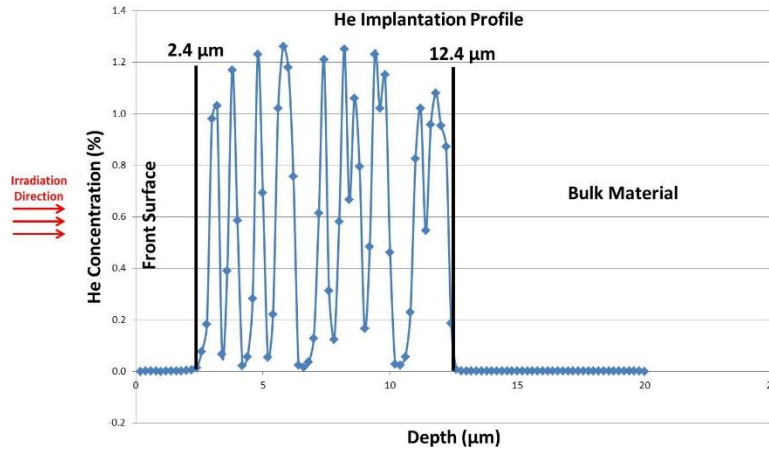


Figure 107. Resultant helium implantation profile in Inconel X-750 spring using Al degrader wheel predicted by SRIM calculations. An approximately uniform amount of He, 1-1.2%, has been implanted in the region 3-12 μm deep, with the exception of two dips at 6 μm and 10 μm which are consequences of non-uniform differences in foil thicknesses of the Al degrader wheel.

Similar to the displacement damage profile, the helium implantation profile shows that 1-1.2% helium has been implanted uniformly into the material between depths of 3-12 μm , with the exception of two dips at 6 μm and 10 μm which are consequences of non-uniform differences in foil thicknesses of the Al degrader wheel.

4.8.1 Nanoindentation: Ion Irradiated Inconel X-750

One of the two helium implanted coils was sliced in half, mounted in cross-section inside of a Bakelite and Epoxy puck, and mechanically polished using the formula in section 4.2.1. Berkovich nanoindentation at a depth of 250 nm with an indent spacing of 5 μm 0-20 μm from the irradiated surface along the outer edge of the coil was performed on this sample in order to obtain hardness changes due to irradiation. SEM images of all indents were taken in order to precisely measure the exact distance between the indent and the irradiated surface. Indents occurring on top of carbide inclusions were removed due to the fact that they are not representative of the behaviour of the bulk material.

4.8.2 In-Situ Gripper Micro-Tensile Testing

One control spring coil and one irradiated spring coil were mounted on an aluminium dovetail insert designed for use in the the Zeiss Ultra Plus scanning electron microscope (SEM) and Zeiss Auriga 60 focused ion beam (FIB). Two non-irradiated specimens and four helium irradiated and implanted specimens were made along the outer edge of the coil as shown in Figure 108. All dog-bone-shaped tensile specimens with rounded edges to avoid unwanted stress-concentrations at the corners were fabricated using the FIB using milling currents of 4 nA and 16 nA to produce rough shapes and 2 nA to produce final smoothly polished geometries in the control spring component with 17-18 μm gauge lengths, 4.0-4.6 μm gauge widths, and 3.5-5.3 μm gauge thicknesses confirmed by 15 keV SEM images.

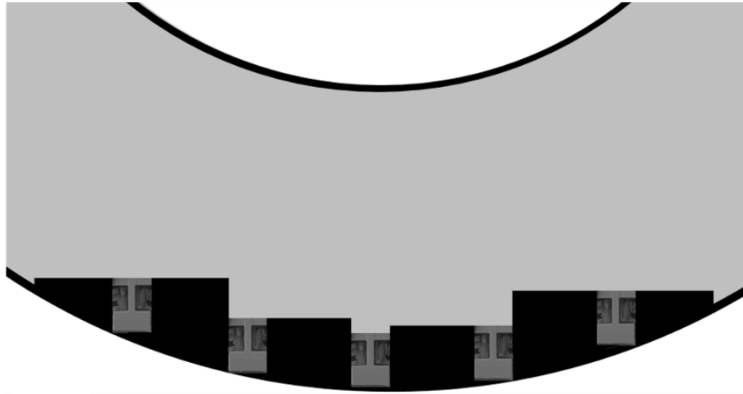


Figure 108. Schematic of micro-tensile tests milled into the outer edge of non-irradiated and He implanted Inconel X-750 coils

Pre-test analysis in the form of electron backscattered diffraction (EBSD) was performed on all gauge sections of the specimens at 4kx magnification with 20 keV electrons using 100 nm step sizes. This analysis includes band contrast, Euler angle color, inverse pole figure x, y (tensile pulling direction), and z direction maps, *hkl* orientations of each grain, quantification of pre-existing lattice rotation within each grain in the specimen, misorientation angles between neighboring grains, and Schmid factor maps which indicate how likely slip events are along the most likely slip plane and slip direction from the 12 available *fcc* slip systems. An example of this analysis along with the SEM picture of a finished tensile specimen can be seen in Figure 109 a-h.

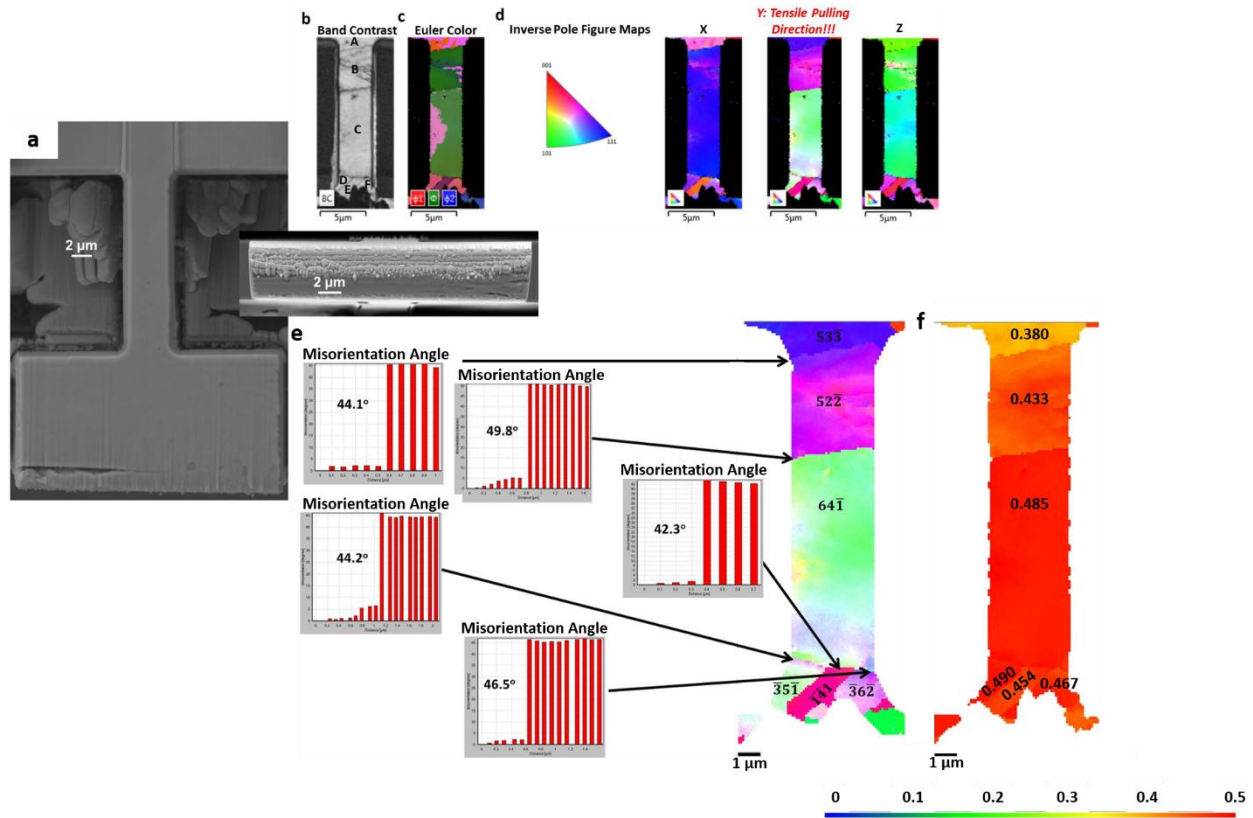


Figure 109. (a) SEM images of a finished micro tensile specimen, EBSD analysis of a micro tensile specimen including (b) band contrast identifying grain boundaries, (c) Euler angle orientation color, (d) inverse pole figure maps in the x, y, and z directions, (e) hkl orientations in the tensile loading direction of each grain with misorientation angles across each grain boundary, (f) Schmid factor map indicating the easiness of slip within each grain

In-situ tensile tests were performed in high vacuum inside of a Zeiss Ultra Plus SEM using a micro-test rig (MTR-3) developed by MicroTesting Solutions (Hilliard, OH, USA) at the Institute of Materials Engineering at ANSTO. Samples were subjected to elongation using an in-house fabricated tungsten gripper pictured in Figure 110. This gripper was made using the Zeiss Auriga 60 FIB and will contact the flat surfaces on the “plug” portion of the specimen and pull it at a displacement controlled (piezoelectric feedback control loop) rate of 5 nm/s, equating to an approximate strain rate of $\dot{\epsilon} = 2.9 \times 10^{-4} \text{ s}^{-1}$. High definition SEM images (2048 x 1535 pixels) can be acquired at small strain intervals during the tests. The displacement or strain can be held constant during the image acquisition by pausing the test. The pause at constant strain will be accompanied by a small stress relaxation ranging from 0.1 to 1 MPa. For each image, the load recorded at the start of acquisition can be used to calculate the engineering stress. The DIC software program *Shift* can then be used after linking

all the images and determine the engineering strain. The mechanical properties elastic modulus, yield strength, total elongation, and failure stress will be determined from engineering stress versus engineering strain curves in order to quantify helium implantation effects.

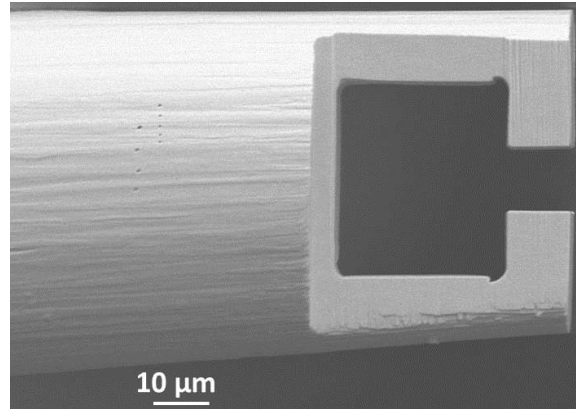


Figure 110. Tungsten gripper for micro-tensile testing

5 Results

5.1 Bulk Component Crush Testing

Component crush testing seen in Figure 111 shows that springs irradiated at the higher temperature exhibit lower strength and ductility compared to springs irradiated at the lower temperature. Extended service results in reduced strength and ductility. In the case of specimens irradiated at an average of 180 °C, ductility decreases by a factor of two after 53 dpa and nearly vanishes by 67 dpa. However, specimens irradiated at an average of 300 °C have completely lost ductility by 53 dpa. More dose results in further loss of strength.

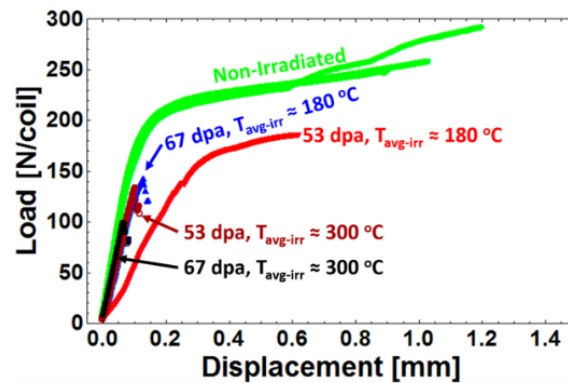


Figure 111. Representative bulk crush testing load-displacement curves of Inconel X-750 specimens at each irradiation condition

5.2 Microhardness Testing

Vickers microhardness measurements from Inconel X-750 specimens seen in Figure 109 show that components irradiated at the lower temperature are softer (~365 VHN) compared to the materials irradiated at higher temperatures (~420-450 VHN) at the highest dose.

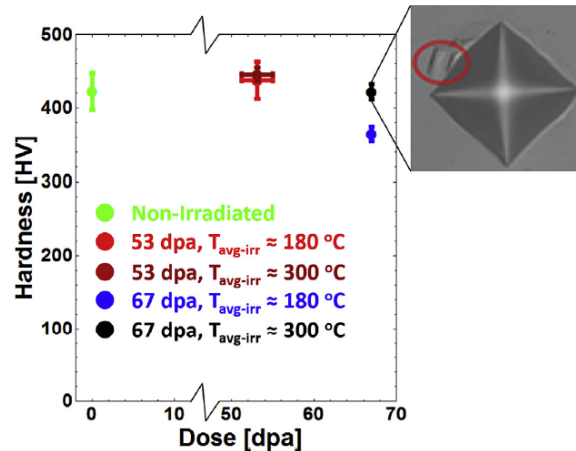


Figure 112. Vickers indentation microhardness values (500 gf) of Inconel X-750 specimens at each irradiation condition with an insert depicting a representative indent. Uneven deformation occurred adjacent to the indent in the 67 dpa material irradiated at 300 °C.

Let it be noted that the hardness data and component crush test data follow opposite trends. Specimens irradiated at higher temperatures have higher hardness values but lower crush test failure loads. This suggests that hardening mechanisms within the bulk matrix material of the components may be much different than the ultimate failure mechanisms. Hardening mechanisms are dictated by the production and distribution of point defects, dislocations, and dislocation loops, whereas ultimate failure mechanisms are believed to be dictated by deformation within grain boundaries.

5.3 In-Situ Micro-Three-Point Bend Testing

Figures depicting the results for each three-point bend specimen will consist of pre- and post-test SEM images, an EBSD map of its top surface indicating grain orientations with respect to the maximum flexural tensile stress direction at the midpoint of the bottom of each micro-beam, and the associated flexural three-point bend stress-strain curves calculated according to equations (106) and (107).

5.3.1 Non-Irradiated Outer Edge Specimens

Specimen 1

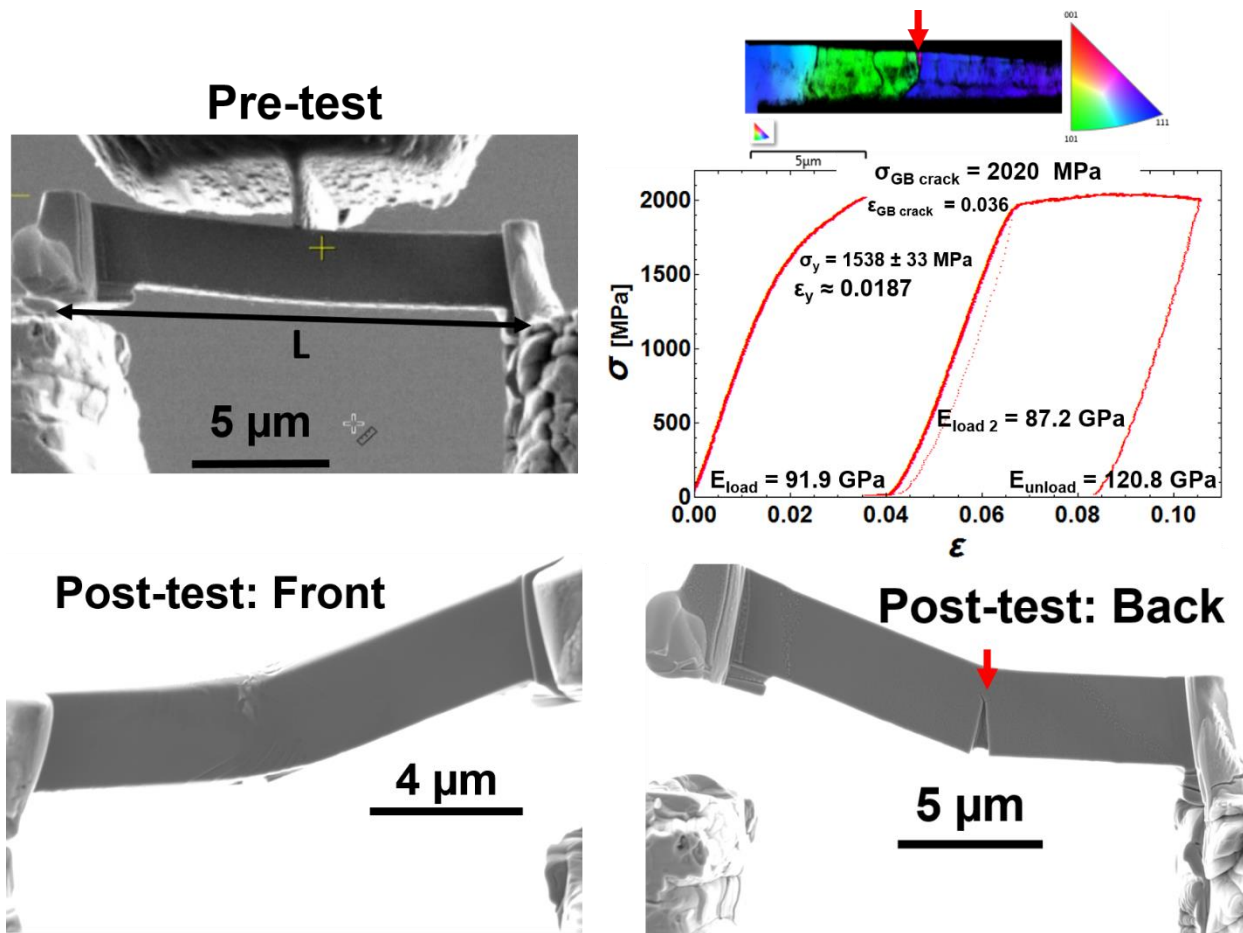


Figure 113. Non-irradiated outer edge three-point bend specimen 1. A crack is believed to have developed along the boundaries of the smallest pink grain indicated by the red arrow after yielding occurred.

Specimen 1 (length $L = 17.32 \pm 0.79 \mu\text{m}$, width $W = 2.56 \pm 0.10 \mu\text{m}$, and height $H = 2.98 \pm 0.03 \mu\text{m}$) extracted from the non-irradiated coil along the outer edge was loaded to a yield stress of $1538 \pm 33 \text{ MPa}$. At a flexural strain of $\sim 3.6\%$ and a stress of 2020 MPa , a dramatic load drop appears as the crack indicated along the back side of the specimen was formed. This crack is believed to be along the boundaries of the smallest pink grain. Note that the pink grain and the neighbouring green grain are the most weakly oriented with respect to the flexural stress direction along the length of the beam. The specimen was loaded further as the crack was observed to open up to a strain of $\sim 10\%$ before final unloading due to undesired contact of the cone of the wedge punch tip with the specimen.

Specimen 2

Specimen 2 (length $L = 16.71 \pm 0.10 \mu\text{m}$, width $W = 3.80 \pm 0.04 \mu\text{m}$, and height $H = 4.60 \pm 0.02 \mu\text{m}$) extracted from the non-irradiated coil along the outer edge was loaded to a yield stress of $2313 \pm 43 \text{ MPa}$. The high yield strength can be attributed to grains that are strongly oriented with respect to the flexural stress direction along the length of the beam (highest Schmid factor less than 0.4). The specimen underwent smooth loading until the mid-span outer fiber strain was about 14%. At this point, the right side support attachment broke down, which led to a jump in the indentation tip displacement and triggered unloading. Deformation did not occur within any of the high angle grain boundaries or twin boundaries within the specimen.

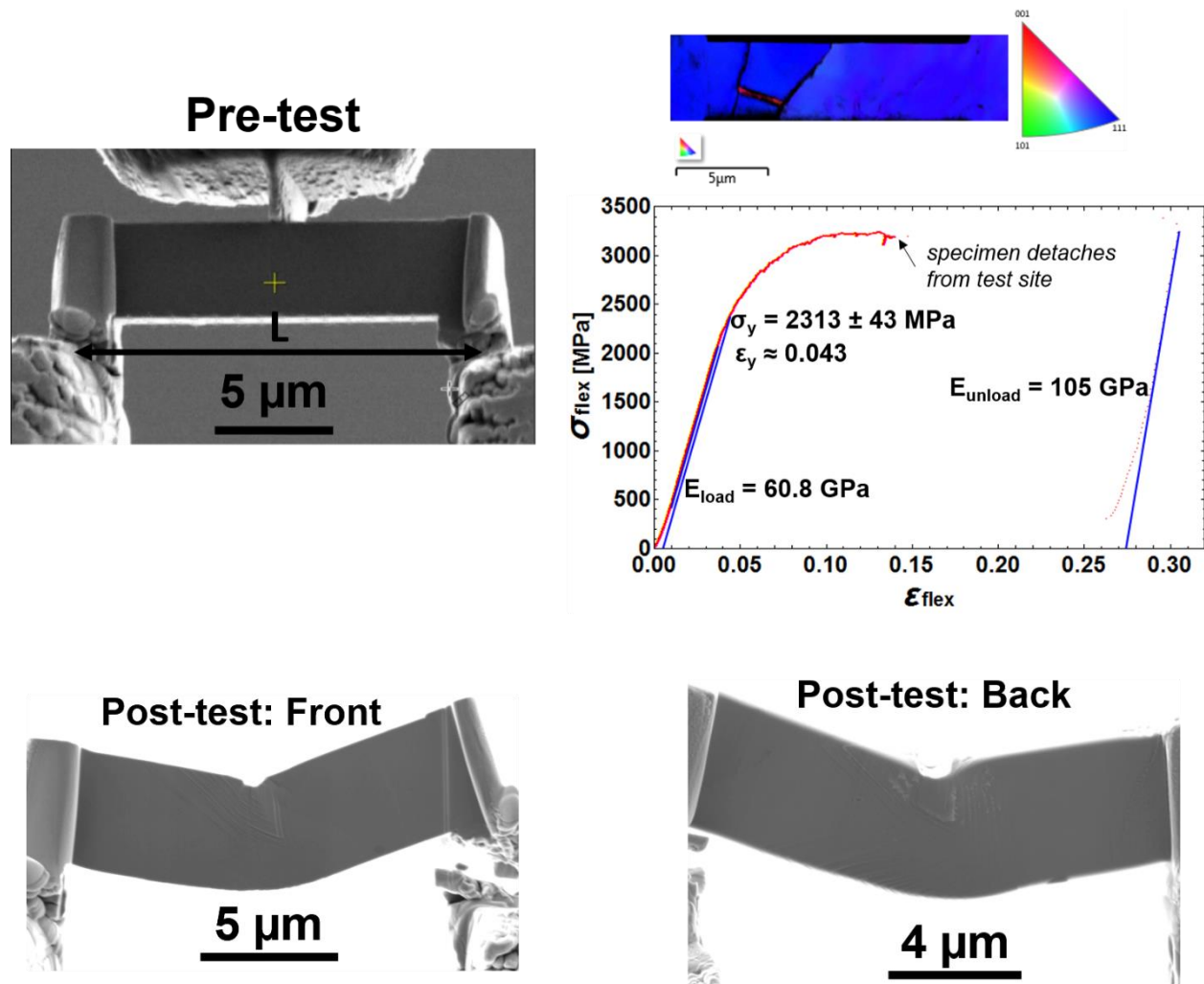


Figure 114. Non-irradiated outer edge three-point bend specimen 2.

Specimen 3

Specimen 3 (length $L = 18.85 \pm 0.41 \mu\text{m}$, width $W = 3.23 \pm 0.54 \mu\text{m}$, and height $H = 3.72 \pm 0.09 \mu\text{m}$) extracted from the non-irradiated coil along the outer edge was loaded to a yield stress of $1868 \pm 25 \text{ MPa}$. At a flexural strain of $\sim 9\%$, the specimen became detached from its test site on the left side. At this point, the left side of the indenter cone came into contact with the specimen and unloading was necessary. There are only parallel twin boundaries within the specimen that do not deform.

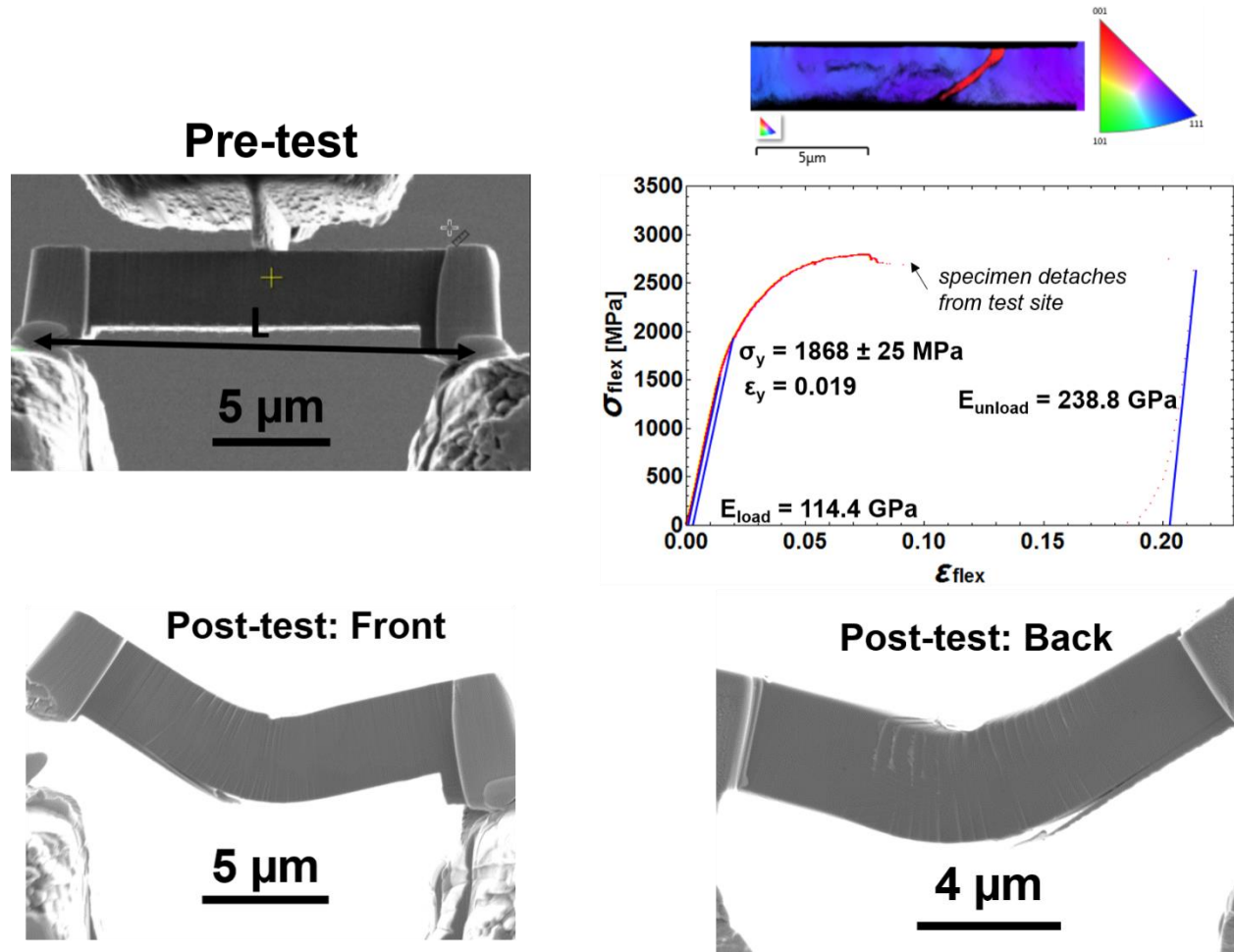


Figure 115. Non-irradiated outer edge three-point bend specimen 3

Specimen 4

Specimen 4 ($L = 17.35 \pm 0.49 \mu\text{m}$, width $W = 3.09 \pm 0.05 \mu\text{m}$, and height $H = 3.11 \pm 0.05 \mu\text{m}$) underwent smooth loading until the mid-span outer fiber strain was about 4%. At this point, the specimen severely bowed. Its yield strength was measured to be $2425 \pm 14 \text{ MPa}$ and significant plasticity in the form of slip bands was observed in multiple grains before detachment occurred.

When abrupt bowing of the micro-beam occurred at 3330 MPa, cracks appeared on the side surfaces of the specimen along what appear to be grain boundaries.

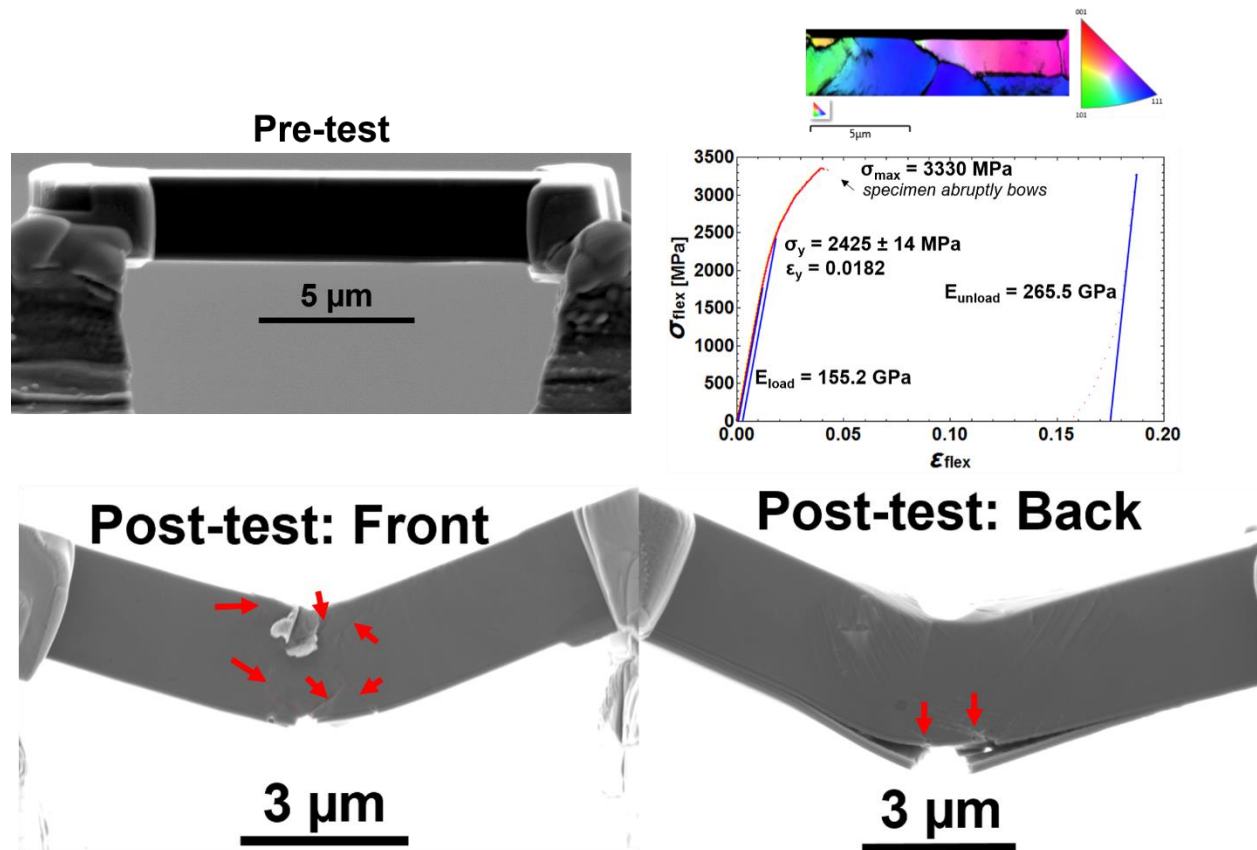


Figure 116. Non-irradiated outer edge three-point bend specimen 4. Potential grain boundary cracks that appeared after the maximum stress value when the beam abruptly snapped are highlighted by the red arrows.

Specimen 5

Specimen 5 ($L = 18.54 \pm 0.63$ μm, width $W = 3.65 \pm 0.15$ μm, and height $H = 4.59 \pm 0.04$ μm) that began in a quasi-constrained state (only attached on one side before beginning testing) underwent smooth loading until the displacement of the indentation tip reached the maximum programmed displacement value of the indenter, 4 μm. At this point, programmed unloading at a rate of 10 nm/s was triggered. More weakly oriented large grains with respect to the flexural stress direction along the length of the beam (highest Schmid factor 0.497) are believed to be responsible for producing a lower yield strength of 1688 ± 3 MPa. Numerous slip steps were observed with no evidence of grain boundary deformation.

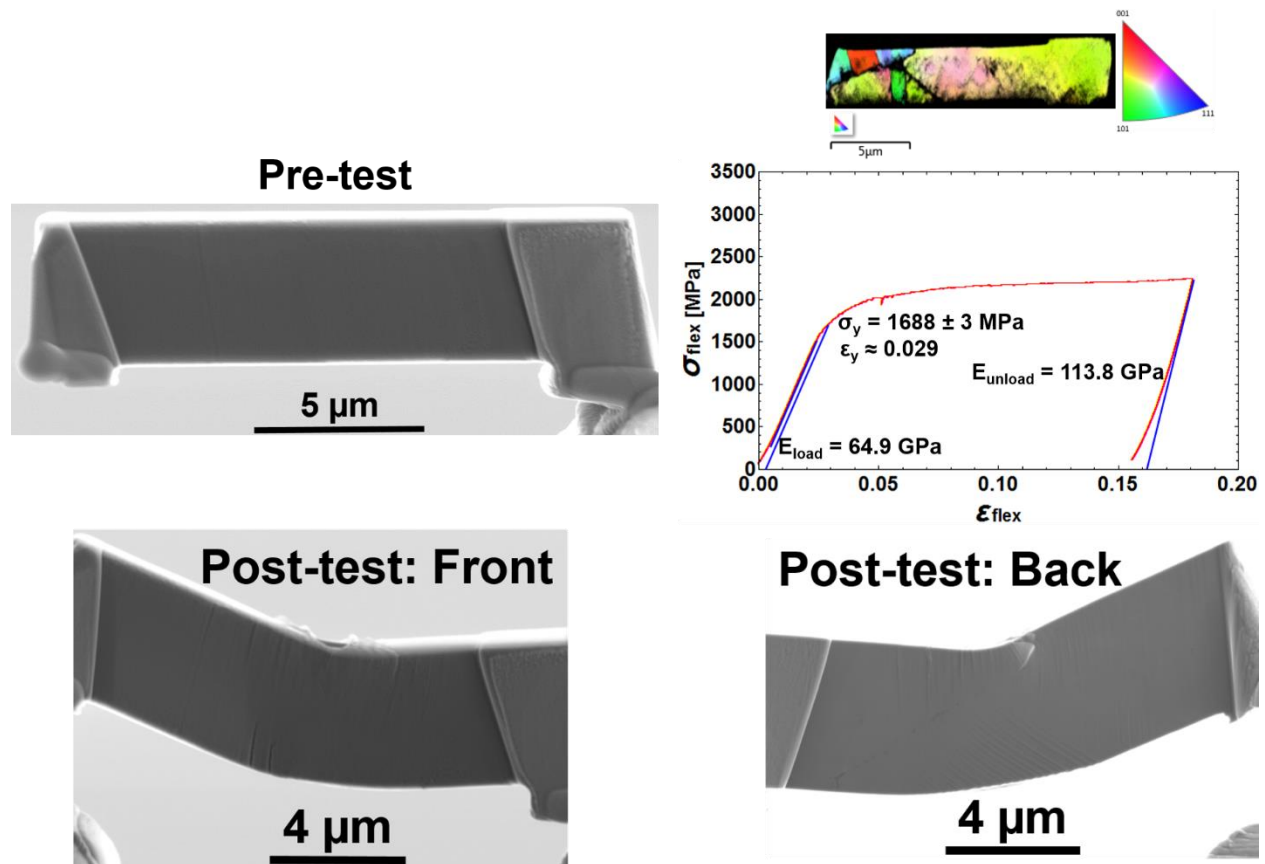


Figure 117. Non-irradiated outer edge three-point bend specimen 5.

5.3.2 Non-Irradiated Center Specimens

Specimen 1

Specimen 1 (length $L = 16.17 \pm 0.08 \mu\text{m}$, width $W = 4.20 \pm 0.02 \mu\text{m}$, and height $H = 4.17 \pm 0.33 \mu\text{m}$) underwent linear elastic loading up until its 0.2% offset yield point of $1397 \pm 3 \text{ MPa}$ and continued smooth loading out to a total flexural strain of 36% at which point the wedge punch indenter reached its maximum programmed displacement of $4 \mu\text{m}$ and the micro-beam was unloaded. No evidence of grain boundary deformation was observed. Multiple slip systems were activated in the more weakly oriented grain of the micro-beam as it became severely plastically deformed.

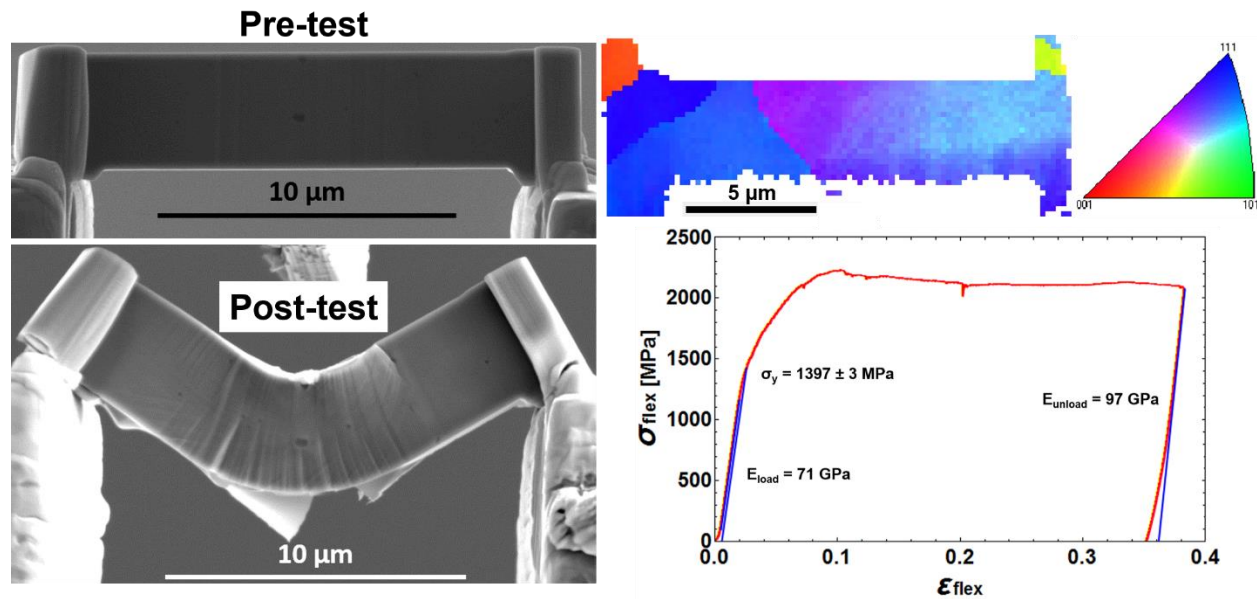


Figure 118. Non-irradiated center three-point bend specimen 1.

Specimen 2

Specimen 2 (length $L = 15.45 \pm 0.55 \mu\text{m}$, width $W = 4.72 \pm 0.01 \mu\text{m}$, and height $H = 3.72 \pm 0.06 \mu\text{m}$) was only constrained on one side to begin the test and underwent linear elastic loading up until its 0.2% offset yield point of $1273 \pm 13 \text{ MPa}$. Four distinct, severe load drops occurred after yielding associated with markings along the bottom of the micro-beam. Slip steps are seen to propagate through a grain boundary on the side surface as shown in the post-test image. At a total flexural strain of 36% the wedge punch indenter reached its maximum programmed displacement of $4 \mu\text{m}$ and the micro-beam was unloaded.

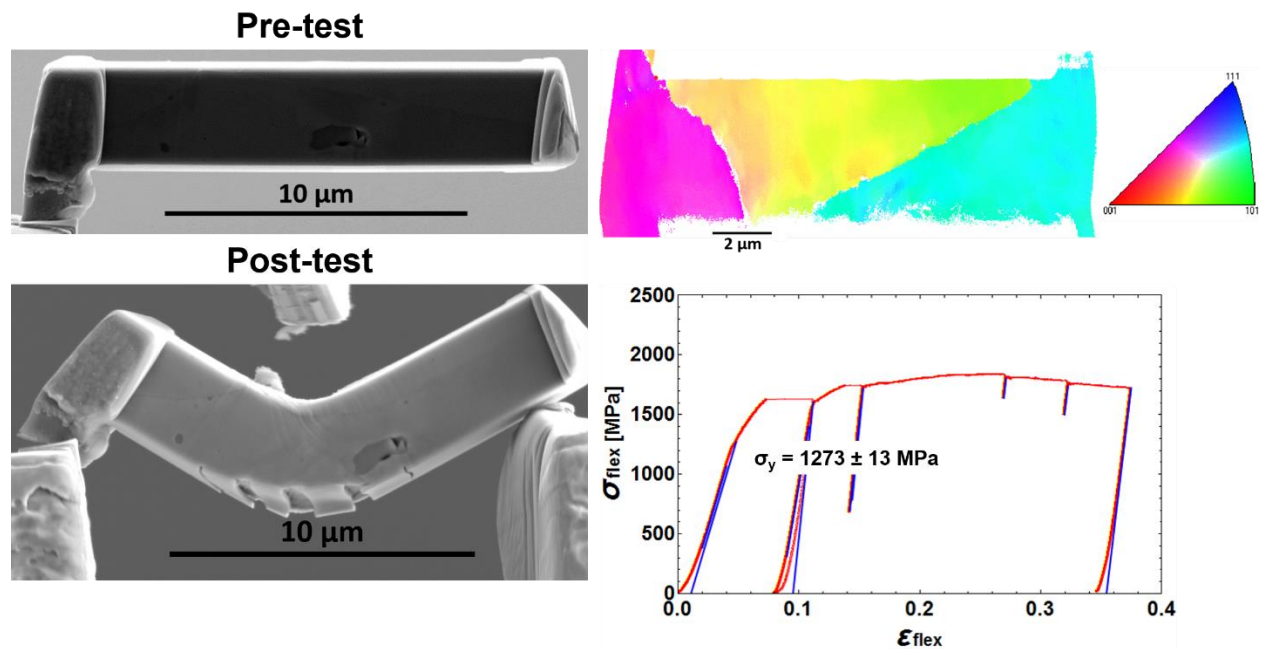


Figure 119. Non-irradiated center three-point bend specimen 2.

5.3.3 54 dpa Low Irradiation Temperature Specimens

Unfortunately, the large lift out foil of 54 dpa material irradiated at an average temperature of 180 °C extracted at the MFC in INL and sent to UC Berkeley for testing did not contain grain boundaries. Therefore, the two micro-bend specimens tested at this irradiation condition were single-grained specimens. The grain orientations of these single-grained specimens were very weakly oriented such that they had Schmid factors close to the maximum, 0.5. Due to the fact that the grains were soft, the wedge punch produced slight imprints into the samples as they became plastically deformed beyond their yield points, generating a more convoluted stress state. In order to avoid this issue with weakly oriented, single-grained, three-point bend specimens, specimen sample thickness and width should be reduced to avoid indentation effects.

Specimen 1

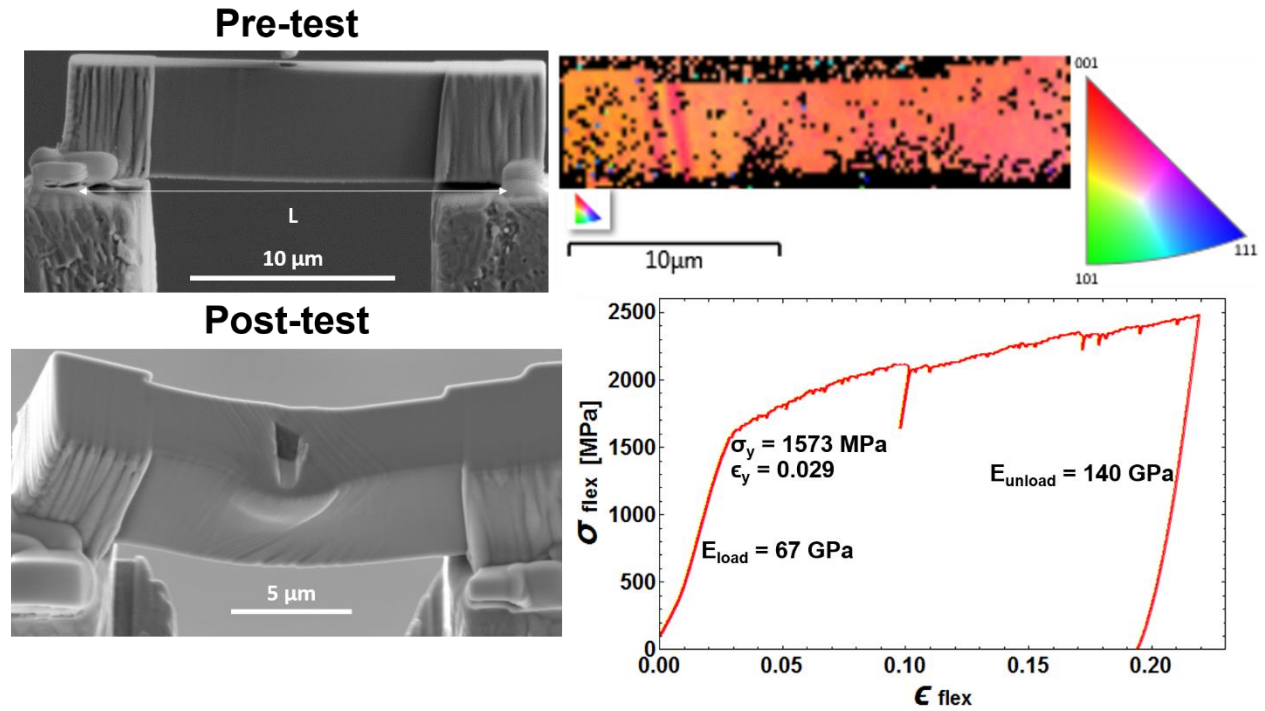


Figure 120. Single-grained 53 dpa, $T_{irr} = 180$ °C, three-point bend specimen 1.

Specimen 1 (length $L = 21.53$ μm , width $W = 4.07 \pm 0.25$ μm , and height $H = 5.74 \pm 0.14$ μm) prepared in a quasi-constrained fashion was loaded to a yield stress of 1573 MPa. Subsequent plasticity produced many parallel slip planes and the specimen was loaded to its maximum programmed displacement of 4 μm before the micro-beam was unloaded.

Specimen 2

Specimen 2 (length $L = 21.03$ μm , width $W = 4.80 \pm 0.35$ μm , and height $H = 5.10 \pm 0.27$ μm) prepared in a quasi-constrained fashion was loaded to a yield stress of 1549 MPa. Subsequent plasticity produced many parallel slip planes and the specimen was loaded to its maximum programmed displacement of 4 μm before the micro-beam was unloaded.

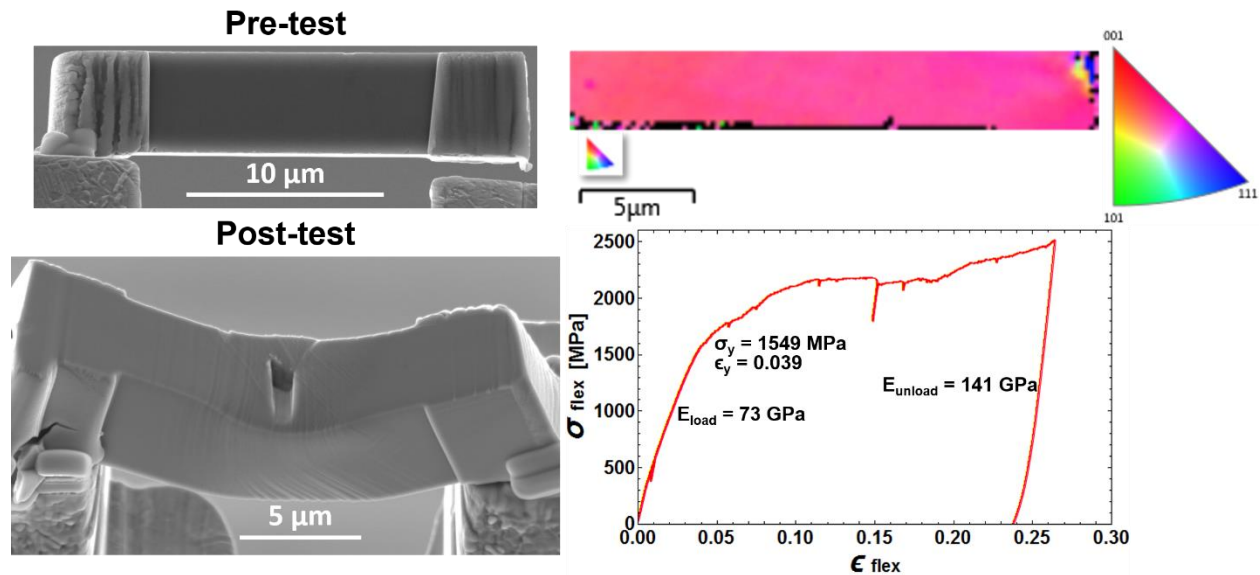


Figure 121. Single-grained 53 dpa, $T_{irr} = 180\text{ }^{\circ}\text{C}$, three-point bend specimen 2.

5.3.4 54 dpa High Irradiation Temperature Specimens

Two specimens of normal three-point bending beam geometries and two specimens with notches in their bottom surfaces in an attempt to concentrate stresses on their grain boundaries were tested. Specimen 1 and Specimen 2 have regular geometries and Specimen 3 and Specimen 4 are notched. The height of the notched specimens was measured as the distance between the top of the specimen and the tip of the notch. The notches appear to have no effect on the yielding behavior of the micro-beams because yield stress values for all four specimens are very similar. No evidence of grain boundary deformation in notched specimens is reported.

Specimen 1

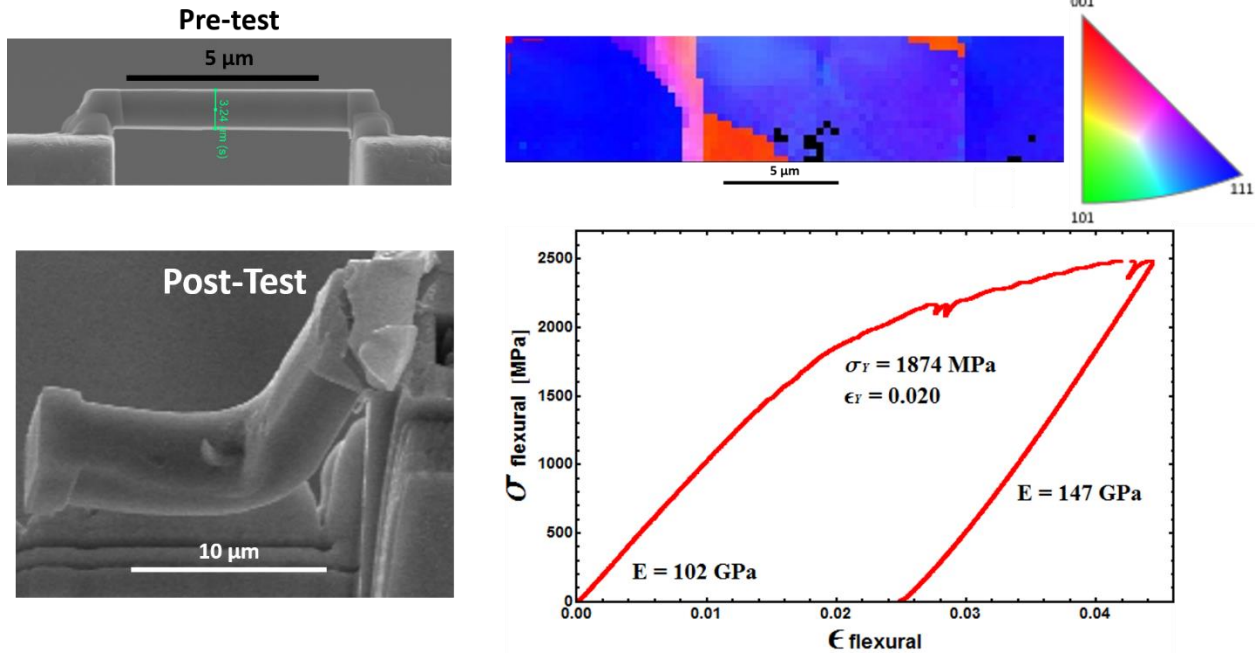


Figure 122. 53 dpa, $T_{irr} = 300\text{ }^{\circ}\text{C}$, three-point bend specimen 1.

Specimen 1 (length $L = 19.15 \pm 0.43\text{ }\mu\text{m}$, width $W = 4.77 \pm 0.10\text{ }\mu\text{m}$, and height $H = 3.38 \pm 0.16\text{ }\mu\text{m}$) was loaded to a yield point of 1874 MPa. Subsequent plastic deformation soon fractured the attachments and caused the specimen to fall into the valley below its test site as it became unconstrained. At this point the specimen was unloaded.

Specimen 2

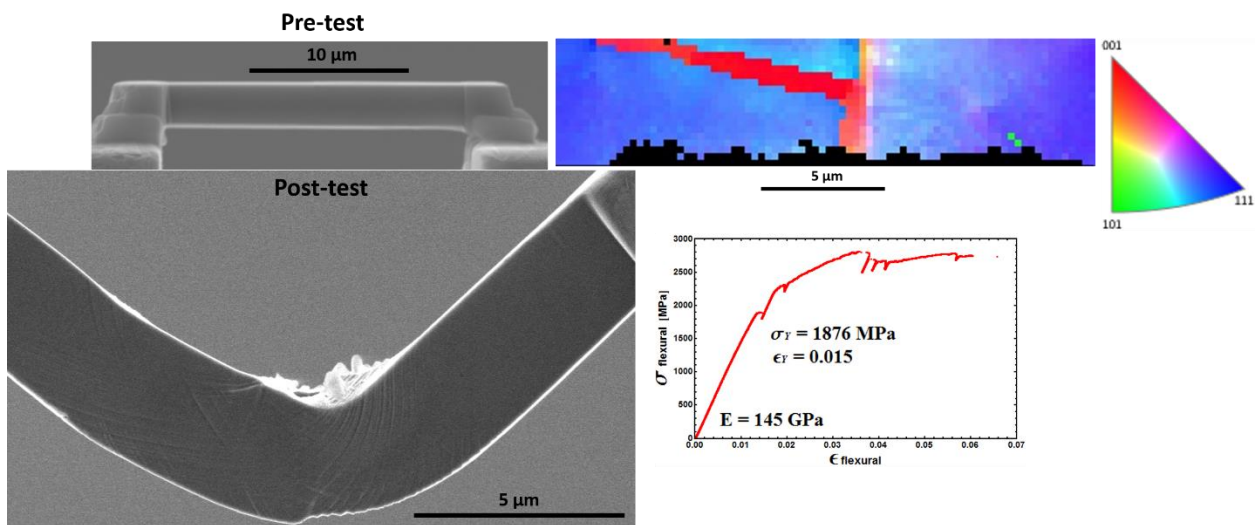


Figure 123. 53 dpa, $T_{irr} = 300\text{ }^{\circ}\text{C}$, three-point bend specimen 2.

Specimen 2 (length $L = 19.74 \pm 0.19 \mu\text{m}$, width $W = 4.89 \pm 0.04 \mu\text{m}$, and height $H = 3.11 \pm 0.89 \mu\text{m}$) was loaded to a yield point of 1876 MPa. Subsequent plastic deformation activated multiple slip systems as seen in the intersecting slip bands in the post test image of the bent micro-beam. After a flexural strain of $\sim 7\%$, the beam detached from its test site and slid into the valley below it at which point the test was unloaded.

Specimen 3

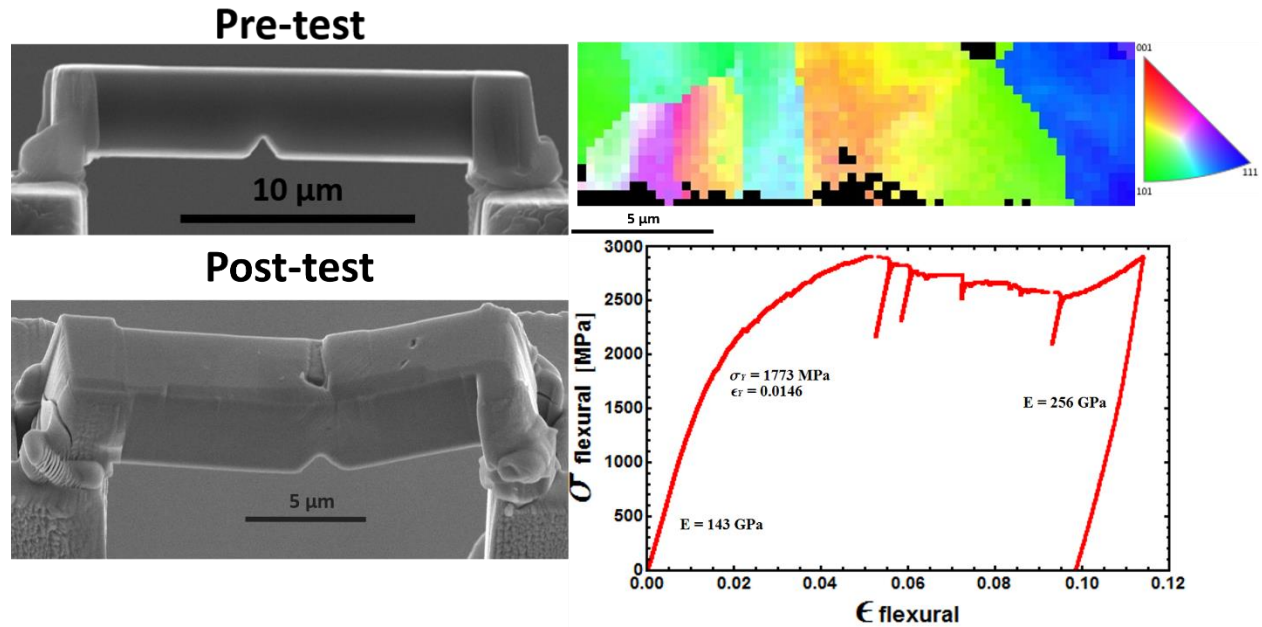


Figure 124. 53 dpa, $T_{irr} = 300 \text{ }^\circ\text{C}$, notched, three-point bend specimen 3.

Specimen 3 (length $L = 16.35 \pm 0.54 \mu\text{m}$, width $W = 5.07 \pm 0.11 \mu\text{m}$, and height $H = 2.93 \pm 0.89 \mu\text{m}$) was loaded to a yield point of 1773 MPa. Many deformation slip planes are observed in the large grain directly under the indenter punch as the specimen is loaded to a maximum stress $\sim 3 \text{ GPa}$. When the flexural strain on the midpoint at the outer fiber reached 9%, the support attachments failed causing a jerk to occur and the specimen was unloaded.

Specimen 4

Specimen 4 (length $L = 14.88 \pm 0.35 \mu\text{m}$, width $W = 5.44 \pm 0.07 \mu\text{m}$, and height $H = 3.17 \pm 0.08 \mu\text{m}$) was loaded to a yield point of 1962 MPa. This specimen containing only an off-centered twin boundary exhibited many parallel slip planes in its larger grain directly under the indenter punch was further loaded to a maximum stress of $\sim 2800 \text{ MPa}$ at a flexural strain on the midpoint at the outer fiber of $\sim 9\%$. At this point, significant deformation induced a large load drop. Loading continued with little increase in stress until a flexural strain of

~16% at which point the cone of the indenter contacted the side of the specimen, and it was unloaded.

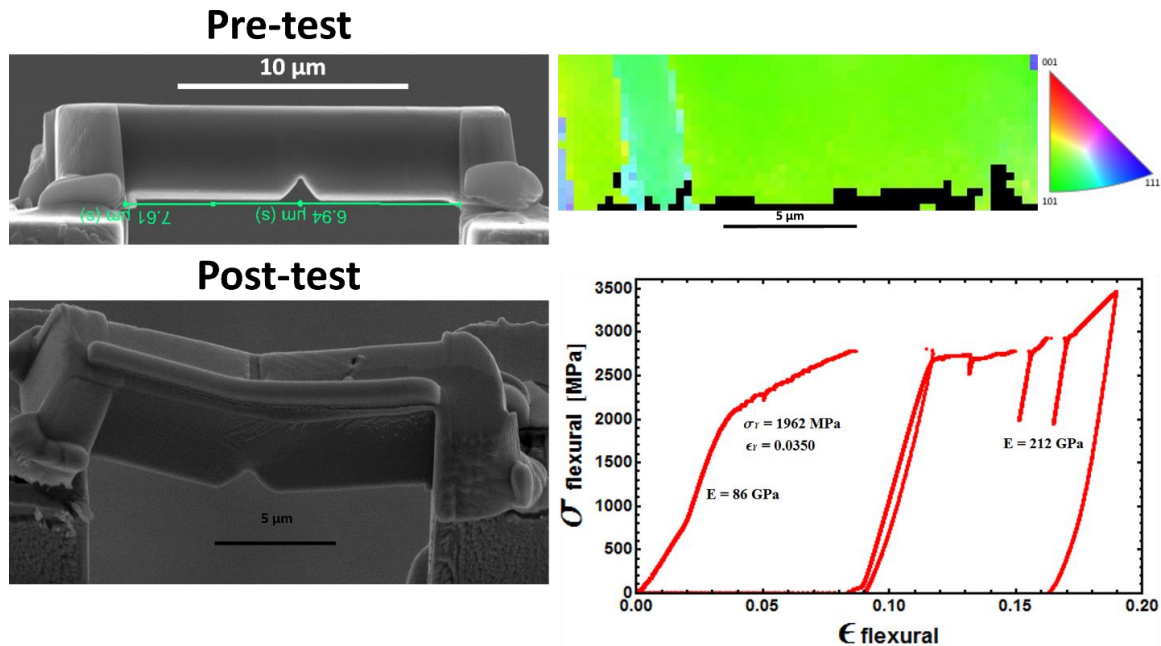


Figure 125. 53 dpa, $T_{irr} = 300\text{ }^{\circ}\text{C}$, notched, three-point bend specimen 4. The thin Pt deposited strip on the post-test image was introduced after the conclusion of the test for the purposes of thinning the sample down for SEM-STEM investigations.

5.3.5 67 dpa Low Irradiation Temperature Specimens

Four micro-bend specimens were manufactured and tested from Inconel X-750 material irradiated to 67 dpa at $180\text{ }^{\circ}\text{C}$; two of them were from the center of the spacer and two of them from within $100\text{ }\mu\text{m}$ from the edge of the spacer.

Center Specimen 1

Specimen 1 taken from the center of the component ($L = 13.38 \pm 1.24\text{ }\mu\text{m}$, width $W = 4.26 \pm 0.03\text{ }\mu\text{m}$, and height $H = 3.01 \pm 0.11\text{ }\mu\text{m}$) was loaded to a yield point of 1491 MPa . Two through-width cracks developed at the bottom surface when the mid-span outer fiber strain was about 8% and the outer fiber stress was 1862 MPa , as shown in the post-test image. There was some partial unloading due to significant deformation. The specimen was then able to reload till the mid-span outer fiber strain was about 10%. At this point, the right side support wedge broke down and the right side of indenter cone came into contact with the specimen, which triggered unloading.

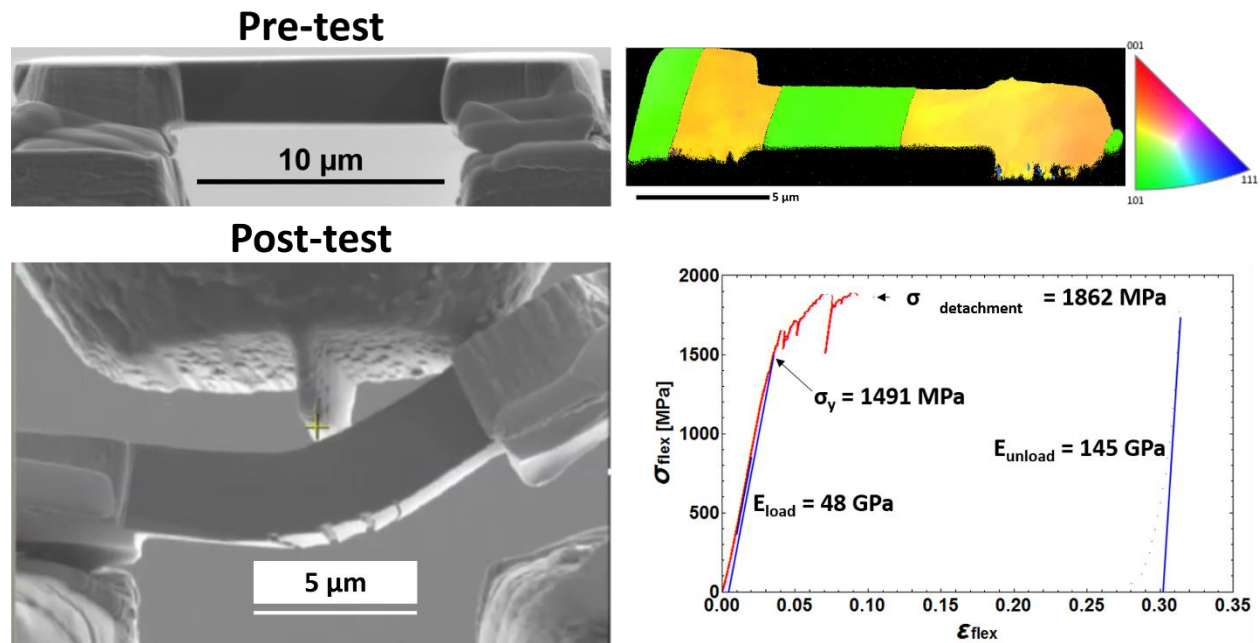


Figure 126. 67 dpa, $T_{irr} = 180\text{ }^{\circ}\text{C}$ three-point bend specimen 1.

Center Specimen 2

Specimen 2 taken from the center of the component ($L = 16.38 \pm 0.71\text{ }\mu\text{m}$, width $W = 6.39 \pm 0.01\text{ }\mu\text{m}$, and height $H = 4.00 \pm 0.10\text{ }\mu\text{m}$) was loaded to a yield point of 1798 MPa. Two through-width cracks and one nearly through-width crack developed at the bottom surface as shown at strains greater than 10%. The center crack, located in the middle of three cracks, formed first when the mid-span outer fiber strain was about 12% and the outer fiber stress was about 2519 MPa. There was some partial unloading due to cracking. The center, main crack developed at the bottom surface as shown in the post-test image in Figure 127 is very likely along the central grain boundary. It is not clear whether the other two cracks are located along the grain boundaries that are located closer to the ends of the micro-beam. The possibility does exist considering that grain boundaries may not be straight and can have angles in the specimen height direction.

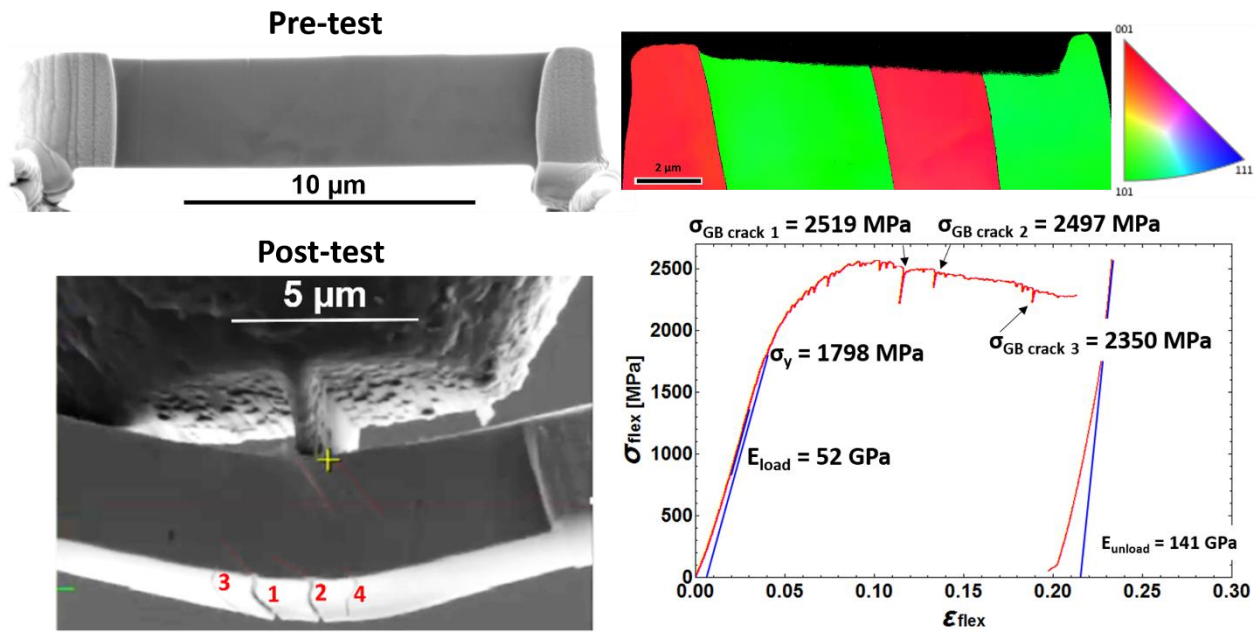


Figure 127. 67 dpa, $T_{irr} = 180\text{ }^{\circ}\text{C}$ three-point bend specimen 2. What appear to be potential grain boundary cracks are highlighted in red.

Edge Specimen 1

Edge specimen 1 ($L = 14.13 \pm 0.70\text{ }\mu\text{m}$, width $W = 2.31 \pm 0.06\text{ }\mu\text{m}$, and height $H = 2.84 \pm 0.21\text{ }\mu\text{m}$) was loaded to a yield point of 2376 MPa. Cracking occurred at the bottom surface near the mid-span location, as shown in the post-test image. The cracks developed at the bottom surface near the mid-span location as shown in the post-test image in Figure 128 are likely along the twin boundaries.

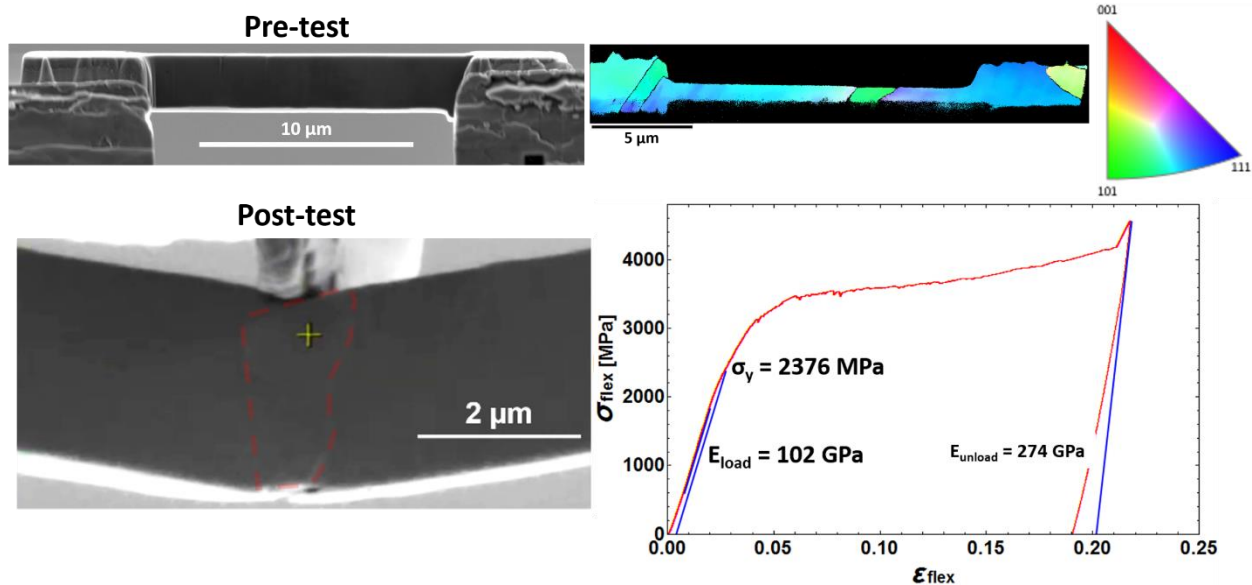


Figure 128. 67 dpa, $T_{irr} = 180\text{ }^{\circ}\text{C}$ three-point bend edge specimen 1. What appear to be potential grain boundary cracks are highlighted in red.

Edge Specimen 2

Edge specimen 2 ($L = 15.40 \pm 1.00\text{ }\mu\text{m}$, a width $W = 5.04 \pm 0.02\text{ }\mu\text{m}$, and a height $H = 3.65 \pm 0.04\text{ }\mu\text{m}$) was loaded to a yield point of 2045 MPa. Continued loading induced an abrupt snapping of the micro-beam at a stress of 2738 MPa as the specimen became unconstrained, leading to unloading at $\sim 4\%$ flexural strain on the midpoint outer fiber. No evidence of grain boundary cracking was observed; many parallel slip bands were imaged post-test.

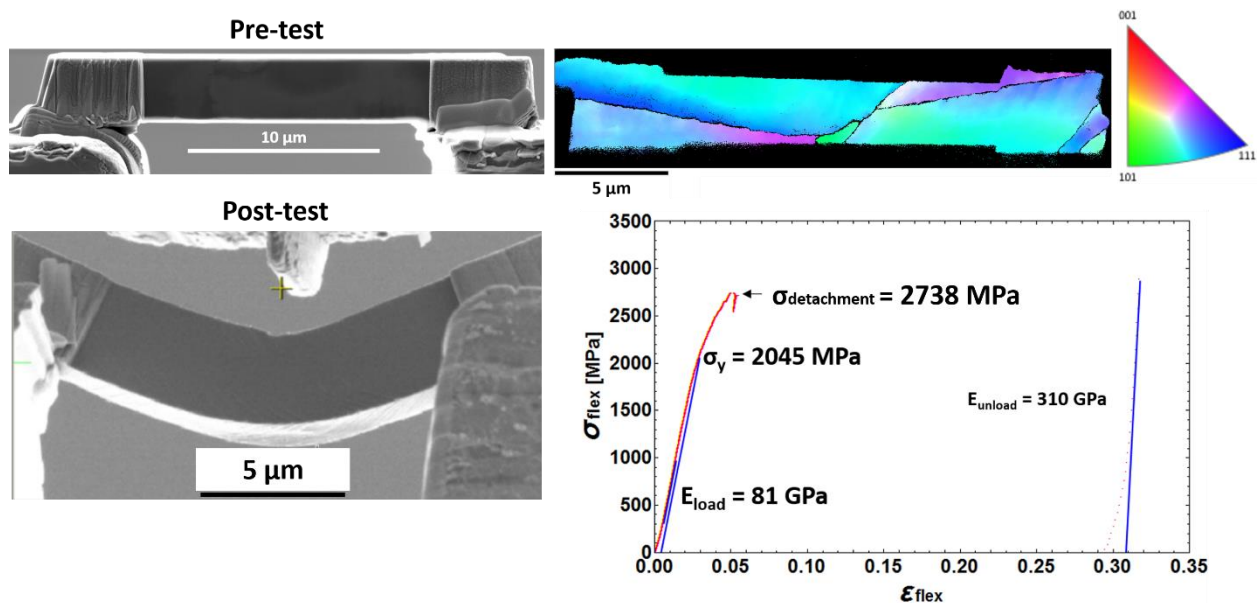


Figure 129. 67 dpa, $T_{irr} = 180\text{ }^{\circ}\text{C}$ three-point bend edge specimen 2.

5.3.6 67 dpa High Irradiation Temperature Specimens

Four micro-bend specimens were manufactured and tested from Inconel X-750 material irradiated to 67 dpa at 300 °C; two of them were from the center of the spacer and two of them from within 100 μm from the edge of the spacer.

Center Specimen 1

Center specimen 1 ($L = 15.03 \pm 0.36 \mu\text{m}$, width $W = 4.00 \pm 0.06 \mu\text{m}$, and height $H = 1.32 \pm 0.06 \mu\text{m}$) was loaded to a yield point of 2360 MPa. Deformation behavior beyond yielding shows dramatic stress increases, which are an artifact of the reduced height of this micro-beam in combination with this micro-beam remaining fully constrained throughout the duration of the test. Observable deformation occurs almost exclusively in the grain on the left, and the test was unloaded when the cone of the indenter punch contacted the severely bent micro-beam on the left-hand side at a flexural stress of $\sim 7.5\%$ on the outer fiber at the midpoint.

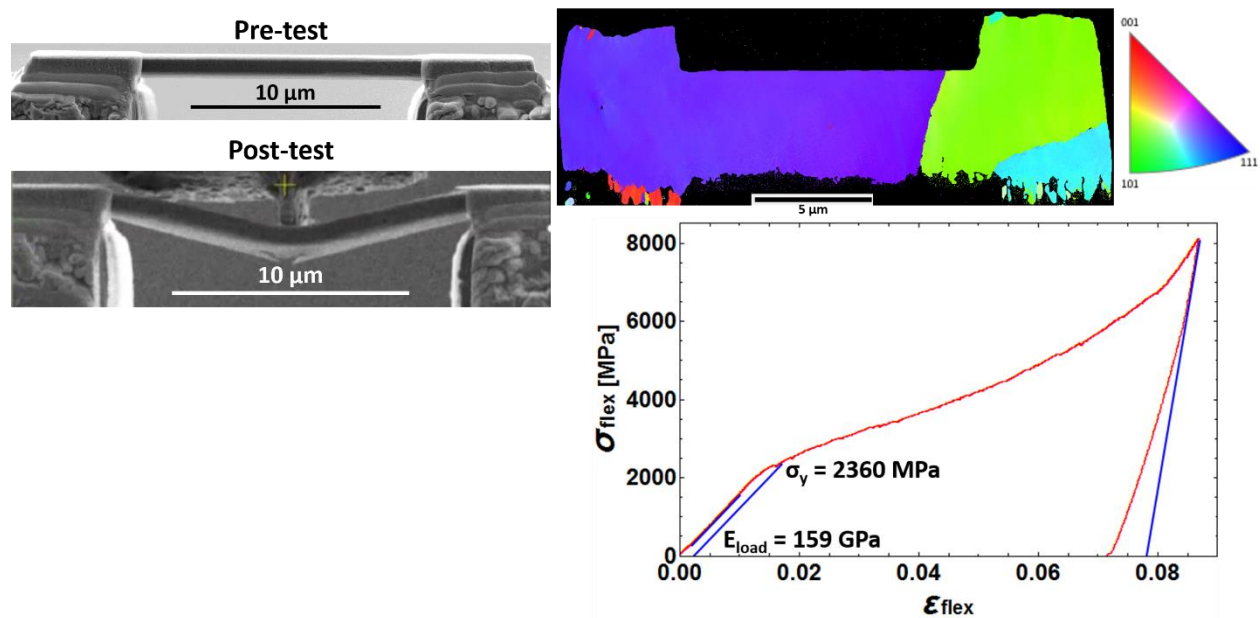


Figure 130. 67 dpa, $T_{irr} = 300 \text{ }^\circ\text{C}$ three-point bend center specimen 1.

Center Specimen 2

Center specimen 2 ($L = 14.80 \pm 0.34 \mu\text{m}$, a width $W = 5.97 \pm 0.14 \mu\text{m}$, and a height $H = 4.25 \pm 0.37 \mu\text{m}$) was loaded to a yield point of 2256 MPa. Further loading to a mid-point outer fiber flexural strain of $\sim 16\%$ at a stress of 3371 MPa caused significant bending when the beam was in an unconstrained state to induce a sharp jump in loading at which point the tip was unloaded.

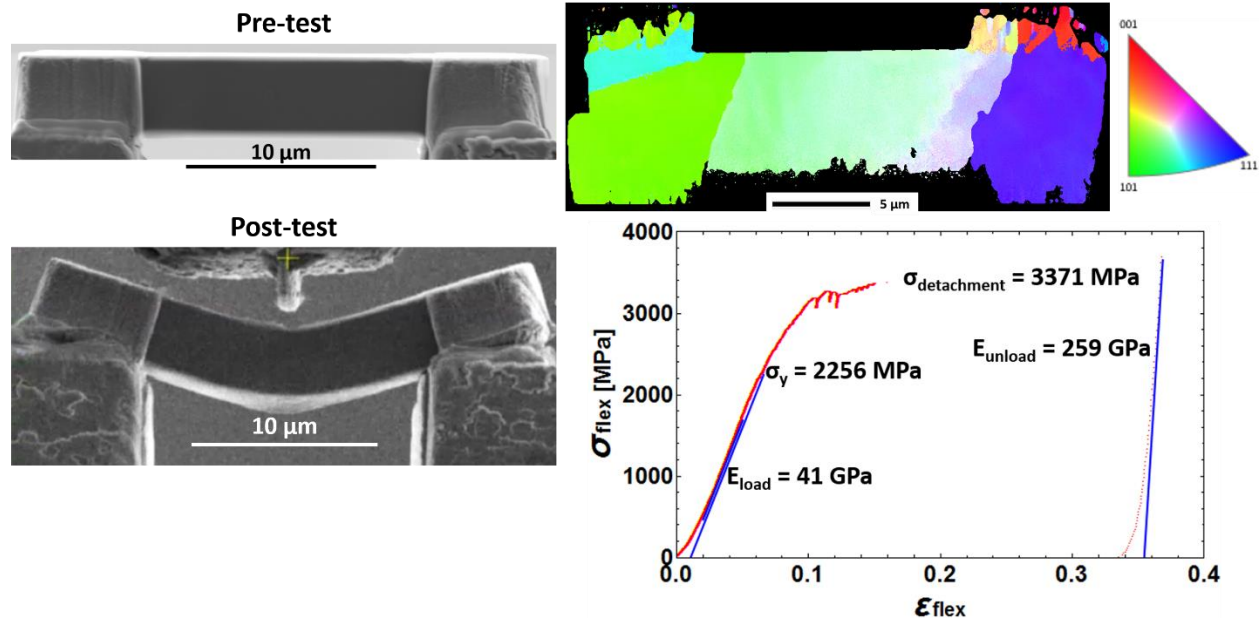


Figure 131. 67 dpa, $T_{irr} = 300$ °C three-point bend center specimen 2.

Edge Specimen 1

Edge specimen 1 ($L = 14.99 \pm 0.28$ μm, a width $W = 2.48 \pm 0.10$ μm, and a height $H = 2.28 \pm 0.07$ μm) was loaded to a yield point of 3380 MPa. Further loading led to a maximum stress of 4402 MPa at a midpoint outer fiber flexural strain of ~5%. At this point severe bending and contact at the side of the tip forced unloading.

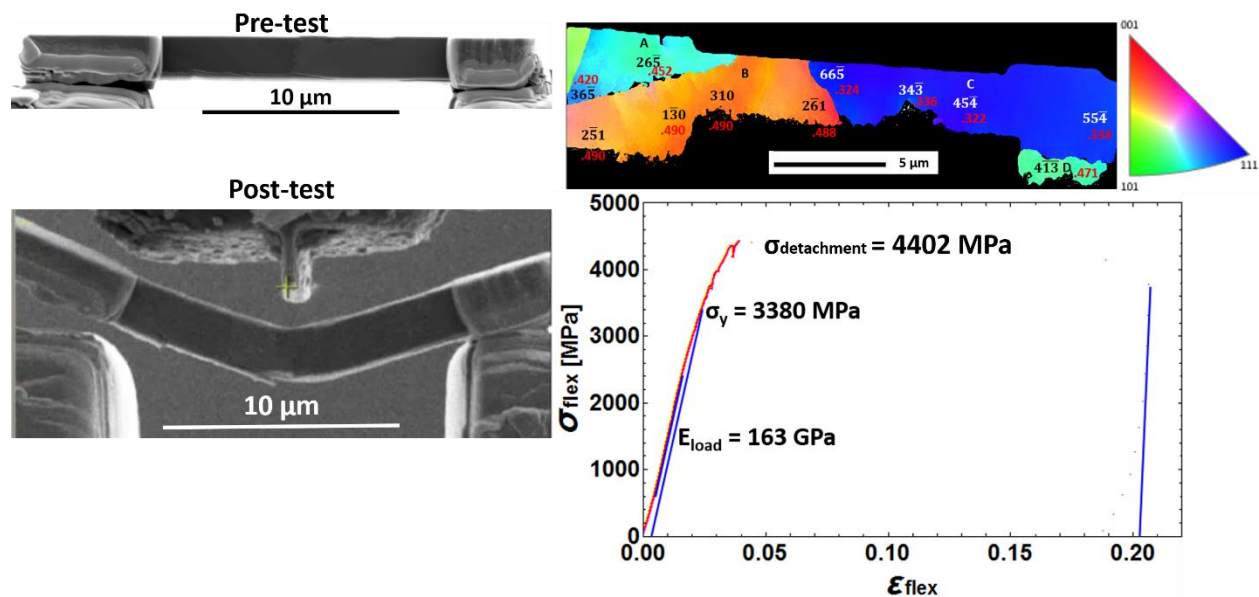


Figure 132. 67 dpa, $T_{irr} = 300$ °C three-point bend edge specimen 1.

Edge Specimen 2

Edge specimen 2 ($L = 15.30 \pm 0.31 \mu\text{m}$, a width $W = 3.55 \pm 0.05 \mu\text{m}$, and a height $H = 3.73 \pm 0.06 \mu\text{m}$) was loaded to a yield point of 2660 MPa. Soon after at a maximum stress of 3011 MPa, complete detachment on the left side after a severe bend of the micro-beam necessitated unloading at a midpoint flexural strain of $\sim 7\%$.

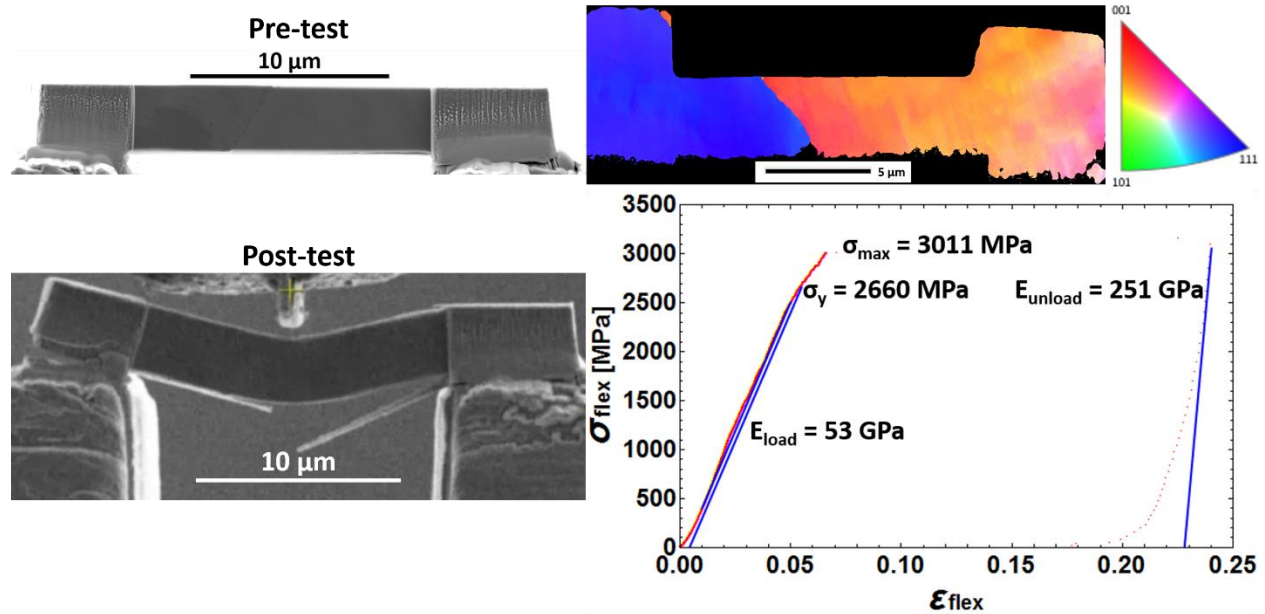


Figure 133. 67 dpa, $T_{irr} = 300 \text{ }^\circ\text{C}$ three-point bend edge specimen 2.

5.3.7 Summary

Representative flexural stress-strain responses of tests on specimens from each dose and temperature condition can be seen in Figure 131. For all tests, complete fracture of the specimens did not occur. In all cases dislocation slip on parallel slip planes along the deformed specimens was observed in real time as imaged by the SEM and in post-test SEM images. A summary of average 0.2% offset yield strength values for all irradiation conditions and spring locations can be found in Table 10.

Table 10: Micro Three-Point Bend Yield Strength and Critical Resolved Shear Stress (CRSS) of Inconel X-750 Spring Material

Irradiation Condition	Non-Irradiated		53 dpa $T_{avg} = 180^\circ\text{C}$	53 dpa $T_{avg} = 300^\circ\text{C}$	67 dpa $T_{avg} = 180^\circ\text{C}$		67 dpa $T_{avg} = 300^\circ\text{C}$	
	Edge	Center	Center	Center	Edge	Center	Edge	Center
Spring Location	Edge	Center	Center	Center	Edge	Center	Edge	Center
Aspect Ratio (L/H)	5:1	4.1:1	4:1	5.6:1	4.6:1	4.3:1	5.4:1	7.4:1
Number of Tests	5*	2	2	4	2*	2*	2	2
$\sigma_{y-0.2\% \text{ offset}}$ (MPa)	2074 ± 309	1335 ± 63	1561 ± 12	1875 ± 70	2211 ± 166	1645 ± 154	3020 ± 509	2308 ± 52
σ_{CRSS} (MPa)	935 ± 162	597 ± 28	763 ± 7	807 ± 42	988 ± 173	757 ± 77	1421 ± 323	1018 ± 95

***Note: Two non-irradiated outer edge specimens, and one edge and one center specimen irradiated to 67 dpa at 180 °C exhibited evidence of grain boundary cracks when loaded well beyond their yield points.**

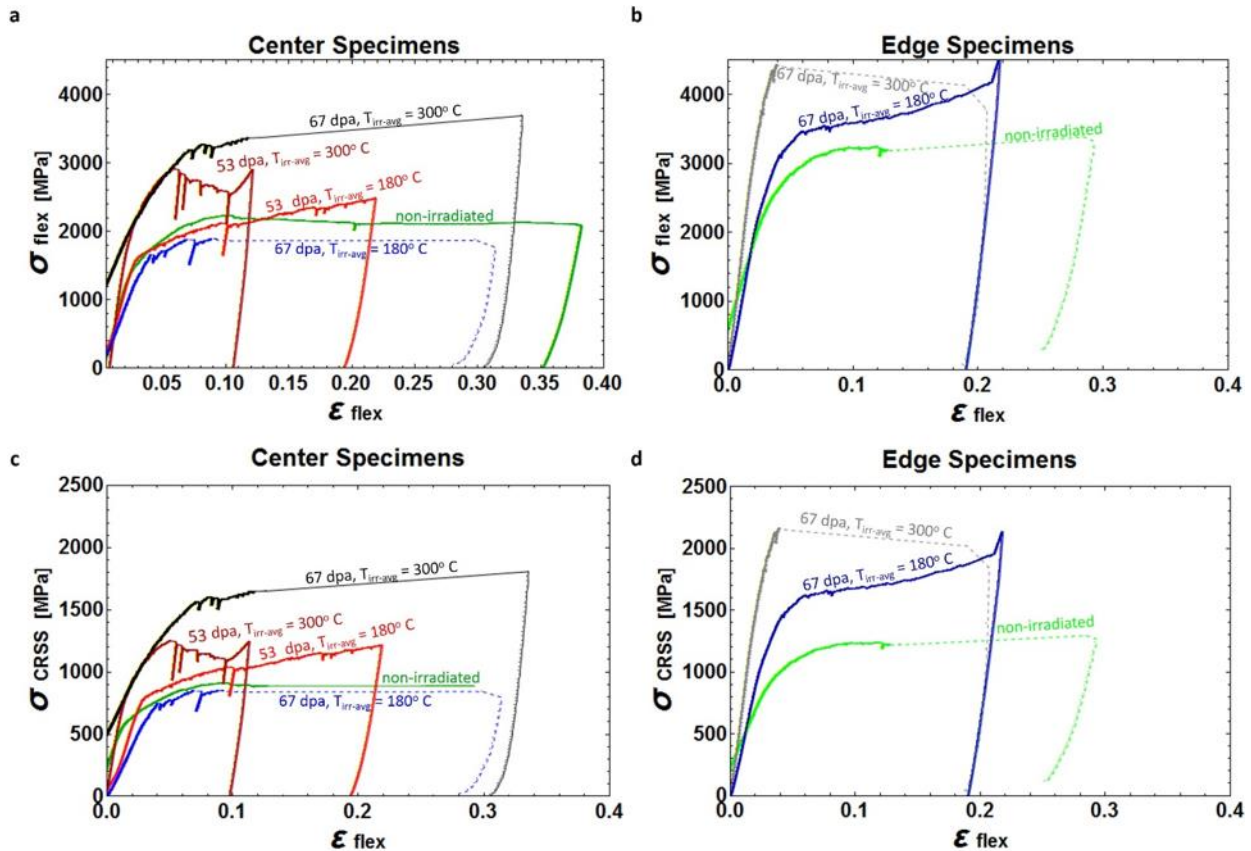


Figure 134. Representative flexural stress-strain curves calculated for the midpoint at the outer fiber of the (a) center and (b) edge specimens according to three-point bend theory for each irradiation condition. Loading curves plotted in terms of the critical resolved shear stress (CRSS) calculated from the matrix orientation at the highest stress point can be seen for the center specimens in (c) and edge specimens in (d).

The results shown in Figure 134 and Table 10 reveal a dramatic pre-existing, non-uniform, cold-working effect on the mechanical properties of Inconel X-750 springs. Material in the outer edge region of the spring was measured to be approximately 740 MPa stronger than material in the center of the spring. As the radiation dose on the component increases, this pre-existing effect remains as seen in the 67 dpa material. A difference in yield strengths between 67 dpa edge and center materials of 712 MPa occurs in the material with a higher irradiation temperature (300 ± 15 °C), and the material with a lower irradiation temperature (120-280 °C) still retains this difference as well. Edge material irradiated to 67 dpa is 566 MPa stronger compared to the center.

A matrix radiation strengthening effect with increasing dose is evident in all high temperature specimens, whereas changes in yield strengths of low temperature specimens appears either negligible or much subtler. High temperature center components irradiated to 53 dpa become strengthened by 540 MPa, and there is a further 530 MPa increase in yield between 53 dpa and 67 dpa components. Overall, this indicates a 1070 MPa increase between non-irradiated and highest dose center specimens. A similar effect is seen in the edge specimens; an approximate 1 GPa increase of yield strength is seen over 67 dpa. However, for low temperature material, non-irradiated, 53 dpa, and 67 dpa center specimens all have similar yield strength values. Edge region low temperature specimens also show similar yields before irradiation and after 67 dpa.

5.4 In-Situ Micro-Push-to-Pull Tensile Testing

Figures depicting the results for each micro-tensile specimen will consist of pre- and post-test SEM images, an EBSD map of its top surface indicating grain orientations with respect to the uniaxial tensile stress direction, and the associated engineering stress-strain curve.

5.4.1 Non-Irradiated Outer Edge Specimens

Specimen 1

Specimen 1 contains a high angle grain boundary at an angle of 32° with respect to the normal direction with the following dimensions: $L = 2.80 \pm 0.15$ μm , $W = 1.65 \pm 0.05$ μm , and $H = 0.99 \pm 0.02$ μm . When the specimen was loaded, it abruptly fractured along its grain boundary at a stress of 1592 MPa with no observable plasticity as seen in its stress-strain curve in Figure 132. No observable slip bands appeared on the specimen until its grain boundary fractured. After fracture, striations are visible in the top grain.

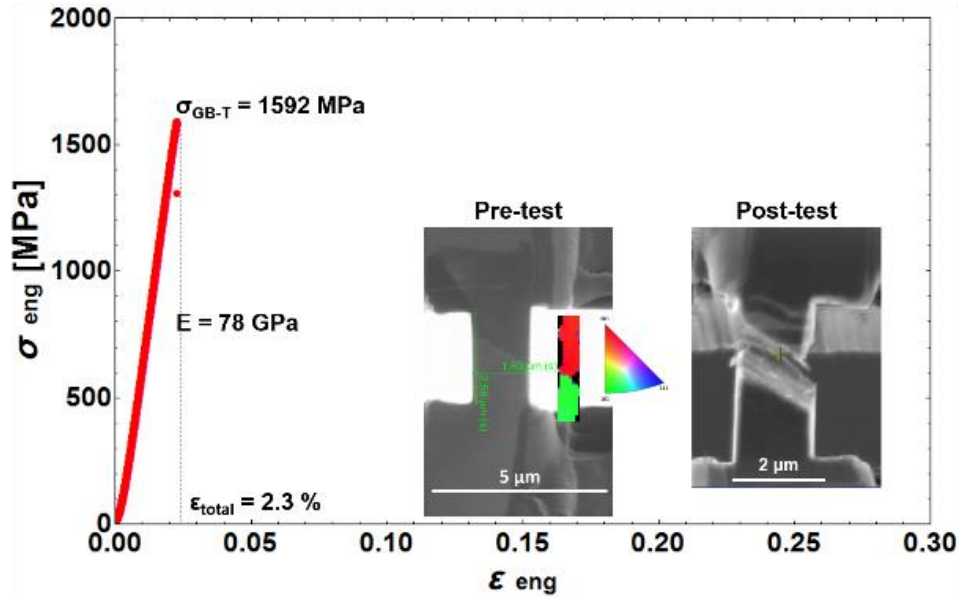


Figure 135. Non-irradiated, outer edge, micro-tensile specimen 1 fractured within its high angle grain boundary (44° misorientation angle)

Specimen 2

Specimen 2 contains a twin boundary at an angle of 5° with respect to the normal direction with the following dimensions: $L = 6.52 \pm 0.17 \mu\text{m}$, $W = 2.03 \pm 0.05 \mu\text{m}$, and $H = 1.20 \pm 0.05 \mu\text{m}$. The specimen yielded in its more weakly oriented bottom grain at a stress of $1001 \pm 7 \text{ MPa}$ as a first slip band appeared in this grain. Further loading produced many parallel slip bands in this grain until fracture occurred at a total elongation of 1.8% at a maximum stress of 1078 MPa.

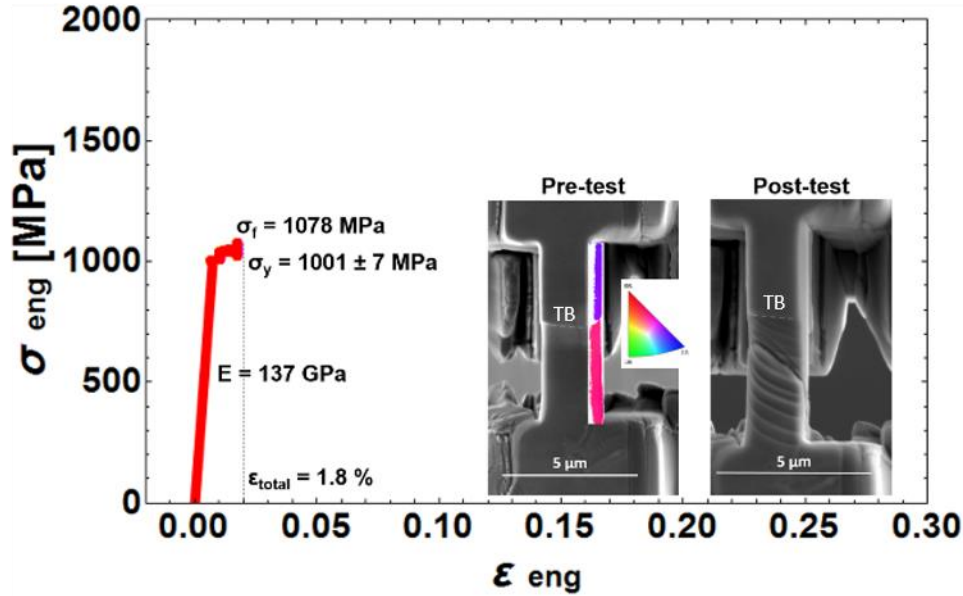


Figure 136. Non-irradiated outer edge micro-tensile specimen 2 containing a twin boundary

5.4.2 Non-Irradiated Center Specimens

Specimen 1

Specimen 1 contains a high angle grain boundary at an angle of 16° with respect to the normal direction with the following dimensions: $L = 1.91 \pm 0.12 \mu\text{m}$, $W = 1.34 \pm 0.02 \mu\text{m}$, and $H = 0.83 \pm 0.03 \mu\text{m}$. Plasticity first occurs in the lower, more weakly oriented grain at a yield point of 1043 MPa, followed by a significant amount of ductility leading to fracture within the lower grain at 16.6% total elongation after a plethora of slip bands were observed on the specimen.

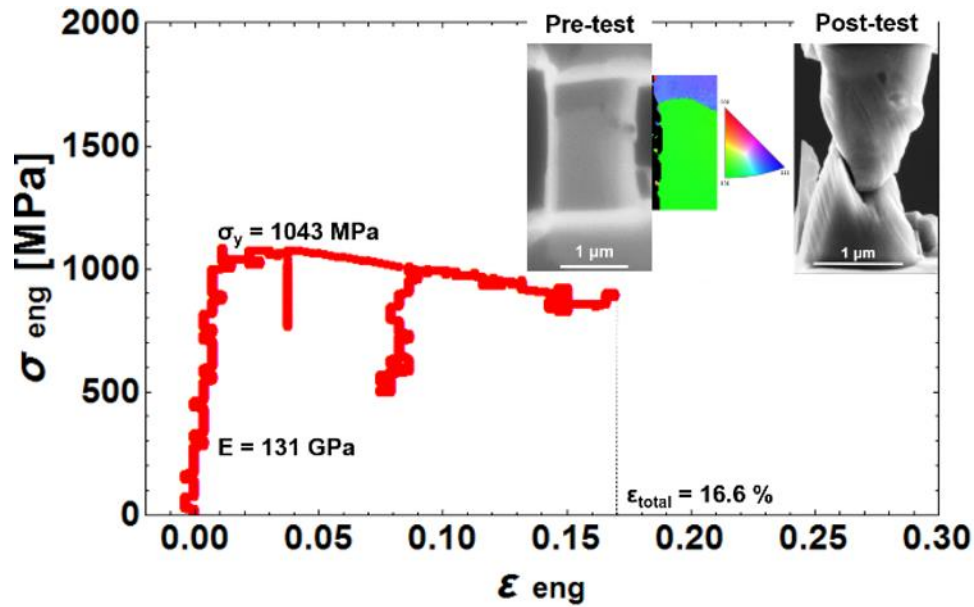


Figure 137. Non-irradiated center micro-tensile specimen 1 containing a high angle grain boundary (40° misorientation angle)

Specimen 2

Specimen 2 contains a both a high angle grain boundary and a twin boundary with the following dimensions: $L = 3.14 \pm 0.58 \mu\text{m}$, $W = 0.92 \pm 0.03 \mu\text{m}$, and $H = 1.19 \pm 0.05 \mu\text{m}$. Slip planes were found first within the top most grain (highest Schmid factor of 0.5). The specimen had a yield stress of 938 MPa and further loading led to necking within this grain which ultimately failed at 11.8% total elongation.

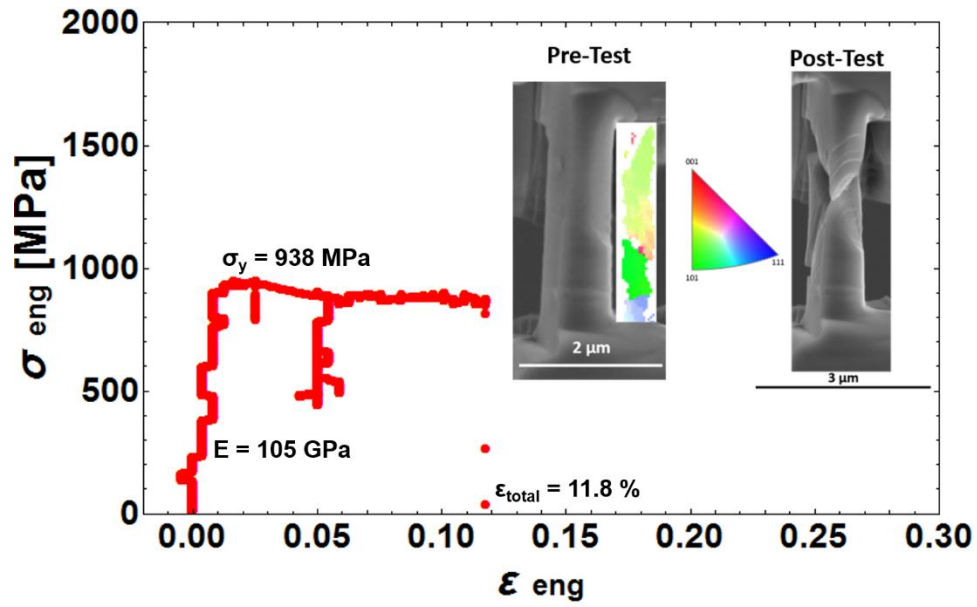


Figure 138. Non-irradiated center micro-tensile specimen 2 containing an upper twin boundary and a lower high angle grain boundary

5.4.3 Non-Irradiated Inner Edge Specimens

Specimen 1

Specimen 1 contains a twin boundary at an angle of 11° with respect to the normal direction with the following dimensions: $L = 3.08 \pm 0.21 \mu\text{m}$, $W = 1.58 \pm 0.04 \mu\text{m}$, and $H = 1.00 \pm 0.05 \mu\text{m}$. This specimen yielded at a stress of 614 MPa and had a maximum stress of 685 MPa. Parallel slip planes traversed across the twin boundary and failure occurred in the upper grain after a total elongation of 33%.

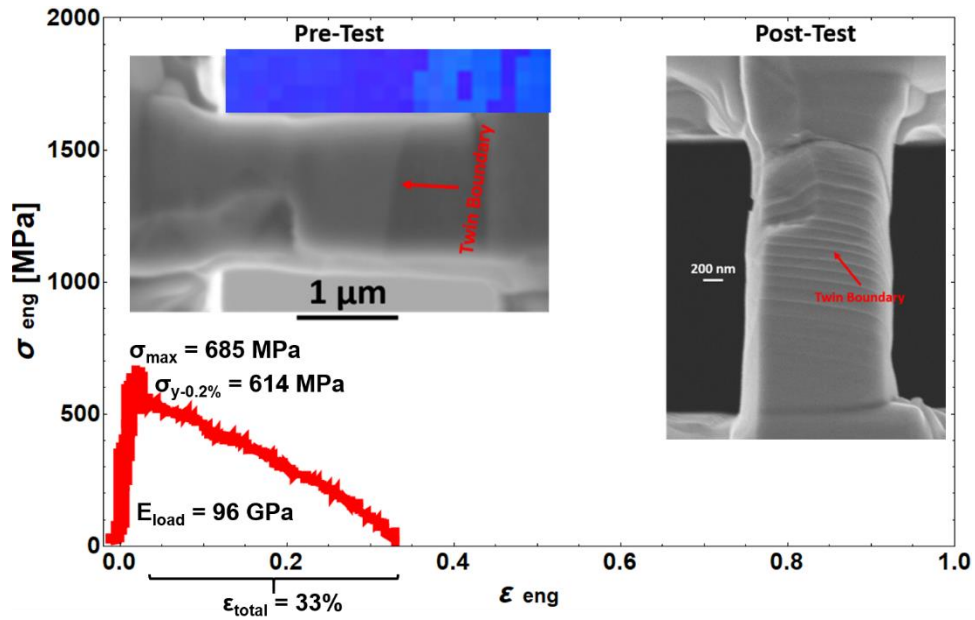


Figure 139. Non-irradiated inner edge micro-tensile specimen 1 containing a twin boundary

Specimen 2

Specimen 2 contains a high angle grain boundary at an angle of 43° with respect to the normal direction with the following dimensions: $L = 3.28 \pm 0.09 \mu m$, $W = 3.02 \pm 0.04 \mu m$, and $H = 1.33 \pm 0.02 \mu m$. This specimen yielded at a stress of 621 ± 9 MPa and had a maximum stress of 640 MPa. Initial deformation occurred in the bottom grain but subsequent deformation caused multiple slip systems to activate and intersect one another in both grains. Shearing parallel to the grain boundary eventually occurred at high strains leading to ultimate failure at 71.5%.

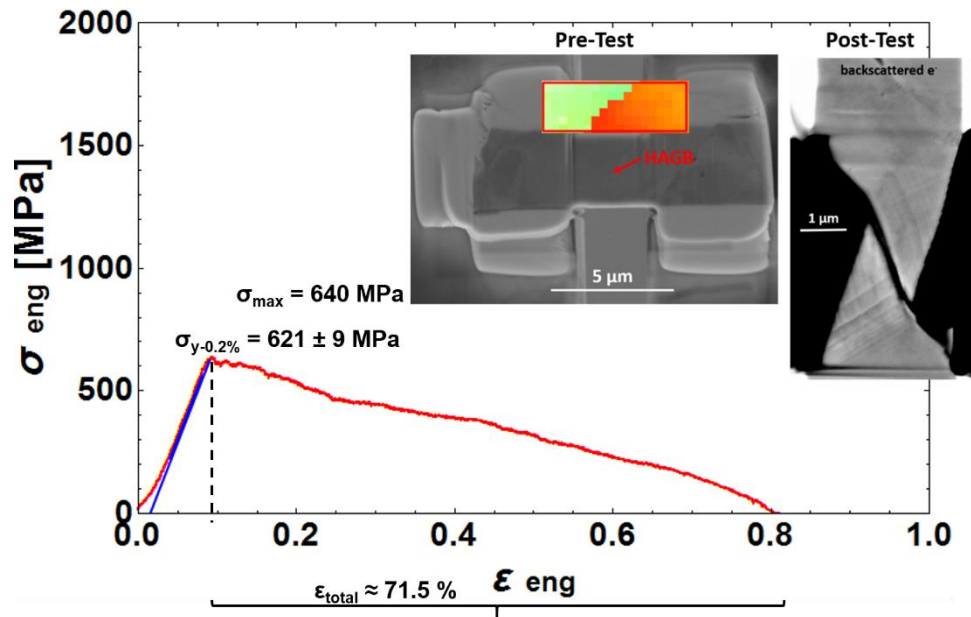


Figure 140. Non-irradiated inner edge micro-tensile specimen 2 containing a twin boundary

Specimen 3

Specimen 3 was a single-grained specimen with the following dimensions: $L = 2.76 \pm 0.24$ μm , $W = 2.72 \pm 0.04$ μm , and $H = 1.41 \pm 0.05$ μm . The specimen yielded at a stress of 767 MPa and reached a maximum stress of 871 MPa. Many parallel slip bands appear as the specimen is stretched to a total elongation of 75.2%.

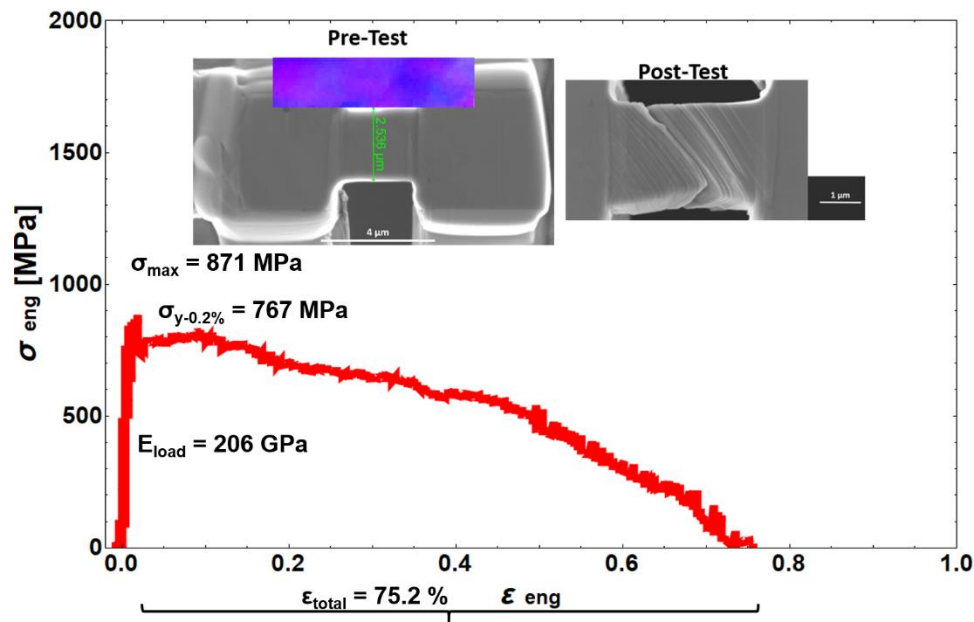


Figure 141. Single-grained non-irradiated inner edge micro-tensile specimen 3

Specimen 4

Specimen 4 was a single-grained specimen with the following dimensions: $L = 2.34 \pm 0.14 \mu\text{m}$, $W = 1.18 \pm 0.01 \mu\text{m}$, and $H = 1.03 \pm 0.01 \mu\text{m}$. The specimen yielded at a stress of 388 MPa and reached a maximum stress of 469 MPa. Significant nearly perfectly plastic behavior followed, leading to a total elongation of 70.4% at failure.

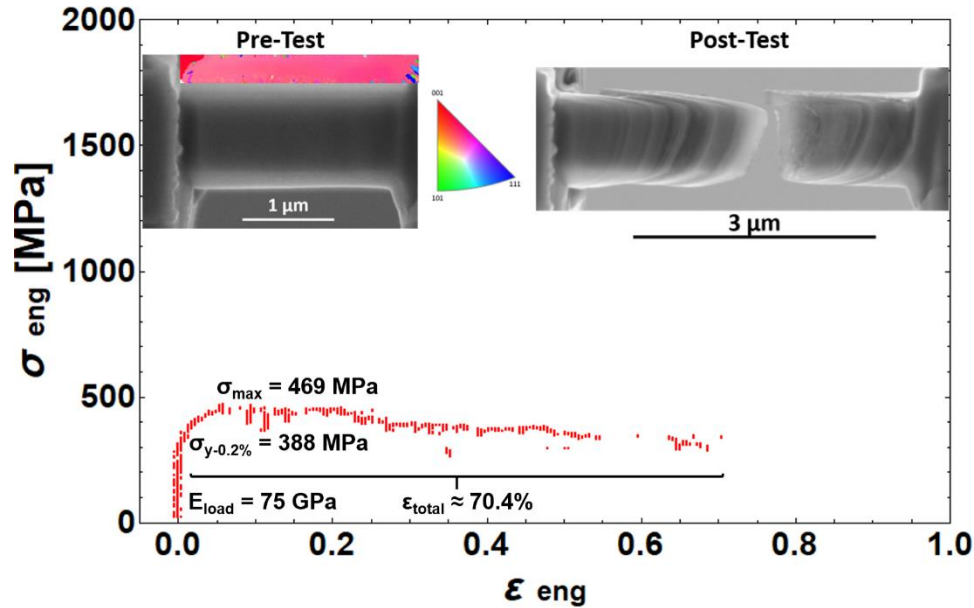


Figure 142. Single-grained non-irradiated inner edge micro-tensile specimen 4

Specimen 5

Specimen 5 contained a twin boundary with the following dimensions: $L = 2.55 \pm 0.14 \mu\text{m}$, $W = 2.76 \pm 0.03 \mu\text{m}$, and $H = 2.31 \pm 0.03 \mu\text{m}$. The specimen yielded at a stress of 696 MPa and reached a maximum stress of 824 MPa. Plasticity initiated at the center of the specimen and propagated throughout it, traversing across the twin boundary in the form of many parallel slip bands. The redeposition visible on the left hand side was accounted for in dimensional measurements so that it does not effect the mechanical properties calculations.

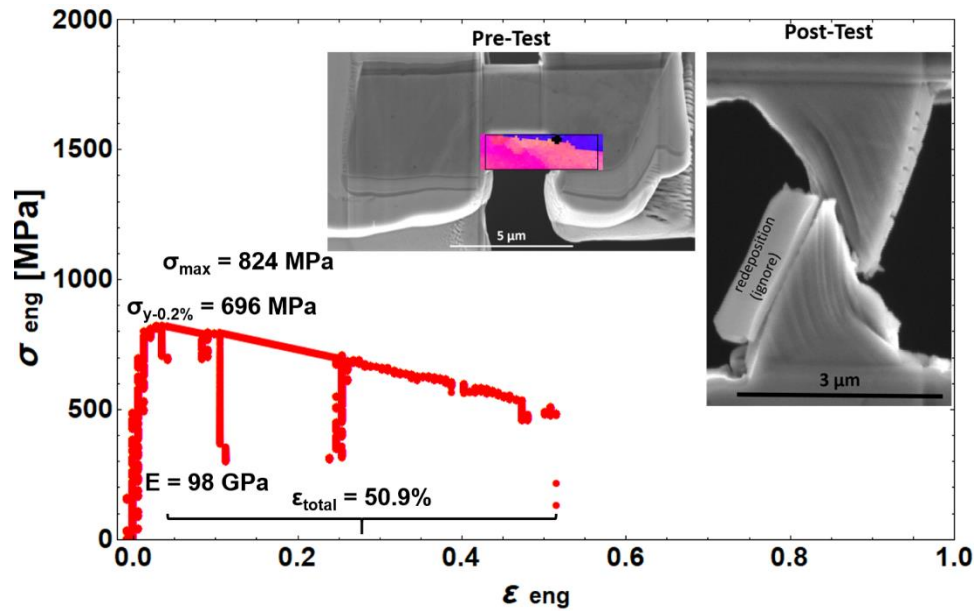


Figure 143. Non-irradiated inner edge micro-tensile specimen 5 containing a twin boundary

Specimen 6

Specimen 6 contained a high angle grain boundary with the following dimensions: $L = 2.46 \pm 0.06 \mu\text{m}$, $W = 1.95 \pm 0.02 \mu\text{m}$, and $H = 1.40 \pm 0.03 \mu\text{m}$. The specimen yielded at a stress of 630 ± 2 MPa and reached a maximum stress of 716 MPa. Visible plastic deformation appeared first within the top, weaker grain very close to the end of the top of the specimen. When higher strains were reached, slip planes are seen crossing the grain boundary. Failure occurred entirely within the top grain at a total elongation of 30.8%.

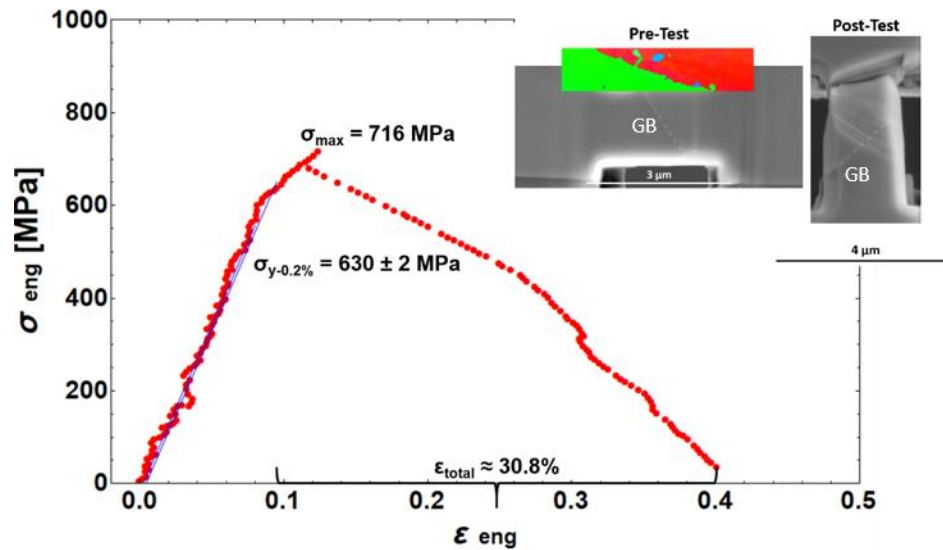


Figure 144. Non-irradiated inner edge micro-tensile specimen 6 containing a high angle grain boundary (misorientation angle $\sim 39^\circ$). Note that the engineering stress-strain curve here has not been corrected by DIC software due to an error with the data acquisition program that records the test video.

Specimen 7

Specimen 7 contained a high angle grain boundary with the following dimensions: $L = 3.03 \pm 0.24 \mu\text{m}$, $W = 2.12 \pm 0.04 \mu\text{m}$, and $H = 1.90 \pm 0.05 \mu\text{m}$. The specimen yielded at a stress of $736 \pm 16 \text{ MPa}$ and reached a maximum stress of 858 MPa . Plasticity initiated in the center of the specimen and propagated throughout. Multiple slip systems were active at the time of failure, which occurs in the lower grain, and a total elongation of 14.1% was reached.

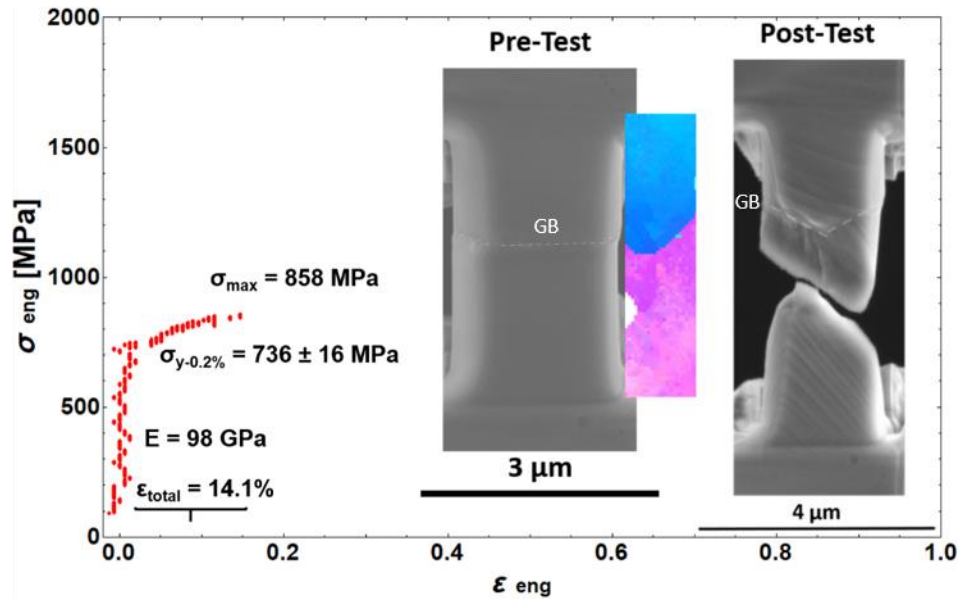


Figure 145. Non-irradiated inner edge micro-tensile specimen 7 containing a high angle grain boundary (misorientation angle $\sim 23^\circ$). Ultimate failure occurs just below the grain boundary in the lower grain.

5.4.4 67 dpa Low Irradiation Temperature Specimens

Edge Specimen 1

Specimen 1, taken $\sim 100 \mu\text{m}$ from the edge of the spacer, irradiated to 67 dpa at 180°C ($L = 2.36 \pm 0.44 \mu\text{m}$, $W = 0.97 \pm 0.03 \mu\text{m}$, and $H = 1.13 \pm 0.03 \mu\text{m}$) with a high angle grain boundary yielded in its more weakly oriented upper grain at a stress of 983 MPa. It reached a maximum stress of 1000 MPa as many slip planes appeared in the upper grain and failure occurred within this grain at a total elongation of 21.3%.

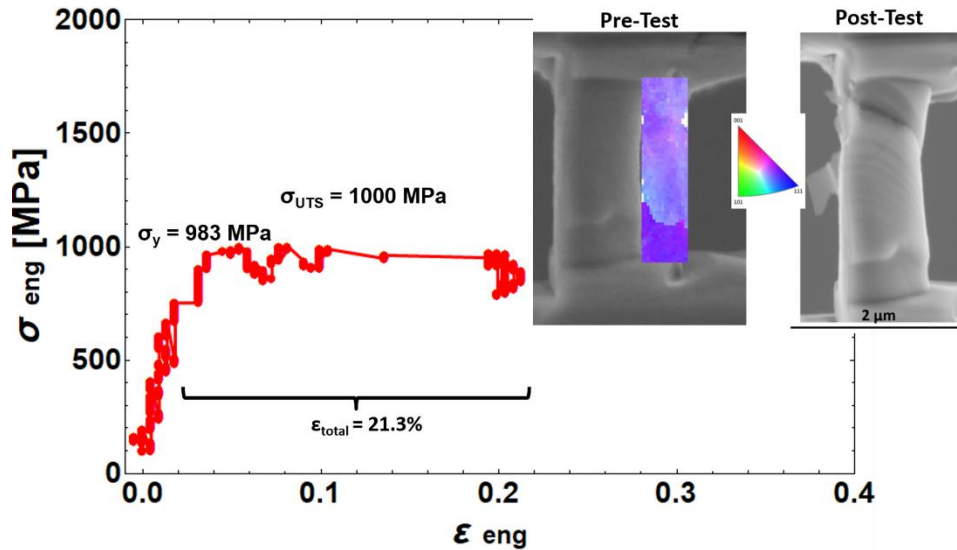


Figure 146. 67 dpa low temperature edge micro-tensile specimen 1 containing a high angle grain boundary (misorientation angle $\sim 51^\circ$)

Edge Specimen 2

Specimen 2, taken $\sim 100 \mu\text{m}$ from the edge of the spacer, irradiated to 67 dpa at 180°C ($L = 2.46 \pm 0.09 \mu\text{m}$, $W = 1.64 \pm 0.02 \mu\text{m}$, and $H = 1.29 \pm 0.05 \mu\text{m}$) with a high angle grain boundary abruptly fractured in its lower grain near its bottom after 1% total elongation at a stress of 891 MPa. Plastic slip planes were observed near the region where fracture occurred in the grain interior. A large carbide inclusion at the bottom corner is believed to be the point of crack initiation leading to failure as seen in the post-test image of the side of the specimen in Figure 147.

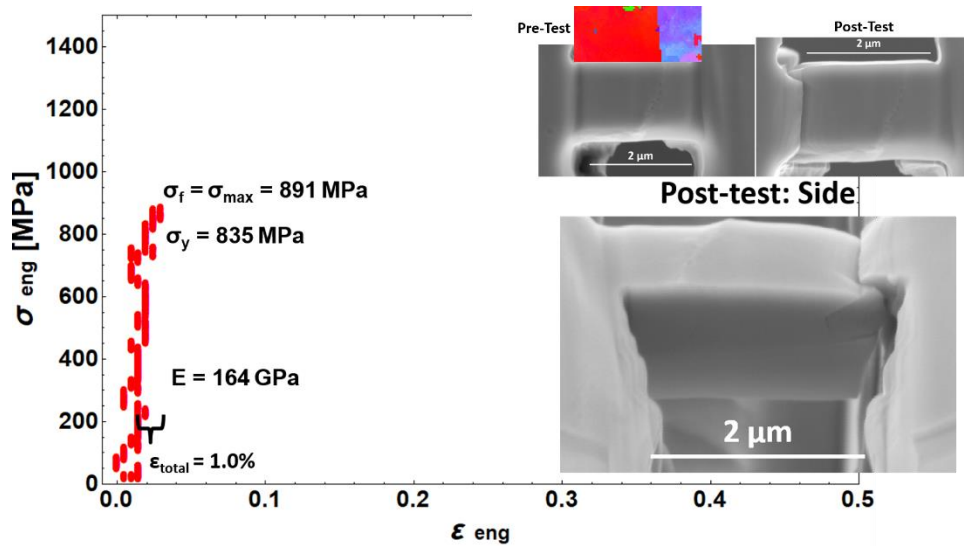


Figure 147. 67 dpa low temperature edge micro-tensile specimen 2 containing a high angle grain boundary (misorientation angle $\sim 54^\circ$). Brittle fracture occurs along the interface of a large inclusion seen on the upper right side surface.

Edge Specimen 3

Specimen 3, a micro-tensile sample containing a high angle grain boundary taken ~ 100 μm from the edge of the spacer, irradiated to 67 dpa at 180 $^\circ\text{C}$ ($L = 2.72 \pm 0.03$ μm , $W = 2.12 \pm 0.02$ μm , and $H = 1.82 \pm 0.02$ μm) yielded in its bottom grain at a stress of 667 MPa. This grain was very ductile and took on significant plastic deformation before the specimen failed at a total elongation of 41.4%.

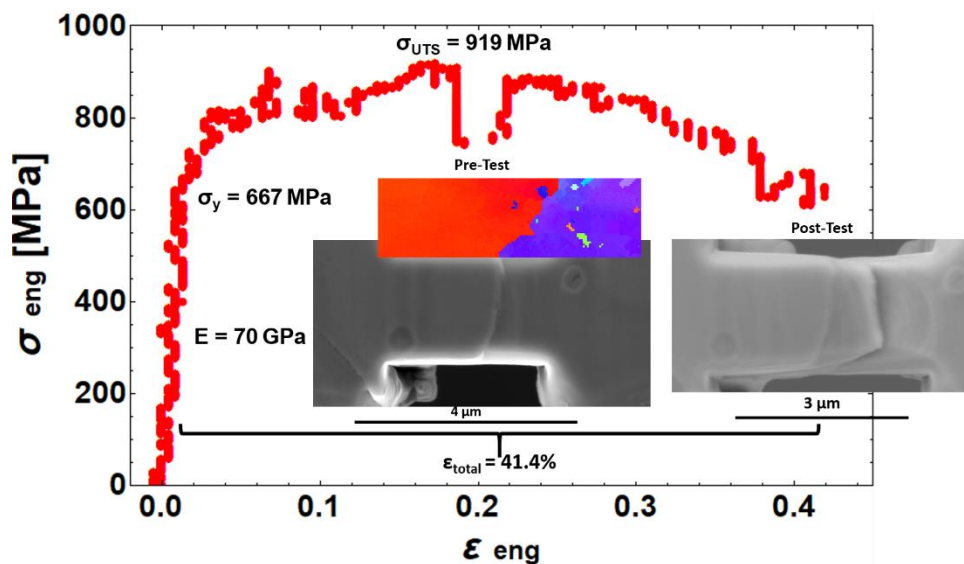


Figure 148. 67 dpa low temperature edge micro-tensile specimen 3 containing a high angle grain boundary (misorientation angle $\sim 54^\circ$)

Edge Specimen 4

Specimen 4, a single-grained micro-tensile sample taken $\sim 100 \mu\text{m}$ from the edge of the spacer, irradiated to 67 dpa at 180°C ($L = 2.51 \pm 0.22 \mu\text{m}$, $W = 1.26 \pm 0.07 \mu\text{m}$, and $H = 1.10 \pm 0.02 \mu\text{m}$) abruptly fractured at the bottom of the gauge at a total elongation of 1% at a stress of 641 MPa.

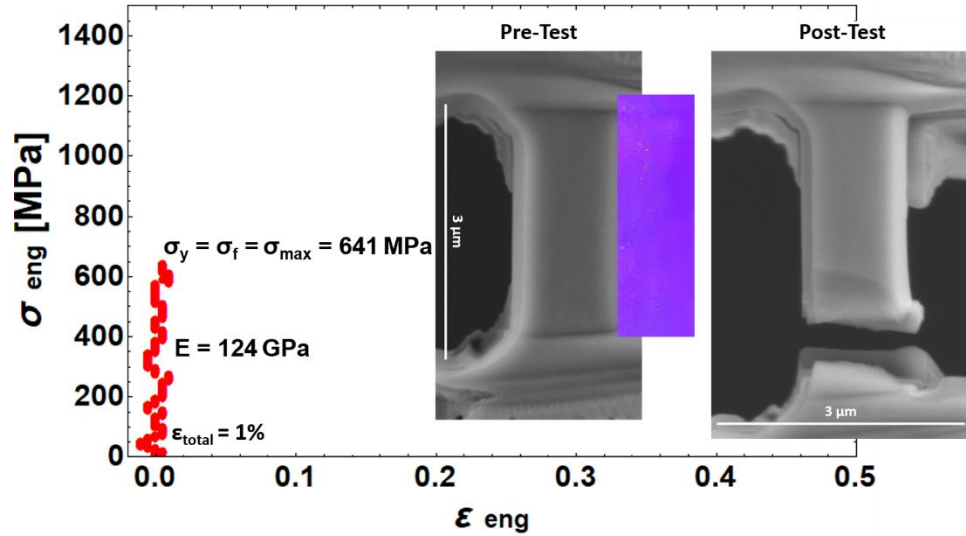


Figure 149. Single-grained 67 dpa low temperature edge micro-tensile specimen 4

Center Specimen 1

A single-grained specimen taken from the center of the garter spring irradiated to 67 dpa at 180°C ($L = 3.50 \pm 0.05 \mu\text{m}$, $W = 1.91 \pm 0.34 \mu\text{m}$, and $H = 2.00 \pm 0.02 \mu\text{m}$) yielded at a stress of 856 MPa, followed by a large load drop as a wide dislocation slip band appeared. The specimen exhibited significant ductility as new smaller parallel slip bands appeared. The specimen ultimately failed along the first large slip step at a total elongation of 26.4%.

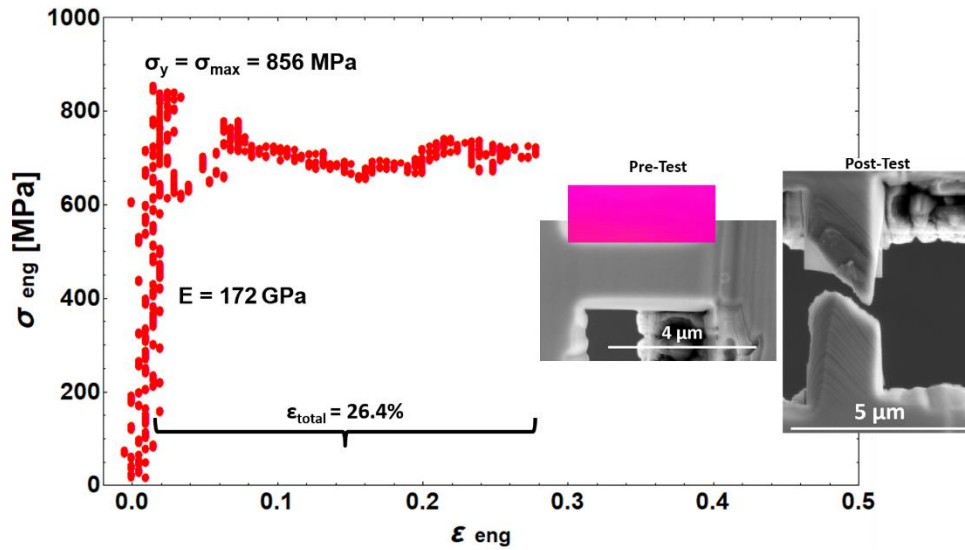


Figure 150. Single-grained 67 dpa low temperature center micro-tensile specimen

5.4.5 67 dpa High Irradiation Temperature Specimens

Edge Specimen 1

Specimen 1, taken $\sim 100 \mu\text{m}$ from the edge of the spacer, irradiated to 67 dpa at $300 \text{ }^\circ\text{C}$ ($L = 2.35 \pm 0.31 \mu\text{m}$, $W = 2.07 \pm 0.03 \mu\text{m}$, and $H = 1.78 \pm 0.05 \mu\text{m}$) with a high angle grain boundary yields in its top grain at a stress of 754 MPa. At higher strains beyond the yield point, the specimen fractures within its bottom grain at a total elongation of 13.7%.

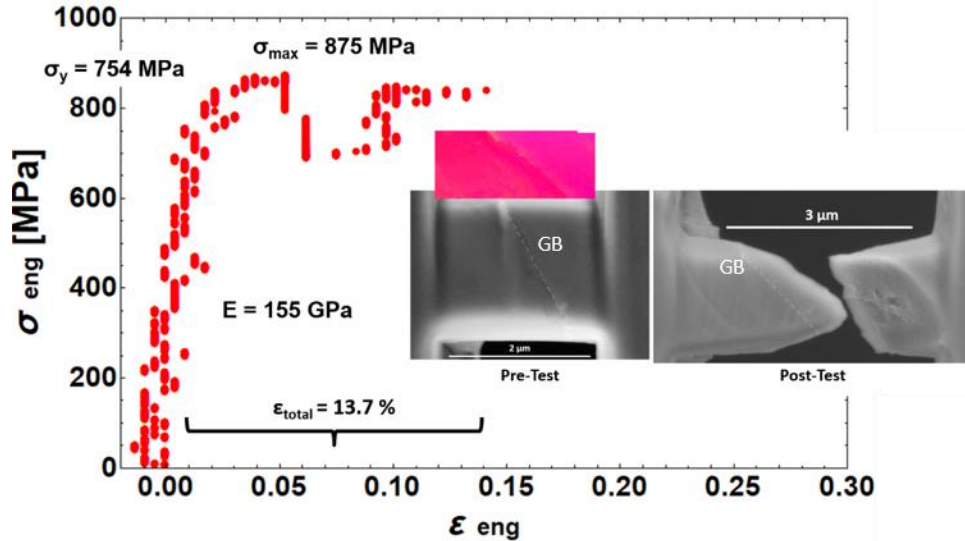


Figure 151. 67 dpa high temperature edge micro-tensile specimen 1 with a high angle grain boundary (28° misorientation angle)

Edge Specimen 2

Specimen 2, a single-grained specimen taken ~ 100 μm from the edge of the spacer, irradiated to 67 dpa at 300 $^\circ\text{C}$ ($L = 3.16 \pm 0.32$ μm , $W = 1.30 \pm 0.03$ μm , and $H = 1.38 \pm 0.02$ μm) failed at a stress of 1006 MPa and exhibited very little ductility. Large, parallel slip bands were observed throughout the length of the specimen. Two slip systems appear to have activated because slip bands are seen intersecting one another left of the fracture point in the post-test image.

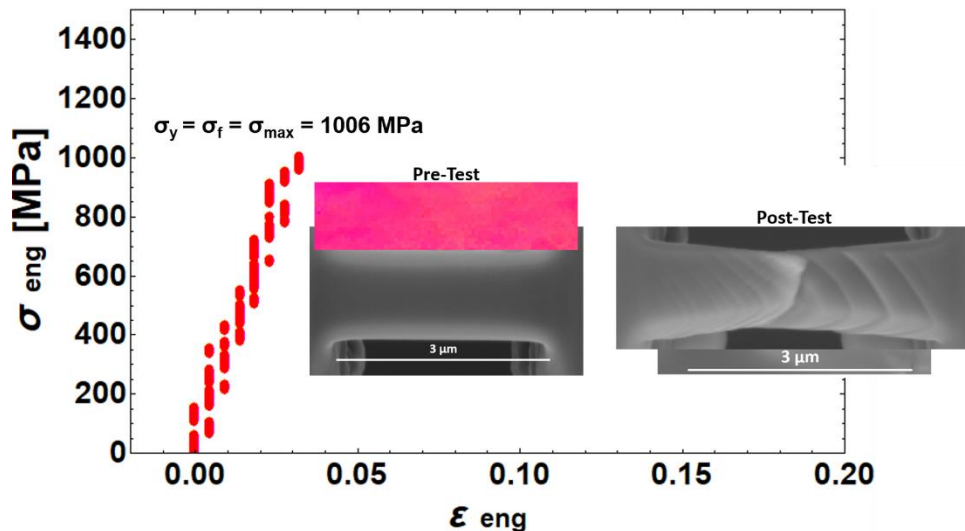


Figure 152. Single-grained 67 dpa high temperature edge micro-tensile specimen 2

Center Specimen 1

The first specimen taken from the center of the spacer irradiated to 67 dpa at 300 °C ($L = 5.66 \pm 0.32 \mu\text{m}$, $W = 1.90 \pm 0.02 \mu\text{m}$, and $H = 2.15 \pm 0.06 \mu\text{m}$) containing a twin boundary fractures below the grain boundary with very little total ductility. Post-test images due reveal slip planes parallel to the line direction of the twin boundary on both sides of the boundary. Presumably, deformation slip must have traversed the twin boundary with little to no impedance at the fracture stress of 659 MPa.

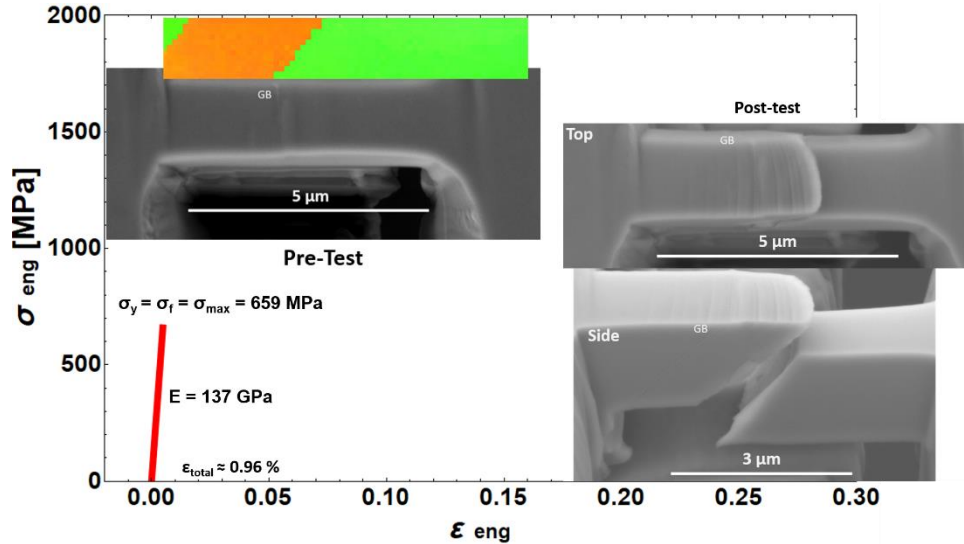


Figure 153. 67 dpa high temperature center micro-tensile specimen 1 containing a twin boundary

Center Specimen 2

The second specimen taken from the center of the spacer irradiated to 67 dpa at 300 °C ($L = 3.40 \pm 0.29 \mu\text{m}$, $W = 1.69 \pm 0.13 \mu\text{m}$, and $H = 1.64 \pm 0.03 \mu\text{m}$) was a single-grained sample containing a large carbide inclusion. The specimen fractured abruptly at a stress of 1235 MPa slightly above the carbide, but not along the matrix-carbide interface.

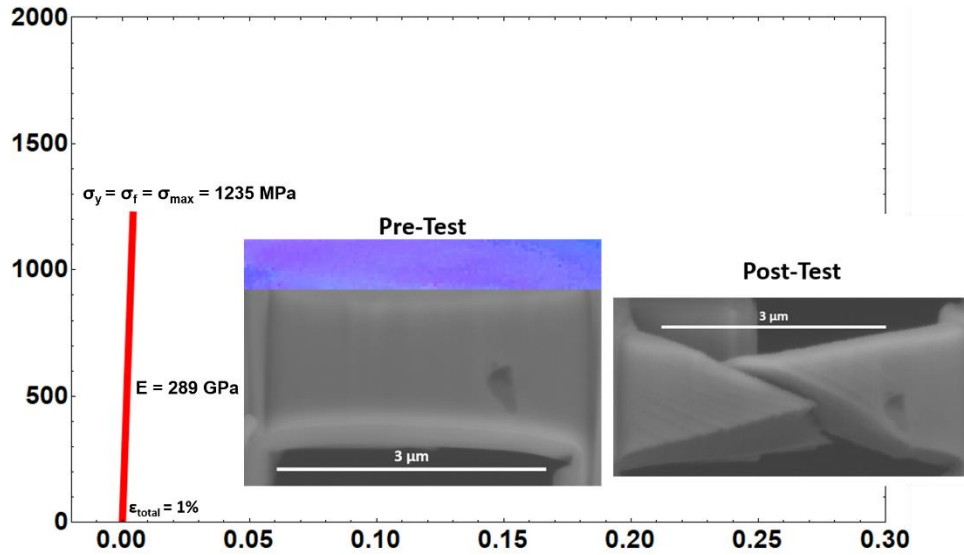


Figure 154. Single-grained 67 dpa high temperature center micro-tensile specimen 2

5.4.6 81 dpa Low Irradiation Temperature Specimen

One specimen from the 81 dpa spacer material irradiated at 180 °C was prepared and tested with the following dimensions: $L = 3.51 \pm 0.12 \text{ } \mu\text{m}$, $W = 1.88 \pm 0.07 \text{ } \mu\text{m}$, and $H = 0.84 \pm 0.02 \text{ } \mu\text{m}$. Although no EBSD map was obtained for this specimen, the visible boundaries are most likely to be twin boundaries due to their parallel nature and separation distance of less than one micron, since the average grain size of the material is $\sim 8 \text{ } \mu\text{m}$. The specimen first fractures along its upper boundary on the right. When viewing the test video frame-by-frame, it appears that the grain boundary crack propagates to the center of the specimen, but then it takes a path through the twin, quickly intersecting the bottom twin boundary, and propagating to the left edge of the specimen at which point the specimen fails. The failure stress of 1136 MPa can be treated as an effective boundary strength for the 81 dpa low temperature material. The specimen had a total elongation of 2.3%, and only minor plasticity within the twin boundary is observed.

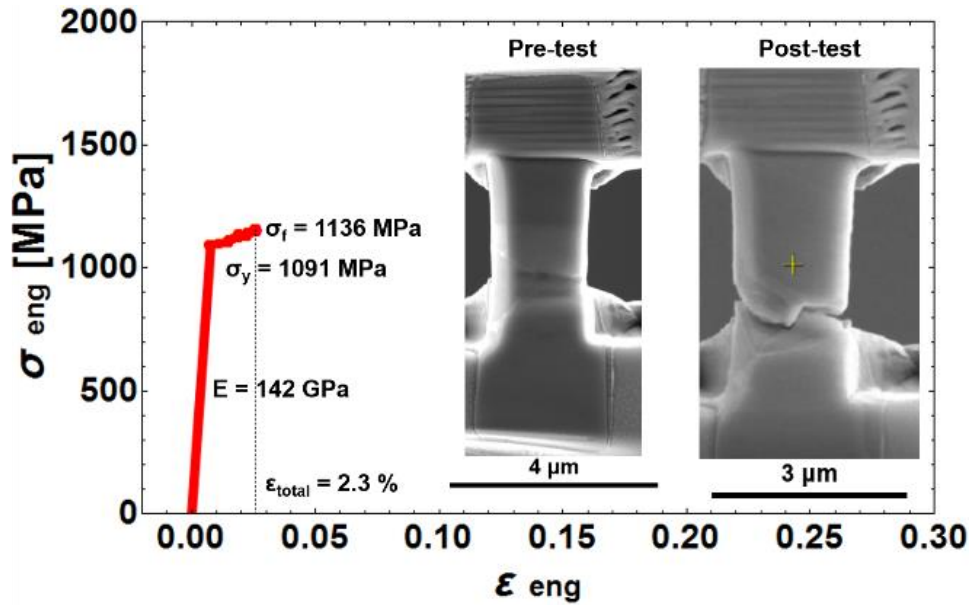


Figure 155. 81 dpa low temperature center micro-tensile specimen

5.4.7 81 dpa High Irradiation Temperature Specimens

Specimen 1

The first specimen extracted from the 81 dpa material irradiated at 300 °C was a single-grained specimen with dimensions $L = 1.75 \pm 0.20 \mu\text{m}$, $W = 1.52 \pm 0.03 \mu\text{m}$, and $H = 0.85 \pm 0.03 \mu\text{m}$. This specimen failed in a brittle manner, exhibiting little plastic behavior in its load-displacement curve during testing. Many large slip bands cover the entire length of the specimen. Its failure stress was measured to be 971 MPa.

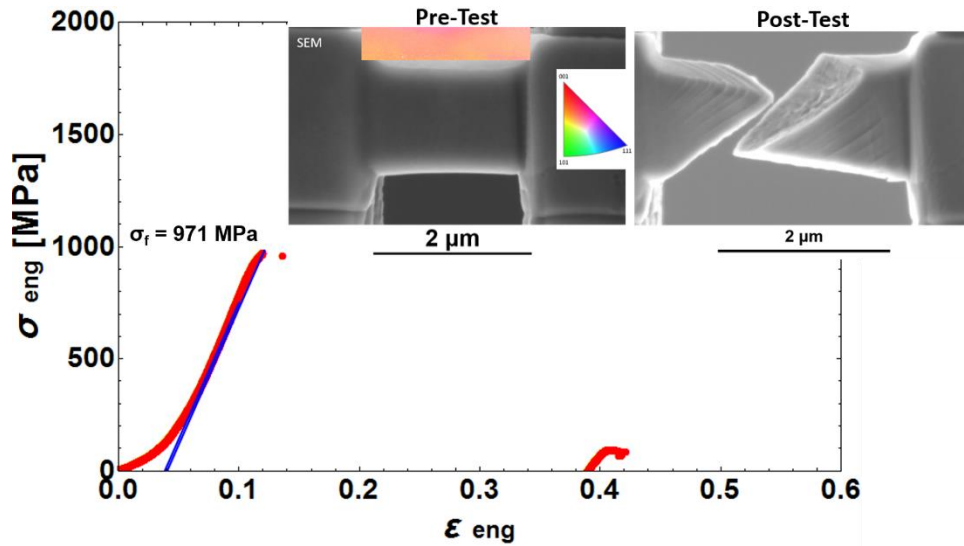


Figure 156. Single-grained 81 dpa high temperature center micro-tensile specimen

Specimen 2

The second specimen extracted from the 81 dpa material irradiated at 300 °C contained a high angle grain boundary with dimensions $L = 2.50 \pm 0.07 \mu\text{m}$, $W = 1.94 \pm 0.02 \mu\text{m}$, and $H = 1.53 \pm 0.02 \mu\text{m}$. Deformation initiated in the upper left in a large grain boundary carbide and a grain boundary crack quickly propagated across the specimen, leading to failure at a total elongation of 5.7%. Because this specimen exhibited grain boundary fracture, the failure stress of $1267 \pm 9 \text{ MPa}$ can be considered a high angle grain boundary strength for the 81 dpa high temperature material. High resolution post-test images reveal many narrow slip bands within the smaller boundary in the upper right, which may explain the minor plasticity in the stress-strain curve between yielding and failure. When viewing the test video, an abrupt fracture within the grain boundary appears simultaneously to these slip bands.

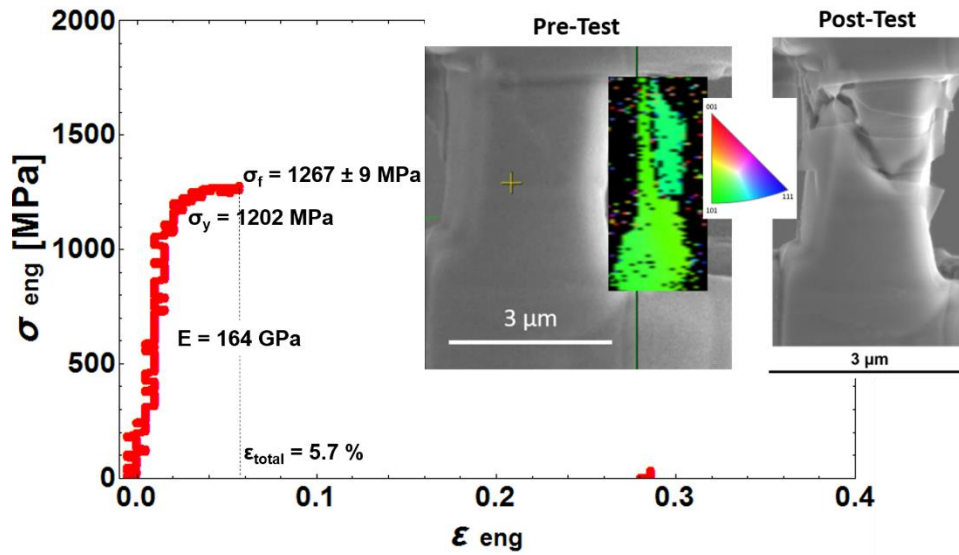


Figure 157. 81 dpa high temperature center micro-tensile specimen with a high angle grain boundary ($\sim 55^\circ$ misorientation angle)

5.4.8 Summary

A compilation of all engineering stress-strain curves for all irradiation conditions studied: non-irradiated, 67 dpa, and 81 dpa at both irradiation temperatures (180 °C and 300 °C) can be found in Figure 155. A mechanical data summary table providing yield strength, failure strength, and total elongation for each specimen tested is given in Table 11. In addition, Table 11 presents the measured angles of each grain boundary with respect to their deviation from the normal plane in both the top and side surfaces of the micro-tensile specimen. Resolved shear and normal stresses on the grain boundaries at the yield point and failure point are calculated accordingly and will be the subject of a discussion section in the next chapter.

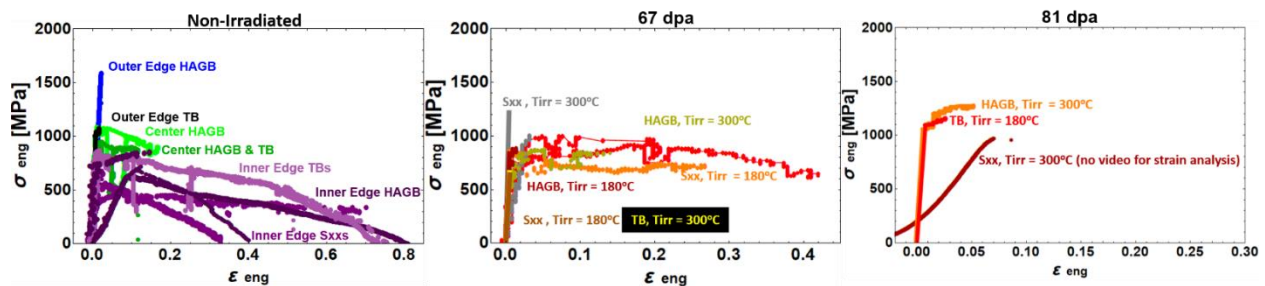


Figure 158. Engineering stress-strain curves of all micro-tensile, push-to-pull, Inconel X-750 specimens

Table 11. Mechanical Data Summary Table for Push-to-Pull Inconel X-750 Micro-tensile Specimens

Irradiation Condition	Component Location	Boundary Type	θ_{GB-Top} [°]	$\theta_{GB-Side}$ [°]	σ_y (MPa)	σ_{CRSS} (MPa)	$\sigma_{GB-N y}$ (MPa)	$\sigma_{GB-shear y}$ (MPa)	$\sigma_{failure/UTS}$ (MPa)	$\sigma_{GB-N failure}$ (MPa)	$\sigma_{GB-shear failure}$ (MPa)	E_{total} (%)
Non-Irradiated	Outer Edge	HAGB	31.6	66.3 ± 6.4	N/A	N/A	N/A	N/A	1592	186	261	2.3
		TB	5.4	64.9 ± 3.9	1001 ± 7	454 ± 2	179 ± 1	36	1078	193	39	1.8
	Center	HAGB	18.0 ± 2.7	20.7 ± 5.1	1043	461	824	101	1086	858	105	16.6
		HAGB & TB closest to center	48.5 ± 0.6	63.0 ± 2.1	938	466	84	187	950	86	190	11.8
	Inner Edge	Sxx	N/A	N/A	388	190	N/A	N/A	469	N/A	N/A	70.4
		Sxx	N/A	N/A	767	313	N/A	N/A	871	N/A	N/A	75.2
		TB	11.0 ± 1.8	1.5 ± 1.1	614	241	591	3	685	660	3	33
		TB	76.4 ± 1.1	44.2 ± 4.6	696	284	20	80	824	23	94	50.9
		HAGB	42.5 ± 0.2	13.7 ± 0.3	621 ± 9	304 ± 4	319 ± 5	71 ± 1	640	329	73	~71.5
		HAGB	1.0 ± 0.3	15.0 ± 2.2	736 ± 16	315 ± 36	687 ± 15	3	858	801	4	14.1
HAGB	32.8 ± 0.6	21.3 ± 3.2	630 ± 2	271 ± 15	386 ± 1	97	716	439	110	~30.8		
81 dpa $T_{irr} = 180$ °C	Center	most likely TB (not confirmed by EBSD)	13.6 ± 3.8	17.8 ± 2.0	1091	N/A	933	72	1136	971	75	2.3
81 dpa $T_{irr} = 300$ °C	Center	Sxx	N/A	N/A	971	476	N/A	N/A	971	N/A	N/A	-
		HAGB	56.1 ± 1.5	29.1 ± 2.1	1202	N/A	286	237	1267 ± 9	301 ± 2	249 ± 2	5.7
67 dpa $T_{irr} = 180$ °C	~100 μ m from Edge	HAGB	2.3 ± 2.0	21.8 ± 8.5	983	459	850	14	1000	865	14	21.3
		HAGB (matrix carbide inclusion)	21.4 ± 1.6	69.9 ± 1.9	835	341	85	92	891	91	98	1.0
		HAGB	10.5 ± 2.7	31.7 ± 1.3	667	253	467	53	919	644	74	41.4
	Center	Sxx	N/A	N/A	641	262	N/A	N/A	641	N/A	N/A	1.0
67 dpa $T_{irr} = 300$ °C	~100 μ m from Edge	Sxx	N/A	N/A	856	381	N/A	N/A	856	N/A	N/A	26.4
		HAGB	28.3 ± 1.3	1.4 ± 1.4	754	342	583	8	875	677	9	13.7
	Center	Sxx	N/A	N/A	1006	456	N/A	N/A	1006	N/A	N/A	3.2
		TB	5.3 ± 2.2	40.7 ± 2.1	659	320	376	30	659	376	30	0.96
Sxx	N/A	N/A	1235	557	N/A	N/A	1235	N/A	N/A	1.0		

Sxx = single-grained, HAGB = high angle grain boundary, TB = twin boundary, CRSS = critical resolved shear stress

Angles are deviations from normal to the loading direction.

$$\sigma_N = \sigma (A/A_{GB}) \cos\theta_{top} \cos\theta_{side}$$

$$\sigma_{Shear} = \sigma (A/A_{GB}) \sin\theta_{top} \sin\theta_{side}$$

Note: The specimen highlighted in red failed along the interface between a large inclusion and the matrix grain interior unlike the rest of the specimens.

5.5 Nanoindentation: Non-Irradiated Inconel X-750

The results from 200 nm deep Berkovich indents confirm the evidence of pre-existing cold-work created during fabrication processes. As seen in the residual strain map in Figure 51, it has been well documented that wire drawing and coiling processes produce residual strains and stresses. Residual compressive stresses remain in the inner diameter region from 10-20% cold working performed to coil the component, whereas 10-20% cold working from coiling in the outer diameter region produces residual tensile stresses. In addition, grinding in the outer region so that the component is “fit to size”

produces additional hardening. The nanoindentation results shown in Figure 159 indicate that the hardness in the center region within 100 μm of the midpoint of the component is 5.0 ± 0.2 GPa, whereas the hardness in regions $> 100 \mu\text{m}$ away from the center is 5.4 ± 0.2 GPa. If only indents within 100 μm of the outer edge are considered (highlighted in blue in Figure 156), the hardness in this region that underwent additional grinding is 6.0 ± 0.5 GPa.

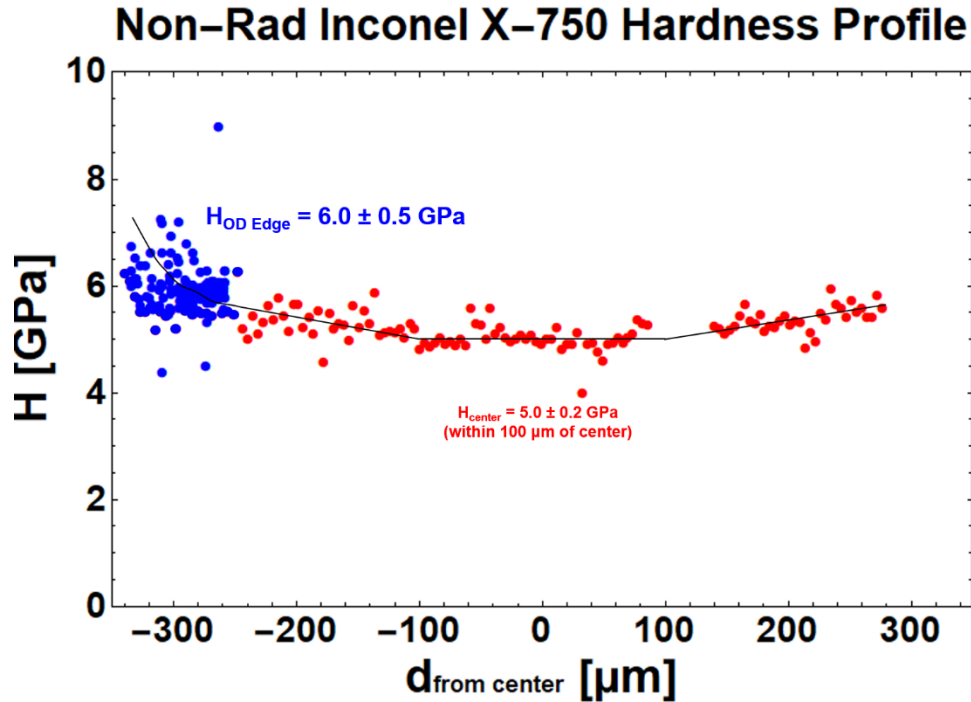


Figure 159. 200 nm Berkovich indents hardness profile performed on the cross-section of a non-irradiated Inconel X-750 component

The elastic modulus of the non-irradiated Inconel X-750 component calculated using equation (32) and the reduced modulus values, E_r , was determined to be 230 ± 22 GPa. The elastic modulus profile is given in Figure 160.

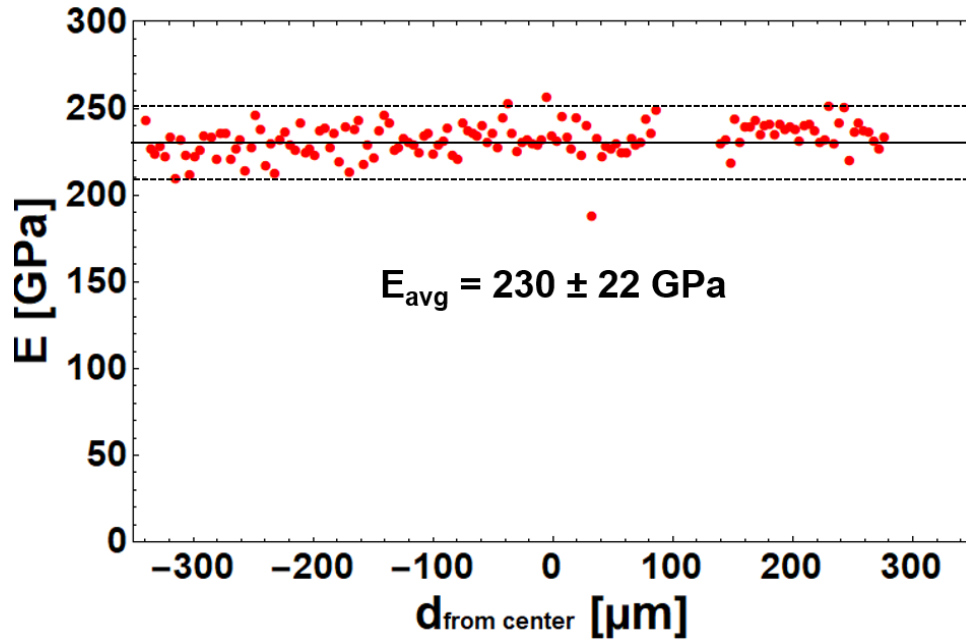


Figure 160. 200 nm Berkovich indents elastic modulus profile performed on the cross-section of a non-irradiated Inconel X-750 component

5.6 Room Temperature Ion Irradiation Studies

5.6.1 Nanoindentation: Ion Irradiated Inconel X-750

Berkovich nanoindentation performed at a depth of 250 nm along the outer edge of a room temperature helium implanted Inconel X-750 sample moving from the edge of the sample, through the helium implanted region and extending into the non-irradiated region quantified irradiation hardening effects. An example SEM image of a batch of indents, and hardness and modulus depth profiles can be seen in Figure 158 a-c. Considering only those indents with plastic zones entirely within the irradiated and non-irradiated regions (plastic zone size $\sim 2.5 \mu\text{m}$), the average hardness of the non-irradiated Inconel X-750 is $6.4 \pm 0.3 \text{ GPa}$, whereas the helium implanted Inconel X-750 has an average hardness of $7.5 \pm 0.3 \text{ GPa}$. The average modulus of the Inconel X-750 spring coil is taken to be $239 \pm 11 \text{ GPa}$. A transition zone of linearly decreasing hardness between the irradiated and non-irradiated regions exists over the course of the first $3 \mu\text{m}$ from the irradiated surface and from $11\text{-}14 \mu\text{m}$, as the material below this region is non-irradiated bulk. The first transition region and differences in moduli as well as hardness occur do to the fact that indents close to the edge also sample the epoxy and Bakelite holder beyond the sample. The second transition region measures hardness changes in irradiation conditions across the depth of the sample moving into its bulk control region.

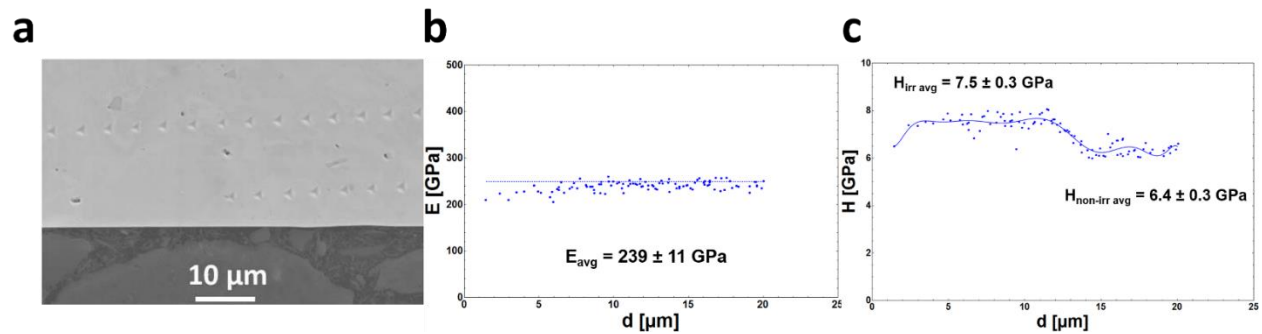


Figure 161. (a) SEM images of two rows of indents at different depths from the surface. (b) profile of the elastic modulus of Inconel X-750 as a function of distance from the irradiated surface (c) hardness profile of the helium implanted Inconel X-750 as a function of distance from the surface

5.6.2 In-Situ Gripper Micro-Tensile Testing

Two non-irradiated micro-tensile specimens and four helium implanted micro-tensile specimens fabricated along the outer edge of the Inconel X-750 coil were tested. Half of the specimens failed in an intergranular manner: both non-irradiated specimens and one helium implanted specimen. Therefore, their three failure stresses will be reported as grain boundary strengths for the outer edge region of the material. Figures depicting the engineering stress-strain curves, pre- and post-test EBSD scans of the specimens in their loading direction, and pre- and post-test high resolution SEM images will be provided for each specimen along with their mechanical properties.

Non-Irradiated Specimen 1

The first specimen fabricated within the non-irradiated outer edge ($L = 17.9 \pm 0.1 \mu\text{m}$, $W = 4.4 \pm 0.5 \mu\text{m}$, and $H = 5.2 \pm 0.5 \mu\text{m}$) fractured abruptly along its twin boundary close to the top of the specimen at a stress of 1399 MPa. This failure strength can be taken as a twin boundary strength for Inconel X-750 along its outer edge. Close observation of the stress-strain curve and post-test EBSD analysis reveals that some plasticity and yielding occurred in the large grain below this twin boundary. The 0.2% offset yield strength is reported as 1275 MPa.

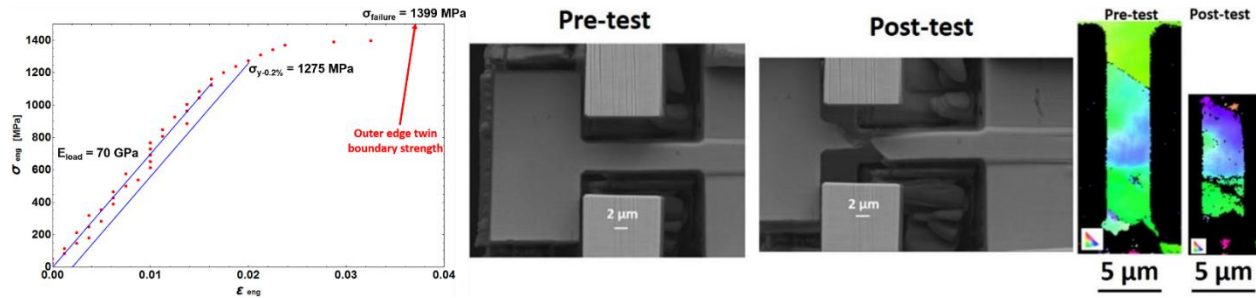


Figure 162. Non-irradiated micro-tensile specimen 1 that fractured in its twin boundary

Non-Irradiated Specimen 2

The second specimen fabricated within the non-irradiated outer edge ($L = 17.3 \pm 0.6 \mu\text{m}$, $W = 4.5 \pm 0.5 \mu\text{m}$, and $H = 4.5 \pm 0.4 \mu\text{m}$) fractured along a high angle grain boundary at a stress of 1684 MPa. Based on the stress-strain curve, a yield stress of 1504 MPa was determined. The post-test EBSD scan does not reveal any evidence of plasticity in the large grain, so it is speculated that the minor plasticity occurred within the grains above the fractured boundary.

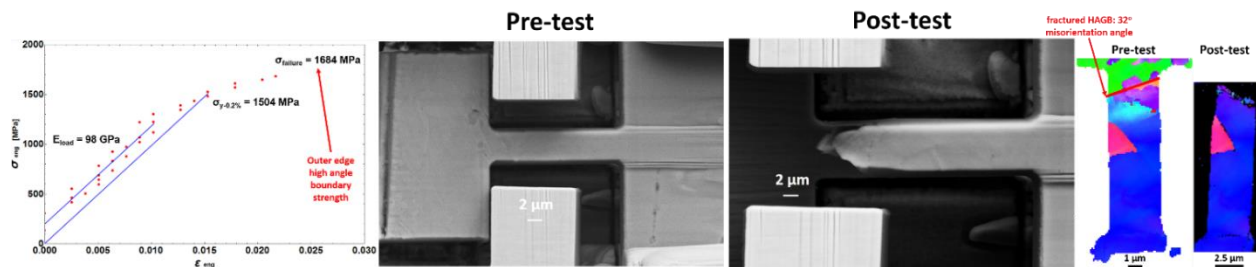


Figure 163. Non-irradiated micro-tensile specimen 2 that fractured within a high angle grain boundary

He Implanted Specimen 1

The first helium implanted specimen ($L = 18.0 \pm 0.2 \mu\text{m}$, $W = 4.2 \pm 0.3 \mu\text{m}$, and $H = 4.2 \pm 0.1 \mu\text{m}$) fractured transgranularly through a nanotwin close to the top of the specimen at a stress of 1302 MPa. Unfortunately, stage drift caused the system to move out of range of the frame grabber, so the strain could not be determined by digital image correlation. Therefore, the loading curve displayed is a nominal displacement versus engineering stress curve. Pre- and post-test EBSD suggests no plasticity occurred and that the failure was a sharp fracture along a cleavage plane.

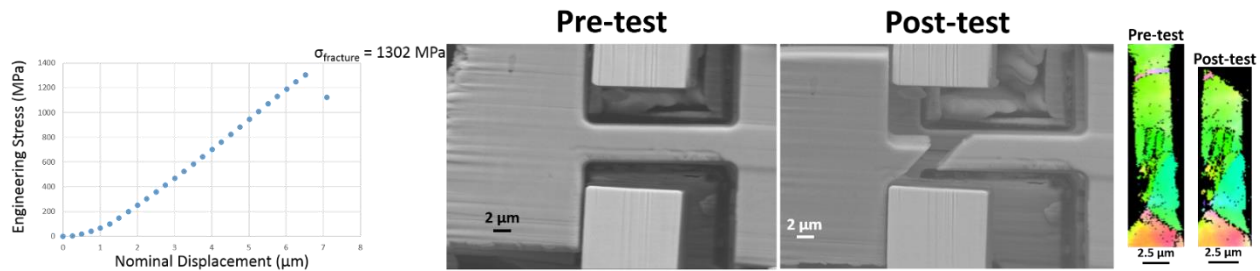


Figure 164. He implanted micro-tensile specimen 1 that fractured transgranularly through its nanotwin

He Implanted Specimen 2

The second helium implanted specimen ($L = 18.3 \pm 0.1 \mu\text{m}$, $W = 4.3 \pm 0.4 \mu\text{m}$, and $H = 3.8 \pm 0.1 \mu\text{m}$) yielded at a stress of 956 MPa. Multiple slip systems were viewed intersecting one another above the fracture point before a maximum stress of 1003 MPa was reached and the specimen failed in the grain interior. Parallel slip planes were also observed in the top grain below the fracture point in agreement with the visible plasticity shown in the post-test EBSD map.

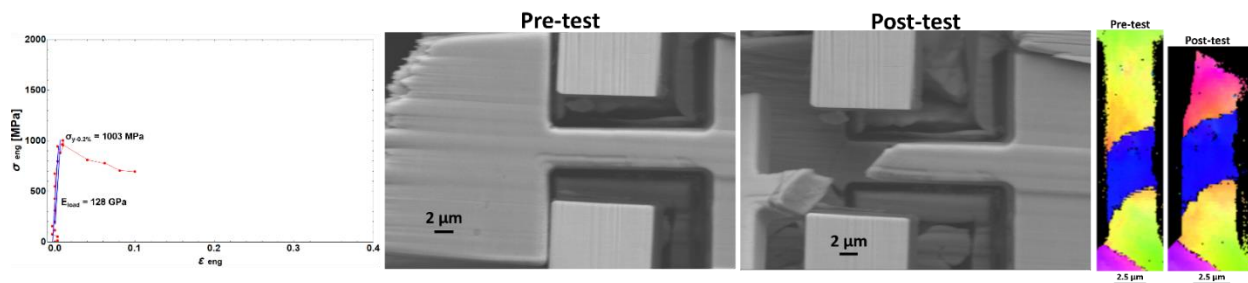


Figure 165. He implanted micro-tensile specimen 2 that fractured transgranularly in its upper grain

He Implanted Specimen 3

The third helium implanted specimen ($L = 20.1 \pm 0.1 \mu\text{m}$, $W = 5.1 \pm 0.4 \mu\text{m}$, and $H = 4.6 \pm 0.1 \mu\text{m}$) fractured within a high angle grain boundary at a stress of 1295 MPa. Almost no plastic deformation was evidenced; only three tiny slip bands are seen directly adjacent to the fractured boundary.

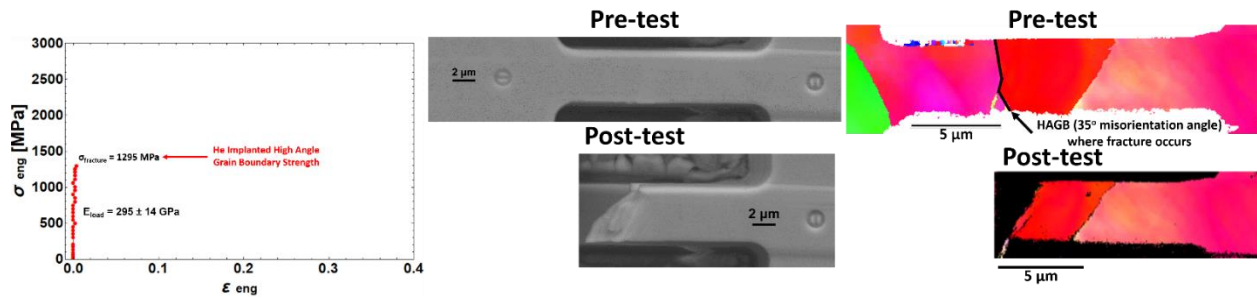


Figure 166. He implanted micro-tensile specimen 3 that fractured along a high angle grain boundary

He Implanted Specimen 4

The fourth helium implanted specimen ($L = 20.1 \pm 0.1 \mu\text{m}$, $W = 5.2 \pm 0.3 \mu\text{m}$, and $H = 4.4 \pm 0.1 \mu\text{m}$) unusually abruptly fractured within its most strongly oriented grain interior at a stress of 2048 MPa. No observable slip bands are seen on the specimen but the fracture inside the grain interior is confirmed by pre- and post-test EBSD analysis.

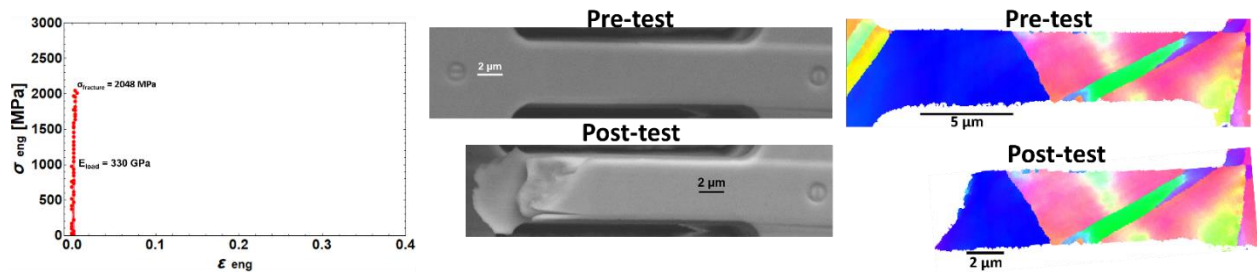


Figure 167. He implanted micro-tensile specimen 4 that fractured within the grain interior

5.6.3 Summary

A summary of the mechanical properties for all outer edge micro-tensile specimens tested in the gripper pulling set-up can be seen in Table 12. The 0.2% yield strength of the Inconel X-750 material before and after helium implantation along the outer edge appears to be unchanged: $\sigma_{y \text{ non-rad}} = 1390 \pm 162 \text{ MPa}$, $\sigma_{y \text{-rad}} = 1327 \pm 504 \text{ MPa}$. Any initial ductility within the outer edge before irradiation, $\epsilon_{\text{total non-rad}} = 2.7 \pm 0.5\%$, appears to have vanished after helium implantation, $\epsilon_{\text{total rad}} = 0.7 \pm 0.2\%$. Ductile helium implanted specimen 2 is considered an outlier. A reduction in high angle grain boundary strength on the order of $\sim 400 \text{ MPa}$ occurs after 1.2 at% helium implantation and 3 dpa displacement damage at room temperature.

Table 12. Mechanical Properties of Outer Edge Bulk Micro-Tensile Specimens

Irradiation Condition	$\sigma_{y-0.2\%}$ (MPa)	$\sigma_{\text{failure-GB}}$ (MPa)	$\sigma_{\text{failure-Grain Interior}}$ (MPa)	ϵ_{total} (%)
Non-Irradiated	1275	1399		3.2
	1504	1684		2.2
He Implanted			1302	0.8
	956		1003	10
		1295		0.5
			2048	0.9

6 Discussion

6.1 In-Situ Micro-Three-Point Bend Testing

Because the initiation of plastic deformation at the yield point is dislocation slip in the region of the specimens directly below the actuator at the outer fiber (highest stress point), an approximation was made that all deformation up until and including the yield point (elastic deformation and the onset of plastic deformation) occurs locally in individual grains below the loading location. Since only a limited number of grains are deformed, it is preferable to take the crystal orientation into account and compare a critical resolved shear stress (CRSS) rather than a yield stress or flexural bending stress. Based on this assumption, critical resolved shear stress (CRSS) values were calculated for the outer fibers of the specimens at the highest stress points using the highest Schmid factors of the grains beneath the wedge punch where slip planes were observed. All 12 possible *fcc* slip directions and slip planes were taken into account. It is assumed that the outer most fiber of the bend bar is in pure tension. These values are reported in the final row of Table 10, and the associated loading curves can be seen in Figures 131c and 131d. It is evident that high temperature components irradiated to doses of 67 dpa necessitate higher CRSS values in order to yield. Increases of 486 MPa in edge components and 421 MPa in center components are observed. However, this approximation produces CRSS values for low temperature components that increase by ~160 MPa within the first 54 dpa and do not change with increased dose. This may suggest a saturation with respect to dose effects in low temperature components. Nonetheless, this approximation may be oversimplified, whereas a complex crystal plasticity model would be needed in order to map out the grain orientations, grain boundaries, and grain boundary planes for each specimen in order to fully characterize the result. However, such a model is not part of this study.

For all irradiated specimens, the results suggest that the material operating at a lower irradiation temperature has a lower yield stress compared to the high

temperature material irradiated to the same dose. Low temperature material yields approximately 300 MPa lower than high temperature material in the same location (center or edge) irradiated to a dose of 54 dpa. For the highest dose material irradiated to 67 dpa, low temperature edge components yield ~800 MPa lower than high temperature edge components, and similarly low temperature center components are ~760 MPa weaker than high temperature center components. Conventional radiation effects in materials suggest that radiation strengthening is a function of defect cluster density [273, 278, 279, 316-318], and it is well known that defect cluster density decreases as irradiation temperature increases [319-321]. The yield strength itself decreases with increasing irradiation temperature except under particular conditions for some γ' containing superalloys, where the γ' precipitates with a sufficient size and density can suppress the decrease in yield strength with increasing temperature [30]. In 304 stainless steel, which has a similar vacancy migration energy compared to the Inconel X-750 material studied here, for irradiation doses greater than or equal to 10 dpa, the steel is softer after irradiation at ~200 °C compared with ~300 °C [322].

The yield strength for the Inconel X-750 spring material investigated here is consistent with the effects described in [322]. The high temperature material had an irradiation temperature of approximately 300 °C, whereas the low temperature material had an irradiation temperature of approximately 180 °C. According to [322], this difference in irradiation temperature would mean that one would expect the low temperature material to yield at an approximate stress of 90% of the yield of the high temperature material. Although this model has been developed for austenitic stainless steels, the Inconel X-750 low temperature material yields at 83% of the high temperature material at 53 dpa, and ~70% of the high temperature material at 67 dpa suggesting similar effects here.

This increasing strength with increasing temperature relationship is also supported by microstructural observations reported in [229]. Due to vacancy migration energies, at lower irradiation temperatures, the material is in a recombination dominated regime, whereas at higher irradiation temperatures the material is in a sink dominated regime. Thus, when interstitial clusters first form in the low temperature material, they are often annihilated through recombination, whereas in the high temperature material, they survive to form dislocation loops. In addition, the lower temperature of the material may allow for more disordering and dissolution of precipitate structures. Finally, cavity densities are much higher but individual cavity sizes are much smaller for the low temperature material, meaning they are more evenly distributed [227, 229]. Overall, the matrix microstructure is much cleaner and more homogeneous in the low temperature material, leaving less obstacles to be overcome during loading deformation, less necessity for dislocation climb of network dislocations,

and ultimately a softer matrix material with a lower yield strength value. These observations hold true for the approximate temperature range 120-330 °C and are supported by the work shown in Figure 63. However, at irradiation temperatures less than or equal to room temperature, recombination effects will not occur, and yield strength increases are expected.

The results from the in-situ three-point bend specimens showing a higher room temperature yield stress at higher irradiation temperatures are in agreement with room temperature hardness measurements from high fluence material shown in Figure 109. However, the failure behavior of the specimens seen in crush testing in Figure 108 has the opposite trend with respect to temperature. This is most likely because the failure load is dependent on the grain boundary strength, which is not necessarily governed by the same microstructural differences that are affecting the matrix yield strength.

Ultimately, the mechanisms for matrix yielding and ultimate failure of neutron irradiated Inconel X-750 spacers are different. Matrix yielding is initially governed by the spacing of ordered second phase γ' precipitates, but irradiation damage creates a different effective defect spacing which governs the new yielding behavior as this precipitation hardened phase loses its order with increasing dose [229, 282, 288, 289]. It is surmised that ultimate failure is a result of intergranular fracturing. It is hypothesized that intergranular failure may be caused by helium preferentially aligning along and weakening grain boundaries is also supported by TEM investigations in [197, 226-229]. The matrix strength is dominated by microstructural features other than cavities (dislocation loops and precipitates) and the radiation-induced changes in these features have a different temperature dependence [227-229, 287, 323].

Two high temperature bending specimens irradiated to a dose of 54 dpa were notched in their centers at the bottom using the FIB such that the notches were located inside of single grains. These notches were confirmed to be within single grains using high resolution FIB ion channeling contrast images of the sides of the specimens. Tests of these two notched specimens did not generate cracking from the notch. Since it is known that notch tips were located inside the grain, no cracking from the notch and significant plastic deformation after yielding suggests that the matrix material has high resistance to cracking under irradiated conditions. Notches produced via FIB line profile rastering can be made relatively fine, but they cannot simulate true crack widths.

However, in the case of the low temperature specimens irradiated to 67 dpa, cracks developed on the bottom of both center and edge specimens. Based on the grain boundary locations indicated by EBSD scans of the top surfaces of the specimens, it is likely that the cracks follow the paths of the grain boundaries, but definite proof is difficult since EBSD after deformation is not possible due to

the fact that the top sample surface, the only one which remains unblocked by sample mounts, is no longer flat. Figure 124 and Figure 125 show representative center and edge specimens for low temperature material irradiated to 67 dpa with cracks that are believed to have propagated along grain boundaries and exited at the bottom of the specimens. Associated stress values for crack initiation are larger than the associated yield stresses: ~3.5 GPa for edge specimens and ~2.5 GPa for center specimens. EBSD images of side and bottom surfaces are not possible due to shadowing effects from sample holders and mounts.

To summarize initial discoveries made on the failure mechanisms of the Inconel X-750 spacers, let it be noted that indication of potential grain boundary failure in the tests of non-irradiated specimens when strained well beyond their yield points occurred only in two outer edge specimens where cold working and grinding effects are the most severe. Matrix grain interiors are believed to be drastically hardened in this region to the point that grain boundary failure is promoted as an alternative deformation pathway. In the case occurring in Figure 110, the nanograin containing boundaries that cracked was surrounded by one neighboring grain with a very low Schmid factor and one neighboring grain with a very high Schmid factor. This difference in grain orientations in addition to the size of the grain is hypothesized to play a role in promoting grain boundary cracking. In the case occurring in Figure 113, three of the four grains contained in the micro-beam are strongly oriented grains close to the $\langle 111 \rangle$ direction with low Schmid factors < 0.4 . The grain boundary cracks are observed only after flexural stresses on the outer fiber at the midpoint of ~3.3 GPa causing the beam to kink, well after it has yielded and accommodated a large amount of plastic deformation, as seen by the high number of slip planes observed.

However, there were multiple indications of cracking along grain boundaries in the irradiated micro-scale tests seen in material taken from both the center of the spacer, seen in Figure 124, and in material taken from the edge of the spacer, seen in Figure 125. This could be linked to the intergranular failure seen in macroscopic crush tests of irradiated specimens, the loading curves of which are seen in Figure 108, particularly in the case of low temperature specimens irradiated to 67 dpa. The irradiated specimen taken from the center of the component shown in Figure 124 is speculated to undergo grain boundary cracking at flexural stresses ~2.3-2.5 GPa, which is not much higher than the flexural yield stress of ~2.0-2.2 GPa.

6.1.1 Testing Limitations

This novel, lift-out, in-situ, micro three-point bend SSMT required the micro-beams to be quasi or fully constrained when loading began (i.e. attached to their test sites via Pt GIS). Otherwise, the tests could not be performed safely and

successfully, in addition to loose, active contamination being present within the FIB workstation chamber. Due to these constraints, micro three-point bend tests deviated significantly from standardized ASTM-like tests, not only just in size but in stress states, as shown in Figure 165 via FEM modelling for a fully constrained beam using a mesh. Plasticization is more concentrated to the center of the beam; high tensile stresses along the axis of the beam do not extend out as far from the center along the length of the beam. As expected, high compressive stress points also exist at the two points where the beam is attached. Increased plastic strain occurs directly under the indenter wedge punch, which may explain why slight indentation marks were left in some specimens after testing. Higher flexural yield stresses exist in the fully constrained set up as displayed in Figure 165, explaining the results summarized in Table 10. Flexural yield stress values for non-irradiated micro-beams extracted from the center of the Inconel X-750 material (no cold-working effects) have yield stresses of 1335 ± 63 MPa, which is ~31% higher on average than the bulk yield strength of Inconel X-750, reported to be 972-1070 MPa. This is in good agreement with the FEM modelling in Figure 165a that predicts a yield strength increase of ~26% in the fully constrained SSMT testing set-up.

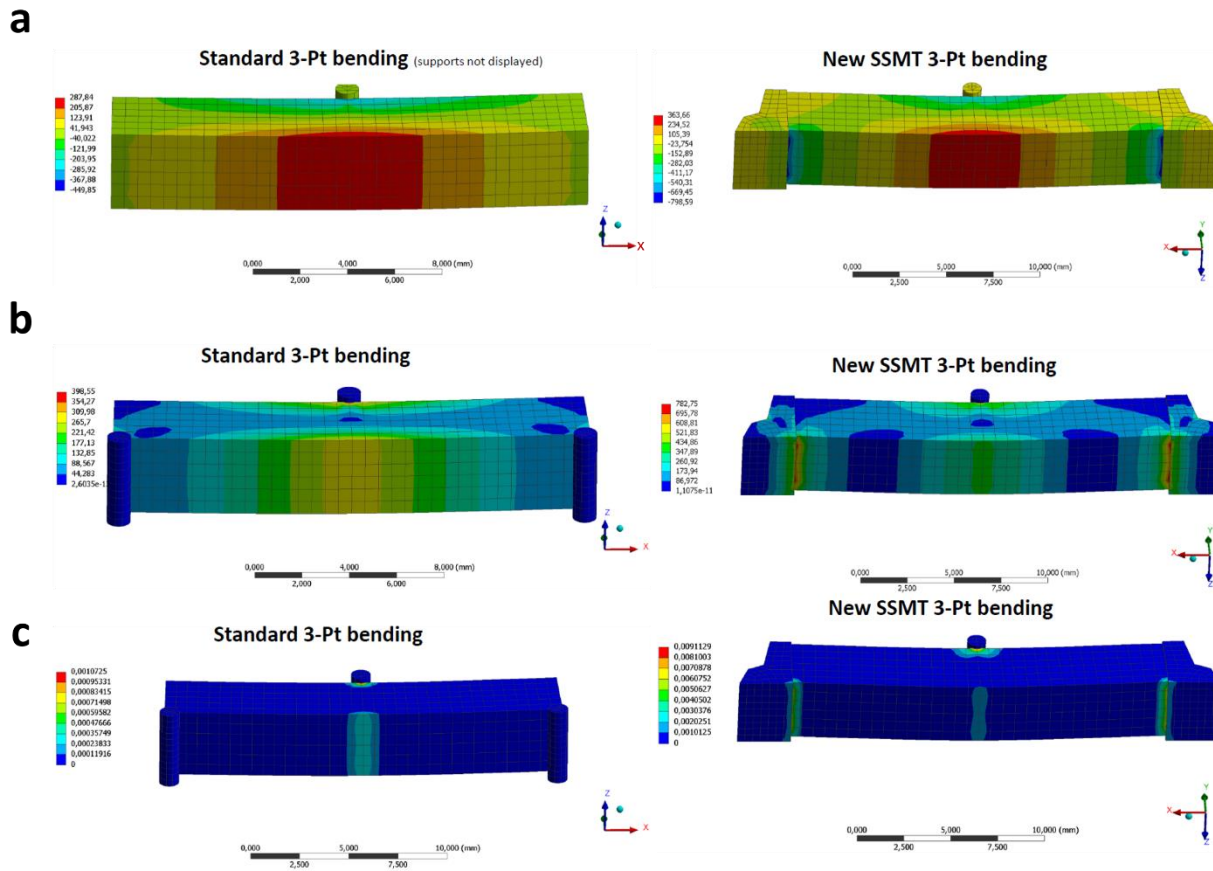


Figure 168. FEM mesh modelling of the (a) normal stresses along the beam axis (tensile and compressive), (b) Von Mises stresses, and (c) plastic strain at the yield point for a standard three-point bend test and a fully constrained SSMT three-point bend test [332]

Because the testing conditions for all micro-beams remained consistent for all irradiation conditions, relative yield strength comparisons between different doses and irradiation temperatures are valid. However, pre-test conditions required for the SSMT necessitate further corrections to arrive at absolute yield strength values. Due to the inherent complexity of the stress state produced when performing a three-point bend test, mechanical properties beyond yield strengths such as ductility properties and failure strengths are rather difficult to obtain. The experiments performed in this study did not load the micro-beams to ultimate failure. Multiple factors are responsible: 1) a maximum displacement limit of 4 μm for accurate readings using the low load transducer in the Hysitron PI 85/88 Picoindenter, 2) severe bending of the specimens leading to contact with the side of the wedge punch indenter cone or specimens falling into the valley beneath their test sites, and 3) the inherent nature of the three-point bending stress state that has a zero-stress neutral axis line, making the test intrinsically incompatible for failure analysis studies. Therefore, a second novel

SSMT producing a uniaxial tensile stress state was developed to obtain more mechanical information.

6.2 In-Situ Micro-Push-to-Pull Tensile Testing

Because irradiated specimens could not be taken from within 10 μm of the edge of the spacer, non-irradiated center specimens are compared to all irradiated specimens. The micro-tensile mechanical properties of irradiated specimens taken $\sim 100 \mu\text{m}$ from the edge of the sample do not show significant differences from the mechanical properties of irradiated specimens taken from the center of the components as seen in Table 11.

6.2.1 Quantifying Cold Working Effects from Material Processing

It has been well documented that cold working prior to precipitation hardening increases the fraction of cellular carbides, and this structure is associated with low ductility and a greater degree of chromium depletion in the surrounding matrix area [324, 325]. In the case of our Inconel X-750 material, the components underwent a cold coiling process after the aging treatment, but micro-tensile testing on non-irradiated outer edge specimens suggests similar low ductility. It is possible that the grain boundary failure can be attributed to stress concentrations from the presence of a large number of grain boundary carbides and η phase Ni_3Ti precipitates which replaces the γ' strengthening nanoprecipitates at the outer edge. Rather abrupt grain boundary decohesion with associated flaking in the case of the high angle grain boundary outer edge specimen was observed. Another possibility to account for the localized failure at the grain boundaries is the zone denuded of γ' precipitates, a precipitate free region (PFZ), that is typically found in these alloys. The combination of carbide accumulation and η phase accumulation on the boundaries and a γ' PFZ would mean that easiest pathway for dislocation motion would be within the limited space of the precipitate free region (PFZ) directly adjacent to the grain boundary. The localized deformation in the PFZ and the grain boundary precipitate structure [326] could account for the intergranular failure mode observed, i.e. flaking along the boundary surface and multiple dimples within the fracture surface seen in Figures 132, 160, and 163. Mills also recognized that plasticity around the grain-boundary carbides leads to a stress concentration at the carbide-matrix interface, which results in a decohesion between the carbide particles and the nickel matrix. The M_{23}C_6 carbides serve as initiation points for micro-voids, which grow and coalesce within the grain boundary denuded zone leading to intergranular failure via a dimple rupture mechanism at room temperature [312].

Unlike high angle grain boundaries, twin boundaries arise as a result of mirrored stacking fault errors and do not serve as nucleation sites for M_{23}C_6 carbides. Thus, as seen in Figure 133, the twin boundary does not fracture, although losses in ductility due to cold-working are still evidenced.

Figure 166 shows a graphical representation of the non-irradiated mechanical properties of the garter spring measured by push-to-pull micro-mechanical testing in the outer edge, center and inner edge. Failure strengths at the outer edge increase by 317 MPa on average as total elongation decreases by 12.2% on average. Clearly, the outer edge region of the material is stronger and less ductile. This is also supported by the nanoindentation results shown in Figure 156. A ~1.0 GPa average increase in hardness measured by 200 nm indents was observed. In addition, larger non-irradiated micro-tensile tests performed on the outer edge region of the material shown in Figure 159 and Figure 160 produced yield stresses ~200-400 MPa higher than the upper bound, non-irradiated, bulk yield stress of the material.

Residual stresses are also hypothesized to play a role in differences in mechanical properties between the inner edge and outer edge of the spring wire. Residual tensile stresses due to cold coiling exist along the outer edge, whereas residual compressive stresses exist along the inner edge. Push-to-pull micro-tensile testing measures the material along the inner edge of the spacer to be the weakest and most ductile as shown in Figure 166. It is speculated that pulling micro-tensile specimens in tension (the opposite of their retained residual stress) causes them to yield at a much lower stress than components with no residual stresses or residual tensile stresses.

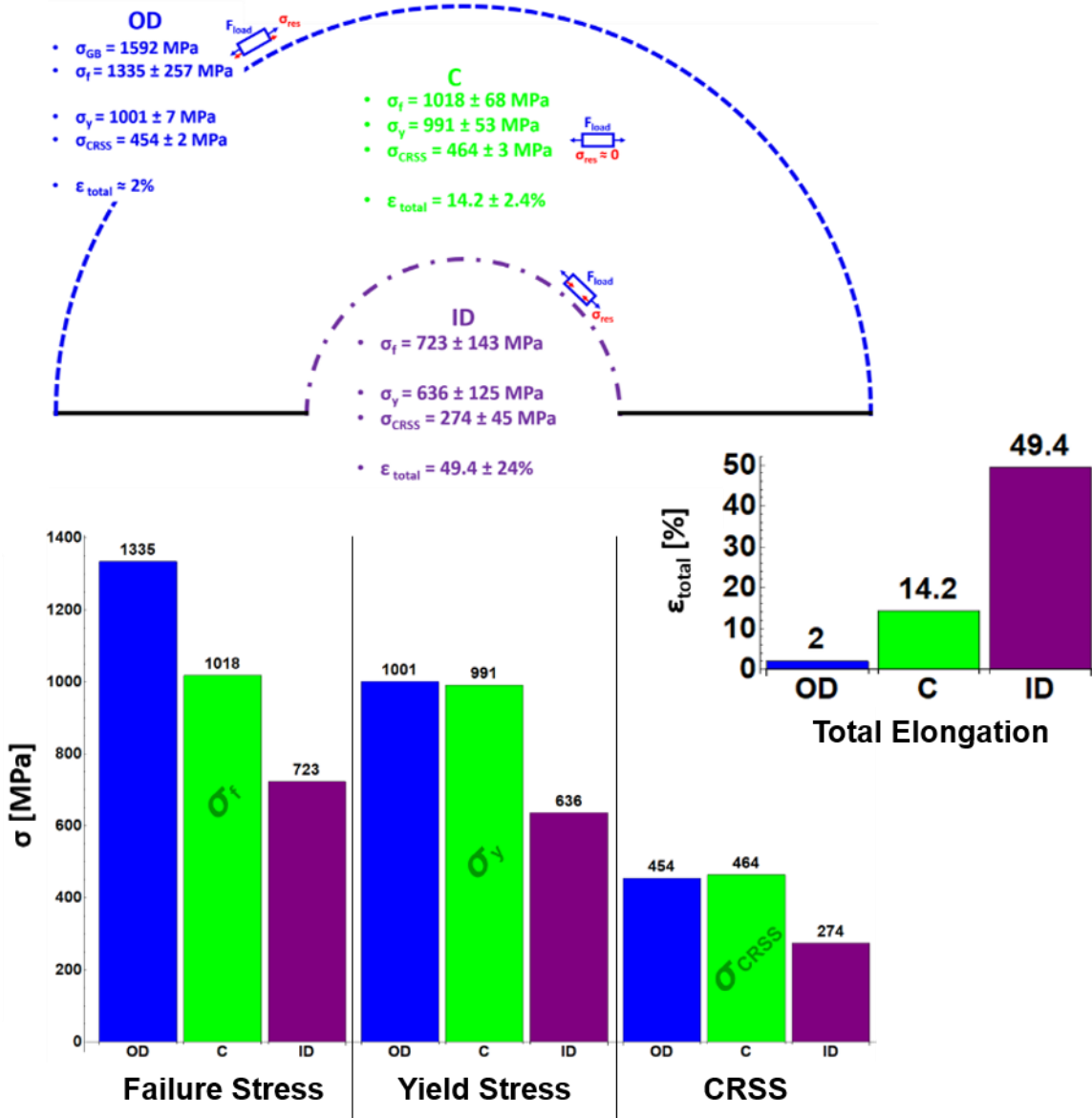


Figure 169. Graphical representation of an Inconel X-750 spacer with mechanical properties measured by push-to-pull micro-tensile testing summarized in each region: outer edge, center, and inner edge. Bar graphs depicting the failure strength, yield strength, critical resolved shear stress (CRSS) calculated from the highest Schmid factor of the grain interior where the first observable slip step appeared, and the total elongation of the specimens are provided on the right hand side.

6.2.2 Critical Resolved Shear Stress

Critical resolved shear stress (CRSS) values were calculated for all micro-tensile specimens where plasticity in the form of slip bands was observed as shown in column 7 of Table 11. The CRSS value was calculated for the grain interior in

which the first observed slip plane appeared using the highest Schmid factor from this grain. It is recognized that CRSS values for specimens containing twin boundaries and high angle grain boundaries are imperfect due to boundary effects, but this parameter is intended to provide an approximate grain boundary independent parameterization of deformation initiation.

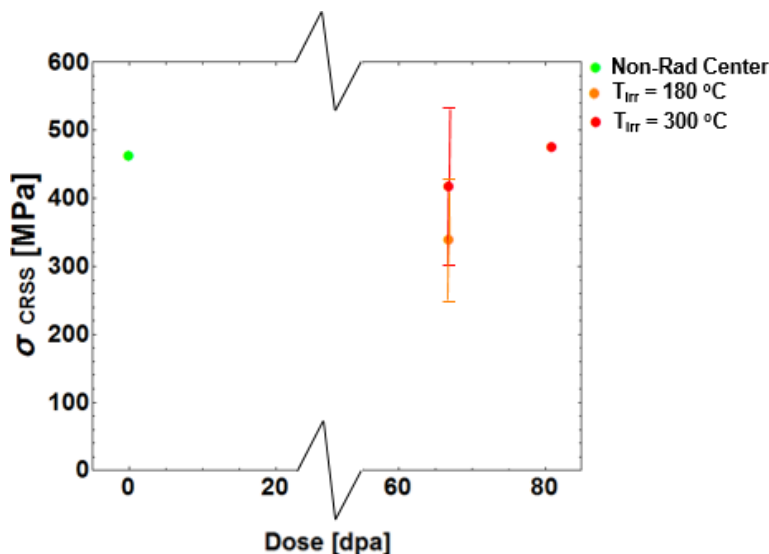


Figure 170. Critical resolved shear stress (CRSS) values calculated from micro-tensile specimens

Specimens irradiated at a higher temperature require higher stresses within their grain interiors in order to initiate deformation. A slight increase in CRSS of 57 MPa on average occurs as high temperature specimens receive more dose from 67 dpa to 81 dpa. The average helium bubble size in the high temperature material is 3-4 nm [229] and bubbles at this size appear to produce significant matrix hardening with increasing dose, as opposed to the the average bubble size of 1 nm in the low temperature material where CRSS values are lower than that of the non-irradiated material. This is in good agreement with [281] suggesting a critical size of 2 nm for helium bubbles to cause hardening in the material. Therefore, it can be surmised that high dose matrix hardening effects in the high temperature material may continually evolve with increasing dose beyond 81 dpa due to an increasing number density of helium bubbles within the material, whereas for the low temperature material, the bubble sizes are too small to have an effect. CRSS values are proposed to remain unchanged in the pinched material.

6.2.3 Yield Strengths

The bulk yield strength of non-irradiated Inconel X-750 material is noted to be 972-1070 MPa in [191]. The new push-to-pull, in-situ, micro-tensile testing

method presented here measures the yield strength of two non-irradiated specimens taken from the center of the spacer, that should be most representative of bulk mechanical properties and not be altered by cold working effects, to be 938 MPa and 1043 MPa, respectively. Therefore, push-to-pull, micro-tensile testing determines the bulk yield strength of the non-irradiated Inconel X-750 well based on these test cases. This is due to the fact that the strength determining features in non-irradiated Inconel X-750 are the second-phase ordered γ' nanoprecipitates. Because these precipitates average 15 nm in size and are dispersed throughout the matrix, specimen size effects can be considered negligible since micro-tensile specimens are $\sim 1\text{-}1.5\ \mu\text{m}$ in length and width and $\sim 2.5\ \mu\text{m}$ in gauge length and thus contain many of the γ' nanoprecipitates. Using a volume fraction for γ' of 4.5%, which is the lower bound for the Inconel X-750 material studied here as reported in [327], and the average volume of a micro-tensile specimen, it can be calculated that > 600 ordered nanoprecipitates are contained in the non-irradiated tensile specimens on average. Thus, the specimens should behave similar to bulk specimens because γ' remains the most important strength determining feature and is abundant. Slight deviations from the bulk value can be attributed to the heterogeneous, non-uniform distribution of γ' throughout the matrix as mentioned in [193], as well as contributions from the differences in orientation of the weakly oriented single grains which deform with respect to the loading direction compared to deformation, which is averaged over many different grains and grain orientations in a bulk sample.

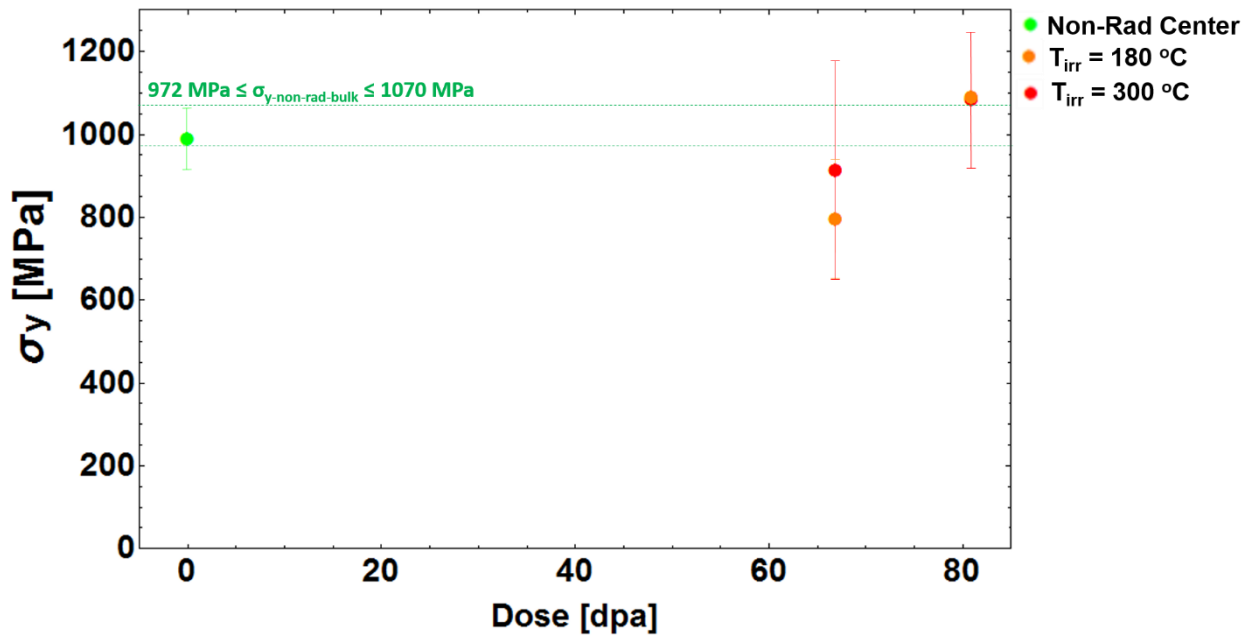


Figure 171. 0.2% offset yield strengths of push-to-pull micro-tensile specimens

Figure 168 depicts the 0.2% offset yield strengths of push-to-pull micro-tensile specimens as a function of dose. The data mirrors that of the CRSS values presented in Figure 167, where at 67 dpa, the lower temperature material has a yield strength 118 MPa lower than the high temperature material on average. It is remarkable that the yield strengths of 67 dpa material irradiated at both temperatures are lower than that of the non-irradiated micro-tensile specimens and the bulk yield strength of Inconel X-750 on average. This irradiation softening can be attributed to γ' being completely disordered and dissolved at high dose. The increase in yield strength from 67 dpa to 81 dpa for the high temperature material can be attributed to an increasing number density of larger 3-4 nm helium bubbles as explained in [281]. The yield strength increase in the low temperature material from 67 dpa to 81 dpa is rather unexpected. However, only one test case exists for this irradiation condition and further tests at the highest dose are required for a better understanding of changes in yield strength of low temperature components.

6.2.4 Failure Strengths and Total Elongations

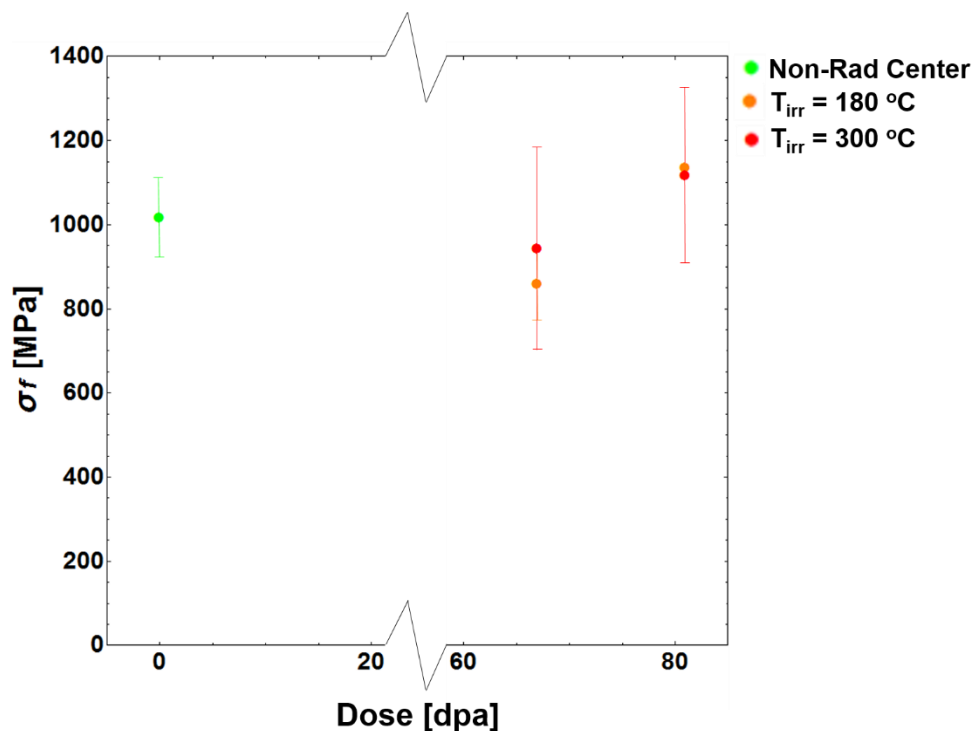


Figure 172. Failure strengths of push-to-pull micro-tensile specimens

Figure 169 portraying the failure strengths of the push-to-pull micro-tensile specimens indicates that for all irradiation conditions, minimal work hardening occurs. The average failure strengths of the specimens are less than or equal to

65 MPa greater than the average yield strengths of the specimens for all doses and irradiation temperatures. Specimens at 67 dpa appear to have slightly lower ultimate strengths than non-irradiated specimens on average, ~75 MPa less for high temperature components and ~160 MPa less for low temperature components. Failure strengths were predicted to be governed by the strengths of the grain boundaries of the specimens due to intergranular fractography images like those in Figure 81b, but based on Figure 169, this does not appear to tell the whole story, due to the increase in failure strengths from 67 dpa to 81 dpa. It is suggested that deformation initiation mechanisms must play a role in increasing the failure strengths of the irradiated components. Large helium bubbles > 2nm are known to harden the matrix interior of the material by forcing dislocations to bow and change paths as they flow through the material. This may explain the behavior in the high temperature material at increasing doses because average helium bubble size and density may continue increasing. More tests are needed to investigate the strength mechanisms of the low temperature material because from the material provided, only one test was able to be performed at this irradiation condition.

The mechanical strength properties CRSS, yield strength, and failure strength all follow the same trend as the microhardness data shown in Figure 109. Material at high dose irradiated at the lower temperature has lower strength properties and hardness. Due to the fact that the majority of all specimens failed within their grain interiors, radiation hardening effects are deemed to be most responsible for this trend.

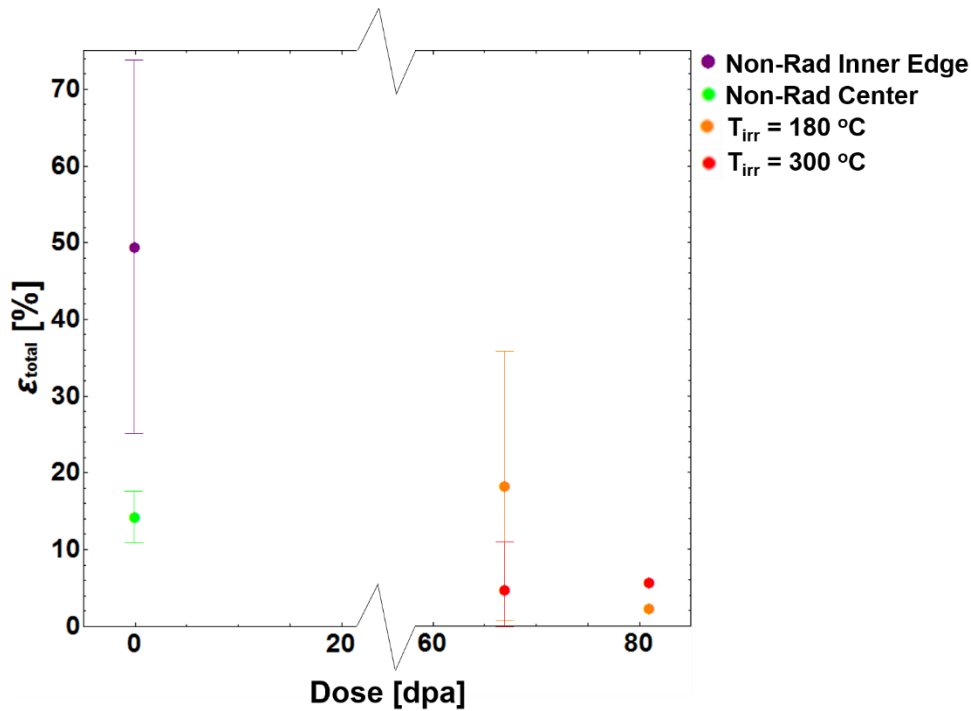


Figure 173. Total elongations of push-to-pull micro-tensile specimens

Before the components were irradiated, they exhibited significant ductility in all regions not ground to be fit to size (i.e. the outer edge): 49.4% total elongation within the inner edge and 14.2% total elongation within the center were measured via push-to-pull micro-tensile testing. Components irradiated to 67 dpa where more specimens were tested to obtain more reliable data, ductility losses are more severe within high temperature components, which is in good agreement with the bulk crush data presented in Figure 108. Total elongations have been reduced to 4.7% in the high temperature material on average, whereas the low temperature material shows less ductility losses on average with a mean total elongation of 18.2%.

Push-to-pull micro-tensile testing is not expected to produce ductility values representative at the component size length scale because of the much larger surface area to volume ratio of the specimens and the lack of a polycrystalline microstructure. When a higher percentage of the specimens border free surfaces, a higher percentage of dislocation slip bands and channels do not have to travel as far before they find a free surface, producing elevated ductility compared to bulk components, where a higher percentage of dislocation motion is in the interior of the material and much more constrained due to the grain boundaries surrounding most grain interiors. However, push-to-pull micro-tensile testing is effective at trending relative changes in ductility as a function of dose and irradiation temperature.

Radiation embrittlement in the form of abrupt fracture after a total elongation of 1.0% along a matrix-carbide interface in 67 dpa low temperature material was observed as shown in Figure 144. However, two high angle grain boundary specimens also irradiated to 67 dpa at 180 °C in Figures 143 and 145 exhibited plastic deformation within their weaker grain interiors and failed within these grains at larger total elongations. Similar behavior was seen in one 67 dpa specimen irradiated at 300 °C that also failed in its grain interior and not along the grain boundary after a total elongation of 13.7%.

6.2.5 Grain Boundary Strengths

One push-to-pull micro-tensile specimen (Figure 132) and two bulk micro-tensile specimens (Figures 159 and 160) all fabricated from the outer edge of non-irradiated Inconel X-750 fractured within their grain boundaries. Grain boundary failures in the outer edge region of the coil have been attributed to excess concentrations of grain boundary carbides and η phase Ni_3Ti precipitates and discussed at length in section 6.2.1. The failure strengths of these three non-irradiated outer edge specimens can be treated as effective, baseline, grain boundary strengths of the Inconel X-750 components. The high angle grain boundary strength of the non-irradiated outer diameter push-to-pull specimen was 1592 MPa, and the high angle grain boundary strength of the non-irradiated outer diameter bulk micro-tensile specimen was 1684 MPa. A second bulk micro-tensile specimen failed along its twin boundary at a stress of 1399 MPa.

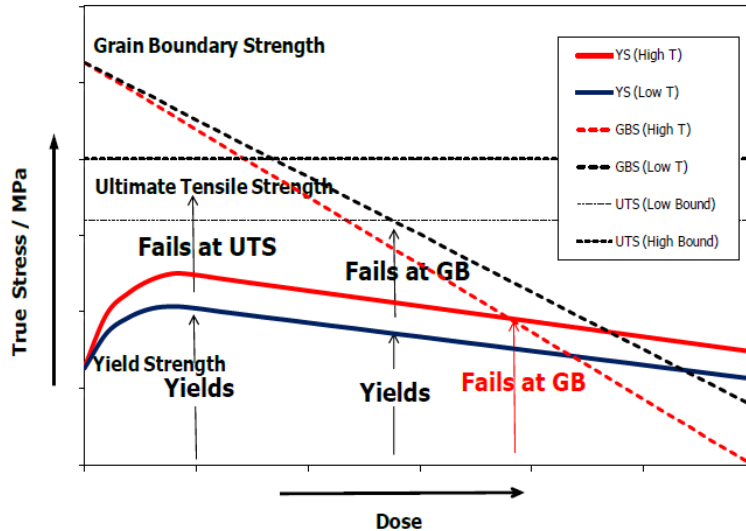


Figure 174. Hypothetical plot proposed by Griffiths [197, 228] depicting the mechanical properties of precipitation-hardened, irradiated Ni-based superalloys as a function of dose. All push-to-pull micro-tensile specimens either yield and fail within their grain interiors or yield first and then fail within a grain boundary, meaning the critical dose highlighted by the red arrow is > 81 dpa for Inconel X-750 if this concept holds true.

Griffiths has proposed a model for the deformation behavior of irradiated, precipitation-hardened Ni-based alloys depicted in Figure 171. This model postulates that grain boundaries continually weaken with increased dose by accumulating more helium bubbles within them to the point that there is a critical dose when the grain boundary strength is lower than the yield strength in the matrix. This model also assumes a continual decrease in yield strength of the material with increasing dose in a much more gradual fashion [197, 228]. Based on the results displayed in Figure 168 from micro-tensile testing, the yield strength of the material does not continually decrease. Instead, it is believed that a yield strength minimum occurs at a critical dose when γ' precipitates are completely disordered and dissolved. At doses above this critical dose, material irradiated at higher temperatures becomes hardened by large helium bubbles and radiation damage (dislocation loops). Material irradiated at lower temperatures is speculated to maintain the yield strength minimum from its critical dose at the point when γ' precipitates are completely disordered and dissolved, but further experiments are needed to confirm this theory.

No push-to-pull micro-tensile specimens irradiated to 67 dpa containing grain boundaries underwent grain boundary failure. Instead, all of them yielded and failed within their grain interiors. Two push-to-pull micro-tensile specimens irradiated to 81 dpa containing boundaries failed within these boundaries after yielding, based on their test videos, high resolution SEM images, and

stress-strain curves given in Figures 152, 154, and 155. The first specimen, a low temperature specimen containing twin boundaries, first fractured along its upper boundary, and this crack eventually propagated through the twin and down to the lower twin boundary, cracking through this bottom boundary and eventually failing. It has been suggested in [308] that crack initiation in hydrogen embrittled, Ni-based superalloys preferentially occurs within twin boundaries, which may explain the behavior seen in the micro-tensile specimen in Figure 152. Although twin boundaries are preferred locations for cracks to initiate, they do not propagate cracks well [308], which may also explain why the crack path deviated from the initial twin boundary where it started. The twin boundary strength of the 81 dpa specimen irradiated at 180 °C was measured to be 1136 MPa, which is still 64-164 MPa stronger than the non-irradiated bulk yield strength of Inconel X-750. The second, high angle grain boundary specimen irradiated at 300 °C (Figure 154) contained a grain boundary carbide in its upper left corner that served as a grain boundary crack initiator. Further straining of the specimen quickly propagated the crack through the specimen's grain boundary leading to failure at a high angle grain boundary strength of 1267 ± 9 MPa, which is also above the yield strength of the material. Even at 81 dpa, the critical dose Griffiths has proposed where the material fails at the grain boundary before it yields has not been reached, if this model is to be taken as true for the behavior of high dose Inconel X-750 components. Figure 172 depicts the grain boundary strengths of Inconel X-750 measured by push-to-pull micro-tensile testing as a function of dose. Although grain boundary strengths do appear to be monotonically decreasing as a function of dose, even at 81 dpa, they remain higher than the bulk yield strength of Inconel X-750.

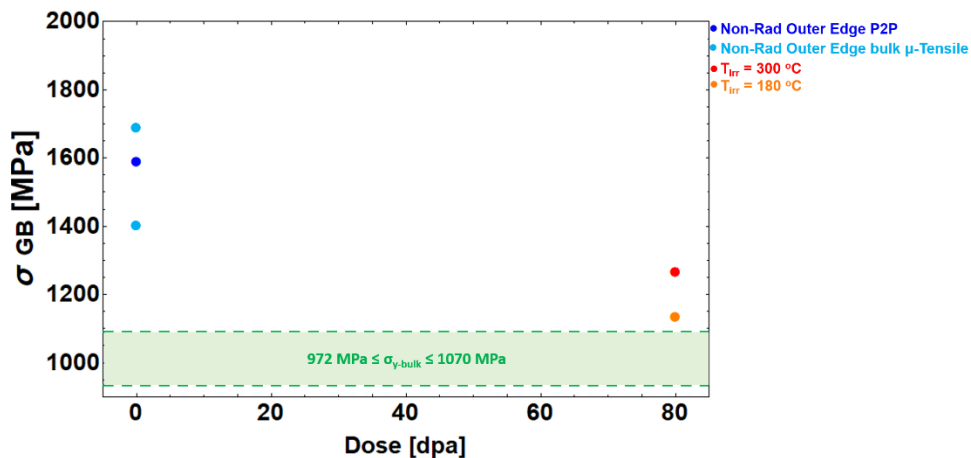


Figure 175. Grain boundary strengths of Inconel X-750 measured by micro-tensile testing

6.2.6 Resolved Normal Stresses on High Angle Grain Boundaries

Helium embrittlement of high angle grain boundaries is postulated to be the most important degradation mechanism in high dose components responsible for controlling their failure stresses, and compromised boundaries are predicted to fail in a decohesive manner. Based on the measured angle of the grain boundary with respect to the loading direction normal plane along both the top surface, θ_{GB-Top} , and side surface, $\theta_{GB-side}$, presented in Table 11, resolved normal stresses on the boundaries at the failure point for each specimen were calculated and given in column 12. The resolved normal stress on the grain boundary at the time of failure can be considered an effective decohesive stress acting to separate the grain boundary. Figure 173 presents the resolved normal stresses on these boundaries at the time of failure as a function of dose.

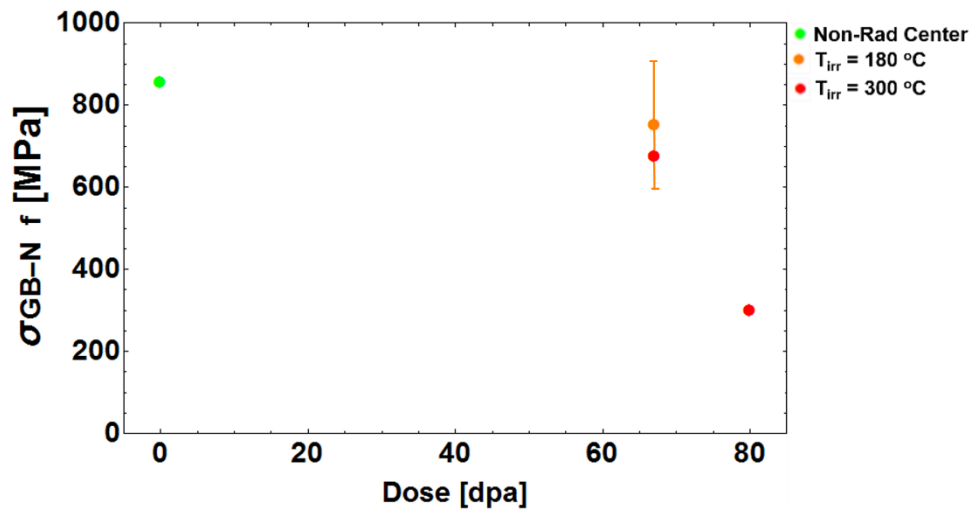


Figure 176. Resolved normal stress on high angle grain boundaries at the time of failure in push-to-pull micro-tensile specimens

The resolved normal stress on the high angle boundaries at the time of failure is lowest for the highest dose specimen irradiated at high temperature, which was the only specimen that incurred grain boundary failure. A trend in Figure 173 indicates that in general, specimens irradiated at 300 °C require less stress normal to their boundaries than specimens irradiated at 180 °C to fail. If ultimate failure in the bulk components is governed by grain boundary decohesion from helium embrittlement, high temperature material is predicted to be most susceptible and fail first at lower loads. Figure 108 is in good agreement with this hypothesis because it reveals that high temperature coils have lower crush strengths. High angle grain boundaries in high temperature, high dose material have larger helium bubbles within them compared to low temperature material irradiated to the same dose. When stresses are applied normal to the boundary,

boundaries filled with larger bubbles are expected to be more compromised and easier to pull apart.

6.2.7 Deformation Mechanisms

It is important to note that all 67 dpa specimens yielded within their grain interiors and did not fail within their grain boundaries but instead sheared and fractured within a dislocation slip band or dislocation channel as viewed in the SEM during testing. This could be attributed to the fact that when deformation initiates within the micro-scale specimens, it does not have to travel far to find a free surface, whereas in bulk specimens, if the initial deformation begins in a grain interior, it will intersect a grain boundary and induce a high stress point on the boundary, leading to intergranular fracture. Nevertheless, the initiation of deformation, meaning the yield point of the highly irradiated components, should be considered important in understanding if the highly irradiated components remain fit for service. Small scale mechanical testing strongly suggests that yielding occurs within the grain interiors, and the grain boundaries are only embrittled to the point that they fracture after traditional plasticity occurs in specimens irradiated to 81 dpa. In these test cases where grain boundary failure occurred in two 81 dpa specimens, a stress concentration initiator in the form of a grain boundary carbide was required to cause boundary failure in the high angle grain boundary. In the case of the twin boundary, it is believed that a separate hydrogen grain boundary embrittlement mechanism caused the boundary failure [308] and not helium bubble boundary embrittlement. Helium bubble grain boundary embrittlement alone in an otherwise clean boundary did not cause grain boundary failure in any push-to-pull micro-tensile specimens.

When coupling the micro-tensile test data with high magnification images from fracture surfaces taken from broken components, the dislocation channeling seen in the micro-tensile tests appears to be reflected as small slip step facets that have step sizes of several hundred nanometers within some grain interiors. Two independent deformation failure pathways may exist in highly irradiated components; some portion of the component fails via preferred dislocation channels in the grain interior and another portion of the component fails in an intergranular nature. The two deformation mechanisms are interlinked because when dislocation channels intersect compromised grain boundaries littered with helium bubbles, they produce significant stresses to fracture the boundary. Once an initial boundary fracture occurs, propagation of the fracture will occur along the boundaries at the component length scale leading to ultimate failure.

A similar type of mixed mode channel fracture in combination with intergranular fracture has been seen in high dose austenitic alloys as presented in [144, 295, 296, 313, 314]. It has been speculated in the literature that elevated

local concentrations of voids and bubbles within grains may coalesce as dislocation slip bands sweep through them. These high density cavity regions are also believed to be the most probable sites within the material to promote dislocation channeling in order to reduce the stored energy in the material to a more energetically favorable state. Compromised matrix-carbide interfaces in grain interiors as shown in Figure 144, which led to the failure of a 67 dpa low temperature micro-tensile specimen, should also be considered as preferential locations of deformation initiation within grain interiors. In order to confirm this theory of transgranular channel fracture via shearing of bridges of material that lie between a row of bubbles, Transmission Electron Microscopy (TEM) on high dose deformed specimens with slip steps is required. This is outside the scope of this thesis, but is strongly suggested as future work.

In high dose austenitic alloys with mixed-mode channel and intergranular fracture, there must be a weighted percentage of grains that incur deformation within them versus grains that show very little signs of plasticity before boundary cracking begins and propagates. Although the push-to-pull micro-tensile work on high dose material performed in this study samples only a limited amount of material, it suggests that the mixed-mode deformation behavior of high dose Inconel X-750 components is approximately ~70% dislocation channeling/slip band events and ~30% intergranular fracture.

Direct intergranular failure mechanisms such as hydrogen embrittlement of twin boundaries and high angle boundary fracture due to stress concentrators like grain boundary carbides as seen in push-to-pull micro-tensile testing also need to be considered. Although this was only seen in two test cases, these tests make up a non-negligible portion of all high dose boundary specimens. Although no evidence of grain boundary failure before yielding was seen in specimens irradiated to 81 dpa, which is a promising result for the nuclear industry, the trend of boundary strength reduction shown in Figure 172 indicates that a higher critical dose on the order of 100 dpa may exist where this occurs.

6.2.8 Testing Challenges

The development of push-to-pull micro-tensile testing as a novel, in-situ SEM, small-scale mechanical test to be applied to active material presented challenges that needed to be overcome before accurate testing could be performed. Figure 174 depicts two of the most prominent issues. As shown on the left, during the process of calibrating and aligning the Hysitron PI 85/88 Picoindenter, specimens were noticed to have pre-deformed before testing could begin. Ambient electrostatic forces and charging due to improper grounding of the Picoindenter and/or stage of the FEI Quanta DualBeam may be responsible. The

pre-determined, fixed port positions of the Pt GIS needle and Omniprobe nanomanipulator inside the FEI Quanta DualBeam chamber do not allow for much flexibility when performing sample mounting onto the P2P test site. A scenario on the right of Figure 174 is shown where minor misalignments of the equipment caused the Pt GIS needle to block the view of the P2P test site.

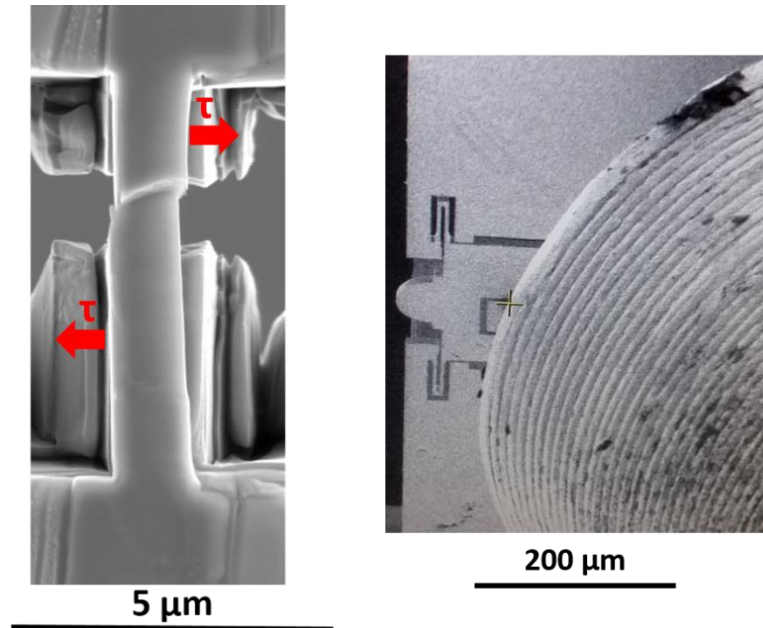


Figure 177. Testing challenges during the development of in-situ, push-to-pull, micro-tensile testing. Specimens became pre-deformed prior to testing during calibration and alignment processes (left). The port positions of the Pt GIS needle and nanomanipulators do not allow for much flexibility within the SEM/FIB chamber. The Pt needle is shown blocking the P2P testing site (right).

In addition, because the activity levels of the bulk material made it unsafe to handle and all active specimens had to be cut from foils shown in Figures 94 and 95, it was difficult to control the exact position and angle of the grain boundaries with respect to the tensile loading direction. It would have been more desirable to perform testing on all specimens that had matching grain boundary angles with respect to the loading direction in order to reduce testing variability.

6.3 Room Temperature Ion Irradiation Studies

6.3.1 Nanoindentation: Ion Irradiated Inconel X-750

An upper bound on the number density of helium bubbles as a result of the increased hardness from ion irradiation can be estimated using the Friedel-Kroupa-Hirsch model [278, 279] and the equation (105), by relating $\Delta\sigma_y$, the change in yield strength between irradiated and non-irradiated material, using M , the geometrical Taylor factor equal to 3.06, μ , the shear modulus of

Inconel X-750 equal to 68.26 GPa [191], b , the Burgers vector of Inconel X-750, equal to $\frac{a_0}{\sqrt{2}} = 0.252$ nm [328], d is the average bubble diameter ≈ 1.5 nm for low temperature irradiations according to [227], and N is the number density of bubbles. This formulation relates changes in yield strength to the number density and diameter of defects within a material. Assuming that the increase in hardness is entirely a result of the introduction of helium bubbles places an upper limit on the density of helium bubbles in the material because in reality displacement damage and increases in dislocation density also play effect. By using Busby's relation between yield strength and hardness relation for fcc metals in [54] given by equation (29) and converting our measured Berkovich nanoindentation values into Vickers hardness units ($H_{V\text{-control}} = 606$ HV, $H_{V\text{-rad}} = 735$ HV), we arrive at an increase in yield strength of $\Delta\sigma_y = 391$ MPa. Substituting all values into the Friedel-Kroupa-Hirsch model and solving for the number density of bubbles gives an upper bound of $N = 7.89 \times 10^{24} \text{ m}^{-3}$. This is on the same order of magnitude as the helium bubble number density of low temperature Inconel X-750 components irradiated to 53 dpa, shown in Figure 175 [227]. Micro-three-point bend tests performed on low temperature 53 dpa material reported $\Delta\sigma_y = 226$ MPa, which is not far off from the increase in cold helium implanted Inconel X-750 with a similar helium bubble number density, although the displacement damage and dose rate of the ion irradiated material is much different.

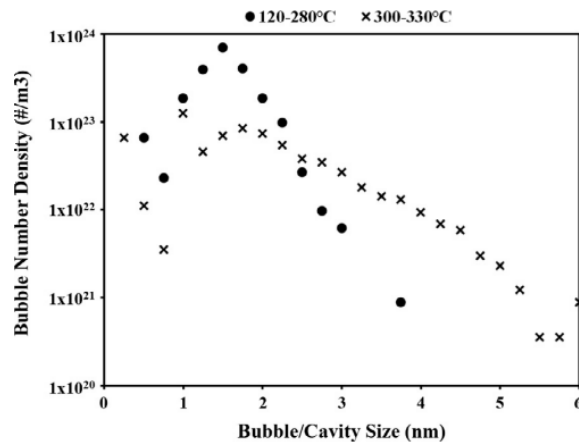


Figure 178. Helium bubble size and density distribution for Inconel X-750 irradiated to 53 dpa (1.8 at% He) at 120-280 °C and 300 °C [227]

6.3.2 In-Situ Gripper Micro-Tensile Testing

In-situ, bulk, gripper style micro-tensile testing on non-irradiated Inconel X-750 specimens fabricated from the outer edge region of the coil fractured along their grain boundaries. The high angle grain boundary specimen produced a boundary strength of 1684 MPa, which was within ~ 100 MPa of the grain boundary

strength of a high angle boundary measured via push-to-pull micro-tensile testing, 1592 MPa. The two different micro-tensile testing methods produce consistent results for the non-irradiated high angle grain boundary strength of Inconel X-750. This suggests that size effects are negligible in this material when shifting from a grain boundary line length of $\sim 4\text{-}5\ \mu\text{m}$ (grain boundary area of $\sim 16\text{-}25\ \mu\text{m}^2$) in the bulk micro-tensile tests down to a grain boundary line length of $\sim 1\text{-}2\ \mu\text{m}$ (grain boundary area of $\sim 1\text{-}4\ \mu\text{m}^2$) in push-to-pull micro-tensile specimens.

Overall, the results given in Table 12 indicate that the outer edge region of Inconel X-750 spacers is extremely heterogeneous. A high degree of material variability exists in this region due to it containing a large number of carbides, η phase Ni_3Ti precipitates, and blocky micron-sized *fcc* (Ti,Nb)C inclusions forming stringers in the extrusion direction that are irregularly distributed within $\sim 20\ \mu\text{m}$ to the outer surface. This region is also expected to contain a high dislocation density because it is the most heavily cold-worked from processing. The total elongation results reflect this; non-irradiated specimens had total elongations 2-3% and irradiated specimens had a median total elongation $\sim 1\%$. The variability along the outer edge of the material is reflected in the large data spread in the yield and failure strengths measured from bulk micro-tensile tests.

6.4 Future Work with SSMT Tensile Testing

The small scale mechanical testing studies performed on high dose Inconel X-750 components have helped to kick start a two year spacer program funded by the Canadian nuclear industry for research and development that will occur at Canadian Nuclear Laboratories (CNL) on material irradiated to doses 0-84 dpa. Because CNL has Fuel and Material Cells (FMC) coupled with an active FEI Versa 3D DualBeam instrument, full cross-sections of thinned material are accessible. This allows for more control in sample selection. Expansion of the capabilities of the in-situ P2P micro-tensile tests planned for the Inconel X-750 spacer program includes coupling electron backscattered diffraction (EBSD) with advanced lift-out techniques in order to target specific grain orientations and specific grain boundaries of interest. By performing a large area EBSD map coupled with advanced in-plane TEM lamella lift-out techniques, any of the following specific boundaries can be selected for testing: solution annealed twin boundaries, deformation twin boundaries, special boundaries containing a coincident site lattice (CSL), and randomly oriented high angle grain boundaries. In addition, a TEM lamella containing the exact same boundary of interest can be lifted out so that the mechanical properties of each boundary type and grain orientation can be profiled as a function of helium bubble matrix densities and helium bubble grain boundary area coverages. Access to a larger sample area to

choose from also allows for full control of the grain boundary angle with respect to the tensile loading direction. Transmission electron microscopy studies are planned to be coupled with in-situ SEM SSMTs in order to better understand the interplay between degradation mechanisms and mechanical properties. The same material deformed via push-to-pull micro-tensile specimens can be thinned for TEM and imaged.

Four push-to-pull testing geometries are suggested for future work on high dose Inconel X-750 material. They are shown in Figure 176. The first involves testing single-grained specimens to provide better statistics on a grain orientation independent quantitative parameterization of the initiation of deformation, namely the critical resolved shear strength (CRSS) of the material. The second involves testing the decohesion strength of the grain boundaries by orienting the grain boundary completely normal to the tensile loading direction. The third involves a mixed-mode stress state with the grain boundary also notched and oriented at a 45° angle with respect to the tensile loading direction. The final test geometry involves testing the shear strength of the grain boundary by orienting it parallel to the tensile loading direction.

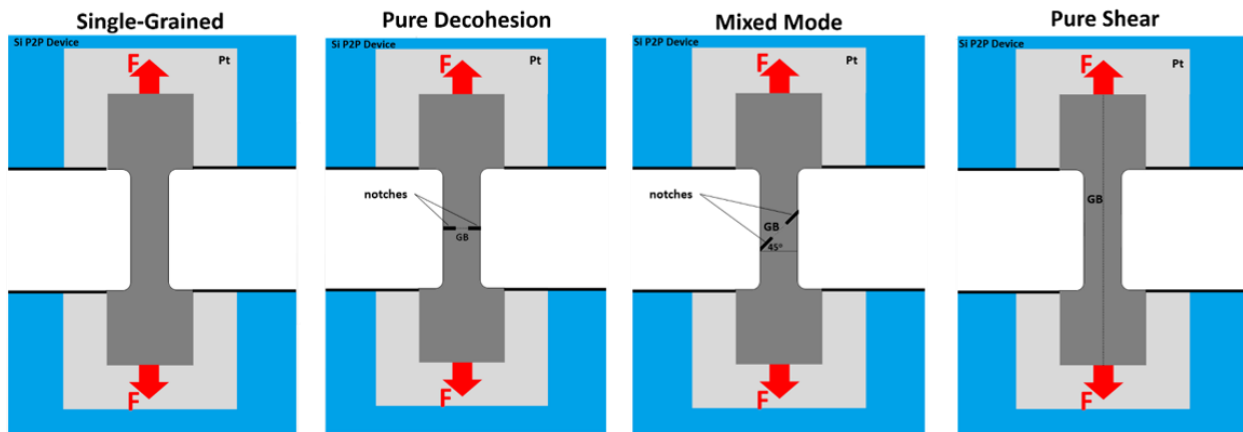


Figure 179. Proposed testing geometries for future in-situ, push-to-pull micro-tensile testing

In order to further assess irradiation effects on failure stresses, specifically grain boundary fracture stresses, it is proposed that specimens can be sharply notched via line profile patterning in the FIB along their grain boundaries to induce grain boundary failure as shown in the two middle test geometries in Figure 176. Mechanistically, if dislocation slip and traditional yielding precede intergranular failure as seen in the 67 dpa and 81 dpa specimens studied in this thesis, the pure shear geometry to the right of Figure 176 should force the interaction of slip steps with the grain boundary in the specimen. A stress concentration produced by the intersection of a slip step or dislocation channel

with a grain boundary may be responsible for causing the intergranular failure in cases where stepped channel failure within the grain interior does not occur.

Because the push-to-pull device is spring loaded, when the test concludes and the flat punch indenter is unloaded, the device contracts and presses the fracture surfaces of the specimen back in contact with each other, so they cannot be observed. To directly observe the exposed fracture surface of each broken micro-tensile specimen, a new lift-out, micro-tensile testing technique would need to be developed as shown in Figure 180 for highly active material. In this case, a dog bone tensile specimen would need to be prepared for an in-plane style FIB lift-out. EBSD of its top surface could be performed before FIB milling to select grain boundaries of interest to test. This lifted out, dog bone, micro-tensile specimen would then be mounted into a Mo TEM grid post test site, with a reverse T-shaped FIB milled slot, and secured using the Pt GIS system. Testing would occur using a gripper similar to the one shown in Figure 110. The bottom portion of the fractured specimen would remain attached to the TEM grid post for post-test high resolution SEM imaging, atomic force microscopy, and transmission electron microscopy.

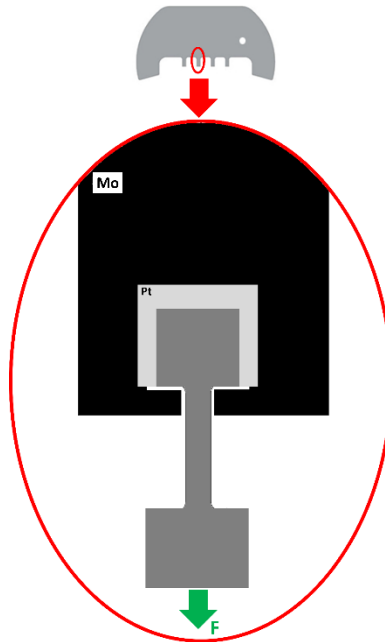


Figure 180. A newly proposed lift-out micro-tensile test for highly activated nuclear material

In order to upscale the testing of the ex-service Inconel X-750 spacers beyond measuring individual grain interior yield points and grain boundary failure strengths and further investigate the mechanisms driving the bulk failure of the component, in-situ SEM meso-scale tensile testing is advised. In this case multiple grain boundaries of various types (annealing and deformation twins,

special boundaries, and random high angle boundaries) will all be contained in a single specimen which is tested to failure. As this test is viewed in the SEM, coupled with EBSD investigations, it can be determined which grain boundaries initiate failure, as well as whether the propagation of the intergranular failure preferentially follows certain grain boundaries as was done for hydrogen charged Inconel 725 specimens in [308], where it was discovered that coherent twin boundaries were most susceptible to crack initiation but most resistant to crack propagation, suggesting that crack initiation and propagation in a hydrogen embrittled material are governed by different processes. Because it is difficult to independently investigate the role of hydrogen embrittlement in ex-service Inconel X-750 spacers since they are also littered with a high density of helium bubbles within their matrix and grain boundaries as well as other radiation defects, it is unknown which radiation effect is the leading cause of failure and how this effect contributes to the overall intergranular ultimate failure of bulk coils. A meso-scale tensile testing approach using specimens $\sim 100 \mu\text{m}$ in width and thickness in order to capture all grain boundary types may further reveal the order of deformation pathways and clear up this uncertainty.

Because the majority of the bi-crystalline in-situ P2P ex-service Inconel X-750 specimens did yield prior to failure and their failure points were within grain interiors, an alternate hypothesis suggests that yielding always precedes brittle failure in the bulk components, even at the highest doses, and that the fracture of bulk components may not be entirely intergranular, but instead that at least some percentage of the fracture planes fall along sharp dislocation channels within grain interiors. In order to further investigate this hypothesis and understand the deformation mechanisms at the onset of plasticity, it is suggested that in situ TEM studies be considered for future work. Thin foils of ex-service material strained in situ in the TEM would allow for visual evidence of dislocation generation and motion and more importantly observations of dislocations intersecting grain boundaries and how the energy dissipated in these high stress events leads to failure. Foils could be specially designed such that dislocations are forced to intersect grain boundaries, which is inevitable in bulk material, in order to study this effect.

7 Conclusions

Two first of their kind, in-situ, small scale mechanical tests (SSMTs) employing scanning electron microscopy (SEM) and focused ion beam (FIB) techniques were invented to test ex-service Inconel X-750 components irradiated to doses of 53, 67, and 81 dpa in CANDU reactors at average irradiation temperatures of 180 °C and 300 °C. The first, a lift-out, three-point bend test quantified the flexural yield stresses of the components as a function of irradiation temperature and dose. Material irradiated at the higher temperature undergoes significant yield

strength increases up to 1 GPa, whereas yield strength increases are negligible for material irradiated at the lower temperature (≤ 310 MPa). Grain boundary cracking after yielding was observed in specimens irradiated to 67 dpa at 180 °C. The second new SSMT was a push-to-pull, micro-tensile test that quantified the yield strengths, failure strengths, and total elongations of the components as a function of irradiation temperature and dose. For some specimens irradiated to 81 dpa, intergranular failure was directly observed after the specimens yielded, so failure stresses quantify grain boundary strengths. Both novel SSMTs also revealed significant regional differences in mechanical properties between the inner diameter, center, and outer diameter of the spacers due to variations in the cold working and grinding of the component that went undetected in bulk component testing. Because all high dose 67 dpa and 81 dpa micro-tensile specimens yielded in their grain interiors, and many of these specimens also failed within their grain interiors, a mixed mode failure mechanism involving dislocation channel fracture and intergranular fracture was proposed. The two failure mechanisms are speculated to be linked because when dislocation channels intersect compromised grain boundaries littered with helium bubbles, they produce significant stresses to fracture the boundary. Once an initial boundary fracture occurs, propagation of the fracture will occur along the boundaries at the component length scale leading to ultimate failure.

8. References

- [1] Kharecha, Pushker A., and James E. Hansen. "Prevented mortality and greenhouse gas emissions from historical and projected nuclear power." *Environmental science & technology* 47.9 (2013): 4889-4895.
- [2] Trainer, Ted. "Can renewables etc. solve the greenhouse problem? The negative case." *Energy Policy* 38.8 (2010): 4107-4114.
- [3] Jean-Baptiste, P., Ducroux, R., 2003. Energy policy and climate change. *Energy Policy* 31, 155–166.
- [4] Sailor, W.C., Bodansky, D., Braun, C., Fetter, S., van der Zwaan, B., 2000. Nuclear power—a nuclear solution to climate change? *Science* 288, 1177–1178.
- [5] Brook, Barry W. "Could nuclear fission energy, etc., solve the greenhouse problem? The affirmative case." *Energy Policy* 42 (2012): 4-8.
- [6] Mearns, Euan. "The Age and Future Size of the Global Nuclear Fleet." *Energy Matters*. 12 September 2016. Web.

- [7] "2015 Key World Energy Statistics" (PDF). IEA. 2016. p. 18. World electricity generation by fuels in 2015; from the international Energy Agency report Key World Energy Statistic, 2016 edition.
- [8] Zinkle, Steven J., and G. S. Was. "Materials challenges in nuclear energy." *Acta Materialia* 61.3 (2013): 735-758.
- [9] <http://www.civil.uwaterloo.ca/watrisk/research.html>
- [10] Manahan, M. P., A. S. Argon, and O. K. Harling. "The development of a miniaturized disk bend test for the determination of postirradiation mechanical properties." *Journal of Nuclear Materials* 104 (1981): 1545-1550.
- [11] Fleury, E., and J. S. Ha. "Small punch tests to estimate the mechanical properties of steels for steam power plant: I. Mechanical strength." *International Journal of Pressure Vessels and Piping* 75.9 (1998): 699-706.
- [12] Baik JM, Kameda J, Buck O. Development of small punch test for ductile-brittle transition temperature measurement of temper embrittled Ni-Cr Steels. In: Corwin WR, Lucas GE, editors. The use of small-scale specimens for testing irradiated material, ASTM STP 888. Philadelphia, PA: ASTM, 1986:92-111.
- [13] R. J. ROARKE and W. C. YOUNG, Formulas for Stress and Strain, 5th ed., McGraw-Hill Book Company, New York (1975).
- [14] Fan Hsiung Huang, Margaret L. Hamilton & Gary L. Wire (1982) Bend Testing for Miniature Disks, *Nuclear Technology*, 57:2, 234-242, DOI: 10.13182/NT82-A26286
- [15] Mao X, Shoji T, Takahashi H. Characterization of fracture behavior in small punch test by combined recrystallization-etch method and rigid plastic analysis. *Journal of Testing Evaluation* 1987;15:30-37.
- [16] Onat ET, Haythornthwaite RM. The load-carrying capacity of circular plates at large deflection. *Journal of Applied Mechanics* 1956; 23:49- 55.
- [17] Lucas, G. E. "The development of small specimen mechanical test techniques." *Journal of Nuclear Materials* 117 (1983): 327-339.
- [18] Wang NM. Large plastic deformation of a circular sheet caused by punch stretching. *Journal of Applied Mechanics, Transactions of the ASME*, paper no. 70-APM-KK, 1970:431-440.
- [19] Guduru, R. K., et al. "Finite element analysis of a shear punch test." *Metallurgical and Materials Transactions A* 37.5 (2006): 1477-1483.

- [20] Goyal, Sunil, et al. "Finite element analysis of shear punch testing and experimental validation." *Materials & Design (1980-2015)* 31.5 (2010): 2546-2552.
- [21] M.B. Toloczko, M.L. Hamilton, and G.E. Lucas: *J. Nucl. Mater.*, 2000, vol. 283–287, pp. 987-91.
- [22] R.K. Guduru, K.A. Darling, R. Kishore, R.O. Scattergood, C.C. Koch, and K.L. Murty: *Ultrafine Grained Mater. III*, TMS, 2004, pp. 565-70.
- [23] R.K. Guduru, K.A. Darling, R. Kishore, R.O. Scattergood, C.C. Koch, and K.L. Murty: *Mater. Sci. Eng. A*, 2005, vol. 395, pp. 307-14.
- [24] G.L. Hankin, M.B. Toloczko, M.L. Hamilton, and R.G. Faulkner: *J. Nucl. Mater.*, 1998, vol. 258–263, pp. 1651-56.
- [25] M.B. Toloczko, R.J. Kurtz, A. Hasegawa, and K. Abe: *J. Nucl. Mater.*, 2002, vol. 307–311, pp. 1619-23.
- [26] M.L. Hamilton and M.B. Toloczko: *J. Nucl. Mater.*, 2000, vol. 283– 287, pp. 488-91.
- [27] M.L. Hamilton, M.B. Toloczko, G.E. Lucas, Recent progress in shear punch testing, in: H. Ullmaier, P. Jung (Eds.), *Miniaturized Specimens for Testing of Irradiated Materials*, Forschungszentrum Julich □ GmbH, 1995, p. 46.
- [28] M.B. Toloczko, M.L. Hamilton, G.E. Lucas, *Proceedings of the workshop on miniaturized specimens for testing of irradiated materials*, IEA International symposium, 1996.
- [29] Foulds JR, Viswanathan R. Small punch testing for determining the material toughness of low alloy steel components in service. *Journal of Engineering Materials and Technology* 1994; 116:457-464
- [30] Toloczko, Mychailo B., et al. "Shear punch tests performed using a new low compliance test fixture." *Journal of nuclear materials* 307 (2002): 1619-1623.
- [31] H.P. Myers, M. Grounes and N.E. Hannerz, *Proc. 3rd Int. Conf. on Peaceful Use of At. Energy*, Geneva (1964) p. 240, 266.
- [32] *The Use of Small-Scale Specimens for Testing Irradiated Material*, Eds. W.R. Convin and G.L. Lucas, ASTM STP 888 (1986).

- [33] W.L. Hu, HEDL-SA-2947-FP (1983).
- [34] W.L. Hu and D.S. Gelles, Proc. Topical Conf. on Ferritic Alloys for Use in Nuclear Energy Technologies, Snowbird, Utah, USA (1983) p. 631.
- [35] W.R. Corwin, R.L. Klueh and J.M. Vitek, J. Nucl. Mater. 122 & 123 (1984) 343.
- [36] H. Kayano, M. Narui and S. Ohta, J. Nucl. Mater. 122 & 123 (1984) 649.
- [37] G.L. Lucas, G.R. Odette, J.W. Shekherd, P. McConnell and J. Perrin, The Use of Small-Scale Specimens for Testing Irradiated Material, ASTM STP 888 (1986) 305.
- [38] R. Ahlstrand, E. N. Klausnitzer, D. Lange, C. Leitz, D. Pastor, and M. Valo, "Evaluation of the Recovery Annealing of the Reactor Pressure Vessel of NPP Nord (Greifswald) Units 1 and 2 by Means of Subsize Impact Specimens," pp. 312-43 in Radiation Embrittlement of Nuclear Reactor Pressure Vessel Steels: An International Review (Fourth Volume), ASTMSTP 1170, L. E. Steele, Ed., American Society for Testing and Materials, Philadelphia, 1993.
- [39] A. D. Amayev, V. I. Badanin, A. M. Kryukov, V. A. Nikolayev, M. F. Rogov, and M. A. Sokolov, "Use of Subsize Specimens for Determination of Radiation Embrittlement of Operating Reactor Pressure Vessels," pp. 424-39 in Small Specimen Test Techniques Applied to Nuclear Reactor Vessel Thermal Annealing and Plant Life Extension, ASTMSTP 1204, W. R. Corwin, F. M. Haggag, and W. L. Server, Eds., American Society for Testing and Materials, Philadelphia, 1993.
- [40] Standard Test Method for Notched Bar Impact Testing of Metallic Materials, ASTM E 23-93a, American Society for Testing and Materials, Philadelphia, 1993.
- [41] E. Klausnitzer, H. Kristof, and R. Leistner, "Assessment of Toughness Behavior of Low Alloy Steels by Subsize Impact Specimens," pp. 3-37 in Transactions of the 8th International Conference on Structural Mechanics in Reactor Technology, Brussels, August 1985, Vol G, International Association for Structural Mechanics in Reactor Technology, 1986.
- [42] E. N. Klausnitzer and G. Hofmann, "Reconstituted Impact Specimens with Small Inserts," pp. 76-90 in Effects of Radiation on Materials: 15th International Symposium, ASTMSTP 1125, R. E. Stoller, A. S. Kumar, and D. S. Gelles, Eds., American Society for Testing and Materials, Philadelphia, 1992.
- [43] G. E. Lucas, G. R. Odette, J. W. Shekherd, and M. R. Krishnadev, "Recent Progress in Subsized Charpy Impact Specimen Testing for Fusion Reactor

Materials Development," pp. 728-33 in *Fusion Technology*, Vol. 10, November 198

[44] B. S. Loudon, A. S. Kumar, F. A. Garner, M. L. Hamilton, and W. L. Hu, "The Influence of Specimen Size on Charpy Impact Testing of Unirradiated HT-9," *J. Nucl. Mater.* 155-157. 662-67 (1988).

[45] H. Neuber, *Theory of Notch Stresses*, Springer, Berlin, 1958

[46] Kayano, H., et al. "Charpy impact testing using miniature specimens and its application to the study of irradiation behavior of low-activation ferritic steels." *Journal of nuclear materials* 179 (1991): 425-428.

[47] Sokolov, Mikhail A., and Randy K. Nanstad. "On impact testing of subsized Charpy V-notch type specimens." *Effects of Radiation on Materials: 17th International Symposium*. ASTM International, 1996.

[48] Lucon, E., et al. *Correlations between standard and miniaturised Charpy-V specimens*. No. BLG--797. Centre de l'Etude de l'Energie Nucleaire, 1998.

[49] L. Prandtl, *Nachr. Ges. Wiss. Gottingen*. (1920) 74.

[50] S.M. Bruemmer et al., *Characterization of Neutron-Irradiated 300-Series Stainless Steels to Assess Mechanisms of Irradiation Assisted Stress Corrosion Cracking*, Final Report, EPRI Project WO4068-20, November 2000.

[51] S. Suzuki, Y. Tanaka, M. Kodama, S. Nishimura, K. Fukuya, S. Shima, K. Nakata, T. Kato, *Mechanical Properties and SSRT results of various kinds of irradiated stainless steels*, Presented at 12th ICG-IASCC meeting, Toronto, Canada, April 1996.

[52] M.B. Toloczko et al., in: *17th International Symposium on Effects of Rad. On Materials*, STP1270, 1996, p. 902.

[53] H.R. Higgy, F.H. Hammad, *J. Nucl. Mater.* 55 (1975) 177.

[54] Busby, Jeremy T., Mark C. Hash, and Gary S. Was. "The relationship between hardness and yield stress in irradiated austenitic and ferritic steels." *Journal of Nuclear Materials* 336.2-3 (2005): 267-278.

[55] D. Tabor, *Br. J. Appl. Phys* 7 (1956) 159.

[56] Eto, Motokuni, and Tatsuo Oku. "Change in electrical resistivity of nuclear graphite during compression tests and a model for its deformation and fracture mechanism." *Journal of Nuclear Materials* 54.2 (1974): 245-253.

- [57] Pitner, A. L. "Fast Reactor Irradiation of Boron Carbide Powder." *Nuclear Technology* 16.2 (1972): 410-417.
- [58] Masafumi NAKATSUKA & Masayuki NAGAI (1987) Reduction of Plastic Anisotropy of Zircaloy Cladding by Neutron Irradiation, (I), *Journal of Nuclear Science and Technology*, 24:10, 832-838, DOI: 10.1080/18811248.1987.9735886
- [59] Dressler, G., K. H. Matucha, and P. Wincierz. "Yield loci of Zircaloy tubing with different textures." *Canadian Metallurgical Quarterly* 11.1 (1972): 177-184.
- [60] Yang, Yong, Clayton A. Dickerson, and Todd R. Allen. "Radiation stability of ZrN under 2.6 MeV proton irradiation." *Journal of Nuclear Materials* 392.2 (2009): 200-205.
- [61] Reed, C. B., et al. "The effect of laser welding process parameters on the mechanical and microstructural properties of V-4Cr-4Ti structural materials." *Journal of nuclear materials* 283 (2000): 1206-1209.
- [62] Hosemann, P., et al. "An exploratory study to determine applicability of nano-hardness and micro-compression measurements for yield stress estimation." *Journal of Nuclear Materials* 375.1 (2008): 135-143.
- [63] Oliver, Warren Carl, and George Mathews Pharr. "An improved technique for determining hardness and elastic modulus using load and displacement sensing indentation experiments." *Journal of materials research* 7.6 (1992): 1564-1583.
- [64] Tabor, David. "A simple theory of static and dynamic hardness." *Proc. R. Soc. Lond. A*. Vol. 192. No. 1029. The Royal Society, 1948.
- [65] Stilwell, N. A., and D. Tabor. "Elastic recovery of conical indentations." *Proceedings of the Physical Society* 78.2 (1961): 169.
- [66] Ternovskii A. P., Alekhin V. P., Shorshorov M. Kh., Khrushchov M. M., and Skvortsov V. N., *Zavod. Lab.* **39**, 1242 (1973).
- [67] Bulychev S. I., Alekhin V. P., Shorshorov M. Kh., Ternovskii A. P., and Shnyrev G. D., *Zavod. Lab.* **41**, 1137 (1975).
- [68] Bulychev S. I., Alekhin V. P., Shorshorov M. Kh., and Ternovskii A. P., *Prob. Prochn.* **9**, 79 (1976).
- [69] Shorshorov M. Kh., Bulychev S. I., and Alekhin V. P., *Sov. Phys. Dokl.* **26**, 769 (1982).

- [70] Bulychev S. I. and Alekhin V. P., *Zavod. Lab.* **53**, 76 (1987).
- [71] Pharr G. M., Oliver W. C., and Brotzen F. R., *J. Mater. Res.* **7**, 613 (1992).
- [72] Sneddon I. N., *Int. J. Engng. Sci.* **3**, 47 (1965)
- [73] Pethica J. B., Hutchings R., and Oliver W. C., *Philos. Mag. A* **48**, 593 (1983).
- [74] Oliver W. C., Hutchings R., and Pethica J. B., in *ASTM STP 889*, edited by Blau P. J. and Lawn B. R. (American Society for Testing and Materials, Philadelphia, PA, 1986), pp. 90–108.
- [75] Kiener, Daniel, et al. "Application of small-scale testing for investigation of ion-beam-irradiated materials." *Journal of Materials Research* 27.21 (2012): 2724-2736.
- [76] A.C. Fischer-Cripps: *Nanoindentation* (Springer, New York, 2004).
- [77] K.L. Johnson: The correlation of indentation experiments. *J. Mech. Phys. Solids* 18, 115 (1970).
- [78] Lupinacci, A., et al. "Characterization of ion beam irradiated 304 stainless steel utilizing nanoindentation and Laue microdiffraction." *Journal of Nuclear Materials* 458 (2015): 70-76.
- [79] Kasada, Ryuta, et al. "A new approach to evaluate irradiation hardening of ion-irradiated ferritic alloys by nano-indentation techniques." *Fusion Engineering and Design* 86.9-11 (2011): 2658-2661.
- [80] W.D. Nix and H. Gao: Indentation size effects in crystalline materials: A law for strain gradient plasticity. *J. Mech. Phys. Solids* 46, 411 (1998).
- [81] Krumwiede, D., et al. "Direct comparison of nanoindentation and tensile test results on reactor-irradiated materials." *Journal of Nuclear Materials* (2017) under review
- [82] T. Milot, *Establishing correlations for predicting tensile properties based on the shear punch test and Vickers microhardness data*, University of California, Santa Barbara, 2013.
- [83] W. C. Oliver and G. M. Pharr, "Measurement of hardness and elastic modulus by instrumented indentation: Advances in understanding and refinements to methodology," *J. Mater. Res.*, vol. 19, no. 1, pp. 3–20, 2004.

- [84] Kareer, A., et al. "An analytical method to extract irradiation hardening from nanoindentation hardness-depth curves." (2017).
- [85] H. Hertz, *Miscellaneous Papers*, MacMillan and Co. Ltd., New York, 1896.
- [86] J.S. Field, M.V. Swain, *J. Mater. Res.* 8 (1993) 297–306.
- [87] J.S. Field, M.V. Swain, *J. Mater. Res.* 10 (1995) 101–112.
- [88] Kalidindi, Surya R., and Siddhartha Pathak. "Determination of the effective zero-point and the extraction of spherical nanoindentation stress–strain curves." *Acta Materialia* 56.14 (2008): 3523-3532.
- [89] Armstrong, D. E. J., et al. "Small-scale characterisation of irradiated nuclear materials: Part II nanoindentation and micro-cantilever testing of ion irradiated nuclear materials." *Journal of Nuclear Materials* 462 (2015): 374-381.
- [90] Pathak, Siddhartha, et al. "Probing nanoscale damage gradients in ion-irradiated metals using spherical nanoindentation." *Scientific reports* 7.1 (2017): 11918.
- [91] C.A. Schuh, *Mater. Today* 9 (2006) 32–40.
- [92] T.H. Courtney, *Mechanical Behavior of Materials*, McGraw-Hill Science/Engineering/Math, 1999.
- [93] Bushby, Andrew J., Steve G. Roberts, and Christopher D. Hardie. "Nanoindentation investigation of ion-irradiated Fe–Cr alloys using spherical indenters." *Journal of Materials Research* 27.1 (2012): 85-90.
- [94] T.T. Zhu, A.J. Bushby, and D.J. Dunstan: Size effect in the initiation of plasticity for ceramics in nanoindentation. *J. Mech. Phys. Solids* 56, 1170 (2008).
- [95] Weaver, Jordan S., et al. "Spherical nanoindentation of proton irradiated 304 stainless steel: A comparison of small scale mechanical test techniques for measuring irradiation hardening." *Journal of Nuclear Materials* 493 (2017): 368-379.
- [96] Anstis, G. R., et al. "A critical evaluation of indentation techniques for measuring fracture toughness: I, direct crack measurements." *Journal of the American Ceramic Society* 64.9 (1981): 533-538.
- [97] Hosemann, Peter, et al. "Mechanical characteristics of SiC coating layer in TRISO fuel particles." *Journal of Nuclear Materials* 442.1-3 (2013): 133-142.

- [98] N.M. Everitt, M.I. Davies, and J.F. Smith: High temperature nanoindentation—The importance of isothermal contact. *Philos. Mag.* 91, 1221 (2011).
- [99] J.M. Wheeler, P. Brodard, and J. Michler: Elevated temperature, in situ indentation with calibrated contact temperatures. *Philos. Mag.* 92, 3128–3141 (2012).
- [100] Z.C. Duan and A.M. Hodge: High-temperature nanoindentation: New developments and ongoing challenges. *JOM* 61, 32–36 (2009).
- [101] B.D. Beaker and J.F. Smith: High-temperature nanoindentation testing of fused silica and other materials. *Philos. Mag. A* 82, 2179–2186 (2002).
- [102] J.M. Wheeler and J. Michler: Elevated temperature, nanomechanical testing in situ in the scanning electron microscope. *Rev. Sci. Instrum.* 84, 045103 (2013).
- [103] J.M. Wheeler, V. Maier, K. Durst, M. Göken, and J. Michler: Activation parameters for deformation of ultrafine-grained aluminium as determined by indentation strain rate jumps at elevated temperature. *Mater. Sci. Eng., A* 585, 108–113 (2013).
- [104] B.D. Beake, G.A. Bell, S.R. Goodes, N.J. Pickford, and J.F. Smith: Improved nanomechanical test techniques for surface engineered materials. *Surf. Eng.* 26 37–49 (2010).
- [105] S. Korte, R.J. Stearn, J.M. Wheeler, and W.J. Clegg: High temperature microcompression and nanoindentation in vacuum. *J. Mater. Res.* 27, 167 (2012).
- [106] A. Reichardt, A. Lupinacci, J. Kacher, Z. Jiao, P. Chou, M. Abad, A. Minor, and P. Hosemann: Development of small scale mechanical testing techniques on ion beam irradiated 304 SS. In *Proceedings of Fontevraud 8—Contribution of Materials Investigations and Operating Experience to LWRs’ Safety, Performance and Reliability France, Avignon, September, 2013.*
- [107] S-W. Lee, L. Meza, and J.R. Greer: Cryogenic nanoindentation size effect in [0 0 1]-oriented face-centered cubic and body centered cubic single crystals. *Appl. Phys. Lett.* 103(10), 101906 (2013).
- [108] Z. Huang, A. Harris, S.A. Maloy, and P. Hosemann: Nanoindentation creep study on an ion beam irradiated oxide dispersion strengthened alloy. *J. Nucl. Mater.* 451, 162–167 (2014).

- [109] V. Maier, B. Merle, M. Göken, and K.J. Durst: An improved long-term nanoindentation creep testing approach for studying the local deformation processes in nanocrystalline metals at room and elevated temperatures. *J. Mater. Res.* 28(9), 1177 (2013).
- [110] I. Sneddon, *Int. J. Eng. Sci.* 3 (1965) 47–57.
- [111] Wörgötter et al., *BHM*, 153. Jg., Heft 7, 2008.
- [112] Uchic, Michael D., et al. "Sample dimensions influence strength and crystal plasticity." *Science* 305.5686 (2004): 986-989.
- [113] J.R. Greer and J.T.M. De Hosson: Plasticity in small-sized metallic systems: Intrinsic versus extrinsic size effect. *Prog. Mater. Sci.* 56, 654 (2011).
- [114] C. Shin, S. Lim, H.H. Jin, P. Hosemann, and J. Kwon: Specimen size effects on the weakening of a bulk metastable austenitic alloy. *Mater. Sci. Eng., A* 622, 67–75 (2015).
- [115] Howard, C., et al. "Investigation of specimen size effects by in-situ microcompression of equal channel angular pressed copper." *Materials Science and Engineering: A* 649 (2016): 104-113.
- [116] Kiener, D., et al. "In situ nanocompression testing of irradiated copper." *Nature materials* 10.8 (2011): 608.
- [117] Hosemann, P., C. Shin, and D. Kiener. "Small scale mechanical testing of irradiated materials." *Journal of Materials Research* 30.9 (2015): 1231-1245.
- [118] Zhang, Haitao, et al. "The design of accurate micro-compression experiments." *Scripta Materialia* 54.2 (2006): 181-186.
- [119] Kiener, D., et al. "FIB damage of Cu and possible consequences for miniaturized mechanical tests." *Materials Science and Engineering: A* 459.1-2 (2007): 262-272.
- [120] Kiener, Daniel, et al. "Advanced nanomechanics in the TEM: effects of thermal annealing on FIB prepared Cu samples." *Philosophical Magazine* 92.25-27 (2012): 3269-3289.
- [121] Pouchon, Manuel A., et al. "Characterization of irradiation damage of ferritic ODS alloys with advanced micro-sample methods." *Experimental mechanics* 50.1 (2010): 79-84.

- [122] Hosemann, P., et al. "Large and small scale materials testing of HT-9 irradiated in the STIP irradiation program." *Experimental mechanics* 51.7 (2011): 1095-1102.
- [123] Stewart, J. L., et al. "Prediction of bulk tensile behavior of dual phase stainless steels using constituent behavior from micropillar compression experiments." *Materials Science and Engineering: A* 534 (2012): 220-227.
- [124] Reichardt, A., et al. "Nanoindentation and in situ microcompression in different dose regimes of proton beam irradiated 304 SS." *Journal of Nuclear Materials* 486 (2017): 323-331.
- [125] Shih C, Katoh Y, Leonard KJ, Bei H, Lara-Curzio E. Determination of interfacial mechanical properties of ceramic composites by the compression of micropillar test specimens. *J Mater Sci* 2013; 48(15):5219e24.
- [126] Kabel, J., et al. "Micro-mechanical evaluation of SiC-SiC composite interphase properties and debond mechanisms." *Composites Part B: Engineering* 131 (2017): 173-183.
- [127] Kabel, Joey, et al. "Ceramic composites: A review of toughening mechanisms and demonstration of micropillar compression for interface property extraction." *Journal of Materials Research* (2018): 1-16.
- [128] A. Lupinacci, J. Kacher, A. Eilenberg, A.A. Shapiro, P. Hosemann, and A.M. Minor: Cryogenic in situ microcompression testing of Sn. *Acta Mater.* 78, 56–64 (2014).
- [129] S. Korte, R.J. Stearn, J.M. Wheeler, and W.J. Clegg: High temperature microcompression and nanoindentation in vacuum. *J. Mater. Res.* 27, 167 (2012).
- [130] S. Korte and W.J. Clegg: Micropillar compression of ceramics at elevated temperatures. *Scr. Mater.* 60, 807 (2009).
- [131] S. Korte, J.S. Barnard, R.J. Stearn, and W.J. Clegg: Deformation of silicon–insights from microcompression testing at 25–500 °C. *Int. J. Plast.* 27, 1853 (2011).
- [132] J.M. Wheeler, C. Niederberger, C. Tessarek, S. Christiansen, and J. Michler: Extraction of plasticity parameters of GaN with high temperature, in situ micro-compression. *Int. J. Plast.* 40, 140–151 (2013).

- [133] M.D. Uchic and D.M. Dimiduk: A methodology to investigate size scale effects in crystalline plasticity using uniaxial compression testing. *Mater. Sci. Eng., A* 400–401, 268–278 (2005).
- [134] Vo, H., et al. "Small-scale mechanical testing on proton beam-irradiated 304 SS from room temperature to reactor operation temperature." *JOM* 67.12 (2015): 2959-2964.
- [135] S. Ozerinc, R.S. Averback, and W.P. King: In situ creep measurements on micropillar samples during heavy ion irradiation. *J. Nucl. Mater.* 451, 104–110 (2014).
- [136] Hosemann, P., C. Shin, and D. Kiener. "Small scale mechanical testing of irradiated materials." *Journal of Materials Research* 30.9 (2015): 1231-1245.
- [137] Hosemann, P., et al. "Development of Ultra Small Scale Mechanical Testing and Localized He Implantation for Nuclear Applications."
- [138] Giancola, D. S., and C. Eberl. "Micro-and nanoscale tensile testing of materials." *Jom* 61.3 (2009): 24.
- [139] D. Kiener, W. Grosinger, G. Dehm, R. Pippan, *Acta Mater.* 56 (2008) 580.
- [140] D. Kiener, W. Grosinger, G. Dehm, *Scr. Mater.* 60 (2009) 148–151.
- [141] Vo, H. T., et al. "In situ micro-tensile testing on proton beam-irradiated stainless steel." *Journal of Nuclear Materials* 493 (2017): 336-342.
- [142] Reichardt, Ashley, et al. "In situ micro tensile testing of He+ 2 ion irradiated and implanted single crystal nickel film." *Acta Materialia* 100 (2015): 147-154.
- [143] Fujii, Katsuhiko, and Koji Fukuya. "Development of micro tensile testing method in an FIB system for evaluating grain boundary strength." *Materials transactions* 52.1 (2011): 20-24.
- [144] Miura, Terumitsu, Katsuhiko Fujii, and Koji Fukuya. "Micro-mechanical investigation for effects of helium on grain boundary fracture of austenitic stainless steel." *Journal of Nuclear Materials* 457 (2015): 279-290.
- [145] D. Di Maio, S.G. Roberts, *J. Mater. Res.* 20 (2005) 299–302.
- [146] C.B. Ponton and R.D. Rawlings: Vickers indentation fracture toughness test Part 1: Review of literature and formulation of standardised indentation toughness equations. *Materials Science and Technology* 5, p. 865 (1989).

- [147] K. E. Petersen, Silicon as a mechanical material: Proc. IEEE. 70, No. 5, (1982).
- [148] C. St. John, The brittle-to-ductile transition in pre-cleaved silicon. Phil. Mag. 32, p. 1194 (1975).
- [149] Stratulat, Alisa, David EJ Armstrong, and Steve G. Roberts. "Micro-mechanical measurement of fracture behaviour of individual grain boundaries in Ni alloy 600 exposed to a pressurized water reactor environment." *Corrosion Science* 104 (2016): 9-16.
- [150] Lozano-Perez, Sergio, et al. "Micromechanical testing of oxidized grain boundaries in Nickel alloys from nuclear reactors." *MRS Online Proceedings Library Archive* 1519 (2013).
- [151] Matoy, Kurt, et al. "A comparative micro-cantilever study of the mechanical behavior of silicon based passivation films." *Thin Solid Films* 518.1 (2009): 247-256.
- [152] Abad, M. D., et al. "Evaluation of the mechanical properties of naturally grown multilayered oxides formed on HCM12A using small scale mechanical testing." *Oxidation of Metals* 84.1-2 (2015): 211-231.
- [153] K.J. Hollis, N.A. Mara, R.D. Field, T.A. Wynn, J.M. Crapps, P.O. Dickerson, J. Therm. Spray Technol. 22 (2013) 233–241.
- [154] Kiener, D., et al. "Cyclic response of copper single crystal micro-beams." *Scripta Materialia* 63.5 (2010): 500-503.
- [155] Kapp, M. W., et al. "Structural instabilities during cyclic loading of ultrafine-grained copper studied with micro bending experiments." *Acta Materialia* 125 (2017): 351-358.
- [156] Howard, C., et al. "The influence of microstructure on the cyclic deformation and damage of copper and an oxide dispersion strengthened steel studied via in-situ micro-beam bending." *Materials Science and Engineering: A* 687 (2017): 313-322.
- [157] I. Kuběna, et al., Fatigue behaviour of ODS ferritic-martensitic Eurofer steel, *Procedia Eng.* 2 (1) (2010) 717–724.
- [158] S. Maekawa, K. Takashima, M. Shimojo, Y. Higo, S. Sugiura, B. Pfister, M.V. Swain, *J. Appl. Phys.* 38 (1999) 7194–7198.

- [159] Y.-C. Wang, J. Hoehbauer, G. Swadener, A. Misra, R.G. Hoagland, M. Nastasi, *Exp. Mech.* 46 (2006) 503–517.
- [160] S. Burger, C. Eberl, A. Siegel, A. Ludwig, O. Kraft, *Sci. Technol. Adv. Mater.* 12 (2011), 054202.
- [161] D.E.J. Armstrong, E. Tarleton, *JOM* 67 (2015) 2914–2920.
- [162] J.P. Best, J. Zechner, J.M. Wheeler, R. Schoepner, M. Morstein, J. Michler, *Philos. Mag.* 96 (2016) 3552–3569
- [163] J. Gibson, D. Armstrong, S. Roberts, *Phys. Scr.* T159 (2014), 014056.
- [164] Wall MA, Dahmen U. Development on an in situ nanoindentation specimen holder for the high voltage electron microscope. *Microsc Microanal* 1997; 3:593–4.
- [165] Wall MA, Dahmen U. An in situ nanoindentation specimen holder for a high voltage transmission electron microscope. *Microsc Res Tech* 1998; 42:248–54.
- [166] Stach EA, Freeman T, Minor AM, Owen DK, Cumings J, Wall MA, et al. Development of a nanoindenter for in situ transmission electron microscopy. *Microsc Microanal* 2001; 7:507–17.
- [167] Bobji MS, Ramanujan CS, Doole RC, Pethica JB, Inkson BJ. An in-situ TEM nanoindenter system with 3-axis inertial positioner. *MRS Proc* 2003:778. U4.5.1-6.
- [168] Nili, Hussein, et al. "In situ nanoindentation: Probing nanoscale multifunctionality." *Progress in Materials Science* 58.1 (2013): 1-29.
- [169] Minor A, Lilleodden E, Stach E, Morris J. In-situ transmission electron microscopy study of the nanoindentation behavior of Al. *J Electron Mater* 2002;31:958–64.
- [170] Minor AM, Lilleodden ET, Stach EA, Morris JW. Direct observations of incipient plasticity during nanoindentation of Al. *J Mater Res* 2004; 19:176–82.
- [171] Minor A, Stach E, Morris J, Petrov I. In-situ nanoindentation of epitaxial TiN/MgO (001) in a transmission electron microscope. *J Electron Mater* 2003; 32:1023–7.
- [172] Minor, Andrew M., et al. "A new view of the onset of plasticity during the nanoindentation of aluminium." *Nature materials* 5.9 (2006): 697.

- [173] De Hosson, Jeff TM, et al. "In situ TEM nanoindentation and dislocation-grain boundary interactions: a tribute to David Brandon." *Journal of materials science* 41.23 (2006): 7704-7719.
- [174] Ohmura, T., et al. "Dislocation–grain boundary interactions in martensitic steel observed through in situ nanoindentation in a transmission electron microscope." *Journal of Materials Research* 19.12 (2004): 3626-3632.
- [175] Lee, Joon Hwan, et al. "Direct observation of Lomer-Cottrell Locks during strain hardening in nanocrystalline nickel by in situ TEM." *Scientific reports* 3 (2013): 1061.
- [176] Lockwood AJ, Inkson BJ. In situ TEM nanoindentation and deformation of Si-nanoparticle clusters. *J Phys D: Appl Phys* 2009; 42:035410.
- [177] Zhou J, Komvopoulos K, Minor AM. Nanoscale plastic deformation and fracture of polymers studied by in situ nanoindentation in a transmission electron microscope. *Appl Phys Lett* 2006; 88:181908.
- [178] Guo, Qiang, et al. "Helium implantation effects on the compressive response of Cu nanopillars." *Small* 9.5 (2013): 691-696.
- [179] Wang, Zhang-Jie, et al. "Mechanical behavior of copper containing a gas-bubble superlattice." *Acta Materialia* 121 (2016): 78-84.
- [180] Landau, Peri, et al. "Deformation of as-fabricated and helium implanted 100 nm-diameter iron nano-pillars." *Materials Science and Engineering: A* 612 (2014): 316-325.
- [181] Ding, Ming-Shuai, et al. "Nanobubble Fragmentation and Bubble-Free-Channel Shear Localization in Helium-Irradiated Submicron-Sized Copper." *Physical review letters* 117.21 (2016): 215501.
- [182] Onimus, F., L. Dupuy, and F. Mompiau. "In situ TEM observation of interactions between gliding dislocations and prismatic loops in Zr-ion irradiated zirconium alloys." *Progress in Nuclear Energy* 57 (2012): 77-85.
- [183] Liu, J., and D. Kaoumi. "Use of in-situ TEM to characterize the deformation-induced martensitic transformation in 304 stainless steel at cryogenic temperature." *Materials Characterization* 136 (2018): 331-336.
- [184] Hintsala, E., et al. "In-situ measurements of free-standing, ultra-thin film cracking in bending." *Experimental Mechanics* 55.9 (2015): 1681-1690.

- [185] <http://www.specialmetals.com/assets/smc/documents/alloys/nickel-duranickel/nickel-200-201.pdf>
- [186] R.C. Read, "The Superalloys, Fundamentals and Applications", Cambridge University Press (2006). isbn-13 978-0-511-24546-6
- [187] A. Strasser and F.P Ford, "*High Strength Ni-alloys in Fuel Assemblies*", ANT International, Molnlycke, Sweden (2012).
- [188] *Superalloys II*. John Willey and Sons, Inc.: 1987.
- [189] W.J. Mills, M.R. lebo, J.J. Kearns, R.C. Hoffman, J.J. Korinko, R.F. luther and G.B. Sykes, "Effect of Irradiation on the Stress Corrosion Cracking Behaviour of Alloy X-750 and Alloy 625", Sixth International Symposium on Environmental Degradation of Materials in Nuclear Power Systems-Water Reactors, TMMM (1993) pp. 633-643.
- [190] R. Cozar and A. Pineau, "Morphology of γ' and γ'' Precipitates and Thermal Stability of Inconel 718 Type Alloys", *Met. Trans.* 4 (1973) 47-59.
- [191] Special Metals Corporation Publication No SMC-067, September 2004.
- [192] G.D. Smith and S.J. Patel, "Superalloys 718, 625, 706 and Derivatives", Edited by E.A. Loria TMS (The Minerals, Metals & Materials Society), 2005.
- [193] O.T. Woo, et al., The microstructure of unirradiated and neutron irradiated Inconel X750, *Microsc. Microanal.* 17 (Suppl 2) (2011).
- [194] Kusabiraki, Kiyoshi, Hajime Komatsu, and Shuuichi Ikeuchi. "Lattice constants and compositions of the metastable Ni₃Nb phase precipitated in a Ni-15Cr-8Fe-6Nb alloy." *Metallurgical and Materials Transactions A* 29.4 (1998): 1169-1174.
- [195] Cayron, C. "Quantification of multiple twinning in face centred cubic materials." *Acta Materialia* 59.1 (2011): 252-262.
- [196] W.J. Mills, Mastel Bernard, Deformation and fracture characteristics for irradiated Inconel X-750, *Nucl. Technol.* 73.1 (1986) 102-108.
- [197] M. Griffiths, The effect of irradiation on Ni-containing components in CANDU® reactor cores: a review, *AECL Nucl. Rev.* 2 (1) (2013).
- [198] L.C. Walters, W.E. Ruther, In-reactor stress relaxation of Inconel X-750 springs, *J. Nucl. Mat.* 68 (1977) 324-333.

- [199] J.J. Olivera, et al., Failure of Inconel X-750 bolts of internals of the CHOOZ-A nuclear power plant. CEA Centre d'Etudes Nucleaires de Fontenay-aux-Roses, 92 (France). Dept. d'Analyse de Surete, 1989.
- [200] Balog, Leonard J., and David E. Boyle. Four pin mounting system for nuclear reactor control rod guide tubes. U.S. Patent No. 4,937,039. 26 Jun. 1990.
- [201] Katayama, Yoshinori, et al. Jet Pump Beam and Method for Producing the Same. U.S. Patent No. 8,879,683. vol. 4 Nov. 2014.
- [202] Fanning, Alan W., William G. Jameson Jr, and Victor E. Hazel. "Nuclear Fuel Assembly. U.S. Patent No. 4,314,884. vol. 9 Feb. 1982.
- [203] Kim, Young Jin, et al, Fuel Rod Assembly and Method for Mitigating the Radiation-enhanced Corrosion of a Zirconium-based Component. U.S. Patent No. 8,792,607. vol. 29 Jul. 2014.
- [204] Marcus Nichol, NEI Nuclear Notes Interview vol. 8, May 2012. <http://neinuclearnotes.blogspot.ca/2012/05/what-happens-during-refueling-outage.html>.
- [205] J. Harris, EPRI report 1003589, "PWR Generic Tube Degradation Predictions – US Recirculating Steam Generators with Alloy 600 TT and Alloy 690TT" (2003).
- [206] M. Le Calvar and I. de Curières, "Corrosion Issues in Pressurized Reactor (PWR) Systems", In: Nuclear Corrosion Science and Engineering (2012) 473-547.
- [207] J. Panter, B. Viguiet, J.-M Cloue, M. Foucault, P. Combrade, E. Andrieu, "Influence Of Oxide Films on Primary Water Stress Corrosion Cracking Initiation of Alloy 600", J. Nucl. Mater. 348 (2006) 213-221.
- [208] S. Morton, S. A. Attanasio, J. S. Fish, M. K. Schurman, "Influence of Dissolved Hydrogen on Nickel Alloy SCC in High Temperature Water", CORROSION 99 (1999).
- [209] G. S. Was, H. H. Tischner and R. M. Latanision, "The Influence of Thermal Treatment on the Chemistry and Structure of Grain Boundaries in Inconel 600", Met. Trans. A., 12 (1981) 1397.
- [210] S.M. Bruemmer and G.S. Was, "Microstructural and microchemical mechanisms controlling inter-granular stress corrosion cracking in light-water-reactor systems", J. Nucl. Mater. 457 (2015) 165-172.

- [211] J.J. Kai, G.P. Yu, C.H. Tsai, M.N. Liu and S.C. Yao, "The Effects of Heat Treatment on Chromium Depletion, Precipitate Evaluation and Corrosion Resistance of Alloy 690", *Met. Trans. A*, 20A (1989) 2057-2067.
- [212] Lu, Yucheng, Sridhar Ramamurthy, and Guylaine Goszczynski. "An aging assessment on ex-service Alloy 800 steam generator tubing." *Nuclear engineering and design* 242 (2012): 91-99.
- [213] H. Coriou, L. Grall, Y. Le Gall and S. Vettier, "Corrosion Fissurante sous Contrainte de l'Inconel dans l'eau à Haute Temperature" in Proceedings of 3eme Colloque de Metallurgie sur la Corrosion, Saclay; North Holland: Amsterdam (1959)161-169.
- [214] A.F. Rowcliffe, L.K. Mansur, D.T. Hoelzer and R.K. Nanstad, "Perspectives on Radiation Effects in Nickel-Base Alloys For Applications In Advanced Reactors", *J. Nucl. Mater.* 392 (2009) 341-352.
- [215] F. A. Garner and H. R. Brager, "Dependence of Neutron Induced Swelling on Composition in Iron-Based Austenitic Alloys," in *Optimizing Materials for Nuclear Applications*, F. A. Garner, D. S. Gelles and F. W. Wiffen, Eds., TMS-AIME, Warrendale, PA (1985) 87-109.
- [216] R.K. Nanstad, D.A. McClintock, D.T. Hoelzer, L. Tan, T.R. Allen, "High Temperature Irradiation Effects in Selected Generation IV Structural Alloys", *J. Nucl. Mater.* 392 (2009) 331-340.
- [217] IAEA Nuclear Energy Series, "Structural Materials for Liquid Metal Cooled Fast Reactor Fuel Assemblies — Operational Behaviour", No. NF-T-4.3 (2012). http://www-pub.iaea.org/MTCD/Publications/PDF/Pub1548_web.pdf
- [218] R.M. Boothby, "Radiation Effects in Nickel-Based Alloys", *Comprehensive Nuclear Materials*, Elsevier, Amsterdam, 4 (2012) 123-150.
- [219] HASTELLOY® N alloy - Haynes International, H-2052B, 2002, available at: www.haynesintl.com/pdf/h2052.pdf
- [220] D. Leblanc, "Molten salt reactors: A new beginning for an old idea", *Nucl. Eng. Des.* 240 (2010) 1644-1656.
- [221] M.H. Yun, J.P. Ennis, H. Nickel and H. Schuster, "The Effect of High Temperature Reactor Primary Circuit Helium on the Formation and Propagation of Surface Cracks in Alloy 800H and Inconel 617", *J. Nucl. Mater.* 125-3 (1984) 258-272.

- [222] K. Natesan, A. Purohit and S.W. Tam, “Materials Behavior in HTGR Environments”, report NUREG/CR-6824, Office of Nuclear Regulatory Research, Washington (2003).
- [223] W.L. Graham, “Corrosion of Metallic Materials in HTR-Helium Environments”, *J. Nucl. Mater.* 171 (1990) 76 – 83.
- [224] C. Cabetand and B. Duprey, “Long Term Oxidation Resistance of Alloys for Gas-Cooled Reactors”, *Nuclear Engineering and Design* 251 (2012) 139–145.
- [225] J. Berka, M.Vilémová and P. Sajdl, “Testing of Degradation of Alloy 800 H in Impure Helium at 760°C”, *J. Nucl. Mater.* 464 (2015) 221–229.
- [226] Judge, C.D., Griffiths, M., Walters, L., Wright, M., Bickel, G.A., Woo, O.T., Stewart, M., Douglas, S.R. and Garner, F., Embrittlement of Nickel Alloys in a Candu* Reactor Environment. In *Effects of Radiation on Nuclear Materials*, Yamamoto, T., Ed. ASTM International: Anaheim, CA, 2012; Vol. 25, pp 161-175.
- [227] Judge, C.D., Gauquelin, N., Walters, L., Wright, M., Cole, J.I., Madden, J., Botton, G.A. and Griffiths, M., *Journal of Nuclear Materials* 2015, 457 (0), 165-172.
- [228] Griffiths, M., Bickel, G.A., Donohue, S.A., Feenstra, P., Judge, C.D., Walters, L. and Wright, M.D. In *Degradation of Ni-Alloy Components in Candu Reactor Cores*, 16th Int. Conference on Environmental Degradation of Materials in Nuclear Power Systems – Water Reactors, Asheville, North Carolina, USA, August 11-15, 2013; Asheville, North Carolina, USA, 2013.
- [229] Zhang, H.K., Yao, Z., Morin, G. and Griffiths, M., *Journal of Nuclear Materials* 2014, 451 (1–3), 88-96.
- [230] Walters, L., Bickel, G.A. and Griffiths, M., The Effects of Microstructure and Operating Conditions on Irradiation Creep of Zr-2.5nb Pressure Tubing. In *Zirconium in the Nuclear Industry: 17th International Symposium*, ASTM International: 2014.
- [231] Griffiths, M., Poff, D., Yao, Z. and Zhang, H.K. In *Performance of Ni Alloy Components in Candu Reactors*, International Conference on Materials Science and Technology, Montreal, Quebec, Canada, October 27-31, 2013; Montreal, Quebec, Canada, 2013.
- [232] Garner, F., Griffiths, M. and Greenwood, L.R., Enhancement of Irradiation Creep of Nickel-Bearing Alloys in Thermalized Neutron Spectra Characteristic of

Lwr and Candu Reactors. In *Effects of Radiation on Nuclear Materials*, Yamamoto, T., Ed. ASTM International: Anaheim, CA, 2012; Vol. 25.

[233] Bickel, G.A., Griffiths, M., Douchant, A., Douglas, S.R., Woo, O.T. and Buyers, A., *Journal of ASTM International* 2011, 8 (2).

[234] Brinkman, Jr A. "Production of atomic displacements by high-energy particles." *American Journal of Physics* 24 (1956): 246-267.

[235] Kwon J, Lee G, Shin C. "Multiscale modeling of radiation effects on materials: pressure vessel embrittlement." *Nucl Eng Technol* 2009; 41(1).

[236] Kinchin, G. H., and R. S. Pease. "The displacement of atoms in solids by radiation." *Reports on progress in physics* 18.1 (1955): 1.

[237] Lindhard, Jens, Morten Scharff, and Hans E. Schiøtt. *Range concepts and heavy ion ranges*. Copenhagen: Munksgaard, 1963.

[238] Thompson, M.W., Wright, S.B., 1965. A new damage for predicting the effect of reactor irradiation on graphite in different neutron spectra. *J. Nucl. Mater.* 16, 146–154.

[239] Norgett, M.J., Robinson, M.T., Torrens, I.M., 1975. A proposed method of calculating displacement dose rates. *Nucl. Eng. Des.* 33, 50–54.

[240] Was, Gary S. "The Displacement of Atoms." *Fundamentals of Radiation Materials Science*. Springer, New York, NY, 2017. 77-130.

[241] Black, G., et al. "Origin and validity of graphite dosimetry units and related conversion factors." *Annals of Nuclear Energy* 94 (2016): 241-250.

[242] J.F. Ziegler, J.P. Biersack, M.D. Ziegler, SRIM 2013, (2013). <http://www.srim.org/>.

[243] J.F. Ziegler, J.P. Biersack, M.D. Ziegler, SRIM - The Stopping and Range of Ions in Matter, SRIM Company, 2008.

[244] ASTM E521 (1996) Standard practice for neutron radiation damage simulation by charged-particle irradiation. Annual Book of ASTM Standards, vol 12.02. American Society for Testing and Materials, Philadelphia.

[245] M. Griffiths, G.A. Bickel and S.R. Douglas, 2010, "Irradiation-Induced Embrittlement of Inconel 600 Flux Detectors in CANDU Reactors", Proceedings of the 18th International Conference on Nuclear Engineering (ICONE18), Xi'an, China, May 17-21 (2010) Paper ICONE18-30121.

- [246] F.A. Garner, L.R. Greenwood, E.R. Gilbert and M. Griffiths, "Impact of Ni-59 (n, alpha) and (n, p) Reactions on DPA Rate, Heating Rate, Gas Generation and Stress Relaxation in Fast, Light Water and CANDU Reactors", Proc. 14th Intern. Conf. on Environmental Degradation of Materials in Nuclear Power Systems (2009).
- [247] L. R. Greenwood, 1983, "A new calculation of Thermal Neutron Damage and Helium Production in Nickel", J. Nucl. Mater. 115 (1983) 137-142.
- [248] L.R. Greenwood, F.A. Garner, 1996, "Hydrogen Generation Arising from the 59Ni (n,p) Reaction and its impact on Fission-Fusion Correlations", J. Nucl. Mater. Vol. 233-237 Part 2 (1996) 1530-1534.
- [249] W.G. Wolfer, "Fundamental Properties of Defects in Metals", Comprehensive Nuclear Materials, Elsevier, Amsterdam, 1.01 (2012) 1-45.
- [250] N.M. Ghoneim and G.L. Kulcinski, "The Use of the Fully Dynamic Rate Theory to Predict Void Growth in Metals", Rad. Effects 41 (1979) 81-89.
- [251] Greenwood, L.R., Garner, F., Oliver, B.M., Grossbeck, M.L. and Wolfer, W.G., *Journal of ASTM International* 2004, 1 (4).
- [252] Zinkle, S.J., 1.03 - Radiation-Induced Effects on Microstructure*. In *Comprehensive Nuclear Materials*, Konings, R. J. M., Ed. Elsevier: Oxford, 2012; pp 65-98.
- [253] Yamamoto, T., Odette, G.R., Kishimoto, H., Rensman, J.-W. and Miao, P., *Journal of Nuclear Materials* 2006, 356 (1-3), 27-49.
- [254] Yamamoto, N., Chuto, T., Murase, Y. and Nagakawa, J., *Journal of Nuclear Materials* 2004, 329-333, Part B (0), 993-997.
- [255] Trinkaus, H. and Ullmaier, H., *Journal of Nuclear Materials* 1988, 155-157, Part 1 (0), 148-155.
- [256] Trinkaus, H. and Ullmaier, H., *Journal of Nuclear Materials* 1994, 212-215, Part 1 (0), 303-309.
- [257] Mansur, L.K. and Grossbeck, M.L., *Journal of Nuclear Materials* 1988, 155-157, Part 1 (0), 130-147.
- [258] Imasaki, K., Hasegawa, A., Nogami, S. and Satou, M., *Journal of Nuclear Materials* 2011, 417 (1-3), 1030-1033.

[259] Hunn, J.D., Lee, E.H., Byun, T.S. and Mansur, L.K., *Journal of Nuclear Materials* 2000, 282 (2-3), 131-136.

[260] Grossbeck, M.L., 1.04 - Effect of Radiation on Strength and Ductility of Metals and Alloys. In *Comprehensive Nuclear Materials*, Konings, R. J. M., Ed. Elsevier: Oxford, 2012; pp 99-122.

[261] Evans, J.H., *Journal of Nuclear Materials* 1977, 68, 129-140.

[262] Dai, Y., Odette, G.R. and Yamamoto, T., 1.06 - the Effects of Helium in Irradiated Structural Alloys. In *Comprehensive Nuclear Materials*, Konings, R. J. M., Ed. Elsevier: Oxford, 2012; pp 141-193.

[263] Edwards, D.J., Simonen, E.P., Garner, F.A., Greenwood, L.R., Oliver, B.M. and Bruemmer, S.M., *Journal of Nuclear Materials* 2003, 317 (1), 32-45.

[264] Edwards, D.J., Garner, F.A., Bruemmer, S.M. and Efsing, P., *Journal of Nuclear Materials* 2009, 384 (3), 249-255.

[265] Endf/B-Vi Nuclear Library, [Http://T2.Lanl.Gov](http://T2.Lanl.Gov).

[266] Olander, Donald R., and Arthur T. Motta. "A new book: 'light-water reactor materials'." *Nuclear Engineering and Technology* 37.4 (2005): 309-316.

[267] Carnahan, N.F. and Starling, K.E., *The Journal of Chemical Physics* 1697, 51 (2).

[268] G.S. Was, in: *Fundamentals of Radiation Materials Science*, 2007, pp. 581.

[269] Stoller, R.E. and Zinkle, S.J., *Journal of Nuclear Materials* 2000, 283-287, Part 1 (0), 349-352.

[270] Orowan, E., *Internal Stresses in Metals and Alloys*. The Institute of Metals: London, 1948.

[271] Bement, A.L.J., *Strength of Metals and Alloys*. ASM International: Metals Park, OH, 1973.

[272] Kelly, P.M., *International Metallurgical Reviews* 1973, 18 (31).

[273] Kocks, U.F., *Materials Science and Engineering* 1977, 27, 291-298.

[274] Zhang, H.K. Irradiation Induced Damage in Candu Spacer Material Inconel X-750. Queen's University, 2013.

- [275] Schäublin, R., Yao, Z., Baluc, N. and Victoria, M., *Philosophical Magazine* 2005, 85, 769-777.
- [276] Yao, Z., Schaublin, R. and Victoria, M., *Journal of Nuclear Materials* 2002, 311, 374-379.
- [277] Knapp, J.A., Follstaedt, D.M. and Myers, S.M., *Journal of Applied Physics* 2008, 103 (013518-1).
- [278] Friedel, J. "Dislocations Pergamon." *New York* (1964): 274.
- [279] F Kroupa, P.B Hirsch Disc. Faraday Soc., 38 (1964), p. 49.
- [280] Young, J.A., Wirth, B.D., Robach, J. and Robertson, I.M. In *Dislocation Interactions with Voids and He Bubbles in Fcc Materials*, 11th International Conference on Fusion Reactor Materials, Kyoto, Japan, December 7-12, 2003; Kyoto, Japan, 2003.
- [281] Simar, A., Voigt, H.-J.L. and Wirth, B.D., *Computational Materials Science* 2011, 50 (5), 1811-1817.
- [282] L.E. Thomas and S.M. Bruemmer, "Radiation-Induced Microstructural Evolution and Phase Stability In Ni-Base Alloy 718", Eighth International Symposium on Environmental Degradation of Materials in Nuclear Power Systems, ANS (1997) 772.
- [283] Nelson, R. S., J. A. Hudson, and D. J. Mazey. "The stability of precipitates in an irradiation environment." *Journal of Nuclear Materials* 44.3 (1972): 318-330.
- [284] Camus, Eric, et al. "Evolution of long-range order and composition for radiation-induced precipitate dissolution." *Physical Review B* 54.5 (1996): 3142.
- [285] Zhang, He Ken, et al. "Microstructural evolution of CANDU spacer material Inconel X-750 under in situ ion irradiation." *Journal of Nuclear Materials* 443.1-3 (2013): 49-58.
- [286] Zhang, He K., et al. "Elevated temperature irradiation damage in CANDU spacer material Inconel X-750." *Journal of Nuclear Materials* 445.1-3 (2014): 227-234.
- [287] Carsughi, Flavio, et al. "Investigations on Inconel 718 irradiated with 800 MeV protons." *Journal of nuclear materials* 264.1-2 (1999): 78-88.
- [288] M.L. Hamilton, F.A Garner, M.B. Toloczko, S.A Maloy, W.F Sommer, M.R. James, P.D Ferguson, M.R. Louthan Jr., "Shear punch and tensile

measurements of mechanical property changes induced in various austenitic alloys by high energy mixed proton and neutron irradiation at low temperatures”, J. Nucl. Mater. 283-287 (2000) 418.

[289] M.R. James, S.A Maloy, F.D Gac, W.F Sommer, J Chen, H Ullmaier, “The mechanical Properties of an Alloy 718 Window after Irradiation in a Spallation Environment”, J. Nucl. Mater. 296 (2001) 139.

[290] W.J. Mills, “Effect of Irradiation on the Fracture Toughness of Alloy 718 Plate and Weld”, J. Nucl. Mater. 199 (1992) 68.

[291] F.A. Garner, “Evolution of Microstructure in Face-Centred Cubic Metals during Irradiation”, J. Nucl. Mater. 205 (1993) 98-117

[292] B.H. Sencer,, G.M Bond, F.A Garner, M.L Hamilton, S.A Maloy, W.F Sommer, “Correlation of radiation-induced changes in mechanical properties and microstructural development of Alloy 718 irradiated with mixed spectra of high energy protons and spallation neutrons”, J. Nucl. Mater. 296 (2001) 145.

[293] Hojna, A. Intergranular Fracture and Fracture Toughness of Irradiated Austenitic Stainless Steels of Reactor Core Internals. In Proceedings of the 16th International Symposium on Environmental Degradation of Materials in Nuclear Power Systems—Water Reactors, Ashville, NC, USA, 11–15 August 2013; NACE: Houston, TX, USA, 2014.

[294] Lynch, S.P. Mechanisms of intergranular fracture. Mater. Sci. Forum 1989, 46, 1–24.

[295] Fukuya, K.; Nishioka, H.; Fujii, K.; Kamaya, M.; Miura, T.; Torimaru, T. Material Property Changes of Stainless Steels under PWR Irradiation. In Proceedings of the International Congress on Advances in Nuclear Power Plants 2009 (ICAPP 2009), Tokyo, Japan, 10–14 May 2009.

[296] Fukuya, K.; Nishioka, H.; Fujii, K.; Kamaya, M.; Miura, T.; Torimaru, T. Fracture behavior of austenitic stainless steels irradiated in PWR. J. Nucl. Mater. 2008, 378, 211–219.

[297] Boothby, R.M. and Harries, D.R., Irradiation-Induced Embrittlement and Precipitation in Nimonic Pe16. UKAEA Atomic Energy Research Establishment: 1981.

[298] J.L. Scott, M.L. Grossbeck, and P.J. Maziasz, “Radiation Effects for Materials in Fusion Reactors”, J. Vac. Sci. Technol., 20(4) (1982) 1297.

- [299] M.B. Toloczko, F.A. Garner, V.N. Voyevodin, V.V. Bryk, O.V. Borodin, V.V. Melnychenko and A.S. Kalchenko, "Ion-Induced Swelling of ODS Ferritic Alloy MA957 Tubing to 500 dpa", *J. Nucl. Mater.* 453 (2014) p. 323.
- [300] Evans, J.H., *Journal of Nuclear Materials* 1977, 68, 129-140.
- [301] F. A. Garner, B. M. Oliver, L. R. Greenwood, M. R. James, P. D. Ferguson, S. A. Maloy, and W. F. Sommer, "Determination of Helium and Hydrogen Yield from Measurements on Pure Metals and Alloys Irradiated by Mixed High Energy Proton and Spallation Neutron Spectra in LANSCE", *J. of Nucl. Mater.* 296 (2001) 66-82.
- [302] B. A. Oliver, F. A. Garner, S. A. Maloy, W. F. Sommer, P. D. Ferguson and M. R. James, "Retention of Very High Levels of Helium and Hydrogen Generated in Various Structural Alloys by 800 MeV Protons and Spallation Neutrons", *Proceedings of Symposium on Effects of Radiation on Materials, 20th International Symposium, ASTM STP 1405*, S. T. Rosinski, M. L. Grossbeck, T. R. Allen, and A. S. Kumar, Eds., American Society for Testing and Materials, West Conshohocken, PA (2001) 612-630.
- [303] G.A. Bickel and M. Griffiths, unpublished results.
- [304] F.A. Garner, E.P. Simonen, B.M. Oliver, L.R. Greenwood, M.L. Grossbeck, W.G. Wolfer and P.M. Scott, "Retention of Hydrogen in Fcc Metals Irradiated at Temperatures Leading to High Densities of Bubbles or Voids", *J. Nucl. Mater.* 356 (2006) 122-135.
- [305] Grove, C.A. and Petzold, L.D. In *Mechanisms of Stress Corrosion Cracking of Alloy X750 in High Purity Water*, International Conference on Corrosion of Nickel Base Alloys, Cincinnati, Ohio, October 23-25, 1984; ASM: Cincinnati, Ohio, 1985.
- [306] Young, G.A., Lewis, N., Hanson, M., Matuszyk, W., Wiersma, B. and Gonzalez, S.C.; KAPL Report LM-01K034; *Microstructural and Microchemical Characterization of Dual Step Aged Alloy X-750 and Its Relationship to Environmentally Assisted Cracking*; May 2001.
- [307] Hasegawa, M., Osawa, M. and Natori, A., in *Japanese buth with English titles for Figures, Tetsu To Hagane*; Japan 1979, 65:8.
- [308] W.J. Mills, M.R. Lebo and J.J. Kearns, "Hydrogen Embrittlement, Grain Boundary Segregation and Stress Corrosion Cracking of Alloy X-750 in Low and High-Temperature Water", *Metall. and Mater. Trans A* 30A (1999) 1579-1596.

- [309] Seita, Matteo, et al. "The dual role of coherent twin boundaries in hydrogen embrittlement." *Nature communications* 6 (2015): 6164.
- [310] Yang, W. J. S. "Grain boundary segregation in solution-treated Nimonic PE16 during neutron irradiation." *Journal of Nuclear Materials* 108 (1982): 339-346.
- [311] Yang, W. J. S., et al. "Post-irradiation ductility loss of Fe-Ni-base precipitation hardenable alloys." *Journal of Nuclear Materials* 132.3 (1985): 249-265.
- [312] W.J. Mills, "Effect of Temperature on the Fracture Toughness Behavior of Inconel X-750", *Fractography and Materials Science*, ASTM STP-733 (1981) 98
- [313] Hojná, Anna. "Overview of Intergranular Fracture of Neutron Irradiated Austenitic Stainless Steels." *Metals* 7.10 (2017): 392.
- [314] Margolin, B.Z.; Kursevich, I.P.; Sorokin, A.A.; Neustroev, V.S. The Relationship of Radiation Embrittlement and Swelling for Austenitic Steel for WWER Internals. In *Proceedings of the ASME 2009 Pressure Vessels and Piping Conference*, Prague, Czech Republic, 26–30 July 2009; ASME: Philadelphia, PA, USA, 2009.
- [315] <https://www.hysitron.com/media/1637/ptpou-r1f.pdf>
- [316] T.J Koppenaal, R.J Arsenault *Metall. Rev.*, 16 (1971), p. 175
- [317] A.L Bement Jr., W.C Leslie (Ed.), *Second International Conference on Strength of Metals and Alloys*, vol. II, American Society for Metals, Metals Park, OH (1970), p. 693
- [318] A.K. Seeger, in: *Second UN Conference on Peaceful Uses of Atomic Energy*, vol. 6, United Nations, New York, 1958, p. 250
- [319] K. Farrell, T.S. Byun, N. Hashimoto, Oak Ridge National Lab., Oak Ridge, TN Report ORNL/TM-2002/63, 2003
- [320] Zinkle, S. J., et al. "Microstructures Of Irradiated And Mechanically Deformed Metals And Alloys: Fundamental Aspects." *MRS Proceedings*. Vol. 792. Cambridge University Press, 2003.
- [321] Hashimoto, N., et al. "Deformation mechanisms in 316 stainless steel irradiated at 60 C and 330 C." *Journal of nuclear materials* 283 (2000): 528-534.
- [322] Lucas, G. E. "The evolution of mechanical property change in irradiated austenitic stainless steels." *Journal of Nuclear Materials*, 206-2 (1993): 287-305.

[323] Sencer, Bulent H., et al. "Microstructural evolution of Alloy 718 at high helium and hydrogen generation rates during irradiation with 600–800 MeV protons." *Journal of nuclear materials* 283 (2000): 324-328.

[324] J.L. Nelson, and S. Floreen, Second International Symposium on Environmental Degradation of Materials in Nuclear Power Systems-Water Reactors, (LaGrange Park, IL: American Nuclear Society, 1986), p. 632.

[325] K. Hosoi, S. Hattori, Y. Urayama, I. Masaoka, and R. Sasaki, International Symposium on Environmental Degradation of Materials in Nuclear Power Systems- Water Reactors, (Houston, TX: NACE, 1984), p. 34.

[326] T. Yonezawa, K. Onimura, O. Sakamoto, N. Sasaguri, H. Nakata, and H. Susukida, International Symposium on Environmental Degradation of Materials in Nuclear Power Systems-Water Reactors (Houston, TX: NACE, 1984), p. 345.

[327] Ha, Jeong Won, et al. "Effect of cold drawing ratio on γ' precipitation in Inconel X-750." *Materials Characterization* 96 (2014): 1-5.

[328] Smith, G. D., and S. J. Patel. "The role of niobium in wrought precipitation-hardened nickel-base alloys." *Proceedings of Superalloys 718* (2005): 625-706.

[329] Knoop, Frederick, Chauncey G. Peters, and Walter B. Emerson. "A sensitive pyramidal-diamond tool for indentation measurements." *Journal of Research of the National Bureau of standards* 23.1 (1939): 39.

[330] Thomas H. Courtney. *Mechanical Behavior of Materials*, 2nd ed. Waveland Press, Inc., pp. 198-205.

[331] Maciejewski, Kimberly E. *The role of microstructure on deformation and damage mechanisms in a Nickel-based superalloy at elevated temperatures*. University of Rhode Island, 2013.

[332] D. Metzger, personal communications, unpublished work.